Probing Intermolecular Interactions and Three-dimensional Packing of Organic Molecules by Solid-State NMR

by

Amy Louise Webber

Thesis

Submitted to the University of Warwick

for the degree of

Doctor of Philosophy

Department of Physics

March 2010

THE UNIVERSITY OF
WARWICK

Contents

List of Tables

List of Figures

Acknowledgments

First and foremost, I would like to thank my supervisor, Dr. Steven P. Brown, for his constant guidance and support throughout my PhD. I also thank him for providing me with the opportunity to carry out ‘proper’, exciting science and for encouraging me to present my research on countless occasions. I would like to express my appreciation to the members of the solid-state NMR group for making my time at Warwick so interesting and enjoyable. In particular, I am grateful to Dr. John Griffin for introducing me to the wonders of NMR experiments, Dr. Johanna Becker-Baldus for all her advice and many interesting discussions and Dr. Nathan Barrow, for his friendship.

I thank the groups of Prof. Lyndon Emsley, Prof. Gian Piero Spada and Dr. Rosa Claramunt for their contributions to this work, along with Dr. Jonathan Yates and Dr. Anne-Christine Uldry for their help with CASTEP calculations and Dr. Paul Hodgkinson for providing the MATLAB fitting routines used in this thesis. Financial support from the EPSRC and the EU-NMR initiative is also gratefully acknowledged.

I am incredibly thankful to all my friends and family, especially my parents, for their love and support throughout my studies. This would not have been possible without you. Finally, for everything, I thank Sam and for providing me with a reason to smile every day, I thank a scientist’s best friend, Alfie.

Made in LaTeX.

Declarations

The work contained in this thesis is a result of my original research, carried out between October 2006 - February 2010, under the supervision of Dr. Steven P. Brown at the University of Warwick. Where contributions of others are included, these are indicated within the text. This work has not been submitted for another degree.

Work presented in chapter 4 and results given in chaper 5 have recently been accepted for publication [1], while those discussed in chapter 8 (specifically §8.3.1) have been published [2]. A complete list of publications to which the author has contributed during the course of this project is given below.

A-C. Uldry, J. M. Griffin, J. R. Yates, M. Pérez-Torralba, M. D. Santa María, A. L. Webber, M. L. L Beaumont, A. Samoson, R. M. Claramunt, C. J. Pickard and S.P. Brown, 'Quantifying Weak Hydrogen Bonding in Uracil and 4- Cyano-4 ethynylbiphenyl: A Combined Computational and Experimental Investigation of NMR Chemical Shifts in the Solid State,' J. Am. Chem. Soc. **130,** 945-954 (2008) [3]

I. Hung, A-C. Uldry, J. Becker-Baldus, A. L. Webber, A. Wong, M. E. Smith, S. A. Joyce, J. R. Yates, C. J. Pickard, R. Dupree and S. P. Brown, 'Probing Heteronuclear ^{15}N-^{17}O and ^{13}C-^{17}O Connectivities and Proximities by Solid-State NMR Spectroscopy,' J. Am. Chem. Soc. **131,** 1820-1834

(2009) [2]

Z. D. Zujovic, C. Laslau, G. A. Bowmaker, P. A. Kilmartin, A. L. Webber, S. P. Brown and J. Travas-Sejdic, ‘Role of Aniline Oligomeric Nanosheets in the Formation of Polyaniline Nanotubes,’ Macromolecules. **43,** 662-70 (2010) [4]

A. L. Webber, B. Elena, J. M. Griffin, J. R. Yates, T. N. Pham, F. Mauri, C. J. Pickard, A. M Gil, R. Stein, A. Lesage, L. Emsley and S. P. Brown, ‘Solid-State NMR Spectroscopy of a Disaccharide: Complete Resonance Assignment from ^{1}H -^{1}H DQ-SQ CRAMPS and ^{1}H (DQ-DUMBO)-^{13}C (SQ) Refocused INEPT 2D Spectra and First-Principles Calculations,’ Phys. Chem. Chem. Phys., *accepted* (2010) [1]

Abstract

Identifying the ordered three-dimensional structures formed by atoms and molecules is essential to understanding the properties of solid-state materials. Solid-state NMR is an extremely sensitive structural probe and offers atomic-level information regarding the three-dimensional packing of molecules and the intermolecular interactions, for example, hydrogen bonding, which control this. Recently, the combination of advanced solid-state NMR experiments and complementary computational techniques have led to the emergence of the field of 'NMR crystallography', which shows great potential for the structural determination of systems where traditional diffraction-based methods are not suitable.

The work in this thesis uses a combined approach of high-resolution MAS NMR experiments and first-principles (GIPAW) calculations of NMR parameters to provide structural insight into a range of challenging organic systems. In particular, ^{1}H-^{13}C and ^{1}H DQ (double-quantum) CRAMPS (combined rotation and multiple pulse spectroscopy) techniques are employed to identify ^{1}H and ^{13}C NMR chemical shifts and close ^{1}H-^{1}H interatomic proximities. A new ^{1}H DQ-^{13}C SQ (single-quantum) experiment is presented that better allows intra- and intermolecular ^{1}H-^{1}H distances to be identified in the pharmaceutical compound, penicillin and the disaccharide, β-maltose monohydrate, notably enabling, for the first time, the full ^{1}H resonance assignment of the latter. Using a similar methodology, a 'spectrum to structure' approach is applied to identify modes of self assembly for guanosine derivatives for which single-crystal diffraction structures could not be obtained. In addition, chemical shift calculations on the full unit cell (348 atoms) of a complex pyrazole allow the complete assignment of experimental ^{1}H, ^{13}C resonances for each of the six independent molecules of the asymmetric unit cell. Finally, hydrogen-bond mediated $^{2h}J_{^{15}\mathrm{N}^{17}\mathrm{O}}$ and $^{2h}J_{^{15}\mathrm{N}^{13}\mathrm{C}}$ couplings across NH$\cdots$O and N$\cdots$HC hydrogen bonds are determined experimentally for the first time by the use of heteronuclear spin-echo experiments. The J couplings, which have also been determined using first-principles calculations, are a quantitative measure of hydrogen-bonding strength.

Abbreviations

AHT	Average Hamiltonian Theory
BABA	BAck-to-BAck
CD	Circular Dichroism
CDS	Chemical Database Service
COSY	COrrelation SpectroscopY
CP	Cross Polarisation
CRAMPS	Combined Rotation And Multiple Pulse Spectroscopy
CSA	Chemical Shift Anisotropy
DFT	Density Functional Theory
DQ / DQC	Double Quantum Coherence
DRAMA	Dipolar Recovery At the Magic Angle
DRAWS	Dipolar Recovery with A Windowless Sequence
DUMBO	Decoupling Under Mind Boggling Optimization
FID	Free Induction Decay
FSLG	Frequency Switched Lee-Goldburg
FWHMH	Full Width at Half Maximum Height
GIAO	Gauge Invariant Atomic Orbital
GIPAW	Gauge Including Projector Augmented Waves
HMQC	Heteronuclear Multiple-Quantum Correlation
HORROR	HOmonucleaR ROtary Resonance
HSQC	Heteronuclear Single-Quantum Correlation
INADEQUATE	Incredible Natural Abundance DoublE QUAntum Transfer Experiment
INEPT	Insensitive Nuclei Enhanced by Polarization Transfer
MAS	Magic Angle Spinning
MQ / MQC	Multiple Quantum Coherence

NMR	Nuclear Magnetic Resonance
NOESY	Nuclear Overhauser Effect SpectroscopY
PAS	Principal Axis System
PMLG	Phase Modulated Lee-Goldburg
POSTC7	Permutationally Offset Stabilized C7
PSD	Proton Spin Diffusion
r.f.	Radiofrequency
SPINAL	Small Phase INcremental ALternation
SQ / SQC	Single Quantum Coherence
TPPI	Two Pulse Phase Incremented
TPPM	Two Pulse Phase Modulated

1

Introduction

The structural characterisation of solid materials is crucial to the physical sciences, as the three-dimensional arrangement of atoms and molecules ultimately determines the chemical and physical properties of a substance. It is also becoming increasingly apparent that there exist many important chemical and biological systems for which traditional diffraction-based methods of structural determination are unsuitable. Nuclear Magnetic Resonance (NMR), however, does not suffer from the same limiting factors as diffraction techniques and therefore represents an extremely powerful, non-invasive probe of molecular structure. Indeed, NMR is now considered an essential characterisation technique for solution-state samples and, with advances in high-resolution magic-angle spinning (MAS) techniques, is being ever more recognised as a valuable experimental approach in the solid state. In particular, the NMR chemical shift offers site-specific information on an atomic level whereby different chemical environments are distinguished, and internuclear spin-spin couplings provide through-bond connectivities or through-space proximities between atoms, enabling vital structural information to be determined.

More recently, the combination of high-resolution solid-state NMR with accurate computational techniques has been shown to offer much insight into the determination of three-dimensional solid-state structures and has been termed 'NMR crystallography' [5–8]. As such, this is now a particularly exciting period of development for solid-state NMR techniques, especially those designed for application to organic powdered materials, as discussed throughout this work. Specifically, a range of advanced experimental NMR methods (primarily, $I = {}^1\!/_2$; ^{1}H, ^{13}C techniques) are presented in combination with first-principles calculations to investigate key intermolecular interactions and the three-dimensional packing of organic molecules in the solid state.

1.1 High-Resolution Solid-State NMR

Although the phenomenon of magnetic resonance in the bulk phase was first reported in 1946 [9, 10], it was not until the development, primarily by Ernst, of (one and two dimensional) Fourier Transform (FT) NMR [11] that the sensitivity of this method for chemical characterisation purposes was truly recognised. Since this time, global interest in NMR has grown remarkably and few scientific research laboratories are without access to an NMR spectrometer for structural and dynamical studies of liquid-state samples. When in solution, molecules possess a natural mobility, causing a narrowing of NMR lineshapes and making the extraction of chemical information relatively straightforward. However, for materials in the solid phase, the beneficial molecular motion is largely absent and the anisotropy present (for spin $I = {}^1\!/_2$ nuclei, due to the chemical shift and the dipolar coupling interaction) is manifested as an inherent broadening of the NMR spectrum, drastically reducing the availability of structural information. It is for this reason that progress in the field of solid-state NMR has been slower than in solution and that much development in this area is focussed upon the quest for better spectral resolution.

The first major milestone for this cause was the development of the magic-angle spinning (MAS) technique by Andrew and Lowe [12–14], which aimed to mimic the molecular motion occurring in the liquid phase by physically rotating solid samples at the ‘magic’ angle (54.74°) with respect to the external magnetic field. In time, this has proved to be a revolutionary concept for the removal of broadening anisotropies such as the chemical shift anisotropy (CSA) and the heteronuclear dipolar coupling interaction, yet this was not truly taken advantage of until many years later, when it was combined with the methodology of Cross Polarization (CP). Originally, the CP sequence was devised using static samples whereby specific double-resonance irradiation led to the transfer of spin magnetization from abundant nuclei to nearby isotopically rare species, significantly enhancing the NMR signal detected from dilute spins [15]. The application of spin decoupling [16], following CP irradiation, was demonstrated to remove the effects of heteronuclear dipolar interactions during data acquisition [17], and yet other anisotropic effects e.g., chemical shift anisotropies (CSAs) still hindered spectral resolution. However, in 1976 Schaefer and Stejskal combined a decoupled CP experiment with a sample rotating at the 'magic' angle, thus also removing the CSA broadenings. Hence, a robust procedure for acquiring high-resolution spectra was established [18]. This proved to be pivotal for the development of solid-state measurements upon carbon-containing materials and, indeed, the ^{13}C CP MAS experiment is still the workhorse solid-state NMR sequence applied to organic molecules today. Almost twenty years later, the availability of advanced spectrometer hardware, notably electronics allowing fast and reliable phase switching, enabled the design of more efficient phase-modulated heteronuclear decoupling schemes [19, 20] that provide even greater line narrowing of dilute-spin NMR spectra. Indeed, in such efficiently ^{1}H-decoupled MAS experiments, it is now possible to obtain resolved ^{13}C and ^{15}N CP MAS spectra of large organic molecules containing many NMR resonances. Most notably, high-resolution, multi-dimensional MAS experiments have allowed the complete structural determination of microcrystalline proteins [21, 22] and efforts have also been made to extend these techniques to other key biological systems such as transmembrane proteins [23] and amyloid fibrils [24].

Despite the many successes that followed the widespread use of ^{13}C and ^{15}N MAS NMR, obtaining high-resolution spectra in the presence of strong homonuclear dipolar couplings (e.g., for ^{1}H-^{1}H and ^{19}F-^{19}F nuclei) has proved to be much more of a challenge. As described by Maricq and Waugh [25], the 'homogeneous' nature of dipolar couplings between many like nuclei leads to a significant broadening of NMR resonances, which is only partially averaged by the use of MAS. Thus, more advanced techniques are needed before ^{1}H experiments of organic materials become commonplace.

An alternative approach to line narrowing in homonuclear-coupled systems was first proposed in the mid-1960's, when radiofrequency (*r.f.*) irradiation techniques were developed to decouple the dipolar spin interactions between same-species nuclei. Lee and Goldburg demonstrated, for ^{19}F spectra of static CaF_2 crystals, that continuous off-resonance *r.f.* could be used to induce spin rotations around a direction inclined at the magic angle, with respect to the external magnetic field [26]. The power of this concept has been advanced by the subsequent development of frequency-switched (FSLG) [27] and phase-modulated (PMLG) [28] modifications. Similarly, multiple-pulse schemes, such as the WHH-4 [29] sequence were presented, using an approach of regularly spaced on-resonance pulses to average out the broadening effects of the homonuclear dipolar interaction. Indeed, the WHH-4 experiment saw the beginning of the development of *windowed* homonuclear decoupling sequences, where the time delays between decoupling pulses were appropriate for points of the NMR signal to be directly acquired.

While the development of MAS and *r.f.*-based decoupling schemes led to marked resolution enhancements in the solid state, it is the combination of these two methodologies into the so-called CRAMPS (Combined Rotation and Multiple Pulse Spectroscopy) approach that has the potential to dramatically extend the boundaries of high-resolution NMR for dipolar-coupled nuclei. In 1977, Gerstein *et al.* demonstrated that considerably greater spectral resolution was possible for ^{19}F linewidths of Kel-F, by the application of the multiple-pulse sequence REV-8 [30] at a MAS frequency of 2.5 kHz, such that both homonuclear dipolar broadening and CSA effects were removed [31].

CRAMPS techniques continued to develop for some time, generally with the use of ‘slow’ MAS speeds, i.e., where the period of rotation was much longer in comparison to the cyclic time period of the decoupling sequence, such that the CSA and homonuclear dipolar interactions were effectively averaged separately by the two simultaneously applied techniques. Later analyses of the two averaging processes of CRAMPS have highlighted the detrimental interference effects that can be encountered when the two characteristic time scales approach a similar magnitude, i.e., homonuclear decoupling was applied at faster MAS speeds [32, 33]. However, the use of such slow rotation speeds in CRAMPS reintroduced difficulties for systems where large CSA interactions were present. This was somewhat worsened by the many advances in magnet technology that led to the use of ever greater external field strenghts, such that the magnitude of CSA interations observed increased, linearly. As such, further strategies were necessary to make CRAMPS more suitable at faster rotation frequencies such that an overlapping of sideband patterns could be avoided for homonuclear dipolar coupled systems.

As the turn of the century approached, and the successes of phase-switched heteronuclear decoupling schemes emerged, attention turned to a similar approach for the homonuclear case and the Phase-Modulated Lee-Goldburg (PMLG) [28], DUMBO (Decoupling Under Mind-Boggling Optimization) [34, 35], and symmetry-based sequences [36, 37], were presented. Importantly, as more sophisticated electronics became available, the stability of such homonuclear decoupling pulse sequences greatly improved and significantly better line-narrowing of coupled-spin NMR spectra became possible.

Also, while CRAMPS techniques were being pursued, there were many considerable mechanical developments in terms of probe and rotor design, such that NMR experiments could be carried out at ever greater MAS frequencies. It was observed that, while the effects of homonuclear dipolar couplings on (e.g., ^{1}H) NMR spectra could not be completely removed under MAS rotation, they could be further reduced by increasing the rotation frequency [38]. Therefore, both ^{1}H fast-MAS [39] and CRAMPS [40] experiments have since been presented in abundance, demonstrating well-resolved proton linewidths for the assignment of ^{1}H chemical shifts in solids. Indeed, remarkable progress has been made by modern ^{1}H CRAMPS techniques, which have demonstrated robust and efficient line-narrowing at a range of spinning frequencies [41–43], including at the current limit of ultra-fast rotation, around 65 kHz [44, 45]. As such, over the last decade or so, the ^{1}H chemical shift has drawn much attention as a powerful probe of molecular structure, notably, of key intermolecular interactions, such as hydrogen-bonding and π-π interactions, that control the self-assembly of organic molecules in the solid-state [46–48].

An equally important development for high-resolution structural studies of organic materials was the impressive portfolio of multidimensional NMR sequences, developed primarily by Emsley and co-workers, that often incorporated efficient ^{1}H CRAMPS techniques. For example, the MAS-J-HMQC [49] and refocused INEPT [50] experiments were adapted from earlier, liquid-state methods [51, 52], to give high-resolution, through-bond (^{1}H-^{13}C) correlation spectra. Thus, by exploiting J-coupled pairs of ^{1}H and ^{13}C nuclei, it became possible to resolve and accurately assign both the ^{13}C and ^{1}H resonances of powdered, organic materials and determine atomic connectivites within molecules. The CRAMPS methodology was also integrated into the powerful ^{1}H double-quantum (DQ) - single quantum (SQ) correlation experiment, to improve the determination of proton-proton proximities in crystalline materials. The two-dimensional DQ-SQ experiment relies on the recoupling [53] of the ^{1}H-^{1}H dipolar coupling to identify close proximities between coupled nuclei. ^{1}H DQ techniques are now well established as a probe of molecular structure and intermolecular packing [46, 54], with fast-MAS experiments having previously been demonstrated for a wide range of organic and inorganic materials [55–61]. With the combinination of ^{1}H DQ recoupling sequences (e.g., POST-C7 [62]) and efficient homonuclear decoupling schemes (e.g., PMLG and DUMBO), the ^{1}H DQ CRAMPS [55, 63, 64] experiment has now become applicable to ever more challenging solid-state materials including the dipeptide, β-AspAla [64], the K salt of penicillin G [65], the small drug molecule, thymol [66], an active pharmaceutical ingredient in a tablet formulation [67] and heterogeneous catalysts [68, 69] and this technique is shown to play a key role in the 'NMR crystallography' approach demonstrated in this work.

1.2 The Emergence of NMR Crystallography

The term 'crystallography' is traditionally interpreted as the determination of the atomic arrangement within a solid, specifically by the use of diffraction based techniques. Indeed, single-crystal diffraction has been the primary method of chemical characterisation for some time. However, there are many cases where it is difficult or currently impossible to obtain sufficiently large single crystals, or the nature of the material in general prevents the use of this method. As such, there is currently much interest in the development of alternative methods for determining the three-dimensional solid-state structure for such cases, with considerable effort being focused on powder diffraction techniques [70, 71], ab-initio crystal structure prediction [72–75], and indeed, high-resolution solid-state NMR. Unlike diffraction methods, NMR is a local probe of atomic-level structure and does not rely on long-range order. It is not surprising, therefore, that a great many structural and dynamical studies have been presented using NMR experiments, not just for crystalline materials, but for a wide range of amorphous and heterogeneous systems [76], many of which are inaccessible by other experimental techniques.

In the context of this thesis, solid-state NMR has much potential to play a significant role in the complete structural determination of crystalline powders, primarily in collaboration with first-principles calculations methods of NMR chemical shifts. Specifically, the GIPAW (Gauge Including Projector Augmented Waves) [77, 78] computational approach, developed over the last decade, is based on Density Functional Theory (DFT) and uses planewave pseudopotentials to provide an accuracte description of electronic charge density, and hence NMR chemical shifts, for periodic solid-state materials. GIPAW has made it possible for NMR parameters to be calculated with surprising accuracy, using existing crystallographic structures such as those determined by single-crystal diffraction, hence, establishing a definitive link between the two complementary characterisation techniques. Experimental and GIPAW-based computational studies have been applied with ever increasing success to a wide range of molecular and materials systems [2, 3, 65, 79–87].

Initially, the comparison of experimental and computational NMR parameters was carried out for well-characterised systems to confirm the accuracy of calculations and, also, to aid the chemical shift assignments of experimental spectra. Since then, this branch of the NMR crystallography approach has been shown to validate accurately the crystal structures of a range of molecular powders [5, 65, 88–94]. In particular, this has been remarkably effective at identifying different three-dimensional crystal structures or *polymorphs* [95] exhibited by identical molecular structures, which often arise due to variations in the crystallisation conditions of ordered materials. Experimental chemical shifts are extremely sensitive to small variations in crystallographic structure, such that analyses of chemical shift changes allow different three-dimensional structures to be distinguished, for example by the use of ^{13}C CP MAS spectra of organic powders. For the same reason, crystallographic splittings of ^{13}C chemical shifts are frequently used to identify the number of independent molecules in the crystallographic asymmetric unit, a further parameter which can be validated against potential crystal structures [5] and also used to highlight different structural polymorphs [96]. Polymorphism has many implications within materials chemistry, in particular with respect to pharmaceutical compounds. Much interest has focussed upon the use of simple, robust solid-state NMR experiments to distinguish different three-dimensional structures of such materials, as has been recently reviewed [97–99]. More recently, ^{1}H DQ CRAMPS NMR techniques have also been shown to identify different polymorphic structures of pharmaceutical compounds via the resolution of ^{1}H chemical shifts and the use of ^{1}H DQ recoupling to identify close proton-proton proximities [67]. Further, quantitative insight into crystallographic packing interactions, such as hydrogen bonding, has been demonstrated by studies of proton chemical shifts [3, 80, 100] and the direct measurement (and calculation) of hydrogen-bond mediated J couplings [2, 81, 101, 102].

Recently, the combined approach of experimental NMR and computational techniques has demonstrated the ab-initio crystal structure prediction of a dipeptide [7, 79, 103] and the small drug molecule thymol [66], whereby structural determination protocols have been presented. Clearly, the advancing field of NMR crystallography boasts enormous successes over the last few years, and there are undoubtedly a wide variety of systems across materials science that would benefit from this flexible, multidisciplinary approach to structural characterisation. Hence, at this stage, it is necessary to establish a reliable collection of experimental methods to further the progress of these structure validation and prediction techniques, a contribution to which will be discussed here.

1.3 Thesis Overview

The work presented in this thesis demonstrates the potential of high-resolution solid-state NMR experiments in combination with first-principles calculations, to determine important crystallographic properties of solids. Much emphasis is placed upon the application of many complementary NMR techniques, notably, applied at natural isotopic abundance, in order to probe key intermolecular interactions and three-dimensional packing in organic powders.

Chapters 2 and 3 provide the theoretical framework and background to the experimental methodologies addressed in this thesis, necessary to interpret the results. Specifically, Chapter 2 establishes the quantum mechanical foundations of NMR theory and demonstrates how advanced experimental methods can be devised via the understanding of angular momentum theory, the density operator and an appreciation of spin interaction Hamiltonians. The experimental methods employed in the following results chapters are introduced in Chapter 3, namely the fundamentals of one and two dimensional Fourier Transform NMR, including sign discrimination techniques and the use of phase cycling to extract information regarding various multinuclear spin interactions and coherences. Practical methods for improving the sensitivity and resolution of NMR data are discussed, including details of the Cross Polarization technique, as well as hetero- and homo-nuclear decoupling schemes. The final sections of this chapter introduce the specific NMR sequences used for the experimental work presented in this thesis such as heteronuclear through-bond correlations and homonuclear DQ techniques, where further experimental details are provided. Finally, a discussion of first-principles NMR calculations is presented, along with an assessment of the computational approaches employed in this work.

Chapter 4 presents the first of the experimental results by introducing the current power of the ^{1}H chemical shift and, in particular, ^{1}H DQ methods as a structural probe. Specifically, the development of the new ^{1}H DQ-^{13}C CRAMPS sequence is presented, which offers increased resolution of ^{1}H DQ spectra via the ^{13}C dimension as well as providing through bond ^{1}H-^{13}C assignments, as is shown with a first application to a penicillin salt. This technique is used to interpret intra-and intermolecular ^{1}H-^{1}H proximities in organic systems, with extension to a particularly demanding case presented in the following chapter. As such, the biologically relevant topic of saccharides is addressed in Chapter 5, where the ability of high-resolution ^{1}H-^{13}C solid-state NMR is demonstrated further. Even simple sugars are a considerable challenge for ^{1}H NMR in the solid-state as the similar chemical environments of the ^{1}H sites result in a narrow spectral range of ^{1}H chemical shifts which are difficult to resolve. For example, the disaccharide presented here (β-maltose monohydrate) contains 24 distinct protons, having ^{1}H chemical shifts that all fall within a narrow range of approximately 3 to 7 ppm. Nevertheless, a combination of advanced experimental techniques and first-principles calculations allow the full assignment of all ^{1}H chemical shifts and an investigation into their behaviour with varying temperature. Chapter 6 demonstrates the ability of multinuclear solid-state NMR experiments to distinguish between two different three-dimensional structures formed by synthetic deoxyguanosine derivatives (also at natural isotopic abundance), notably the *G-quartet* and *G-ribbon* assemblies. Using limited existing crystallographic information, a 'spectrum to structure' approach is then applied to predict the structural arrangements of a range of further RNA-base derivatives, for which single-crystal diffraction structures are not available.

In Chapter 7, ^{1}H-^{13}C correlation methods are applied to a complex crystalline pyrazole system to provide further insight into crystal packing, notably, in an ambitious effort to distinguish between the many (Z'=6) individually distinct molecules of the asymmetric unit cell. With the aid of GIPAW calculations on the complete 348 atoms within the unit cell, and 2D through-bond correlation experiments, all ^{1}H and ^{13}C NMR chemical shifts are assigned for each of the six independent molecules of the structure. Finally, Chapter 8 presents the application of the heteronuclear spin-echo experiment to [^{15}N$_2$, ^{17}O$_2$]uracil and [^{15}N, ^{13}C$_2$]4-cyano-4'-ethynylbiphenyl for the detection, and importantly quantitative measurement, of *intermolecular* $^{2h}J_{^{15}\mathrm{N}^{17}\mathrm{O}}$ and $^{2h}J_{^{15}\mathrm{N}^{13}\mathrm{C}}$ couplings for NH$\cdots$O and NH$\cdots$C hydrogen bonds, that control the molecular packing in the solid state.

2

NMR Theory

NMR spectroscopy is designed to observe the bulk nuclear magnetism arising from the behaviour of atomic nuclei within a magnetic field, in order to determine atomic-level information. This chapter outlines the quantum mechanical theory needed to understand this phenomenon, including the formalisms used to describe nuclear spin systems and their time evolution, and examines how static and oscillating magnetic fields are used to perturb these systems such that measurements of the macroscopic NMR signal can be made. The internal spin interactions are also introduced, and their effects upon NMR spectra are described, specifically regarding the determination of structural and dynamical properties of solid-state materials. The introduction presented here draws upon the works of Mehring [104], Levitt [105], Duer [106] and Hore *et al.* [107].

2.1 Nuclear Spin Systems

Along with familiar physical properties such as mass, energy or charge, subatomic particles also possess an intrinsic quantity known as *spin* angular momentum which is quantised into discrete values of $\hbar$ and is identified by the spin angular momentum quantum number, I. This takes a non-negative integer or half-integer value and is determined, for atomic nuclei, by the composite nucleons of the isotope.

For each nucleus with spin, I, there exists $2I + 1$ possible spin states which are degenerate in the absence of an external magnetic field. Application of a magnetic field lifts the degeneracy of the spin energy levels, resulting in an energy difference between the states. Fundamentally, this arises due to the interaction of a magnetic moment, $\boldsymbol{\mu}$, with the applied static magnetic field, $\mathbf{B}_0$. This is referred to as the Zeeman interaction and is described, using classical notation by Eq. 2.1:

$$E = -\boldsymbol{\mu} \cdot \mathbf{B}_0. \tag{2.1}$$

Expressing this in terms of quantum mechanical operators we find that the Zeeman Hamiltonian, $\hat{\mathscr{H}}_Z$, describing the energy of the system in this external field is given by

$$\hat{\mathscr{H}}_Z = -\hat{\mu} \cdot \mathbf{B}_0 = -\gamma\hbar\hat{I} \cdot \mathbf{B}_0 \tag{2.2}$$

where the gyromagnetic ratio, γ, is the constant of proportionality between the magnetic moment operator, $\hat{\mu}$, and the spin operator, $\hat{I}$, and $\hbar$ is the reduced Planck constant ($\hbar = h/2\pi$). For an axial field described only along the z-direction, the Zeeman Hamiltonian becomes

$$\hat{\mathscr{H}}_Z = -\gamma\hbar\hat{I}_z \cdot B_0 \tag{2.3}$$

with $\hat{I}_z$ being the z-component of the spin angular momentum operator. In angular frequency units ($\mathrm{rad\,s^{-1}}$), the Zeeman interaction is given by the Larmor frequency, $\omega_0 = -\gamma B_0$, and hence is dependent upon the size of the external field applied. As γ is a constant for each nuclear isotope, different characteristic Larmor frequencies are observed for different spin types in a fixed external field. As such, the relation between the quantized spin states along the direction of the external field and their respective energies is simplified to:

$$\hat{\mathscr{H}}_Z = \omega_0\hat{I}_z. \tag{2.4}$$

Eq. 2.4 is expressed in angular frequency units where the factor of $\hbar$ is omitted. This convention will be applied from this point forward to all energy operators ($\hat{\mathscr{H}}$).

The NMR experiment exploits the quantization of energy levels for $I \neq 0$ nuclei in a magnetic field by measuring the changes in energies of the various spin states. These energies are very specifically sensitive to the electronic properties and chemical environments of the nuclei and hence NMR spectra contain much information regarding the internal atomic structure and dynamics of materials.

2.1.1 Angular Momentum Operators

The state of any quantum mechanical system is concisely described by the quantum mechanical wavefunction, $|\psi\rangle$, which contains information regarding all physical properties of the system. This information is extracted from the wavefunction by applying the appropriate *operator*, $\hat{A}$, corresponding to the desired physical quantity, where the result is often expressed in terms of the quantum number(s) associated with that operator. Experimental measurements of this quantity are then predicted to yield, on average, a value known as the *expectation value* of that operator, $\left\langle \hat{A} \right\rangle$, given by

$$\left\langle \hat{A} \right\rangle = \langle\psi| \hat{A} |\psi\rangle \, . \tag{2.5}$$

Specifically, nuclear spin wavefunctions are expressed by the functions, $|I, m\rangle$, where I and m are the total spin angular momentum quantum number, and the magnetic quantum number, respectively. Information relating to the spin properties of the nucleus is then extracted from these functions by application of the relevant angular momentum operator, namely, $\hat{I}_x$, $\hat{I}_y$, $\hat{I}_z$ or $\hat{I}^2$ which are the x, y, and z components of the nuclear spin, and the magnitude of the nuclear spin squared, respectively. This set of operators are linked by the relation $\hat{I}^2 = \hat{I}_x^2 + \hat{I}_y^2 + \hat{I}_z^2$, as well as the commutation relations:

$$\left[\hat{I}^2, \hat{I}_z\right] = 0 \tag{2.6}$$

$$\left[\hat{I}_x, \hat{I}_y\right] = i\hat{I}_z \text{ (and subsequent cyclic permutations).} \tag{2.7}$$

These equations state that, at any given time, the total spin angular momentum squared commutes only with one component of spin angular momentum, and that the individual components themselves do not commute with each other. In this context, the z-component, and hence the $\hat{I}_z$ operator, is described in Eq. 2.6, since the external magnetic field is defined along this axis, commonly referred to as the *longitudinal* axis. Similarly, the x-y orientation is described in NMR geometry as the *transverse* plane.

The $|I, m\rangle$ spin wavefunctions are, in fact, *eigenfunctions* of the $\hat{I}^2$ and $\hat{I}_z$ operators and (as a consequence of Eq. 2.4) the Zeeman Hamiltonian operator, hence they are commonly referred to as the Zeeman eigenfunctions, with eigenvalue equations for the spin operators given by

$$\hat{I}^2 |I, m\rangle = I(I+1) |I, m\rangle \tag{2.8}$$

$$\hat{I}_z |I, m\rangle = m |I, m\rangle . \tag{2.9}$$

For an orthornormal set of wavefunctions, the expectation values of the total squared spin angular momentum and z-component of angular momentum are (from Eq. 2.5) $I(I+1)$ and m, respectively. As such, m is often referred to as the z-component or projection of angular momentum onto the magnetic field direction, and takes values $-I < -I+1 ... < +I$, resulting in the $2I+1$ possible spin eigenstates described above.

The majority of work presented in this thesis concerns spin $I = 1/2$ nuclei, for which m takes values of $+1/2$ and $-1/2$. The Zeeman eigenstates of such systems are typically referred to as $|\alpha\rangle$ (*spin up*) and $|\beta\rangle$ (*spin down*) states, where

$$\hat{I}_z |\alpha\rangle = +\tfrac{1}{2} |\alpha\rangle \tag{2.10}$$

$$\hat{I}_z |\beta\rangle = -\tfrac{1}{2} |\beta\rangle . \tag{2.11}$$

As such, from Eq. 2.4 it follows, for a z-aligned field, that the corresponding energies of the basis eigenstates are:

$$\hat{\mathscr{H}}_Z |\alpha\rangle = +\tfrac{1}{2}\omega_0 |\alpha\rangle \tag{2.12}$$

$$\hat{\mathscr{H}}_Z |\beta\rangle = -\tfrac{1}{2}\omega_0 |\beta\rangle . \tag{2.13}$$

and so the difference in energy between the two states is equal to the Larmor frequency (in units of $\hbar$). The complete spin wavefunction for a spin $I = 1/2$ nucleus is now described as a superposition of the $|\alpha\rangle$ and $|\beta\rangle$ basis states and is written as a linear combination of these:

$$|\psi\rangle = c_\alpha |\alpha\rangle + c_\beta |\beta\rangle \tag{2.14}$$

where $c_\alpha$and c_β are complex coefficients which measure the contribution of each state to the total superposition. Applying Eq. 2.5, the expectation value of the $\hat{I}_z$ operator is,

$$\begin{aligned}\left\langle \hat{I}_z \right\rangle &= \tfrac{1}{2}(c_\alpha c_\alpha^* - c_\beta c_\beta^*) \\ &= \tfrac{1}{2}|c_\alpha|^2 - \tfrac{1}{2}|c_\beta|^2\end{aligned} \tag{2.15}$$

where, for normalisation $|c_\alpha|^2 + |c_\beta|^2 = 1$. Therefore, the longitudinal component of spin angular momentum is directly related to the respective probabilities of the system being found in either of the two states.

The non-commutation of the $\hat{I}_z$ operator with the $\hat{I}_x$ and $\hat{I}_y$ components, given in Eq. 2.7, indicates that the two transverse spin operators do not share the $|\alpha\rangle$ and $|\beta\rangle$ eigenstates. Instead, these spin operators act to interconvert between the two states:

$$\hat{I}_x |\alpha\rangle = \tfrac{1}{2} |\beta\rangle \qquad \hat{I}_x |\beta\rangle = \tfrac{1}{2} |\alpha\rangle \tag{2.16}$$

$$\hat{I}_y |\alpha\rangle = \tfrac{1}{2}i |\beta\rangle \qquad \hat{I}_y |\beta\rangle = -\tfrac{1}{2}i |\alpha\rangle\,. \tag{2.17}$$

Similarly, the expectation values for the transverse components are expressed as:

$$\left\langle \hat{I}_x \right\rangle = \tfrac{1}{2}(c_\alpha c_\beta^* + c_\beta c_\alpha^*) \tag{2.18}$$

$$\left\langle \hat{I}_y \right\rangle = \tfrac{i}{2}(c_\alpha c_\beta^* - c_\beta c_\alpha^*). \tag{2.19}$$

Comparing Eqs. 2.15, 2.18 and 2.19, it is clear that the expectation value of the longitudinal component of spin angular momentum is directly related to the self-products of the coefficients, $c_\alpha c_\alpha^*$ and $c_\beta c_\beta^*$, whereas the transverse components are determined by the cross products, $c_\alpha c_\beta^*$, and $c_\beta c_\alpha^*$. This result allows a more concise mathematical notation of the spin system to be defined, as is discussed in the following section.

2.2 The Density Operator and Product Operator Formalisms

2.2.1 Isolated spin $I = 1/2$ systems, Populations and Coherences in NMR

For the two eigenstates of a single spin $I = 1/2$ nucleus, a linear mathematical notation (such as Eq. 2.14) is adequate to describe the complete spin wavefunction, and hence the spin components and expectation values of spin measurements are also described in a linear fashion. However, for $I > 1/2$ nuclei, for which the number of potential eigenstates and associated coefficients increases as $2I+1$, or, indeed, for multiple spin systems, many more terms exist, resulting in a lengthy mathematical description. As such, it is convenient to construct a matrix representation for the spin system, operators and observable quantities which can be easily visualised for any value, I. In this context, the *density operator* is defined:

$$\hat{\rho} = \overline{|\psi\rangle \langle\psi|} \tag{2.20}$$

with a corresponding matrix representation, which for a spin $I = 1/2$ nucleus is of the form:

$$\hat{\boldsymbol{\rho}} = \begin{pmatrix} c_\alpha c_\alpha^* & c_\alpha c_\beta^* \\ c_\beta c_\alpha^* & c_\beta c_\beta^* \end{pmatrix}. \tag{2.21}$$

The overbar in Eq. 2.20 indicates that this description is used in reference to the *ensemble average* of the entire spin system of wavefunctions, and corresponds to the bulk macroscopic average of spins, i.e., that which is measured during an experiment. For simplicity of notation, this overbar is omitted below.

The matrix forms of the spin operators for a single $I = 1/2$ nucleus contain elements corresponding to the eigenvalues of the appropriate $|\alpha\rangle$ and $|\beta\rangle$ states, defined by Eqs. 2.10, 2.11, 2.16 and 2.17, such that:

$$\hat{I}_x = \begin{pmatrix} 0 & \frac{1}{2} \\ \frac{1}{2} & 0 \end{pmatrix}, \hat{I}_y = \begin{pmatrix} 0 & -\frac{1}{2}i \\ \frac{1}{2}i & 0 \end{pmatrix}, \hat{I}_z = \begin{pmatrix} \frac{1}{2} & 0 \\ 0 & -\frac{1}{2} \end{pmatrix}. \tag{2.22}$$

Comparison of Eqs. 2.21 and 2.22 to Eqs. 2.15, 2.18 and 2.19, shows that the products of coefficients used to determine the expectation values of the angular momentum components can easily be extracted as elements of the density matrix. The diagonal elements of the density matrix contain self-products of the complex coefficients, upon which the $\hat{I}_z$ (longitudinal) expectation value, depends. These are also the only non-zero elements which appear in the $\hat{I}_z$ operator matrix. Similarly, the off-diagonal terms of the density matrix i.e., those containing cross-product terms of complex coefficients, contribute to the $\hat{I}_x$ and $\hat{I}_y$ (transverse) expectation values, and these same elements are non-zero in the $\hat{I}_x$ and $\hat{I}_y$ operator matrices.

In this context, it is appropriate to introduce the concepts of *populations* and *coherences* in NMR, by further considering a general wavefunction whose coefficients are expressed as the product of a real coefficient, (a_α or a_β) and a phase term (ϕ_α or ϕ_β) i.e.,

$$|\psi\rangle = a_\alpha e^{i\phi_\alpha} |\alpha\rangle + a_\beta e^{i\phi_\beta} |\beta\rangle \,. \tag{2.23}$$

The density matrix for an *individual* spin is then:

$$\hat{\boldsymbol{\rho}} = \begin{pmatrix} a_\alpha^2 & a_\alpha a_\beta e^{i(\phi_\alpha - \phi_\beta)} \\ a_\alpha a_\beta e^{-i(\phi_\alpha - \phi_\beta)} & a_\beta^2 \end{pmatrix} . \tag{2.24}$$

Now, considering the average over a system of many isolated spins; if each individual component spin is in an identical state to its neighbours, the density matrix of the ensemble will be identical to that given in Eq. 2.24. However, if the ensemble is such that the individual spins exist in subtly different states, the phase factors will vary randomly across the system. In this case, when considering the *ensemble average*, these random phase factors will interfere destructively resulting in off-diagonal terms equal to zero in the density matrix:

$$\hat{\boldsymbol{\rho}} = \begin{pmatrix} a_\alpha^2 & 0 \\ 0 & a_\beta^2 \end{pmatrix} . \tag{2.25}$$

The diagonal elements of Eqs. 2.24 and 2.25 are identical, and hence the $\hat{I}_z$, i.e., the $|\alpha\rangle$ and $|\beta\rangle$ basis states, are the same for both pure and mixed ensembles of spins. These are described as the *populations* of the basis states, and as was shown for $\left\langle \hat{I}_z \right\rangle$ in Eq. 2.15, relate directly to the probabilities of spins existing in or *populating* the eigenstates. For example, for a spin system in an external magnetic field and at thermal equilibrium, the ensemble average contains a mixture of populations of the $|\alpha\rangle$ and $|\beta\rangle$ states, the exact populations of which will be determined by Boltzmann statistics as:

$$\hat{\boldsymbol{\rho}} = \begin{pmatrix} p_\alpha & 0 \\ 0 & p_\beta \end{pmatrix} \tag{2.26}$$

where p_α and p_β are the probabilities of the spins existing in either of the two states. The population difference between the states is directly proportional to the z component of spin angular momentum, which over the ensemble is referred to as the bulk longitudinal magnetization. Often, the scaling factor is simply omitted and it is stated that the density operator at thermal equilibrium is equivalent to I_z (see ref[107] §8.4).

Returning, now, to the off-diagonal terms of the matrices in Eqs. 2.24 and 2.25, i.e., those which are proportional to the transverse $\hat{I}_x$ and $\hat{I}_y$ components, non-zero terms only exist for pure ensembles which possess a *phase coherence* between the individual component spins. It is this coherence, specifically, a Single-Quantum Coherence (SQC) that is detected in the form of bulk transverse magnetization, during an NMR experiment (see §2.2.3). Importantly, from Eq. 2.26 it is clear that a spin ensemble at thermal equilibrium contains only population states and so coherences must be introduced into the system by some other means. This is achieved by the application of resonant, oscillating magnetic fields in the form of radiofrequency *r.f.* pulses, as is shown below (see §2.3.2).

The density operator and matrix notations provide a convenient mechanism for extracting the products of coefficients corresponding to populations and coherences of spin systems in an external field. These can also be visualised diagrammatically by considering the form of the Zeeman energy levels. The *product operator* description of the spin components, I_x, I_y, I_z (often written without ˆ for clarity) link the quantum mechanical description to the classical

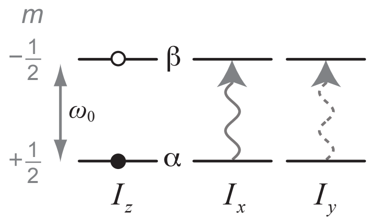

Figure 2.1. Product operator representation of an isolated spin $I = 1/2$ nucleus in a magnetic field using the energy levels of the $|\alpha\rangle$ and $|\beta\rangle$ states. The difference in energy, in units of $\hbar$, is given by the Larmor frequency, $\omega_0 = -\gamma B_0$. I_z gives the occupation or *population* of energy levels, with the difference in shading implying an equilibrium distribution. I_x, I_y (single-quantum $\Delta m = +1/2 - -1/2 = 1$) *coherences* are shown as the relationships between the basis states. The solid and dashed lines represent the phase difference of $\pi/2$ (90°) between I_x and I_y.

vector representation of the bulk magnetization in the spin system [108]. As will be shown in §3.3 this notation provides a simplified alternative to the density matrix analysis under certain interactions, most usefully for describing the evolution of nuclei under the influence of 'weak' spin-spin couplings. Fig. 2.1 presents the energy level diagrams for an isolated $I = 1/2$ nucleus corresponding to the product operator description. The quantized spin states and energy levels are taken from Eqs. 2.12 and 2.13.

2.2.2 A pair of coupled $I = 1/2$ nuclei

Much of the power of NMR lies with the ability to probe spin-spin couplings between pairs of nuclei as is described in §3.3 and §3.4. Both the density matrix and product operator notations are well suited to describe the coupling of nuclear spins. For example, the combined wavefunction of two $I = 1/2$ nuclei, I and S, is written linearly as

$$|\psi\rangle = c_{\alpha\alpha}\,|\alpha_I\alpha_S\rangle + c_{\alpha\beta}\,|\alpha_I\beta_S\rangle + c_{\beta\alpha}\,|\beta_I\alpha_S\rangle + c_{\beta\beta}\,|\beta_I\beta_S\rangle \tag{2.27}$$

with a corresponding density matrix:

$$\hat{\boldsymbol{\rho}} = \begin{pmatrix} c_{\alpha\alpha}c^*_{\alpha\alpha} & c_{\alpha\alpha}c^*_{\alpha\beta} & c_{\alpha\alpha}c^*_{\beta\alpha} & c_{\alpha\alpha}c^*_{\beta\beta} \\ c_{\alpha\beta}c^*_{\alpha\alpha} & c_{\alpha\beta}c^*_{\alpha\beta} & c_{\alpha\beta}c^*_{\beta\alpha} & c_{\alpha\beta}c^*_{\beta\beta} \\ c_{\beta\alpha}c^*_{\alpha\alpha} & c_{\beta\alpha}c^*_{\alpha\beta} & c_{\beta\alpha}c^*_{\beta\alpha} & c_{\beta\alpha}c^*_{\beta\beta} \\ c_{\beta\beta}c^*_{\alpha\alpha} & c_{\beta\beta}c^*_{\alpha\beta} & c_{\beta\beta}c^*_{\beta\alpha} & c_{\beta\beta}c^*_{\beta\beta} \end{pmatrix}. \tag{2.28}$$

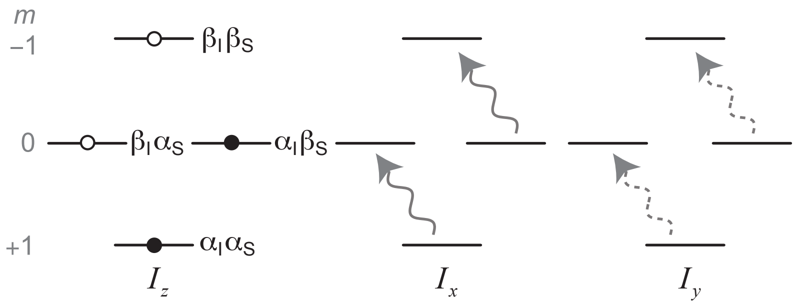

Figure 2.2. Product operator representation of *in-phase* operators for a $I = 1/2$ nucleus, in the presence of a coupled spin, $S = 1/2$, using the conventions defined in Fig. 2.1.

Equally, the matrix form of the angular momentum operators corresponding to $\hat{I}$ and $\hat{S}$ for a two-spin system are obtained by the direct products of the one-spin matrices given in Eq. 2.22 with the identity matrix e.g., as shown here for $\hat{I}$ components:

$$\hat{I}_x = \begin{pmatrix} 0 & 0 & \frac{1}{2} & 0 \\ 0 & 0 & 0 & \frac{1}{2} \\ \frac{1}{2} & 0 & 0 & 0 \\ 0 & \frac{1}{2} & 0 & 0 \end{pmatrix}, \hat{I}_y = \begin{pmatrix} 0 & 0 & -\frac{1}{2}i & 0 \\ 0 & 0 & 0 & -\frac{1}{2}i \\ \frac{1}{2}i & 0 & 0 & 0 \\ 0 & \frac{1}{2}i & 0 & 0 \end{pmatrix}, \hat{I}_z = \begin{pmatrix} \frac{1}{2} & 0 & 0 & 0 \\ 0 & \frac{1}{2} & 0 & 0 \\ 0 & 0 & -\frac{1}{2} & 0 \\ 0 & 0 & 0 & -\frac{1}{2} \end{pmatrix}. \tag{2.29}$$

Equivalent $\hat{S}$ matrices are calculated by reversing the order of the direct product and can be found in Appendix A. These are referred to as *in-phase* product operators, the representative energy levels of which are given in Fig. 2.2. For the matrices given in Eq. 2.29, it can again be seen, that $\hat{I}_z$ (corresponding to populations) has only diagonal non-zero elements, whereas $\hat{I}_x, \hat{I}_y$ (coherences) have only non-zero off-diagonal elements, corresponing to relationships *between* the four two-spin basis states, $|\alpha_I \alpha_S\rangle, |\alpha_I \beta_S\rangle, |\beta_I \alpha_S\rangle, |\beta_I \beta_S\rangle$.

Where there exists a coupling between the pair of spins, the nine two-spin operators obtained as a combination of the $\hat{I}$ and $\hat{S}$ spin states by multiplying the corresponding matrices, are of relevance. For example

$$2\hat{I}_x\hat{S}_z = 2 \begin{pmatrix} 0 & 0 & \frac{1}{2} & 0 \\ 0 & 0 & 0 & \frac{1}{2} \\ \frac{1}{2} & 0 & 0 & 0 \\ 0 & \frac{1}{2} & 0 & 0 \end{pmatrix} \cdot \begin{pmatrix} \frac{1}{2} & 0 & 0 & 0 \\ 0 & -\frac{1}{2} & 0 & 0 \\ 0 & 0 & \frac{1}{2} & 0 \\ 0 & 0 & 0 & -\frac{1}{2} \end{pmatrix} = \begin{pmatrix} 0 & 0 & \frac{1}{2} & 0 \\ 0 & 0 & 0 & -\frac{1}{2} \\ \frac{1}{2} & 0 & 0 & 0 \\ 0 & -\frac{1}{2} & 0 & 0 \end{pmatrix} \tag{2.30}$$

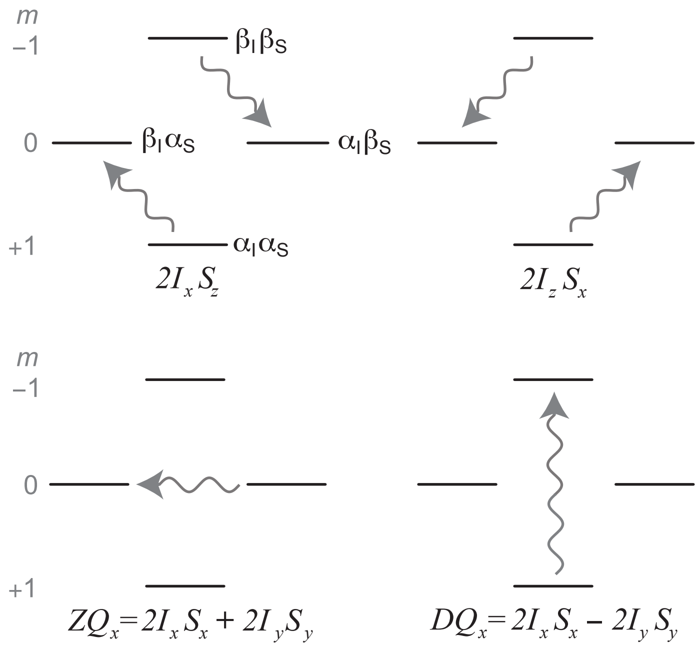

Figure 2.3. Product operator representation of *x-anti-phase* and *multiple-quantum* operators for a coupled pair of $I = 1/2$ nuclei, I and S, using the conventions described in Fig. 2.1.

where a factor of 2 is included for normalisation. A full list of two-spin operator matrices is given in Appendix A.

Fig. 2.3 shows some energy-level representations of the *anti-phase* operators $2\hat{I}_x\hat{S}_z$ and $2\hat{I}_z\hat{S}_x$ along with those corresponding to multiple-quantum coherences (MQC) in the two-spin system. Specifically, the x-components of zero-quantum (ZQ) and double-quantum (DQ) operators for a two-spin $I = S = 1/2$ system consist of the mixed two-spin operators containing no z component; $(\hat{I}_x\hat{S}_x, \hat{I}_y\hat{S}_y, \hat{I}_x\hat{S}_y, \hat{I}_y\hat{S}_x)$. These are named according to the resulting coherence orders between the basis states, with $\Delta m = (0 - 0) = 0$, and $\Delta m = (1 - -1) = 2$ or $\Delta m = (-1 - 1) = -2$, respectively; of particular interest in this work is the double quantum coherence (DQC) between a pair of $I = 1/2$ nuclei, which can be manipulated in order to probe coupling interactions between the nuclear spins.

Computing the matrix for the DQ_x term:

$$\begin{aligned} DQ_x &= \frac{1}{2}\left(2\hat{I}_x\hat{S}_x - 2\hat{I}_y\hat{S}_y\right) \\ &= \begin{pmatrix} 0 & 0 & 0 & \frac{1}{2} \\ 0 & 0 & \frac{1}{2} & 0 \\ 0 & \frac{1}{2} & 0 & 0 \\ \frac{1}{2} & 0 & 0 & 0 \end{pmatrix} - \begin{pmatrix} 0 & 0 & 0 & -\frac{1}{2} \\ 0 & 0 & \frac{1}{2} & 0 \\ 0 & \frac{1}{2} & 0 & 0 \\ -\frac{1}{2} & 0 & 0 & 0 \end{pmatrix} = \begin{pmatrix} 0 & 0 & 0 & \frac{1}{2} \\ 0 & 0 & 0 & 0 \\ 0 & 0 & 0 & 0 \\ \frac{1}{2} & 0 & 0 & 0 \end{pmatrix} \end{aligned} \tag{2.31}$$

the non-zero elements are those corresponding to the coherence between the $|\alpha_I\alpha_S\rangle$ and $|\beta_I\beta_S\rangle$ states, as shown in Fig. 2.3. Consequently, these elements of the density matrix for the two-spin system (Eq. 2.28) contain information regarding DQC present in the spin system and are examined to determine spin-spin coupling information.

The above analysis demonstrates that for a system containing m spin states, it is possible to generate various orders (Δm) of coherence between the energy levels. For an isolated $I = 1/2$ nucleus, this is limited to $\Delta m = 1$ by transitions between the single $|\alpha\rangle$ and $|\beta\rangle$ basis states, whereas for coupled pairs of $I = 1/2$ nuclei, $\Delta m = 0$ and $\Delta m = 2$ may also be created, the latter of which offers information regarding the spin couplings present in the system. It should be noted that many higher coherence orders are then possible for systems of multiple $I = 1/2$ nuclei as well as isolated $I > 1/2$ nuclei but these will not be discussed here. Importantly, whilst anti-phase and non-single-quantum coherences can be generated amongst spin systems, an NMR signal can be induced only by transverse in-phase SQC. As such, sophisticated pulse sequences are designed to manipulate spins and internuclear couplings so as to indirectly acquire the information inherent to the other states, notably multiple-quantum coherence (see §3.3 and §3.4 for descriptions of such pulse sequences used in this thesis).

2.2.3 Evolution of the Density Operator: The NMR Signal

The SQC that is detected by the spectrometer as the NMR signal results from the precession at the Larmor frequency of the bulk magnetization of the spin ensemble (in the tranverse plane). The evolution of this magnetization generates a time-varying signal in a surrounding coil and electronic circuit by the process of electromagnetic induction. Therefore, a description of the spin ensemble behaviour *over a period of time*, i.e., the density operator, $\hat{\rho}(t)$, is needed to describe the induced NMR signal.

For any arbitrary wavefunction, $|\psi\rangle$, the time-dependent Schrodinger equation describes the time evolution of a system as

$$\tfrac{d}{dt}\left|\psi\right\rangle = -i\hat{\mathscr{H}}\left|\psi\right\rangle \tag{2.32}$$

where $\hat{\mathscr{H}}$ is a time-independent Hamiltonian operator acting on the system. Using Eq. 2.20, this is developed into an equivalent interpretation for $\hat{\rho}(t)$:

$$\tfrac{d}{dt}\hat{\rho}(t) = -i\left[\hat{\mathscr{H}}, \hat{\rho}(t)\right], \tag{2.33}$$

the solution of which is:

$$\begin{aligned}\hat{\rho}(t) &= e^{-i\hat{\mathscr{H}}t}\hat{\rho}(0)e^{i\hat{\mathscr{H}}t}\\ &= \hat{U}(t)\hat{\rho}(0)\hat{U}(t)^{-1}.\end{aligned} \tag{2.34}$$

$\hat{U}(t)$ is the *propagator* which describes the Hamiltonian acting between times $t = 0$ and $t = t$. For a constant i.e., time-independent Hamiltonian, this is simply:

$$\hat{U}(t) = \exp\left(-i\hat{\mathscr{H}}t\right). \tag{2.35}$$

However, if the Hamiltonian acting during the time period $t = 0$ to $t = t$ is not constant, but can be separated into piecewise Hamiltonians, each acting successively for a period of time, for example, $\hat{\mathscr{H}}_1$ applies during t_1, then $\hat{\mathscr{H}}_2$

for t_2, etc. the propagator becomes the product of these terms:

$$\hat{U}(t) \; = \; e^{-i\hat{\mathscr{H}}_n t_n} ... e^{-i\hat{\mathscr{H}}_3 t_3} e^{-i\hat{\mathscr{H}}_2 t_2} e^{-i\hat{\mathscr{H}}_1 t_1} \tag{2.36}$$

Similarly, as the Hamiltonian itself may be time dependent, this can be expressed by many Hamiltonians acting successively over infinitesimally small time periods dt, with the propagator now defined as an integral:

$$\hat{U}(t) \; = \; \hat{T} e^{-i \int_o^t \hat{\mathscr{H}}(t)' dt'} \tag{2.37}$$

where $\hat{T}$ is the Dyson time ordering operator, and is necessary when the $\hat{\mathscr{H}}(t)$ operator acting does not commute with itself at different times.

Eq. 2.34 demonstrates that the behaviour of the spin ensemble over time can be wholly described based on a knowledge of the initial density operator at a time $t = 0$, and the propagators which subsequently act on the system. The subsequent NMR signal, $s(t)$, resulting from the transverse magnetization of the spin ensemble at some later time, t, is determined by calculating the expectation value corresponding to this physical observable. For the purposes of sign discrimination (see §3.1.1), both I_x and I_y components of the spin magnetization in the transverse plane are detected. This is achieved by use of the lowering operator $\hat{I}_- = \hat{I}_x - i\hat{I}_y$, such that the SQC detected is, by convention, considered to have coherence order, $p = -1$. The expectation value is then obtained by taking the trace of the scalar product of $\hat{\rho}(t)$ with the transpose, complex conjugate of the lowering operator, $\hat{I}_-^\dagger = \hat{I}_+$:

$$\begin{aligned} s(t) &= Tr\left[\hat{\rho}(t)\hat{I}_+\right] \\ &= Tr\left[\hat{U}(t)\hat{\rho}(t=0)\hat{U}(t)^{-1}\hat{I}_+\right] \end{aligned} \tag{2.38}$$

where $\hat{I}_+ = \hat{I}_x + i\hat{I}_y$, hence providing *real* (I_x) and *imaginary* (I_y) components of the signal. The form of the NMR signal, $s(t)$, given by Eq. 2.38 is calculated for an isolated $I = 1/2$ system in §2.3.2.

2.2.4 Average Hamiltonian Theory

The propagators described in Eqs 2.36 and 2.37 indicate that the series of exponential terms corresponding to each of the acting Hamiltonians must be calculated to describe the time evolution of the spin system. This can be greatly simplified if a propagator can be written which depends on one *average* Hamiltonian, $\bar{\mathscr{H}}$, which has the same overall effect as the series written above [109]. Further, if this Hamiltonian is periodic with a period of t_p, and its effect on the system is only considered at times separated by this period, it is only necessary to calculate the single average Hamiltonian at these points, i.e.:

$$\hat{U}(t) \; = \; e^{-i\bar{\mathscr{H}}t_p} = \; e^{-i\hat{\mathscr{H}}_n t_n}...e^{-i\hat{\mathscr{H}}_3 t_3}e^{-i\hat{\mathscr{H}}_2 t_2}e^{-i\hat{\mathscr{H}}_1 t_1}. \tag{2.39}$$

The series of exponential operators are evaluated using the Magnus expansion [110] to give

$$\bar{\mathscr{H}}(t_p) = \bar{\mathscr{H}}^0 + \bar{\mathscr{H}}^1 + ..., \tag{2.40}$$

where the first and second order terms, are, respectively:

$$\bar{\mathscr{H}}^0 = \frac{1}{t_p}\left(\hat{\mathscr{H}}_1 t_1 + \hat{\mathscr{H}}_2 t_2 + ...\right) \tag{2.41}$$

$$\bar{\mathscr{H}}^1 = -\frac{i}{2t_p}\left(\left[\hat{\mathscr{H}}_2 t_2, \hat{\mathscr{H}}_1 t_1\right] + \left[\hat{\mathscr{H}}_3 t_3, \hat{\mathscr{H}}_1 t_1\right] + \left[\hat{\mathscr{H}}_2 t_2, \hat{\mathscr{H}}_3 t_3\right]...\right). \tag{2.42}$$

This is a particularly appropriate result for solid-state NMR experiments which, often, and throughout this work, are recorded using the *Magic Angle Spinning* (MAS) technique (see §2.4.3), whereby the sample is physically rotated about a fixed axis with respect to the external magnetic field. Such a rotation naturally imposes a periodicity on the Hamiltonian of $t_p = \tau_r$, where τ_r is the time period of one physical rotation. Therefore, to a first-order approximation, the average Hamiltonian acting during a MAS NMR experiment is then simply the average of the piecewise Hamiltonians which operate during one cyclic period. If the individual $\hat{\mathscr{H}}_i$ operators acting during the time period commute with one another this term is generally sufficient, hence the propagator is considered as a linear sum of successive interactions:

$$\hat{U}(t) \;=\; e^{-i\bar{\mathscr{H}}_0\tau_r} \;=\; e^{-\frac{i}{\tau_r}\left(\hat{\mathscr{H}}_1 t_1+\hat{\mathscr{H}}_2 t_2+\ldots\right)} \tag{2.43}$$

For the case where successive Hamiltonians no longer commute, higher order terms of the average Hamiltonian must also be considered to accurately describe the behaviour the system, as will be seen in (§2.4.5).

2.3 External Interaction Hamiltonians

Under the approximations made in §2.2.4, and from Eq. 2.34, a nuclear spin ensemble under Magic Angle Spinning conditions can be considered to evolve under the effect of a total average Hamiltonian, $\bar{\mathscr{H}}_{total}$, which can be written as the sum of the various interaction Hamiltonians active during that time. These interactions can be classified as *external*; chiefly, the interaction of the spin system with external magnetic fields, and *internal*; spin-spin interaction effects, such that:

$$\bar{\mathscr{H}}_{total} = \hat{\mathscr{H}}^{ext} + \hat{\mathscr{H}}^{int} \tag{2.44}$$

where

$$\hat{\mathscr{H}}^{ext} = \hat{\mathscr{H}}_Z + \hat{\mathscr{H}}_{RF} \tag{2.45}$$

$$\hat{\mathscr{H}}^{int} = \hat{\mathscr{H}}_{CS} + \hat{\mathscr{H}}_D + \hat{\mathscr{H}}_J + \hat{\mathscr{H}}_Q. \tag{2.46}$$

For clarity, the superscript 0 term is omitted from the Hamiltonian operators, although the first-order approximation is still applied in the following discussion where the Zeeman Hamiltonian, $\hat{\mathscr{H}}_Z$, is assumed to be dominant.

The $\hat{\mathscr{H}}^{ext}$ term consists of the Zeeman interaction (as described initially in §2.1), and the perturbing interaction of oscillating radiofrequency (*r.f.*) magnetic fields, $\hat{\mathscr{H}}_{RF}$, which are used to create specific spin coherences. The Hamiltonians of the internal spin interactions, used to reveal chemical information, are described in more detail in §2.4.

In general, the interaction Hamiltonians can be represented using Cartesian tensors, as

$$\hat{\mathscr{H}}_\Lambda = \hat{\mathbf{I}} \cdot \tilde{\mathbf{A}} \cdot \hat{\mathbf{S}} = \begin{bmatrix} \hat{I}_x & \hat{I}_y & \hat{I}_z \end{bmatrix} \begin{bmatrix} A_{xx} & A_{xy} & A_{xz} \\ A_{yx} & A_{yy} & A_{yz} \\ A_{zx} & A_{zy} & A_{zz} \end{bmatrix} \begin{bmatrix} \hat{S}_x \\ \hat{S}_y \\ \hat{S}_z \end{bmatrix} \tag{2.47}$$

where $\tilde{\mathbf{A}}$ is second rank tensor, $\hat{\mathbf{I}}$ represents a spin operator and $\hat{\mathbf{S}}$ may be an external field or a second spin operator.

2.3.1 External Hamiltonians in the Rotating Frame

The Cartesian form of the Zeeman interaction between the nuclear spin, $\hat{\mathbf{I}}$, and the static external magnetic field, $\hat{\mathbf{B}}_0$, is expressed as:

$$\hat{\mathscr{H}}_Z = \hat{\mathbf{I}} \cdot \tilde{\mathbf{Z}} \cdot \hat{\mathbf{B}}_0 \tag{2.48}$$

where $\tilde{\mathbf{Z}}$ is related to the identity matrix by

$$\tilde{\mathbf{Z}} = -\gamma \begin{pmatrix} 1 & 0 & 0 \\ 0 & 1 & 0 \\ 0 & 0 & 1 \end{pmatrix} \tag{2.49}$$

and γ is the gyromagnetic ratio. The geometry of the NMR experiment is defined such that, in the *laboratory frame* (where the NMR signal is measured) the external field is aligned along the z-direction, i.e., $\hat{\mathbf{B}}_0 = \begin{bmatrix} 0 & 0 & \hat{B}_0 \end{bmatrix}$, and similarly, a spin system at thermal equilibrium inside this field exists in a population state corresponding to the z-component angular momentum operator, $\mathbf{I} = \begin{bmatrix} 0 & 0 & \hat{I}_z \end{bmatrix}$. Hence, Eq. 2.48 simplifies to:

$$\hat{\mathscr{H}}_Z = -\gamma \mathbf{B}_0 I_z = \omega_0 \hat{I}_z \tag{2.50}$$

as was given in Eq. 2.3 in §2.1. It is typical for field strengths, B_0, to be quoted relative to the Larmor frequency ($\omega_0 = -\gamma B_0$) of the highly sensitive ^{1}H nucleus, and given in units of Hz, i.e., $\omega/2\pi$. Magnetic fields used for solid-state NMR are generally of the order of 5 - 20 Tesla, corresponding to Larmor frequencies of hundreds of MHz (10^8 Hz) with the current upper limit being 1 GHz (10^9 Hz), due to superconductivity technology.

Much weaker magnetic fields can also be used to manipulate nuclear spin systems, provided that they oscillate with a frequency close to (or *resonant* with) the natural Larmor frequency of the nuclei of interest, i.e., $\omega_{rf} \approx \omega_0$. Therefore, as above, this oscillation must also be of the order of 10^8-10^9 Hz, which falls into the radiofrequency (*rf*) regime. Typically, these fields need only be applied for short ($<< 1\,\mathrm{s}$) timescales and are hence referred to as *r.f. pulses*, of magnitude B_1. The oscillating pulses must be applied perpendicular to the external field, i.e., in the transverse plane, to cause an effect on the spin system, and in general, take the form of:

$$\begin{aligned}\hat{\mathbf{B}}_1 &= 2B_1(\cos[\omega_{rf}t + \phi])\mathbf{i} \\ &= B_1(\mathrm{e}^{+i\omega_{rf}t} + \mathrm{e}^{-i\omega_{rf}t})\mathbf{i} \quad \text{if } \phi = 0\end{aligned} \tag{2.51}$$

hence, two counter rotating components of frequencies $+\omega_{rf}$ and $-\omega_{rf}$, where ϕ is the initial phase of the pulse and $\mathbf{i}$ is the unit vector along the x-axis. Only one of these component frequencies is close to the resonance frequency of the nuclei, which by convention, is taken as the positive frequency, ω_{rf}, and so the effect of the latter component is effectively removed. In the Cartesian basis, the Hamiltonian for such a pulse is then:

$$\hat{\mathscr{H}}_{RF} = \hat{\mathbf{I}} \cdot \tilde{\mathbf{Z}} \cdot \hat{\mathbf{B}}_1 = -\gamma B_1[\hat{I}_x \cos(\omega_{rf}t + \phi) + \hat{I}_y \sin(\omega_{rf}t + \phi)]. \tag{2.52}$$

It is convenient and usual in NMR to express this Hamiltonian in a reference frame which is rotating at a frequency, ω_{rf}, about the laboratory frame axis, such that Eq. 2.52 becomes time independent. Hence, the Hamiltonian of an oscillation *rf*-pulse in the *rotating* frame is now:

$$\hat{\mathscr{H}}^{rot}_{RF} = \omega_1[\hat{I}_x \cos(\phi) + \hat{I}_y \sin(\phi)] \tag{2.53}$$

therefore, the initial phase of the pulse defines the initial position of the *r.f.* pulse in the x-y plane of the rotating frame. For example, an initial phase

$\phi = 0$, reduces Eq. 2.53 to:

$$\hat{\mathscr{H}}_{RF}^{rot} = \omega_1 \hat{I}_x \tag{2.54}$$

and so defines the form of a radiofrequency pulse applied along the x-axis. In the above expressions, the frequency $\omega_1 = -\gamma B_1$ (commonly known as the *nutation frequency*) represents the magnitude or strength of the magnetic field due to the *r.f.* pulse applied. As for the case of the static field (given by ω_0), the size of this interaction is also dependent upon the type of nucleus observed (via γ), combined with the size of the alternating current achievable by the NMR electronics. Typically, ω_1 is of the order 10^4-10^5 Hz and, as such, $\hat{\mathscr{H}}_{RF}$ is some orders of magnitude smaller than the dominating Zeeman Interaction, $\hat{\mathscr{H}}_Z$.

Now, expressing the Zeeman Hamiltonian in the rotating frame, Eq. 2.50 becomes:

$$\hat{\mathscr{H}}_Z^{rot} = \Omega \hat{I}_z \tag{2.55}$$

where $\Omega = \omega_0 - \omega_{rf}$, the *resonance offset* frequency of the observed nucleus, conveniently describes the oscillation frequency with respect to the carrier frequency of the *r.f.* pulse. In this respect, by observing NMR signals as this frequency *difference*, instead of absolute values in MHz, more managable values of nuclear frequencies are discussed. Experimentally, this corresponds to 'mixing down' of the induced NMR signal oscillating at the Larmor frequency with the *r.f.* carrier, as is performed by the electronics of the NMR spectrometer, generally yielding nuclear spin offsets of the order of kHz (the largest observable effects correspond to the magnitude of ω_1).

2.3.2 Evolution of the Density Operator due to External Interactions

The rotating frame description provides simplified, time-independent expressions of the external interaction Hamiltonians (Eqs. 2.53 and 2.55) which can be used to compute the evolution of the density matrix for a $I = 1/2$ system under the effect of static and oscillating magnetic fields.

Firstly, for an equilibrium spin ensemble in a static field, we expect an initial (at time, $t = 0$) state of bulk magnetization aligned along the z-axis (see discussion of Eq. 2.26):

$$\hat{\rho}(0) = \hat{I}_z = \begin{pmatrix} \frac{1}{2} & 0 \\ 0 & -\frac{1}{2} \end{pmatrix}. \tag{2.56}$$

Then, considering the propagator for an applied radiofrequency pulse, along the x-direction of the rotating frame:

$$\hat{U}(t) = e^{-i\omega_1 t \hat{I}_x} = \begin{pmatrix} \cos(\frac{1}{2}\omega_1 t) & -i\sin(\frac{1}{2}\omega_1 t) \\ -i\sin(\frac{1}{2}\omega_1 t) & \cos(\frac{1}{2}\omega_1 t) \end{pmatrix} \tag{2.57}$$

(using matrix diagonalisation of the $\hat{I}_x$ operator, given in ref[107]). The density matrix at a later time, $t = t$, under the effect of this *r.f.* pulse, is (from Eq. 2.34):

$$\begin{aligned} \hat{\boldsymbol{\rho}}(t) &= \begin{pmatrix} \cos(\frac{1}{2}\omega_1 t) & -i\sin(\frac{1}{2}\omega_1 t) \\ -i\sin(\frac{1}{2}\omega_1 t) & \cos(\frac{1}{2}\omega_1 t) \end{pmatrix} \begin{pmatrix} \frac{1}{2} & 0 \\ 0 & \frac{1}{2} \end{pmatrix} \begin{pmatrix} \cos(\frac{1}{2}\omega_1 t) & i\sin(\frac{1}{2}\omega_1 t) \\ i\sin(\frac{1}{2}\omega_1 t) & \cos(\frac{1}{2}\omega_1 t) \end{pmatrix} \\ &= \frac{1}{2}\begin{pmatrix} \cos(\omega_1 t) & i\sin(\omega_1 t) \\ -i\sin(\omega_1 t) & -\cos(\omega_1 t) \end{pmatrix}. \end{aligned} \tag{2.58}$$

Comparing Eqs. 2.56 and 2.58, it is clear that the effect of the radiofrequency pulse upon the equilibrium population state of the ensemble is to generate off-diagonal terms in the density matrix, hence coherences, between the spin eigenstates. The expectation values of each of the spin component operators are:

$$\left\langle \hat{I}_x(t) \right\rangle = Tr\left\{ \hat{\rho}(t)\hat{I}_x \right\} = \begin{pmatrix} \frac{1}{4}i\sin(\omega_1 t) & \frac{1}{4}\cos(\omega_1 t) \\ -\frac{1}{4}\cos(\omega_1 t) & -\frac{1}{4}i\sin(\omega_1 t) \end{pmatrix} = 0 \tag{2.59}$$

$$\left\langle \hat{I}_y(t) \right\rangle = Tr\left\{ \hat{\rho}(t)\hat{I}_y \right\} = \begin{pmatrix} -\frac{1}{4}\sin(\omega_1 t) & -\frac{1}{4}i\cos(\omega_1 t) \\ -\frac{1}{4}i\cos(\omega_1 t) & -\frac{1}{4}\sin(\omega_1 t) \end{pmatrix} = -\frac{1}{2}\sin(\omega_1 t) \tag{2.60}$$

$$\left\langle \hat{I}_z(t) \right\rangle = Tr\left\{ \hat{\rho}(t)\hat{I}_z \right\} = \begin{pmatrix} \frac{1}{4}\cos(\omega_1 t) & -\frac{1}{4}i\sin(\omega_1 t) \\ -\frac{1}{4}i\sin(\omega_1 t) & \frac{1}{4}\cos(\omega_1 t) \end{pmatrix} = \frac{1}{2}\cos(\omega_1 t). \tag{2.61}$$

Therefore, for a resonant B_1 pulse applied along the x axis, the bulk magnetization of the spin ensemble is rotated from its initial equilibrium $\hat{I}_z$ state, around the axis along which the pulse was applied at a frequency, ω_1. The *r.f.* pulse is said to cause a *nutation* of the magnetization, where ω_1 defines the frequency of spin nutation. Similarly, for a pulse of duration t_{rf}, the angle that the magnetization will have nutated from its initial state is the flip angle, $\beta = \omega_1 t_{rf}$.

In product operator notation, the above analysis is written:

$$I_z \xrightarrow{\beta_x} I_z\cos\beta - I_y\sin\beta \tag{2.62}$$

Importantly, for $\beta = \pi/2$, i.e., a 90° *r.f.* pulse, the resulting spin magnetization state will be aligned along the $-y$ direction, $-I_y$, of the transverse plane. Similarly, for a 90° pulse with a phase corresponding to application along the y-axis of the rotating frame, product operator theory gives:

$$I_z \xrightarrow{\beta_y} I_z\cos\beta + I_x\sin\beta \tag{2.63}$$

resulting in a final spin state, at the end of the pulse duration, of $+I_x$. At this point, the system is once again only under the effect of the Zeeman interaction, given by $\hat{\mathscr{H}}_Z^{rot}$, and the above procedure can be repeated, assuming $t = 0$, to examine the effect of this Hamiltonian. Therefore, for an initial state:

$$\hat{\boldsymbol{\rho}}(0) = \hat{I}_x = \begin{pmatrix} 0 & \frac{1}{2} \\ \frac{1}{2} & 0 \end{pmatrix} \tag{2.64}$$

and a propagator corresponding to the Zeeman Hamiltonian, from Eq. 2.55:

$$\hat{U}(t) = e^{-i\Omega \hat{I}_z t} = \begin{pmatrix} \exp(-\frac{1}{2}i\Omega t) & 0 \\ 0 & \exp(\frac{1}{2}i\Omega t) \end{pmatrix}. \tag{2.65}$$

Eq. 2.34 then gives:

$$\begin{aligned} \hat{\boldsymbol{\rho}}(t) &= \begin{pmatrix} \exp(-\frac{1}{2}i\Omega t) & 0 \\ 0 & \exp(\frac{1}{2}i\Omega t) \end{pmatrix} \begin{pmatrix} 0 & \frac{1}{2} \\ \frac{1}{2} & 0 \end{pmatrix} \begin{pmatrix} \exp(\frac{1}{2}i\Omega t) & 0 \\ 0 & \exp(-\frac{1}{2}i\Omega t) \end{pmatrix} \\ &= \begin{pmatrix} 0 & -\frac{1}{2}e^{-i\Omega t} \\ \frac{1}{2}e^{i\Omega t} & 0 \end{pmatrix}. \end{aligned} \tag{2.66}$$

Examining the terms of the density matrix terms after the time, t, it is clear from the non-zero off-diagonal terms that the transverse spin components continue to evolve. Measurement of this transverse magnetization for the time-domain NMR signal, is then, from Eq. 2.38:

$$\begin{aligned} s(t) &= Tr\left[\hat{\boldsymbol{\rho}}(t)\hat{I}_+\right] \\ &= Tr\left\{\begin{pmatrix} 0 & \frac{1}{2}e^{-i\Omega t} \\ \frac{1}{2}e^{i\Omega t} & 0 \end{pmatrix} \begin{pmatrix} 0 & 1 \\ 0 & 0 \end{pmatrix}\right\} \\ &= Tr\begin{pmatrix} 0 & 0 \\ 0 & \frac{1}{2}e^{i\Omega t} \end{pmatrix} \\ &= \tfrac{1}{2}e^{i\Omega t} \\ &= \tfrac{1}{2}\left(\cos(\Omega t) + i\sin(\Omega t)\right) \end{aligned} \tag{2.67}$$

where the real and imaginary parts of $s(t)$ correspond to the $\hat{I}_x$ and $\hat{I}_y$ components of the spin magnetization, respectively. In term of product operators, the evolution of the system under an offset frequency, Ω, over a time t, is then written:

$$I_x \xrightarrow{\Omega t} I_x \cos \Omega t + I_y \sin \Omega t. \tag{2.68}$$

The product operator descriptions given in Eqs. 2.62, Eqs. 2.63 and 2.68 offer a simplified description of the spin magnetization behaviour under the effects of *r.f.* pulses and periods of free evolution, which comprise the simple ($\pi/2 -$ *acquire*) pulse sequence (see 3.1.1). This description is used in chapter 3 to describe the effects of advanced many-pulse NMR sequences.

The physical interpretation of Eq. 2.68 is that the static field causes the transverse magnetization of the spin to rotate around the z-axis of the field, which induces a time-varying current in the detection coil (the Larmor frequency is mixed down with the carrier frequency by the spectrometer electronics such that the resonance offset $\Omega = \omega_0 - \omega_{rf}$ is observed). §3.1.1 goes on to describe the method by which this signal is processed to determine the characteristic (offset) frequencies present in the system.

2.4 Internal Spin Hamiltonians

The internal spin Hamiltonians describe interactions between a nuclear spin and its surrounding environment. Therefore, an analysis of these Hamiltonians provides a description of how detailed information about the internal chemical properties of the system can be extracted. Before considering the specific forms of the internal Hamiltonians, it is necessary to appreciate the various interaction frames in which the interactions are best described.

2.4.1 Spherical Tensors and Frame Transformations

In §2.3.1, the external interaction Hamiltonians were introduced in the Cartesian axis system of the laboratory frame (later simplified to the rotating frame), where the NMR signal is measured. Each internal interaction Hamiltonian is most conveniently defined in its own Principal Axis System (PAS), where only the diagonal terms of the $\tilde{\mathbf{A}}$ interaction tensor (Eq. 2.47) are present, however, this system does not usually coincide with the laboratory frame (as defined by the dominant Zeeman interaction). Therefore, each interaction must be transformed from its specific PAS into the laboratory frame such that the effect of the internal Hamiltonian on the NMR signal is correctly described.

By expressing the interaction Hamiltonians using an irreducible spherical tensor representation, the frame transformations are greatly simplified. In this way, Eq. 2.47 becomes:

$$\hat{\mathscr{H}}_\Lambda = \sum_{j=0}^{2} \sum_{m=-j}^{+j} (-1)^m A_{jm} \hat{T}_{j-m} \tag{2.69}$$

where A_{jm} and $\hat{T}_{j-m}$ are the irreducible spherical tensors representing the spatial and spin components, respectively, of the interaction, Λ, and j and m describe the order and rank of the tensors, respectively, taking values $j = 0, 1, 2$ and $m = -j < -j + 1... < +j$. In general, the spin $\hat{T}_{j-m}$ terms are defined in the laboratory frame unless stated otherwise (i.e., $\hat{T}_{j-m}^{PAS}$, below).

In the principal axis system (P), only certain terms of the Hamiltonian will be non-zero, thus simplifying Eq. 2.69 to the terms:

$$\hat{\mathscr{H}}_\Lambda^{PAS} = A_{00}^{PAS} \hat{T}_{00}^{PAS} + A_{20}^{PAS} \hat{T}_{20}^{PAS} + A_{22}^{PAS} \hat{T}_{2-2}^{PAS} + A_{2-2}^{PAS} \hat{T}_{22}^{PAS}. \tag{2.70}$$

By this notation, transforming $\hat{\mathscr{H}}_\Lambda^{PAS}$ into the laboratory frame, $\hat{\mathscr{H}}_\Lambda^{LAB}$, involves only a manipulation of the A_{jm} spatial terms, which is carried out as a *rotation* between the two frames of reference. Such a transformation is described, for example, between the frames (X, Y, Z) and (x, y, z) as a rotation about the Euler angles, (α, β, γ), which define three successive rotations, namely: the (X, Y, Z) frame is initially rotated by α about Z to produce the (X', Y', Z') frame. (X', Y', Z') then rotates by angle β about the new Y' axis to give (X'', Y'', Z''). Lastly the (X'', Y'', Z'') frame is rotated by γ about the Z'' axis to give the (x, y, z) frame. This is equivalent to the description whereby the (X, Y, Z) frame is initially rotated by γ about Z to produce the (X', Y', Z') frame, (X', Y', Z') then rotates by angle β about the previous Y axis to give (X'', Y'', Z'') and the (X'', Y'', Z'') frame is rotated by α about the Z axis to give the desired (x, y, z) frame. Both are summarised by the rotation operator $\mathbf{R}(\alpha,\beta,\gamma)$, in terms of the individual rotations:

$$\begin{aligned}\mathbf{R}(\alpha,\beta,\gamma) &= \mathbf{R}_{z''}(\gamma)\,\mathbf{R}_{y'}(\beta)\,\mathbf{R}_{z}(\alpha)\\ &= \mathbf{R}_{z}(\alpha)\,\mathbf{R}_{y}(\beta)\,\mathbf{R}_{z}(\gamma) \qquad (2.71)\end{aligned}$$

where, for each of the $\mathbf{R}_a$ rotations about an axis a, by angle θ, it is known that $\mathbf{R}_a(\theta) = \exp(-i\theta\hat{I}_a)$, thus, Eq. 2.71 becomes:

$$\mathbf{R}(\alpha,\beta,\gamma) = \exp\left(-i\alpha\hat{I}_z\right)\exp\left(-i\beta\hat{I}_y\right)\exp\left(-i\gamma\hat{I}_z\right). \qquad (2.72)$$

For the irreducible spherical tensor terms described in Eq. 2.69, such a frame transformation is described by the rotation matrix

$$D^{j}_{m'm}(\alpha\beta\gamma) = \exp(-im'\alpha)\;\; d^{j}_{m'm}(\beta)\;\; \exp(-im\gamma) \qquad (2.73)$$

with the elements, $d^{j}_{m'm}(\beta)$, known as reduced Wigner rotation matrices:

$$d^{j}_{m'm}(\beta) = \langle jm'|\exp\left(-i\beta\hat{J}_y\right)|jm\rangle. \qquad (2.74)$$

Applying the rotation matrix described in Eq. 2.73 to the spatial tensor component of an interaction in its PAS, A^{PAS}_{jm}, allows the laboratory form of the interaction to be described:

$$A^{LAB}_{jm} = \sum_{m'=-j}^{+j} A^{PAS}_{jm'} D^{j}_{m'm}(\alpha_{PL},\beta_{PL},\gamma_{PL}) \qquad (2.75)$$

where $(\alpha_{PL},\beta_{PL},\gamma_{PL})$ are the Euler angles between the PAS and laboratory frames. Thus, the interaction Hamiltonian (Eq. 2.70) in the laboratory frame is given by:

$$\hat{\mathscr{H}}_{\Lambda}^{LAB} = \sum_{j=0}^{2}\sum_{m=-j}^{+j}(-1)^m A^{PAS}_{jm'} D^{j}_{m'm}(\alpha_{PL},\beta_{PL},\gamma_{PL})\hat{T}_{j-m}. \qquad (2.76)$$

The above analysis does not, however, take into consideration the frame of reference (specifically the *rotor* frame) which is introduced to the experiment by the use of the Magic Angle Spinning technique. This is discussed further, below, in the context of the chemical shift anisotropy, in §2.4.3.

It should be noted that, as the Hamiltonian tensors for the external field interactions are essentially represented by the unit vector (see Eqs. 2.48, 2.49 and 2.52), they are independent of the frame transformations described above. In addition, the static and oscillating fields are used to define the laboratory and rotating frame axes where the NMR signal is described, hence it is not necessary to consider the external interactions in spherical tensor form.

2.4.2 The Secular Approximation

The expression derived for the first-order Hamiltonian in the Laboratory frame (Eq. 2.76) can be simplified further by a consideration of the contribution of each spin interaction to the first-order average Hamiltonian. Using first-order perturbation theory, the Zeeman interaction is treated as the dominant interaction within the spin system, with all other interactions then being considered as smaller perturbations, such that:

$$\bar{\mathscr{H}}_{total} = \hat{\mathscr{H}}_0 + \hat{\mathscr{H}}_1 \tag{2.77}$$

where

$$\hat{\mathscr{H}}_0 = \hat{\mathscr{H}}_Z \tag{2.78}$$

$$\hat{\mathscr{H}}_1 = \hat{\mathscr{H}}_{RF} + \hat{\mathscr{H}}_{CS} + \hat{\mathscr{H}}_Q + \hat{\mathscr{H}}_D + \hat{\mathscr{H}}_J. \tag{2.79}$$

By this approximation, the wavefunctions of the total Hamiltonian, $\bar{\mathscr{H}}_{total}$, are well described by the eigenfunctions of the dominant interaction, $\hat{\mathscr{H}}_Z$, i.e., the Zeeman basis states, $|I, m\rangle$, as in §2.1.1. For this to hold, the eigenfunctions of the perturbations, $\hat{\mathscr{H}}_1$, must also be the Zeeman eigenfunctions, and so the Hamiltonians of $\hat{\mathscr{H}}_0$ and $\hat{\mathscr{H}}_1$ must commute. To a first-order approximation, the only parts of the $\hat{\mathscr{H}}_1$ interactions which affect the spin energy levels are those which commute with the Zeeman Hamiltonian, i.e., those with spins terms, $\hat{T}_{jm}$, which (by Eq. 2.4) commute with $\hat{I}_z$:

$$\left[\hat{I}_z, \hat{T}_{jm}\right] = m\hat{T}_{jm}. \tag{2.80}$$

This condition is only satisfied, for so-called *secular* terms whereby the tensor order equals zero i.e., $m = 0$. As such, under the secular approximation, the first-order Hamiltonian in the laboratory frame is only given by the tensors with $m = 0$:

$$\hat{\mathscr{H}}^{LAB} = A_{00}^{LAB}\hat{T}_{00} + A_{20}^{LAB}\hat{T}_{20}. \tag{2.81}$$

Those interaction Hamiltonians that do not commute with the Zeeman interaction will have higher order energy corrections which must be taken into account. Often, these can be neglected, as long as the terms are much smaller in magnitude than the Zeeman interaction. Therefore, it is necessary to appreciate the relative sizes of all the interaction Hamiltonians acting upon the spin system to ensure that this approximation is valid, as was considered for $\hat{\mathscr{H}}_{RF}$ in §2.3.1.

2.4.3 Chemical Shielding, the Chemical Shift and the Magic-Angle Spinning Technique

The chemical shielding interaction describes the indirect effect of the surrounding electronic environment upon the interaction between the nuclear spin, $\hat{\mathbf{I}}$, and the external field, $\mathbf{B}_0$. As a result of the static field, electron currents are generated around the nucleus, which, in turn, create secondary local magnetic fields that act to shield the nuclear spin from $\mathbf{B}_0$. In Cartesian form, this is described as:

$$\hat{\mathscr{H}}_{CS} = \gamma\hat{\mathbf{I}} \cdot \tilde{\sigma} \cdot \mathbf{B}_0 \tag{2.82}$$

with $\tilde{\sigma}$ being the electronic shielding tensor, which, in the principal axis system of the interaction, contains only non-zero diagonal components:

$$\tilde{\sigma}^{PAS} = \begin{pmatrix} \sigma_{xx}^{PAS} & 0 & 0 \\ 0 & \sigma_{yy}^{PAS} & 0 \\ 0 & 0 & \sigma_{zz}^{PAS} \end{pmatrix}. \tag{2.83}$$

Under the secular approximation (hence, in the laboratory frame), Eq. 2.81

states that the Hamiltonian describing this interaction is given by:

$$\hat{\mathscr{H}}_{CS}^{LAB} = A_{00}^{CS,LAB}\hat{T}_{00}^{CS} + A_{20}^{CS,LAB}\hat{T}_{20}^{CS} \tag{2.84}$$

where the spatial, $A^{CS,LAB}$, and spin, $\hat{T}^{CS}$, components of the shielding interaction are given as irreducible spherical tensors in the laboratory frame, and $A^{CS} = \gamma\tilde{\sigma}$. The first term of Eq. 2.84 is invariant to rotations betweens frames of reference, i.e., $A_{00}^{CS,LAB} = A_{00}^{CS,PAS}$, and so defines the isotropic component of the chemical shift interaction. The second term, however, is determined by performing a frame transformation of the spatial component in the PAS, using Eq. 2.75 where for the case of $\eta = 0$:

$$\begin{aligned} A_{20}^{CS,LAB} &= A_{20}^{CS,PAS} \sum_{m'=-2}^{2} D_{m'0}^{2}\left(\alpha_{PL}, \beta_{PL}, \gamma_{PL}\right) \\ &= A_{20}^{CS,PAS} \sum_{m'=-2}^{2} d_{m',0}^{2}\left(\beta_{PL}\right) e^{-im'\alpha_{PL}} \end{aligned} \tag{2.85}$$

and combining with the $\hat{T}_{20}^{CS}$ spin term to give the anisotropic part of the chemical shielding Hamiltonian in the laboratory frame. Computing these terms leads to the general expression (including η) for the chemical shielding Hamiltonian in the laboratory frame, for which the chemically shielded nuclear frequency, ω_{cs}, is defined, such that:

$$\begin{aligned} \hat{\mathscr{H}}_{CS}^{LAB} &= -\,\omega_0\left(\sigma_{iso} + \sigma_{aniso}\frac{1}{2}\{3\cos^2\beta_{PL} - 1 + \eta\sin^2\beta_{PL}\cos 2\alpha_{PL}\}\right)\hat{I}_z \\ &= -\,\omega_{cs}\hat{I}_z \end{aligned} \tag{2.86}$$

where the isotropic and anisotropic chemical shifts, and asymmetry parameter, are defined in terms of the shielding tensor in its principal axis system, by

$$\begin{aligned} \sigma_{iso} = \frac{1}{3}(\sigma_{xx}^{PAS} + \sigma_{yy}^{PAS} + \sigma_{zz}^{PAS}), \quad \sigma_{aniso} &= \sigma_{zz}^{PAS} - \sigma_{iso} \\ \text{and} \quad \eta &= \frac{\sigma_{xx}^{PAS} - \sigma_{yy}^{PAS}}{\sigma_{aniso}} \end{aligned} \tag{2.87}$$

respectively. Eq. 2.86 is a particularly important result; firstly, it demonstrates that the *observed* resonance frequency of a nucleus inside an external field is modified from ω_0 (see Eq. 2.4) due to the surrounding atomic electrons. Therefore, nuclei existing in different electronic environments (i.e., different atomic sites, bonding geometries etc.) are observed at differently shielded frequencies, making the NMR measurement an extremely sensitive probe of chemical structure.

It also should be noted that, as the shielding interaction is directly proportional to the external field (Eq. 2.82), the size of this interaction is inherently dependent upon the magnitude of B_0 applied. To remove this dependency, it is appropriate to represent the shifted nuclear frequency, not on an absolute scale of Hz, but with respect to some reference compound. This quantity, known as the *chemical shift*, δ, is expressed in parts per million (ppm), where the conversion is given (for the isotropic component) in Eq. 2.88:

$$\delta_{iso} = \frac{(\sigma_{iso}^{LAB}(ref) - \sigma_{zz}^{LAB})}{1 - \sigma_{iso}^{LAB}(ref)} \times 10^6 = \frac{\omega_0^{CS} - \omega_0(ref)}{\omega_0(ref)} \times 10^6 = \frac{\Omega^{CS} - \Omega(ref)}{\omega_0 \text{ in MHz}} \tag{2.88}$$

By analogy to the chemical shielding, δ is defined as a second-rank tensor, with principal components such that $\left|\delta_{zz}^{PAS} - \delta_{iso}\right| \geq \left|\delta_{xx}^{PAS} - \delta_{iso}\right| \geq \left|\delta_{yy}^{PAS} - \delta_{iso}\right|$ (according to the Haeberlen convention [111]). The components are physically represented as dimensions tracing an ellipsoid, as given in Fig. 2.4e below. Similarly, the quantities:

$$\delta_{aniso} = \delta_{zz}^{PAS} - \delta_{iso} \tag{2.89}$$

$$\eta = \frac{\delta_{xx}^{PAS} - \delta_{yy}^{PAS}}{\delta_{aniso}} \tag{2.90}$$

are defined to give the total observed observed chemical shift in static NMR experiments as:

$$\delta = \delta_{iso} + \delta_{aniso}\frac{1}{2}\{3\cos^2\beta_{PL} - 1 + \eta\sin^2\beta_{PL}\cos 2\alpha_{PL}\} \tag{2.91}$$

In general, as the shift is determined by the electronic ground states of an atom, heavier elements tend to have larger chemical shift ranges. For the ^{1}H, ^{13}C, ^{15}N and ^{17}O nuclei considered in this thesis, isotropic shifts typically range from $10^0 - 10^3$ ppm, with anisotropies of $10^1 - 10^2$ ppm, thus, many orders of magnitude smaller than the Zeeman interaction.

The anisotropic component of the chemical shift causes δ to be dependent upon the orientation of the nucleus with respect to the laboratory frame (given by the Euler Angles α_{PL}, β_{PL}, γ_{PL}). For liquid-state samples, the molecules undergo a rapid tumbling such that, on the NMR timescale, the orientation of the nuclei is not well defined. Therefore, the anisotropic component of the chemical shift is averaged out over all orientations (i.e., the integral of Eq. 2.91 over all angles is zero), resulting in a single, isotropic shift for each electronic environment. Similarly, for a solid in the form of a single crystal, whereby all molecules exist in the same orientation with respect to the external field, each of the distinct chemical sites produce a single chemical shift frequency on the NMR spectrum that changes as the single crystal is rotated. However, for a static powdered sample consisting of small single crystals of many different orientations, a distribution of chemical shifts is observed as a result of the Chemical Shift Anisotropy (CSA). The form of this distribution or *powder pattern* is dependent upon the principal components of the shift tensor, as is demonstrated in Fig. 2.4(a,b), thus, NMR spectra can be used to determine, not only the magnitude of the electronic shielding, but also the orientation of electronic environments.

While the anisotropic powder pattern lineshape contains orientational information, it also presents a broadening of the NMR resonance frequency. For multiple nuclear sites, this often results in overlapped lineshapes which are difficult to deconvolute, and thus much of the chemical information is lost.

2.4.4 The Chemical Shift under Magic Angle Spinning

It is possible to remove the anisotropic component of the chemical shift interaction (and other anisotropic interactions, e.g., the dipolar coupling - see §2.4.5) by physically rotating the powder at an angle (specifically, the magic angle) which is fixed with respect to the external field. To understand this effect, it is necessary to define a new frame of reference, the rotor frame, the geometry of which is described in Fig. 2.4e. As such, the determination of

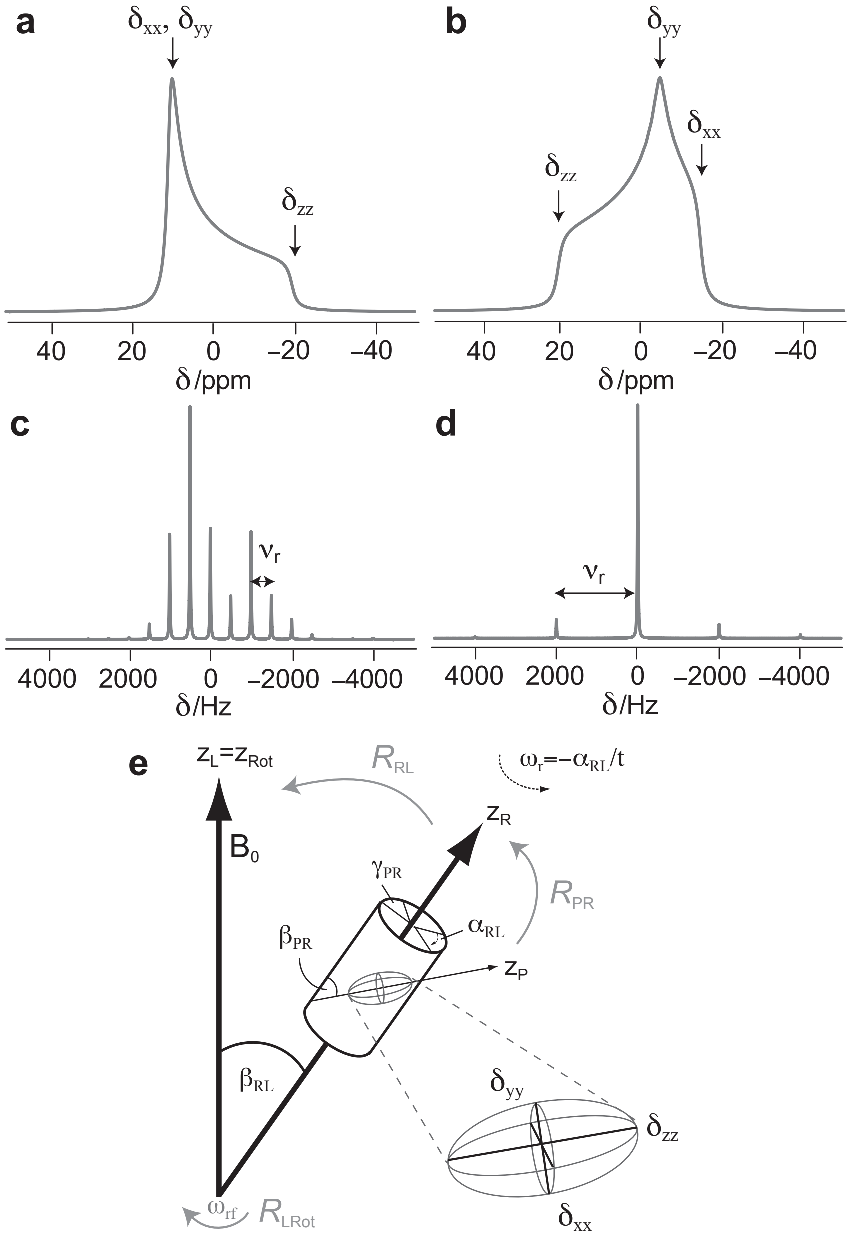

Figure 2.4. Chemical Shift Anisotropy powder lineshapes for an isolated $I = 1/2$ nucleus under (a,b) static and (c,d) Magic Angle Spinning (MAS), $\nu_r =$ (c) 500 Hz, (d) 2000 Hz, conditions, where $\nu_r = \omega_r/2\pi$. The shape of the powder pattern is determined by the principal values of the chemical shift tensor, $\delta_{xx}, \delta_{yy}, \delta_{zz}$. Spectra were simulated using SIMPSON [112], where $\delta_{iso} = 0$ ppm or (a,c,d) $\delta_{aniso} = -20$ ppm and $\eta = 0$ or (b) $\delta_{aniso} = 20$ ppm, $\eta = 0.5$ and convoluted with 20 Hz Lorentzian line-broadening. The chemical shift axis is given in (a,b) ppm or (c,d) Hz for $\omega_0/2\pi = 100$ MHz, showing that the spinning sidebands under MAS are separated by ν_r. The vertical axes of the spectra are normalised. (e) Representation of the axis systems and frame transformations used in MAS NMR. Solid black arrows indicate the z-directions of the Principal Axis System (P) (shown for the chemical shielding tensor of an isolated spin), the Rotor (R), and the coincident Laboratory (L) and Rotating (Rot) frames. Grey arrows describe the transformations between axis systems, which are described as rotations, R, using Eq. 2.71. The Euler angles (α, β, γ) between the axis systems are labelled; the MAS rotor is inclined at an angle of β_{RL} with respect to the external field, and the rotation frequency of the rotor is given such that $\omega_r = -\alpha_{RL}/t$.

the interaction Hamiltonian in the laboratory frame now requires a consideration of two successive frame transformations given by the tensor rotations (see §2.4.1) from the principal axis to the rotor frame, $\mathbf{R}_{PR}(\alpha_{PR}, \beta_{PR}, \gamma_{PR})$, and then from the rotor to the laboratory frame, $\mathbf{R}_{RL}(\alpha_{RL}, \beta_{RL}, \gamma_{RL})$ - see Fig. 2.4e. According to Eq. 2.75, the anisotropic spatial component is now transformed by the two $D^{j}_{m'm}$ rotation matrices:

$$\begin{aligned} A_{20}^{CS,LAB} &= A_{20}^{CS,PAS} \sum_{m'=-2}^{2} D^2_{0m'}(\alpha_{PR}, \beta_{PR}, \gamma_{PR}) D^2_{m'0}(\alpha_{RL}, \beta_{RL}, \gamma_{RL}) \\ &= A_{20}^{CS,PAS} \sum_{m'=-2}^{2} d^2_{0m'}(\beta_{PR}) d^2_{m'0}(\beta_{RL}) e^{-im'(\gamma_{RL}^{CS}-\alpha_{RL})}. \end{aligned} \tag{2.92}$$

Fig. 2.4e also indicates the form of the Euler angles for this double transformation, including the β_{PR} and β_{RL} angles between the z-axes of the principal and rotor, and rotor and laboratory frames, respectively, where the latter is a parameter under the control of the experimentalist. The additional transformation to the rotor frame also introduces a time dependence to the spatial tensor, given by the angle, $\alpha_{RL} = -\omega_r t$, i.e., depending upon the rotation frequency of the sample. This causes the interaction Hamiltonian to become periodic with a period equivalent to $\tau_r = 2\pi/\omega_r$ and, as stated in §2.2.4 (under the Average Hamiltonian approximation), the effect of sample spinning can be explained by considering the form of the Hamiltonian at points separated by this periodic time interval. Experimentally, this is achieved by detecting the NMR signal only at points separated by τ_r, known as rotor-synchronous detection. This is equivalent to considering the integral of the time-dependent term of the Hamiltonian, over one rotor period, i.e., $\int_0^{\tau_r} e^{-im'(\gamma_{PR}+\omega_r t)} dt$, the solution of which is only non-zero when $m' = 0$. Under this condition, Eq. 2.92 becomes

$$\begin{aligned} \left\langle A_{20}^{CS,LAB} \right\rangle_{\tau_r} &= A_{20}^{CS,PAS} d^2_{00}(\beta_{PR}) d^2_{00}(\beta_{RL}) \\ &= A_{20}^{CS,PAS} \frac{1}{2}(3\cos^2\beta_{PR} - 1)\frac{1}{2}(3\cos^2\beta_{RL} - 1) \end{aligned} \tag{2.93}$$

and the orientational dependence is now solely dependent upon the β Euler angles. By aligning the MAS rotor at an axis with respect to the external field, such that $\beta_{RL} = \cos^{-1}\left(1/\sqrt{3}\,\right) = 54.74°$ i.e., the *magic angle*, this anisotropic term is reduced to zero over one complete physical rotation of the sample.

Importantly, when the NMR signal is not acquired in a rotor-synchronous manner, as is often the case, the $m' \neq 0$ terms of Eq 2.92 must also be considered. Computing the remaining reduced Wigner rotation matrices for the magic angle condition yields the result:

$$\begin{aligned} A_{20}^{CS,LAB} = A_{20}^{CS,PAS}(&\frac{1}{2}\sin^2\beta_{PR}\cos(2\gamma_{PR} + 2\omega_r t) \\ &- \sqrt{2}\sin 2\beta_{PR}\cos(\gamma_{PR} + \omega_r t)) \end{aligned} \tag{2.94}$$

and so the periodicity of the anisotropic interaction remains. This is manifested in the NMR spectrum by the appearance of spinning sidebands, whereby, as the sample is rotated, the powder pattern is divided into narrow resonances separated, in Hz, according to the frequency of rotation, ($\nu_r = \omega_r/2\pi$) with lineshape intensity being increasingly concentrated into a peak at the isotropic shift frequency as ν_r increases (see Figs. 2.4c and 2.4d). If the rotation frequency of the MAS rotor is significantly greater than the size of the anisotropy, the spinning sidebands are of very low intensity such that narrow, individual resonances are resolved.

2.4.5 Dipolar coupling

All nuclear spins interact directly with one another as a result of the secondary magnetic fields generated by the particles themselves. The Hamiltonian of this interaction, the through-space dipole-dipole coupling, is therefore derived from the classical description of two interacting magnetic particles:

$$\hat{\mathscr{H}}_D = 2\sum_{i<j}\hat{\mathbf{I}}_i \cdot \tilde{\mathbf{D}} \cdot \hat{\mathbf{S}}_j \tag{2.95}$$

For a pair of spins, I and S, of the same isotopic species, this is described as a *homonuclear* coupling, whereas for different species it is a *heteronuclear* interaction. The dipolar tensor, D, contains principal values such that

$$D_{xx}^{PAS} = -d/2\ ,\, D_{yy}^{PAS} = -d/2\ ,\, D_{zz}^{PAS} = +d \tag{2.96}$$

where the dipole coupling constant d in Hz is given by:

$$d = (-\hbar \left(\frac{\mu_0}{4\pi}\right) \frac{\gamma_I \gamma_S}{r^3})/2\pi \tag{2.97}$$

and μ_0 is the permeability of free space. The magnitude of the through-space interaction between two spins is related to the gyromagnetic ratios of both nuclei, γ_I, γ_S and the inverse-cubed separation, r, between them. Importantly, the dependence of the dipolar interaction upon the nuclear separation allows interatomic distances to be quantitatively determined. Experimental techniques designed to exploit this property, hence revealing key structural parameters, are discussed in §3.4.

Much of this thesis considers homonuclear ^{1}H-^{1}H dipolar couplings in organic materials, where the ^{1}H nuclei (*protons*) are commonly separated by short distances. For example, the proton-proton separation within a CH$_2$ group is typically 1.8 Å, which, combined with the product of the large gyromagnetic ratio, $\gamma_{^1\mathrm{H}}$, results in homonuclear couplings of the order of $d = -20\,000$ Hz. For comparison, the heteronuclear ^{1}H-^{13}C dipolar coupling at the same internuclear separation would be only approximately -5000 Hz, due to the smaller contribution of $\gamma_{^1\mathrm{H}}\gamma_{^{13}\mathrm{C}}$, whereas the same heteronuclear pair at 1 Å (such as a directly bonded CH site) would also approach a coupling of $-20\,000$ Hz. As the strongest interactions are still 10^4 times smaller than the Zeeman interaction, the dipolar coupling Hamiltonian in the laboratory frame can be assessed under the secular approximation. By Eq. 2.97, the dipolar tensor in the principal axis system is traceless, $A_{00}^{D,PAS} = 0$, and so only the anisotropic term of Eq. 2.81 remains, to give:

$$\hat{\mathscr{H}}_D^{LAB} = A_{20}^{D,LAB} \hat{T}_{20} \tag{2.98}$$

In the principal axis system the spatial component is written:

$$A_{20}^{D,PAS} = \sqrt{6} d. \tag{2.99}$$

Referring back to §2.4.3, this spatial tensor ungoes identical transformations into the laboratory frame, as described for the chemical shielding term,

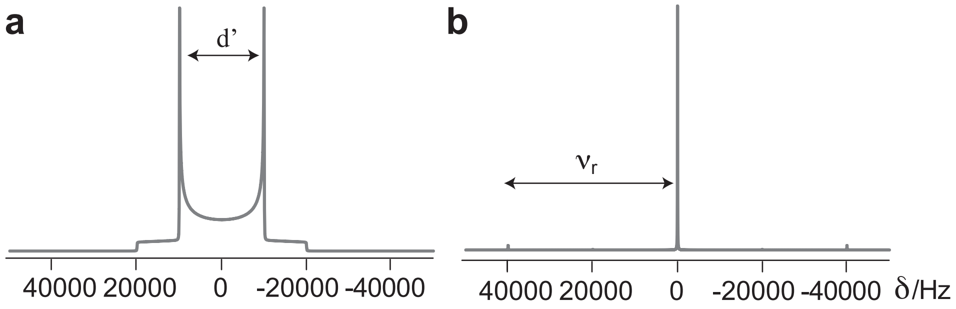

Figure 2.5. Powder lineshapes for a pair of heteronuclear dipolar coupled $I = 1/2$ nuclei under (a) static and (b) Magic Angle Spinning (40 kHz) conditions. Spectra were simulated using SIMPSON [112] for a dipolar coupling, $|d| = 20\,\text{kHz}$, and were convoluted with 20 Hz Lorentzian line-broadening. The vertical axes of the spectra are normalised.

$A_{20}^{CS,PAS}$ for both the static case (i.e., by a rotation $\mathbf{R}_{PL}$), and under magic angle spinning ($\mathbf{R}_{PR}, \mathbf{R}_{RL}$). The secular, first-order average Hamiltonian for the dipolar coupling is then given by Eq. 2.100 or 2.101, respectively:

$$\hat{\mathscr{H}}_D^{LAB,static} = A_{20}^{LAB}\hat{T}_{20} = \sqrt{6}d\frac{1}{2}(3\cos^2\beta_{PL} - 1)\hat{T}_{20} \tag{2.100}$$

$$\left\langle \hat{\mathscr{H}}_D^{LAB,MAS} \right\rangle_{\tau_r} = A_{20}^{LAB}\hat{T}_{20} = \sqrt{6}d\frac{1}{2}(3\cos^2\beta_{PR} - 1)\frac{1}{2}(3\cos^2\beta_{RL} - 1)\hat{T}_{20}. \tag{2.101}$$

Thus, the same orientational dependence of the interaction is observed as described for the CSA above (with $\eta = 0$), resulting in anisotropic powder lineshapes under static conditions, and (by analogy to Eq. 2.94) the appearance of spinning sidebands under non-rotor-synchronised observation, when β_{RL} is set to the magic angle. Figure 2.5 demonstrates the appearance of the static powder pattern, known as a Pake doublet, for a single pair of heteronuclear coupled spins, and the effect of fast MAS on the NMR spectrum. By the same principle as for the chemical shift anisotropy, magic angle spinning is said to *average out* the dipolar coupling over one complete physical rotation of the sample. Similarly, when ν_r is larger in magnitude than the coupling interaction, spinning sidebands are of very low intensity such that (to a good approximation) narrow lineshapes are observed at only the isotropic chemical shift frequencies (see Fig. 2.5b where $\nu_r = 40\,\text{kHz}$). Clearly, this adds a demand onto the required rotation frequencies in strongly dipolar coupled systems in order to achieve high resolution NMR lineshapes of powdered samples.

The case of homonuclear dipolar couplings in many-spin systems is more complex: Compare the form of the spin terms of the Hamiltonian for a pair of heteronuclear and homonuclear dipolar coupled spins, in the static case:

$$\hat{\mathscr{H}}_{D,Het}^{LAB,static} = d'(2\hat{I}_z\hat{S}_z) \tag{2.102}$$

$$\begin{aligned} \hat{\mathscr{H}}_{D,Hom}^{LAB,static} &= d'(3\hat{I}_z\hat{S}_z - \hat{\mathbf{I}}\cdot\hat{\mathbf{S}}) \\ &= d'(2\hat{I}_z\hat{S}_z - (\hat{I}_x\hat{S}_x + \hat{I}_y\hat{S}_y)) \end{aligned} \tag{2.103}$$

where $d' = d\frac{1}{2}(3\cos^2\beta_{PL} - 1)$ and the matrix forms of the spin operators are:

$$2\hat{I}_z\hat{S}_z = \begin{bmatrix} \frac{1}{2} & 0 & 0 & 0 \\ 0 & -\frac{1}{2} & 0 & 0 \\ 0 & 0 & -\frac{1}{2} & 0 \\ 0 & 0 & 0 & \frac{1}{2} \end{bmatrix}, \quad (\hat{I}_x\hat{S}_x + \hat{I}_y\hat{S}_y) = \begin{bmatrix} 0 & 0 & 0 & 0 \\ 0 & 0 & \frac{1}{2} & 0 \\ 0 & \frac{1}{2} & 0 & 0 \\ 0 & 0 & 0 & 0 \end{bmatrix}. \tag{2.104}$$

For the heteronuclear case, only the $2\hat{I}_z\hat{S}_z$ spin term, containing diagonal components, is present and thus the spin eigenstates are simply the product Zeeman states $(\alpha\alpha, \alpha\beta, \beta\alpha, \beta\beta)$. Thus, $\hat{\mathscr{H}}_{D,Het}^{LAB}$ acts as a first-order energy shift to the Zeeman interaction. The magnitude of these energy shifts are given by the expectation values of $d'\left\langle 2\hat{I}_z\hat{S}_z \right\rangle$ (from Eq. 2.5):

$$d' \langle\alpha\alpha| 2\hat{I}_z\hat{S}_z |\alpha\alpha\rangle = d' \langle\beta\beta| 2\hat{I}_z\hat{S}_z |\beta\beta\rangle = \quad \tfrac{1}{2}d' \tag{2.105}$$

$$d' \langle\alpha\beta| 2\hat{I}_z\hat{S}_z |\alpha\beta\rangle = d' \langle\beta\alpha| 2\hat{I}_z\hat{S}_z |\beta\alpha\rangle = \quad -\tfrac{1}{2}d' \tag{2.106}$$

as shown in Fig. 2.6b.

However, the homonuclear dipolar Hamiltonian given in Eq. 2.103 also contains the term $(\hat{I}_x\hat{S}_x + \hat{I}_y\hat{S}_y)$, often referred to as the *flip-flop* term, and expressed using the raising and lowering operators, $(\hat{I}_-\hat{S}_+ + \hat{I}_+\hat{S}_-)$. The matrix representation of this term (see Eq. 2.104) shows non-zero off-diagonal elements which correspond to mixings of the $\alpha\alpha$ and $\beta\beta$ states. Therefore, the spin eigenstates of the homonuclear dipolar Hamiltonian are no longer simply the product Zeeman eigenstates $(\alpha\alpha, \alpha\beta, \beta\alpha, \beta\beta)$, but are now linear combinations of them. The form of this Hamiltonian results in different first-order energy

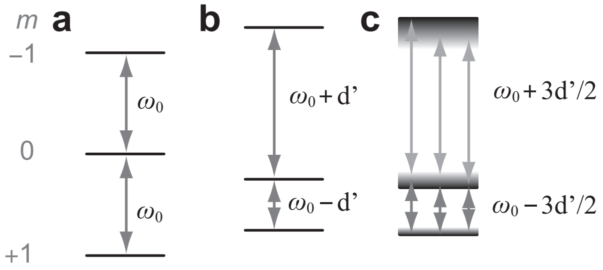

Figure 2.6. Energy levels for dipolar coupled $I = 1/2$ nuclei. (b) The heteronuclear dipolar coupling, of frequency d, causes a shift of the Zeeman energy levels in (a) due to the $2\hat{I}_z\hat{S}_z$ term given in Eq. 2.102. This gives rise to the powder pattern given in Fig. 2.5a in the static case, with a Pake doublet horn-to-horn splitting equal to $d' = d\frac{1}{2}(3\cos^2\beta_{PL} - 1)$ in Hz. (c) Under the homonuclear dipolar coupling, a different energy shift is observed such that an equivalent horn-to-horn doublet splitting of $3d'/2$ Hz is seen in static spectra. In this case, the *flip-flop* term in Eq. 2.103 causes a mixing of the basis states, which for a many-spin system leads to a range of transition frequencies between the energy levels and hence a distinct broadening of the NMR spectrum.

shifts compared to the heteronuclear case (and thus an energy difference of $3d'/2$ in Fig. 2.6c compared to d' in Fig. 2.6b).

Further, for systems containing many pairs of homonuclear coupled spins, the number of eigenstates is directly related to the number of nuclei present, and the Hamiltonians describing each of the coupled pairs will not commute with one another at different times. Therefore, measurements made upon the system will result in a distribution of frequencies given by spin transitions between many different eigenstates, as represented by the shaded levels in Fig. 2.6c. This results in a *homogeneous* [25] broadening of the NMR resonance for homonuclear coupled systems which, for a large number of spins, approximates to a Gaussian-like static lineshape. As a result of the non-commutation of the dipolar Hamiltonians, the first-order approximation of AHT is no longer valid and a residual line broadening remains under MAS. This broadening is ultimately a result of the higher order energy terms of the Magnus expansion and it has been shown that the effect of these higher order terms is reduced as the MAS frequency is increased leading to narrower linewidths at higher MAS frequencies [39]. This is demonstrated for the ^{1}H-^{1}H dipolar-broadened spectrum of *L*-alanine in Fig. 3.11a,b. §3.2.2 also describes the additional experimental techniques that are used throughout this work in order to achieve high-resolution ^{1}H spectra in powdered, organic materials.

2.4.6 J coupling

The J coupling is an indirect spin interaction occuring between pairs of nuclei, mediated by the bonding electrons between them. It is independent of the external magnetic field, and is a measureable quantity for pairs of heteronuclear and homonuclear atoms linked by a small number of chemical bonds. For spins, $\hat{\mathbf{I}}$ and $\hat{\mathbf{S}}$, the Hamiltonian is written in Cartesian form as:

$$\hat{\mathscr{H}}_J = \sum_{i<j} \hat{\mathbf{I}}_i \cdot \tilde{\mathbf{J}} \cdot \mathbf{S}_j \tag{2.107}$$

where $\tilde{\mathbf{J}}$ is the J-coupling tensor. In general, this tensor contains isotropic and anisotropic components of a similar form to the dipolar coupling, however, the J anisotropy is typically small compared to the dipolar coupling and is usually ignored for the light elements considered in this thesis. The isotropic J coupling is then the scalar average or trace of this tensor, $J_{iso} = \frac{1}{3}\mathrm{Tr}\{\mathbf{J}\} = \frac{1}{3}(J_{xx}+J_{yy}+J_{zz})$ hence this interaction is frequently termed the *scalar* coupling.

J is the smallest of the internal interactions, typically of the order of $(J_{iso}/2\pi =)\ 10^0 - 10^2$ Hz (e.g., a one-bond ^{1}H-^{13}C J coupling of a CH group, $J_{^1\mathrm{H},^{13}\mathrm{C}}$, is approximately 100 Hz), yet this varies considerably due to local molecular structure. In a similar manner to the dipolar interaction, to a first approximation, the scalar interaction causes a shift in the Zeeman states, resulting in a splitting of the NMR resonance. However, as J is generally smaller than the apparent linewidth of most nuclear resonances in the solid state (see §3.1.1), it is rarely observed directly. §3.3 describes some experimental techniques that are used in this thesis to indirectly probe the through-bond interaction in solids to give structural assignments of materials and map out atomic connectivities.

3

Experimental Methods

This chapter provides details of the experimental techniques used to record high-resolution solid-state NMR spectra (under Magic Angle Spinning) such that key structural information can be determined for crystalline powder samples. Firstly, the standard detection and processing methods of the NMR signal are described, notably Fourier Transform spectroscopy, quadrature detection and phase cycling. Some of the limitations of MAS NMR are then addressed, regarding the signal intensity of spins of low natural abundance and the spectral resolution of dipolar coupled systems, and the experimental techniques used to overcome these challenges are introduced. Finally, the more advanced techniques used in this work are discussed, for example, the exploitation of double quantum coherences and magnetization transfers via through-bond J couplings, in order to gain information about internuclear proximities and chemical bonds within organic systems. The experimental pulse sequences employed in later chapters are presented.

3.1 One and Two Dimensional FT NMR

3.1.1 Quadrature detection in 1D

In Chapter §2, it was established that, under the influence of an external B_0 magnetic field and on-resonance radiofrequency irradiation, $I \neq 0$ nuclei generate a measurable, time-varying signal, $s(t)$. Ignoring the effect of the internal spin interactions, $s(t)$ exhibits an oscillation with a characteristic offset frequency, Ω, in the rotating frame. The signal is detected as an induced

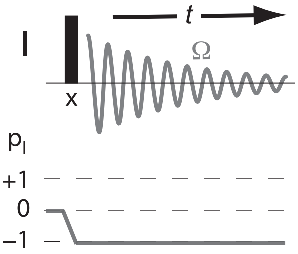

Figure 3.1. Pulse sequence and corresponding coherence transfer pathway diagram (see §3.1.4) for a '$\pi/2 - acquire$' experiment on spin, I. The solid bar represents a radiofrequency pulse, applied here along the x-axis of the rotating frame. In this work, solid black bars are used to represent a pulse duration such that the flip angle $\beta = \pi/2$ radians or 90°. The pulse generates a single quantum coherence (detected as $p = -1$) which is represented by the real part of the decaying time-domain signal. In the rotating frame, the frequency of oscillation detected is given by the offset, Ω.

current in a coil of wire aligned perpendicular to the external field, the form of which is determined by taking the expectation value of the $\hat{I}_-$ operator applied to the spin system, (as given in Eq. 2.38). The previous analysis of $s(t)$ conveniently neglected the effects of transverse relaxation [105], whereby the decay of the signal can usually be described by an exponential function with characteristic dephasing time, T_2. As such, the NMR signal is often referred to as a Free Induction Decay (FID), where the decaying time-domain signal is described by the complex function in Eq. 3.1. As described below, the detection of both real (cosine) and imaginary (sine) components of the signal, known as *quadrature detection*, is carried out such that the *sign* of the offset frequency, Ω can be determined.

$$s(t) = \tfrac{1}{2} \exp\left(+i\Omega t\right) \exp(-t/T_2) = \tfrac{1}{2} \left(\cos(\Omega t) + i \sin(\Omega t)\right) \exp(-t/T_2). \quad (3.1)$$

The most basic manipulation of spin magnetization required to generate this signal is given by a simple '$\pi/2 - acquire$' NMR experiment (where $\pi/2$ refers to the flip angle, β, of the *r.f.* pulse (see §2.3.2). This is represented by the schematic pulse sequence diagram shown in Fig. 3.1.

The information content of the oscillating time-domain signal is visualised more effectively as a resonance peak within a frequency-domain spectrum, $S(\omega)$, obtained by the Fourier transformation of Eq. 3.1 such that:

$$\begin{aligned} S(\omega) &= \int_{0}^{+\infty} s(t)\exp(-i\omega t)dt \\ &= \frac{1/T_2}{\left[(1/T_2)^2 + (\omega-\Omega)^2\right]} - i\frac{\omega-\Omega}{\left[(1/T_2)^2 + (\omega-\Omega)^2\right]} \\ &= A^+ - iD^+. \end{aligned} \tag{3.2}$$

The frequency spectrum then also consists of a real part, an absorptive Lorentzian, A^+, and an imaginary part, a corresponding dispersive Lorentzian, D^+, both with positions on the frequency axis given by the offset, Ω. (The superscript in this notation refers to the detection of a positive offset frequency ($\Omega > 0$) in the spectrum, as is relevant for the discussion in §3.1.2. Fig. 3.2 shows the form of the real and imaginary parts of the time and frequency-domain spectra given by Eqs. 3.1 and 3.2, respectively. As can be seen in (Fig. 3.2c), the absorptive lineshape has an intrinsically narrower linewidth than the dispersive resonance (Fig. 3.2d), thus provides better resolution and less spectral crowding when multiple resonances are detected. For the lineshape $S(\omega)$ in Eq. 3.2, the linewidth or *full width at half maximum height* (FWHMH) of an absorptive resonance peak is given by $(2/T_2)$ rad s^{-1} or $(1/\pi T_2)$ Hz.

It is important to record both real and imaginary components of the signal, (by the application of the $\hat{I}_{-}^{\dagger} = \hat{I}_{+} = \hat{I}_x + i\hat{I}_y$ operator), as opposed to measuring only one of the transverse components, in order to determine the *sign* of the offset frequency. For example, (ignoring the effects of relaxation) the form of $s(t)$ resulting from the measurement of $\hat{I}_x$, only, is:

$$\begin{aligned} s(t) &= Tr\left[\hat{\rho}(t)\hat{I}_x\right] \\ &= \tfrac{1}{2}\cos(\Omega t) = \tfrac{1}{4}\left(\exp\left(+i\Omega t\right) + \exp\left(-i\Omega t\right)\right) \end{aligned} \tag{3.3}$$

which, after Fourier transformation gives

$$\begin{aligned} S(\omega) &= \frac{1}{2}\left(\frac{(1/T_2) - i\left(\omega-\Omega\right)}{\left[(1/T_2)^2 + (\omega-\Omega)^2\right]}\right) + \frac{1}{2}\left(\frac{(1/T_2) - i\left(\omega+\Omega\right)}{\left[(1/T_2)^2 + (\omega+\Omega)^2\right]}\right) \\ &= \tfrac{1}{2}\left(A^+ + A^-\right) - \tfrac{1}{2}i\left(D^+ + D^-\right) \end{aligned} \tag{3.4}$$

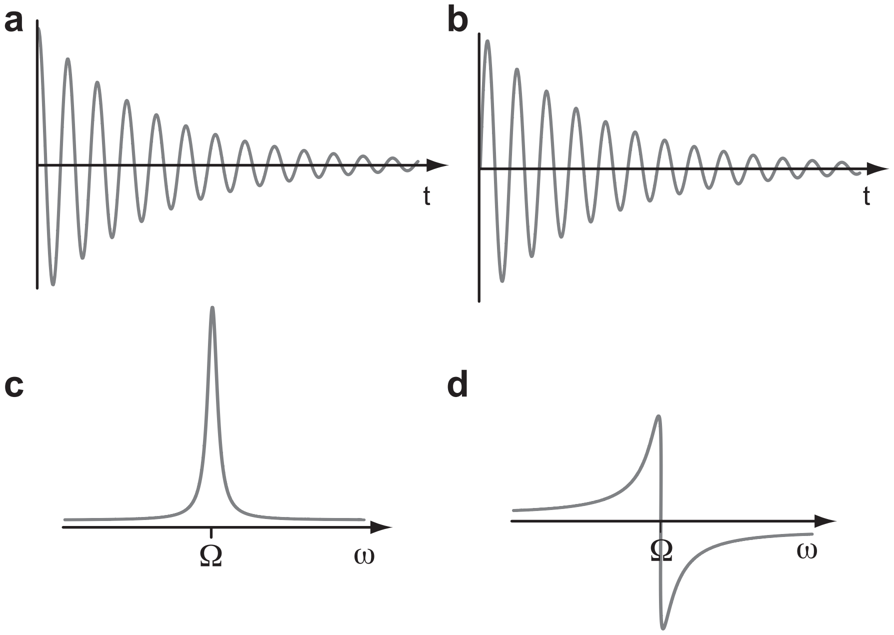

Figure 3.2. Simulated (SIMPSON) [112] time-domain signals (a, b) and corresponding Fourier Transformed frequency spectra (c, d) for a spin system with offset frequency, Ω. The real part is given by a cosine function in time (a) and an absorptive, A, shaped peak in frequency (c), whilst the imaginary part is a sine function (b) and dispersive, D, lineshape (d), see Eq. 3.2. Lorentzian line-broadening of 20 Hz was applied to all signals to simulate the effect of T_2 relaxation.

in the frequency domain. The detected signal now consists of oscillation frequencies at both $+\Omega$ and $-\Omega$, which appears as a mirroring of the frequency-domain spectrum about the central axis. Thus, without acquiring both real ($\hat{I}_x$) and imaginary ($\hat{I}_y$) signals (i.e., *quadrature detection*) it is not possible to determine the sign of the offset value, $+\Omega$. This method of sign discrimination is simple to implement in one-dimensional experiments by the use of two phase-sensitive detectors, 90° out of phase with one another. In higher dimensional experiments, as discussed in §3.1.2, further methodologies must be employed to achieve this effect, whilst also retaining pure absorption-mode lineshapes.

3.1.2 Two Dimensional Lineshapes

A major advantage of NMR is that *multidimensional* spectra can be recorded by introducing time evolution periods into the experimental sequence which are successively incremented, such that different spin interactions can be probed in a single experiment. For two-dimensional sequences, the time period during

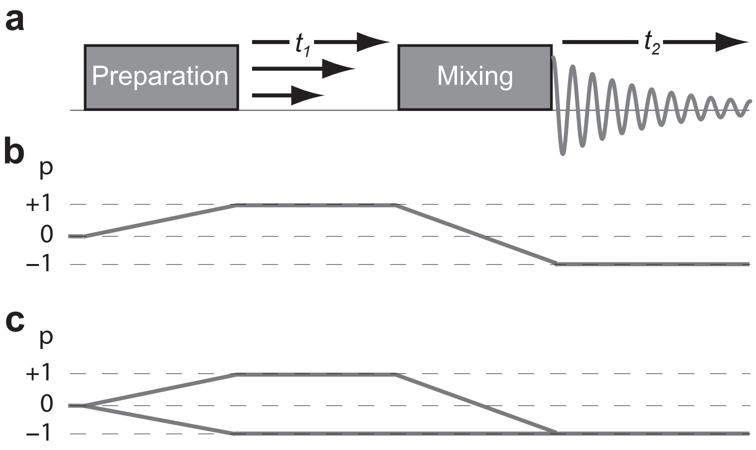

Figure 3.3. A representative two-dimensional NMR pulse sequence where the preparation and mixing pulse(s) generate coherences observed in t_1 and t_2, respectively. The coherence transfer pathways shown in (b,c) describe the evolution of single quantum coherences ($|p| = 1$) in both dimensions, where the data is phase- (b) or amplitude- (c) modulated with respect to t_1, as determined by the phase cycling of the preparation pulse (see §3.1.4).

which the signal is acquired is referred to as t_2, with the additional, incremented period named t_1, with increment, Δt_1. As shown in Fig. 3.3a, *preparation r.f.* pulses are used to generate spin coherences which are detected during the t_1 period, and *mixing* pulses create the final detectable coherences, measured in t_2. In order to induce an NMR signal physically in the receiver coil, the latter coherence must be of the order $p = -1$.

The general form of the signal resulting from the experiment described in Fig. 3.3a, assuming that the spin system evolves only under the effect of a frequency offset during both t_1 and t_2 is:

$$s(t_1, t_2) = \exp\left(-ip\Omega t_1\right)\exp(-t_1/T_2^1)\exp\left(i\Omega t_2\right)\exp(-t_2/T_2^2) \tag{3.5}$$

where T_2^2 and T_2^1 are the transverse relaxation times relating to t_2 and t_1, respectively and p is the coherence order selected in t_1. As will be shown in §3.1.4, *phase cycling* of the *r.f.* pulses and signal receiver allows different coherences, p, to evolve and be observed during the indirect t_1 period. For the specific phase cycle that allows only the evolution of $p = +1$ in t_1, represented by the coherence transfer pathway in Fig. 3.3b, Eq. 3.5 becomes:

$$s_{pm}(t_1, t_2) = \exp\left(-i\Omega t_1\right)\exp(-t_1/T_2^1)\exp\left(+i\Omega t_2\right)\exp(-t_2/T_2^2) \tag{3.6}$$

where the *pm* subscript indicates that this describes a signal which is *phase modulated* with respect to Ω_1. Fourier transformation with respect to both t_2 and t_1 produces a 2D frequency domain spectrum with the direct and indirect frequency axes, ω_2, and ω_1, respectively, as shown in Fig. 3.4. Transforming, firstly, with respect to t_2

$$S_{pm}(t_1,\omega_2) = \left(\exp\left(-i\Omega t_1\right)\exp(-t_1/T_2^1)\right)\left(A_2^+ - iD_2^+\right) \tag{3.7}$$

where the subscripts of A_2^+ and D_2^+ refer to the resonances in the ω_2 dimension. Then, Fourier transforming Eq. 3.7 with respect to t_1, gives:

$$\begin{aligned} S_{pm}(\omega_1,\omega_2) &= \left(A_1^- - iD_1^-\right)\left(A_2^+ - iD_2^+\right) \\ &= \left(A_1^- A_2^+ - D_1^- D_2^+\right) - i\left(A_1^- D_2^+ - D_1^- A_2^+\right) \end{aligned} \tag{3.8}$$

This expression shows that only resonances with a negative frequency in ω_1 are observed (A_1^-, D_1^-), hence sign discrimination is achieved by recording 2D experiments in a phase-modulated manner. However, both real and imaginary parts of Eq. 3.8 contain mixtures of absorptive and dispersive terms, giving rise to *phase-twist* lineshapes in the two-dimensional spectrum, as shown in Fig. 3.4b,c. In comparison to the pure absorptive lineshape ($A_1^- A_2^+$) given in Fig. 3.4a, the linewidth of the phase-twisted resonances is considerably larger, and so generation of these lineshapes is an undesirable consequence of the phase-modulated experiment.

Consider, instead, a 2D experiment which is phase cycled such that both $p = \pm 1$ are observed in the indirect dimension, i.e., the coherence pathway illustrated in Fig. 3.3c. $s(t)$ is now *amplitude modulated* with respect to t_1 :

$$\begin{aligned} s_{am,\cos}(t_1,t_2) &= \left(\exp\left(+i\Omega t_1\right) + \exp\left(-i\Omega t_1\right)\right)\exp(-t_1/T_2^1)\exp\left(+i\Omega t_2\right)\exp(-t_2/T_2^2) \\ &= \left(2\cos\left(+\Omega t_1\right)\right)\exp(-t_1/T_2^1)\exp\left(+i\Omega t_2\right)\exp(-t_2/T_2^2) \end{aligned} \tag{3.9}$$

Fourier transformation with respect to t_2 gives:

$$S_{am}(t_1,\omega_2) = \left(\exp\left(+i\Omega t_1\right) + \exp\left(-i\Omega t_1\right)\right)\exp(-t_1/T_2^1)\left(A_2^+ - iD_2^+\right) \tag{3.10}$$

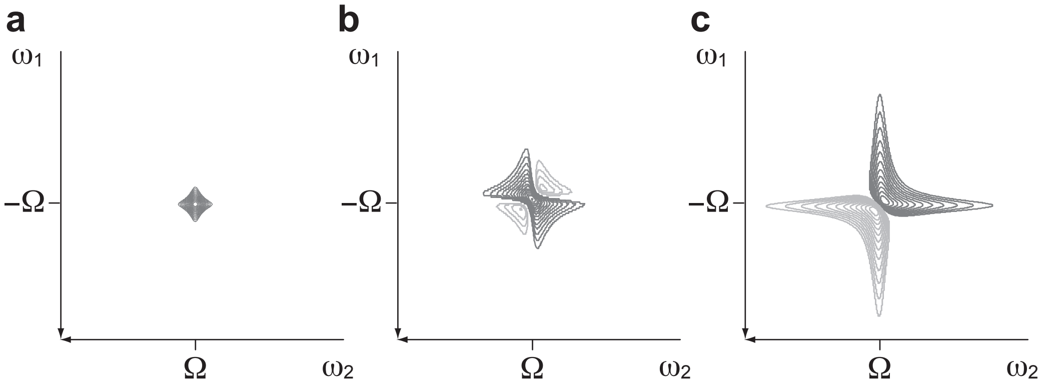

Figure 3.4. Simulated two-dimensional frequency-domain spectra with direct axis, ω_2, and indirect axis, ω_1, showing signal lineshapes of (a) the pure absorptive type ($A_1^- A_2^+$) and phase twist lineshapes of the form (b) $A_1^- A_2^+ - D_1^- D_2^+$ (c) $A_1^- D_2^+ - D_1^- A_2^+$. Resonances were simulated using the SIMPSON [112] program and were convoluted with 50 Hz line-broadening in both-dimensions. All spectra are shown with a base contour at 6 % of the maximum peak height.

The signal is then manipulated using a *hypercomplex* Fourier Transform, whereby the real and imaginary parts of the signal are separated before the transformation is performed with respect to t_1. Discarding the imaginary term in Eq. 3.10 removes the dispersive component of the lineshape, D_2 such that:

$$s_{am}^{\mathrm{Re}}(t_1, \omega_2) = (\exp(+i\Omega t_1) + \exp(-i\Omega t_1)) \exp(-t_1/T_2^1) A_2^+ \tag{3.11}$$

and after Fourier transformation with respect to t_1

$$\begin{aligned} S_{am}^{\mathrm{Re}}(\omega_1, \omega_2) &= \left[\left(A_1^- - iD_1^-\right) + \left(A_1^+ - iD_1^+\right)\right] A_2^+ \\ &= \left[A_1^- + A_1^+\right] A_2^+ - i\left[D_1^- + D_1^+\right] A_2^+. \end{aligned} \tag{3.12}$$

Hence, the real part of the signal produces lineshapes which are fully absorptive in both dimensions. However, resonances are observed at both positive (A_1^+) and negative (A_1^-) frequencies in the indirect dimension, i.e., mirrored across the central $F_1(\omega_1)$ axis such that the sign of Ω_1 is not determined for experiments recorded in this way. Sign discrimination is achieved for amplitude-modulated 2D spectra, by recording the signal according to the States [113], TPPI [114] or combined States-TPPI [115] methods.

3.1.3 The States Technique

Established by States *et al.* [113], this technique acquires two amplitude-modulated signals for each Δt_1 increment of the two-dimensional experiment. The first signal takes the form described in Eq. 3.9 ($s_{am,\cos}(t_1, t_2)$). The second is then recorded whereby the phase of the preparation pulse(s) is increased by $\pi/2|p|$, where $|p|$ is the desired coherence order during t_1. This causes the modulation in the indirect dimension for the second signal to be shifted by a phase of $\pi/2$ with respect to the first, hence, a sine-modulated signal is observed:

$$\begin{aligned} s_{am,\sin}(t_1, t_2) &= \left(\exp\left(+i\Omega t_1\right)\exp\left(+i\tfrac{\pi}{2}\right) + \exp\left(-i\Omega t_1\right)\exp\left(-i\tfrac{\pi}{2}\right)\right)\exp(-t_1/T_2^1) \\ &\qquad \cdot \exp\left(+i\Omega t_2\right)\exp(-t_2/T_2^2) \\ &= \left(\exp\left(+i\Omega t_1\right) - \exp\left(-i\Omega t_1\right)\right)\exp(-t_1/T_2^1)\exp\left(+i\Omega t_2\right)\exp(-t_2/T_2^2) \\ &= \left(2i\sin\left(+\Omega t_1\right)\right)\exp(-t_1/T_2^1)\exp\left(+i\Omega t_2\right)\exp(-t_2/T_2^2). \end{aligned} \tag{3.13}$$

Fourier transforming Eq. 3.13 with respect to t_2, and discarding the resulting imaginary term yields:

$$S^{\mathrm{Re}}_{am,\sin}(t_1, \omega_2) = \left(\exp\left(+i\Omega t_1\right) - \exp\left(-i\Omega t_1\right)\right)\exp(-t_1/T_2^1)A_2^+ \tag{3.14}$$

and after Fourier transformation with respect to t_1:

$$S^{\mathrm{Re}}_{am,\sin}(\omega_1, \omega_2) = \left[A_1^- - A_1^+\right]A_2^+ - i\left[D_1^- - D_1^+\right]A_2^+. \tag{3.15}$$

Finally, taking the difference of the two absorptive terms of the cosine- (Eq. 3.12) and sine- (Eq. 3.15) modulated signals produces a fully absorptive resonance centred only at the positive offsets in both t_1 and t_2:

$$\left[A_1^- + A_1^+\right]A_2^+ - \left[A_1^- - A_1^+\right]A_2^+ = 2A_1^+A_2^+ \tag{3.16}$$

An alternative approach for 2D sign-discrimination is the TPPI (Two Pulse Phase Incremented) [114] method, where only one FID is recorded for each Δt_1 increment, however the increment is halved to $\Delta t_1 = 1/2sw_1$ (where

Table 3.1. Pulse Phases used for the two, x and y, signals recorded according to the States and States-TPPI techniques. Pulse (and receiver) phases are often expressed in terms of the Cartesian axes of the transverse plane. For the above description, 0° = x, 90° = y, 180° = $-x$, 270° = $-y$. Adapted from ref.[115]

	States			States-TPPI		
	Prep. ϕ		Rec. ϕ	Prep ϕ		Rec. ϕ
	x	y		x	y	
t_1	0	90	0	0	90	0
$t_1 + \Delta t_1$	0	90	0	180	270	180
$t_1 + 2\Delta t_1$	0	90	0	0	90	0

sw_1 is the spectral width of the indirect frequency dimension, in Hz) and the phase of the preparation pulses is shifted by $\pi/2|p|$ for *each successive* Δt_1 measurement. This has the effect of modulating the coherence order by a phase dependent upon the t_1 increment, such that a real Fourier transform then provides sign discriminant data. There is a disadvantage of the TPPI method where Δt_1 is restricted, for example where it must be synchronised with the rotor period of the MAS rotation, as it may be that not all resonances are contained within the spectral width that is reduced by two as compared to the States method. As such, the States method, or the combined States-TPPI [115] methods have been used out of preference throughout this work. The latter technique combines the principles of both methods, such that, as in States, two FID signals are recorded 90° out of phase with one another, however, the phase of the preparation pulses and the receiver is not reset for successive increments of Δt_1, but is inverted by a phase change of 180°. Table 3.1 shows explicitly how these methods are implemented during two-dimensional acquisition.

3.1.4 Phase Cycling

In the previous chapter, the concept of spin coherence was introduced, where an analysis of the density matrix described the generation of coherence within a spin system by the use of resonant *r.f.* irradiation. Coherence essentially represents a relation between the m eigenstates of the nuclei in the system, where the order of the coherence is given by Δm (as given schematically in Figs. 2.1-2.3). Thus, whilst it is only in-phase, single quantum coherence ($\Delta m = \pm 1$)

that physically induces the NMR signal, the application of *r.f.* pulses can generate many different orders of coherence, depending on the number of available spin eigenstates. For example, in §2.2.2, it was stated that double-quantum coherence ($\Delta m = \pm 2$) may be generated for systems containing pairs of coupled $I = 1/2$ nuclei, and as will be shown, DQC can be used to probe internuclear couplings.

NMR experiments can be designed to generate and (indirectly) observe different coherence orders, so as to extract specific information about the internal interactions amongst the nuclei. The desired spin coherence at each point of the experimental sequence is represented by the coherence transfer pathway diagram, as given below each of the sequences presented in this work (e.g., in Figs. 3.1 and 3.3, previously).

Observation of only desired coherences is achieved by altering the phases of the applied *r.f.* pulses and the signal receiver between successive acquisitions of the FID [116]. Specifically, one or more pulse phases are succesively shifted by $\Delta\phi°$, i.e., *cycled* through N steps, where $\Delta\phi = 360°/N$. The acquired signal then gains a modulation with respect to the various coherences within the system such that, over one complete cycle of N acquisitions, undesired coherences interfere destructively and only desired coherences are detected by the receiver. Explicitly [107]:

i. A phase cycle of N steps allows the desired pathway Δp, along with pathways $\Delta p + nN$ (where n is an integer) to be selected. All other pathways are suppressed.

ii. A shift, $\Delta\phi$, applied to the phase(s) of a pulse (or group of pulses) causes a coherence, undergoing a change in coherence order Δp, to experience a phase shift of $-\Delta\phi\Delta p$, as detected by the receiver.

The number of steps of the cycle, N, (and consequently, the phase shift $\Delta\phi$) can theoretically take any value, but the receiver phase is best defined as 0°, 90° (switch real and imaginary), 180° (negate) or 270° (switch real and imaginary and negate).

The phase cycle required to observe, for example, a coherence order change of $\Delta p = \pm 2$ is determined by applying the above principles: A cycled

Table 3.2. Pulse phases and shift effect of a four-step phase cycle on desired ($\Delta p = 2$) and undesired ($\Delta p = -1$) coherences, where all are given in degrees. The receiver is set to follow the cycle of the desired coherence phase, and so will not be synchronised with the phase shift of an unwanted coherence.

	Pulse	Effect of Pulse Phase		Receiver
		Desired Coherence ($\Delta p = 2$)	Undesired coherence ($\Delta p = -1$)	
Step No.	ϕ	$-\Delta\phi\Delta p = -2\Delta\phi$	$-\Delta\phi\Delta p = \Delta\phi$	ϕ_{rec}
1	0	0	0	0
2	90	180	90	180
3	180	0	270	0
4	270	180	360	180

pulse of $N = 4$ steps selects coherence changes $\Delta p = \pm 2, \pm 6, \pm 10$ etc. When applied to a system of $I = 1/2$ nuclei, the multiple quantum coherences of orders $|\Delta p| = 6, 10$ are considered to be negligible, thus a cycle where $N = 4$, $\Delta\phi = 90°$, is sufficient in this case. Table 3.2 shows the phase shifts caused to the desired coherence order ($\Delta p = \pm 2$), and also to an undesired coherence (for example $\Delta p = -1$) by this four-step cycle. The receiver is set to follow the phase shift of the desired coherence order, such that the latter undesired coherence is effectively averaged to zero, or *cycled out* over N steps. Thus all experiments must be recorded using an integer multiple of N acquisitions for this selection technique to be effective.

As DQC ($\Delta p = \pm 2$) will not directly induce an NMR signal, its evolution can be observed only in the indirect dimension of a two-dimensional experiment. In general, an NMR sequence of this form is described in Fig. 3.5, where the coherence transfer pathway diagram indicates that the signal will be amplitude modulated with respect to t_1 (see §3.1.2). Comparing the coherence pathway of this experiment with that shown in Fig. 3.3, it should be noted that the initial and final coherence order points of any NMR sequence are fixed such that the system always begins, at equilibrium, with a population state ($p = 0$), and the measured SQC is given, by convention, as $p = -1$. Therefore, for a pulse sequence consisting of q sets of pulses, only $q - 1$ events must be cycled as the coherence route of the remaining pulse is, thus, fixed.

The phase cycle required for the DQ ($\Delta p = \pm 2$) excitation pulse of phase, ϕ_a, has been considered in the above example to be of $N = 4$ steps.

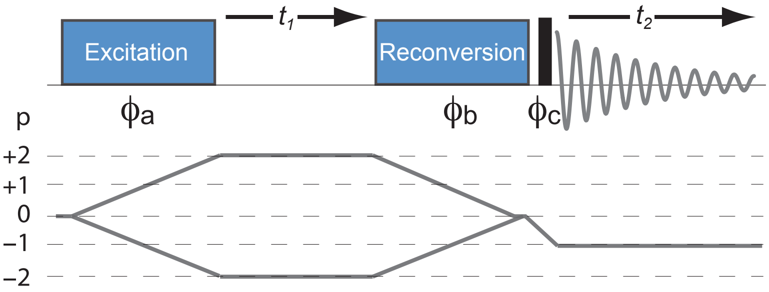

Figure 3.5. NMR pulse sequence and coherence transfer pathway diagram for an amplitude-modulated two-dimensional experiment, where double-quantum coherence is observed in the indirect dimension. The preparation and mixing pulses are referred to as the excitation and reconversion of the DQC, such that $|p| = 2$ is generated, evolves in t_1 and is then reconverted back to a population state ($p = 0$). The $\pi/2$ pulse then creates observable single-quantum coherence for detection in t_2. Specific pulse sequences used to excite and reconvert DQC are discussed in §3.4. The labels, ϕ, refer to the phases of the (sets of) pulses.

Considering, then, the cycle for the 90° pulse, of phase ϕ_c, required to select a coherence change of $\Delta p = -1$ for detection; the lowest convenient number of steps is also $N = 4$, for which changes in coherence orders of $\Delta p = -1, 3, 7, -5...$ are selected. Again, for a system of $I = 1/2$ nuclei, coherence orders $p \geq 2$ are considered to be negligible. The four step phase cycle of ϕ_c is combined in a *nested* fashion with that of ϕ_a to produce an overall 16-step cycle for the experiment and the receiver phase is then set to follow the sum of the phase changes resulting from the desired coherence orders of both the cycled pulses, as given in Tab. 3.3.

Tab. 3.3 also shows how the States method is implemented in this experiment to achieve sign discrimination of the resonances in the indirect dimension. Recall, from §3.1.3, that for each Δt_1 increment, two signals are recorded, 90° out of phase with one another, by incrementing the phase of the pulses *before* t_1 by $\pi/2\,|p|$. For the desired coherence (here $|p| = 2$) this corresponds to an additional shift of 45° applied to ϕ_a. The cycling techniques are combined such that the dataset is recorded where, sequentially:

· 16 FIDs cycled, $t_1 = 0$, $S_{\cos}$, · 16 FIDs cycled, $t_1 = 0$, $S_{\sin}$,

· 16 FIDs cycled, $t_1 = \Delta t_1$, $S_{\cos}$, · 16 FIDs cycled, $t_1 = \Delta t_1$, $S_{\sin}$...

When processed by hypercomplex Fourier Transform, this results in a 2D DQ-SQ correlation spectrum with absorptive, sign discriminant resonances in

Table 3.3. Pulse phases and shift effect (given in degrees) of the nested 16-step phase cycle used for a 2D DQ-SQ experiment. Pulse phases, ϕ_a, ϕ_c, are each cycled through four steps to select the coherences described in Fig. 3.5, resulting in total phase shifted signal $S_{\cos}$. The $S_{\sin}$ signal, required for States processing in ω_1 [113], is acquired by incrementing the phase of ϕ_a by $90°/|p_{(t_1)}| = 45°$. The receiver is set to follow the total phase shift of $S_{\cos}$ during the acquisition of both FIDS such that $S_{\cos}$ and $S_{\sin}$ are recorded 90° out of phase.

Step No.	Pulse ϕ_a		Shift (a) $(-\Delta p_a\Delta\phi_a = -2\Delta\phi_a)$		Pulse ϕ_c	Total Shift (rec) $(-(\Delta p_a\Delta\phi_a + \Delta p_c\Delta\phi_c) = -2\Delta\phi_a + \Delta\phi_c)$	
	$S_{\cos}$	$S_{\sin}$	$S_{\cos}$	$S_{\sin}$		$S_{\cos}$	$S_{\sin}$
1	0	45	0	90	0	0	90
2	90	135	180	270	0	180	270
3	180	225	0	90	0	0	90
4	270	315	180	270	0	180	270
5	0	45	0	90	90	90	180
6	90	135	180	270	90	270	0
7	180	225	0	90	90	90	180
8	270	315	180	270	90	270	0
9	0	45	0	90	180	180	270
10	90	135	180	270	180	0	90
11	180	225	0	90	180	180	270
12	270	315	180	270	180	0	90
13	0	45	0	90	270	270	0
14	90	135	180	270	270	90	180
15	180	225	0	90	270	270	0
16	270	315	180	270	270	90	280

both dimensions and DQC information displayed in ω_1. §3.4 describes the DQ-SQ experiments used in this work (specifically, using the BABA [117] and POST-C7 [62] double-quantum recoupling sequences) where this 16-step phase cycle is employed, and presents a representative two-dimensional spectrum (Fig. 3.14b).

Unless otherwise stated, the phase cycles used for other experimental sequences in this work can be found in the references provided for each sequence in this chapter.

3.2 Advanced Techniques: Improving Resolution and Sensitivity

As with most spectroscopic methods, it is important to be able to detect a signal, clearly distinguishable from the noise level, on a reasonable experimental timescale. The total time for each NMR experiment is determined by the number of co-added FID signals and the repetition delay between successive acquisitions. In general, a sufficient delay is needed for the nuclear magnetization to relax back to a longitudinal state, indicated by the relaxation time, T_1, of the system. For two-dimensional experiments, this is further multiplied by the number of t_1 increments required to achieve sufficient resolution in the indirect dimension (and then doubled for the implementation of States or States-TPPI (§3.1.3)).

In general, the amplitude of the signal detected during each measurement is directly related to the total amount of bulk magnetization generated for a given nuclear system, hence the number of nuclei of interest present in the sample. As such, an NMR spectrum resulting from the direct excitation of spin magnetization, also provides an indication of the relative number of atomic sites, identifiable from the relative intensities of individual chemical shift frequencies. To maximise the total intensity of the signal detected, there is an obvious advantage to studying as large a sample volume as possible. However, under the MAS technique, the sample volume is restricted by the size of the spinning rotor (a cylindrical container of fixed diameter) which is selected based on the desired frequency of rotation suitable for the experiment. For example, a strongly dipolar-coupled ^{1}H system may require ultra fast spinning frequencies of up to 70 kHz in order to sufficiently resolve the resonances, for which the sample volume is restricted to 3.8 µl in a 1.3 mm diameter rotor. As ^{1}H nuclei have the highest inherent sensitivity of the commonly observed NMR nuclei, the signal to noise ratio is still favourable, even for such small sample sizes. Conversely, a less sensitive nucleus such as ^{13}C (where $\gamma(^{13}\mathrm{C})= \frac{1}{4}\gamma(^1\mathrm{H})$, for which strong anisotropic interactions are not such a challenge, it is more appropriate to use a larger diameter rotor (e.g., 4 mm, containing 80 µl of material), subsequently spinning at a slower rotation rate.

Often, a compromise must be sought between the sensitivity and resolution obtainable for each experiment.

In this work, high-resolution ^{1}H data are obtained by the use of simultaneous MAS and homonuclear decoupling (see §3.2.2) as opposed to fast MAS techniques, therefore the majority of spectra presented were recorded for samples contained in rotors of diameter 3.2 mm or 4 mm at a spinning frequency of 12.5 kHz

3.2.1 Dilute spins: Cross Polarization and Heteronuclear Decoupling

A further complication in the search for high signal sensitivity is the issue of *natural isotopic abundance*. For atoms which possess a variety of nuclear isotopes i.e., different numbers of component neutrons, each will have a different gyromagnetic ratio, γ and thus Larmor frequency, ω_0, such that they are probed separately by an NMR experiment. Similarly, differing isotopes of the same atomic species may also possess different spin numbers, I. The natural abundance of any given isotope determines the percentage of atoms of a given sample of that isotopic form. For example, ^{1}H is naturally over 99.9 % abundant, (with the remaining fraction composed of ^{2}H, ^{3}H nuclei) such that a measurement made, where $\omega_{rf} \approx \omega_0(^1\text{H})$, will detect a signal from almost all of the hydrogen atoms in the material.

Conversely, this creates a particular challenge for the observation of NMR signals from *dilute* nuclei, for example, in organic systems, the $I = 1/2$ carbon (^{13}C) or nitrogen (^{15}N) isotopes. At natural isotopic abundance, the majority (98.9 %) of carbon atoms exist as ^{12}C nuclei ($I = 0$), that can not be manipulated by NMR. The remaining fraction ($^{13}\text{C}_{na}$ =1.1 %) exist as the ($I = 1/2$) isotope ^{13}C, such that approximately only one carbon nucleus out of every hundred atoms produces a detectable NMR signal (similarly, $^{15}\text{N}_{na}$ =0.4 %). One technique for enhancing the amount of magnetization present for *dilute* nuclei, is to isotopically label materials such that a higher percentage of atoms are of the desirable spin state, however this can be an extremely costly chemical procedure (in time and resources).

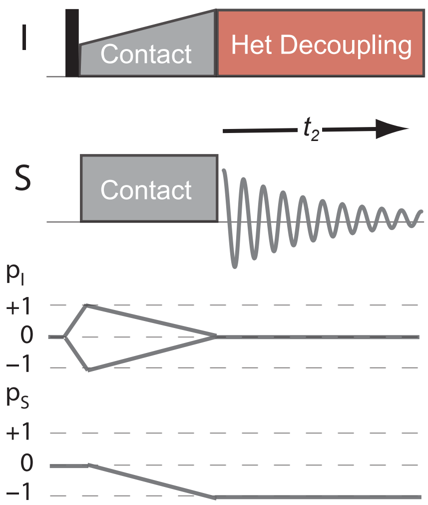

Figure 3.6. Cross polarization (CP) pulse sequence used to enhance the sensitivity of a dilute spin, S, in the presence of an abundant spin, I. Initial transverse magnetization is generated by application of a $90°_I$ pulse, which is transferred to S during the *contact* period, where simultaneous pulses are applied to both spin channels, according to the Hartmann-Hahn condition given in Eq. 3.17. Often, a pulse of *ramped* amplitude [118, 119] is used to broaden the matching conditions for the spin system, as applied to I, here. During acquisition of the resulting S NMR signal, *heteronuclear decoupling* is applied to I (see below). All the pulse sequences described in this work use red blocks of pulses to describe periods of dipolar decoupling, and blue for dipolar *recoupling* as in §3.4.

An experimental method for increasing the signal sensitivity of $I = 1/2$ nuclei is the Cross Polarization (CP) technique, developed by Hartmann and Hahn [15], which employs double-resonance irradiation of the system such that a dilute spin, S, derives an initial magnetization state from a network of abundant spins, I, that are in close proximity via the heteronuclear dipolar coupling interaction. By this method, the amount of bulk magnetization of the dilute spin is increased, thus directly improving the signal intensity. A further benefit of the CP experiment is that the repetition delay between successive acquisitions of S signal is now determined by the T_1 relaxation time of I, which is generally faster, such that many measurements of the FID can be acquired over a shorter experimental time period. Fig. 3.6 presents the pulse sequence diagram for the cross polarization experiment, which is applied throughout later chapters of this thesis for $I = {}^1H$, $S = {}^{13}C$, ${}^{15}N$. Direct excitation of ^1H under CP, or otherwise, is usually achieved by a 90° pulse, 2.5 µs in duration, i.e., ν_1 =100 kHz.

During the double-resonance irradiation period, the amplitudes of the *contact* pulses are optimised such that the nutation frequencies of the nuclei coincide (for a static experiment);

$$\gamma_I B_{1I} = \gamma_S B_{1S}. \tag{3.17}$$

The I-S magnetization transfer resulting from the CP contact pulses is analysed is terms of thermodynamic processes and two-spin Average Hamiltonian Theory in refs[120] and [121], respectively, where the maximum possible enhancement is given by γ_I/γ_S, i.e., ≈ 4 for $I = {}^1$H, $S = {}^{13}$C. Under MAS, the match condition given in Eq. 3.17 is modified to

$$\gamma_I B_{1I} = \gamma_S B_{1S} \pm n\omega_r \tag{3.18}$$

where $n = 1, 2$. As the dipolar coupling is averaged out over complete rotations of magic angle spinning (§2.4.5), where the degree of averaging increases with ν_r, the efficiency of the CP transfer process is reduced at faster rotation speeds. CP is observed to be more efficient under fast MAS when a *ramped* contact pulse is applied on one of the channels (see Fig. 3.6) [118, 119].

It should also be noted that the generally quantitative nature of the NMR resonances is no longer exhibited under the CP technique as the S magnetization is now derived via a transfer process that depends on the heteronuclear dipolar coupling. Instead, the amplitudes of the spectral resonances are now (semi-quantitatively) determined by the relative I-S proximities, as well as the effect of any motional processes.

The presence of the dipolar coupling interaction within a nuclear spin system causes an anisotropic broadening of the measured spin resonance, (see §2.4.5) which is generally undesirable in the solid-state. While the MAS technique aims to remove the orientational dependence of this interaction and successfully narrows linewidths for comparably small couplings, it is often also necessary to apply *decoupling* irradiation as part of the NMR pulse sequence, to average the spin component of the coupling Hamiltonian.

For the case of a double resonance experiment, such as CP, it is the *heteronuclear* (i.e., to ^{1}H (I) spins) dipolar coupling that is assumed to be the dominant anisotropic interaction acting on the detected spin, S. Considering the form of the heteronuclear dipolar Hamiltonian (Eq. 2.102): specifically the spin term, $\hat{I}_z\hat{S}_z$, it can be shown that continuous irradiation applied at $\omega_0(I)$, causes I to oscillate between the $|\alpha\rangle$ and $|\beta\rangle$ states (for $I = {}^1\!/_2$). Thus, applying *r.f.* decoupling to the I nuclei whilst S signal is acquired, further removes the effect of the dipolar coupling and increases the resolution of the S resonances. When applied in the form of a single *continuous wave* of *r.f.* irradiation [122], the efficiency of the dipolar averaging is generally proportional to the amplitude of the decoupling field, i.e., the corresponding nutation frequency, $\nu_1 = \omega_1/2\pi$ in kHz. However, strong *r.f.* fields applied throughout the acquisition of the FID cause prolonged heating of the sample and NMR equipment and can result in irreversible damage, particularly to samples containing high salt or water concentrations such as those of a biological nature. As such, it is desirable to apply decoupling fields at low amplitude, yet still obtaining highly resolved spectra. Further, both MAS and *r.f.* irradiation introduce a specific periodicity to the dipolar Hamiltonian, such that at certain ν_r, ν_1 conditions the effects interfere destructively to negate the averaging effect. Many decoupling schemes have been developed to increase the efficiency of line-narrowing across a range of rotation frequencies, generally, where the irradiation is divided into blocks of pulses of varying phase [123]. Heteronuclear decoupling schemes used in this work, are the TPPM [19] and SPINAL-64 [20] sequences, (where the phase-switching is described in Fig. 3.7) which are generally applied at $\nu_1(^1\text{H}) = 100\,\text{kHz}$ and for MAS spinning frequencies, $\nu_r = \omega_r/2\pi = 12.5\,\text{kHz}$.

3.2.2 Abundant Nuclei: Homonuclear decoupling

For the case of abundant ^{1}H nuclei, the signal is highly sensitive but poorly resolved due to strong (homogeneous) homonuclear dipolar-broadening mechanisms, as discussed in §2.4.5. While the effect of these broadening mechanisms is reduced as ν_r increases, even at very fast spinning speeds (e.g., 70 kHz), adequately resolved ^{1}H spectra are still possible only for relatively ‘small’ ^{1}H net-

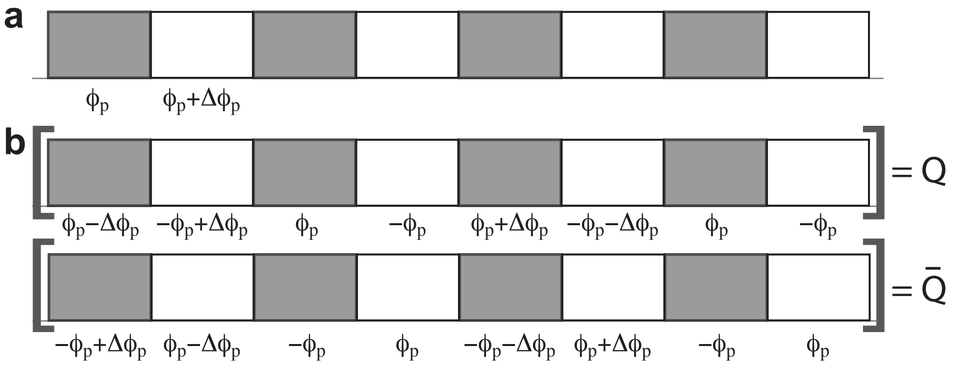

Figure 3.7. Phase modulated heteronuclear decoupling schemes (a) TPPM [19] and (b) Blocks Q and $\bar{Q}$ which make up the SPINAL-64 [20] sequence: $Q\bar{Q}\bar{Q}Q\bar{Q}QQ\bar{Q}$. In this work, ϕ_p and $\Delta\phi_p$ are (a) 0°, 15° and (b) 15°, 5°, respectively. Each pulse duration corresponds to a flip angle of slightly less than 180° (i.e., 5 µs for ν_1 =100 kHz) in work shown here.

works. This thesis demonstrates the application of *r.f.* pulse schemes (*homonuclear* decoupling sequences) along with MAS (i.e., the CRAMPS method) to achieve efficient line-narrowing of dipolar coupled resonances for a variety of organic systems. This section first illustrates the concept of homonuclear decoupling by considering the first two presented sequences, Lee-Goldburg [26] and WHH-4 [29].

Returning to the expressions derived for the homonuclear dipolar Hamiltonian (Eqs. 2.100 and 2.101), the orientational dependence is given by $\frac{1}{2}(3\cos^2\beta - 1)$, where $\beta = \beta_{PL}$ in the static case and both $\beta = \beta_{PR}, \beta = \beta_{RL}$ terms are considered under MAS. For the latter case of MAS, a complete physical rotation about the root of this expression, the *magic* angle, $\beta_{RL} = \arccos(1/\sqrt{3}) = \arctan(\sqrt{2})$, averages the spatial term of the interaction Hamiltonian to zero. The angle, defined with respect to the z-direction (i.e., the static B_0 field), describes an axis along $< 111 >$, where the x, y and z axes are all represented by a unit vector, as shown in Fig. 3.8a.

Hence, applying the magic angle geometry to the Cartesian spin terms of the dipolar Hamiltonian describes the condition where the spin magnetization effectively rotates around the $< 111 >$ axis in the rotating frame. This can be achieved by manipulation of the spin system, with either continuous-amplitude, off-resonance ($\omega_0 - \omega_{rf} = \Omega$) *r.f.* pulses, or multiple-pulse, on-resonance ($\omega_0 - \omega_{rf} = 0$) irradiation.

Eqs. 2.53 and 2.55 describe the Hamiltonians for oscillating and static

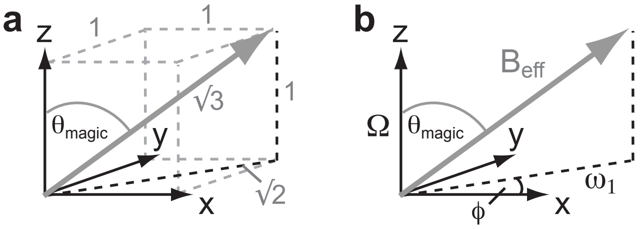

Figure 3.8. (a) The axis given in grey is aligned at ($\theta_{magic} = \arccos(1/\sqrt{3}) = \arctan(\sqrt{2})$) to the z direction, and lies along the $< 111 >$ plane with respect to the x, y and z Cartesian axes. (b) The Lee-Goldburg condition [26]: a pulse of phase, ϕ, with offset and amplitude such that $\omega_1/\Omega \;=\sqrt{2}$ is aligned at the magic angle to the external field, in the rotating frame.

magnetic fields in terms of the spin operators, $\hat{I}$, and field amplitudes (expressed as angular frequencies), $\omega = -\gamma B$, such that both fields are stationary in time and of well defined position in the Cartesian-spin basis. A pulse of arbitrary phase, ϕ, from x (in the transverse plane) has an amplitude ω_1, while a static field in the z-direction is given by the amplitude $\omega_0 - \omega_{rf} = \Omega$, i.e., the resonance offset compared to the *r.f.* carrier frequency. By this description, for a pulse applied on resonance, i.e., $\Omega = 0$, the spins are no longer affected by the field along z and instead nutate around the axis of the applied pulse with frequency ω_1, as described in §2.3.2. However, an off-resonance pulse with a finite value of Ω causes the spins to nutate around an effective field inclined *between* the transverse plane and the z-axis. Specifically, a decoupling pulse applied such that $\omega_1/\Omega \;=\sqrt{2}$ (known as the Lee-Goldburg condition [26]), places this effective field at the magic angle with respect to z, as shown in Fig. 3.8b. A complete rotation of the bulk magnetization about this effective field (using a 360° pulse) then averages the spin components of the dipolar coupling Hamiltonian, removing the anisotropic effect from the spectrum, where the effective nutation frequency ($\sqrt{{\omega_1}^2 + \Omega^2}$) is comparable to the dipolar interaction.

Variants of the technique, namely, Frequency-Switched and Phase-Modulated Lee-Goldburg (FSLG [27], PMLG [28]) allow even greater line-narrowing efficiencies. The continuous nature of Lee-Goldburg decoupling initially restricted its application to indirect time periods (e.g., t_1, periods of evolution, τ or ^{1}H homonuclear decoupling during the acquisition of a ^{13}C FID), until the development of *windowed* sequences such as wPMLG [124], that incorporated free evolution periods amongst the irradiation so that the NMR signal can be sampled directly.

Alternatively, on-resonance decoupling schemes may be applied in the form of cycled multiple pulses separated by periods of free evolution, such that windows for FID acquisition points are inherent to the sequence. The pulses are designed so that the spin magnetization exists along each of the x, y, and z axes for the same amount of time during one cycle, i.e., effectively aligned along the $< 111 >$ axis between them. Signal detection then takes place at specifically synchronised points such that the spin part of the dipolar Hamiltonian is averaged to zero over the complete cycle, again, removing broadening effects from spectrum. This principle was first demonstrated for the WHH-4 or WaHuHa [29] sequence given in Fig. 3.9a. An analysis of this in terms of the dipolar Hamiltonian in the 'toggling frame' is now provided, to a first-order approximation in Average Hamiltonian Theory (AHT) (see §2.2.4). In this toggling frame, an on-resonance pulse is said to rotate the form of the interaction Hamiltonian, whilst otherwise ignoring the effect of the *r.f.* Hamiltonian. Then, assuming that the interaction Hamiltonians commute over a given time period (here, the cycle time, t_c) this description allows the system to be well defined by AHT.

Returning to the expression for the secular homonuclear dipolar Hamiltonian in the laboratory frame under static conditions (Eq. 2.103) this is abbreviated to the z-dipolar Hamiltonian in the toggling frame, $\hat{\mathscr{H}}_{zz}^{D}$ (Eq. 3.19), on account of the $\hat{I}_z\hat{S}_z$ term. Transformations are fully described by this spin term as the scalar $\hat{\mathbf{I}} \cdot \hat{\mathbf{S}}$ term is unaffected by spin rotations.

$$\hat{\mathscr{H}}_{zz}^{D} = d'(3\hat{I}_z\hat{S}_z - \hat{\mathbf{I}} \cdot \hat{\mathbf{S}}) \tag{3.19}$$

In the toggling frame, a pulse, $90°_{-x}$, rotates the frame such that the interaction Hamiltonian $\hat{\mathscr{H}}_{yy}^{D}$ acts in the following τ period of free precession, and a further $90°_{y}$ pulse rotates the frame once more such that $\hat{\mathscr{H}}_{xx}^{D}$ acts during 2τ, as described in Fig. 3.9b. By AHT (Eq. 2.41), over the complete cycle ($t_c = 6\tau$)

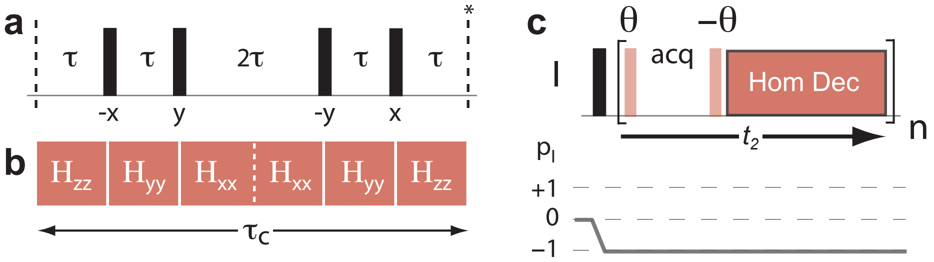

Figure 3.9. (a) The WHH-4 Scheme: 90° pulses with a phase that is sequentially shifted by 90° are separated by evolution periods τ and 2τ [29] such that the sequence is naturally windowed. The FID is sampled once over each cycle period, t_c, at the point labelled by the asterisk (*) to effectively average the homonuclear dipolar interaction. (b) The form of the homonuclear dipolar coupling Hamiltonian in the toggling frame during each evolution period [104]. (c) Pulse sequence for continuous, windowed homonuclear decoupling applied during the direct dimension.

shown in this figure, the average dipolar Hamiltonian is given by

$$\begin{aligned}\bar{\mathscr{H}}_D^0 =& \frac{\hat{\mathscr{H}}_{xx}^D\tau + \hat{\mathscr{H}}_{yy}^D\tau + 2\hat{\mathscr{H}}_{zz}^D\tau + \hat{\mathscr{H}}_{yy}^D\tau + \hat{\mathscr{H}}_{xx}^D\tau}{6\tau} \\ =& \frac{1}{3}\left(\hat{\mathscr{H}}_{xx}^D + \hat{\mathscr{H}}_{yy}^D + \hat{\mathscr{H}}_{zz}^D\right).\end{aligned} \tag{3.20}$$

It then follows that

$$\hat{\mathscr{H}}_{xx}^D+\hat{\mathscr{H}}_{yy}^D+\hat{\mathscr{H}}_{zz}^D = d'[(3\hat{I}_x\hat{S}_x-\hat{\mathbf{I}}\cdot\hat{\mathbf{S}})+(3\hat{I}_y\hat{S}_y-\hat{\mathbf{I}}\cdot\hat{\mathbf{S}})+(3\hat{I}_z\hat{S}_z-\hat{\mathbf{I}}\cdot\hat{\mathbf{S}})] = 0 \tag{3.21}$$

as $\hat{\mathbf{I}}\cdot\hat{\mathbf{S}} = \hat{I}_x\hat{S}_x + \hat{I}_y\hat{S}_y + \hat{I}_z\hat{S}_z$, and so the dipolar Hamiltonian cancels to zero under this pulse sequence.

Importantly, for the chemical shift Hamiltonian, which is linear in $\hat{I}_z$ ($\hat{\mathscr{H}}_{zz}^{CS} = -\omega_{cs}\hat{I}_z$ - see Eq. 2.86) but is not traceless, the same rotations in the toggling frame give:

$$\bar{\mathscr{H}}_{CS}^0 = \frac{1}{3}\left(\hat{\mathscr{H}}_{xx}^{CS} + \hat{\mathscr{H}}_{yy}^{CS} + \hat{\mathscr{H}}_{zz}^{CS}\right) \neq 0 \tag{3.22}$$

Under this decoupling scheme, the chemical shift Hamiltonian evolves under an effective field aligned along $< 111 >$, such that the *scaled projection* of the chemical shift onto the x-y plane is detected by the signal receiver. By the geometry given in Fig. 3.8, the scaling factor is approximately $1/\sqrt{3} \approx 0.57$. Generally, this value deviates due to the experimental imperfections of the *r.f.* pulses, where scaling factors that are close to unity are preferable to allow better resolution of individual resonances.

Homonuclear decoupling schemes were originally devised in the static regime and later combined with MAS to give the CRAMPS (Combined Rotation and Multiple Pulse Spectroscopy) approach, producing higher-resolution spectra than by either technique, alone [31, 126, 127]. However, as noted in §1.1, complications are observed as a result of the interfering periodicities induced by each technique upon the interaction Hamiltonians. Nevertheless, in the past decade, various ^{1}H homonuclear decoupling sequences have been demonstrated to function well at moderate and fast MAS frequencies (see §1.1). In this thesis, the DUMBO (Decoupling Under Mind-Boggling Optimization) [34] decoupling approach is employed. This family of decoupling sequences (see also [35, 41]) was introduced by the Emsley group, in an effort to reduce the experimental imperfections arising from the use of discrete 90° phase shifts (in e.g., WHH-4, MREV-8 [30], BLEW-12 [125] etc. - see Fig. 3.10a-d) whereby the phases vary according to a smooth periodic function, represented as a Fourier series. Starting with Fourier coefficients adapted from the windowless BLEW-12 sequence (Fig. 3.10c,d), the DUMBO-1 scheme (Fig. 3.10e) was devised by a numerical optimization of decoupling performance upon a *static*, computed two-spin (^{1}H) system, and later directly experimentally optimised for ^{1}H spectra under MAS, specifically at $\nu_r = 22\,\text{kHz}$ and 12.5 kHz, leading to the eDUMBO$_{22}$ (Fig. 3.10f) and eDUMBO$_{12.5}$ schemes [35], respectively. It has since been shown that eDUMBO$_{22}$ provides efficient line narrowing for indirectly detected experiments at a range of spinning frequencies 12.5-65 kHz [66], with chemical shift scaling factors close to 0.57.

^{1}H CRAMPS experiments presented in this work employ eDUMBO$_{22}$ (or FSLG in chapter 7) throughout indirect time-evolution periods, whereas windowed wDUMBO-1 [41] is preferred for direct ^{1}H detection. In general, a decoupling amplitude of $\nu_1 = 100\,\text{kHz}$ is used, corresponding to a DUMBO cycle time (6π) of 30 µs. Empirical optimisation of this duration gave best results of 32 µs for eDUMBO$_{22}$ and 24 µs for wDUMBO-1, where the phase is switched across 320 steps. Each cycle is surrounded, before and after, by a short prepulse, that aligns the magnetization perpendicular to the effective $< 111 >$ axis during the decoupling block. These are given by the flip angle

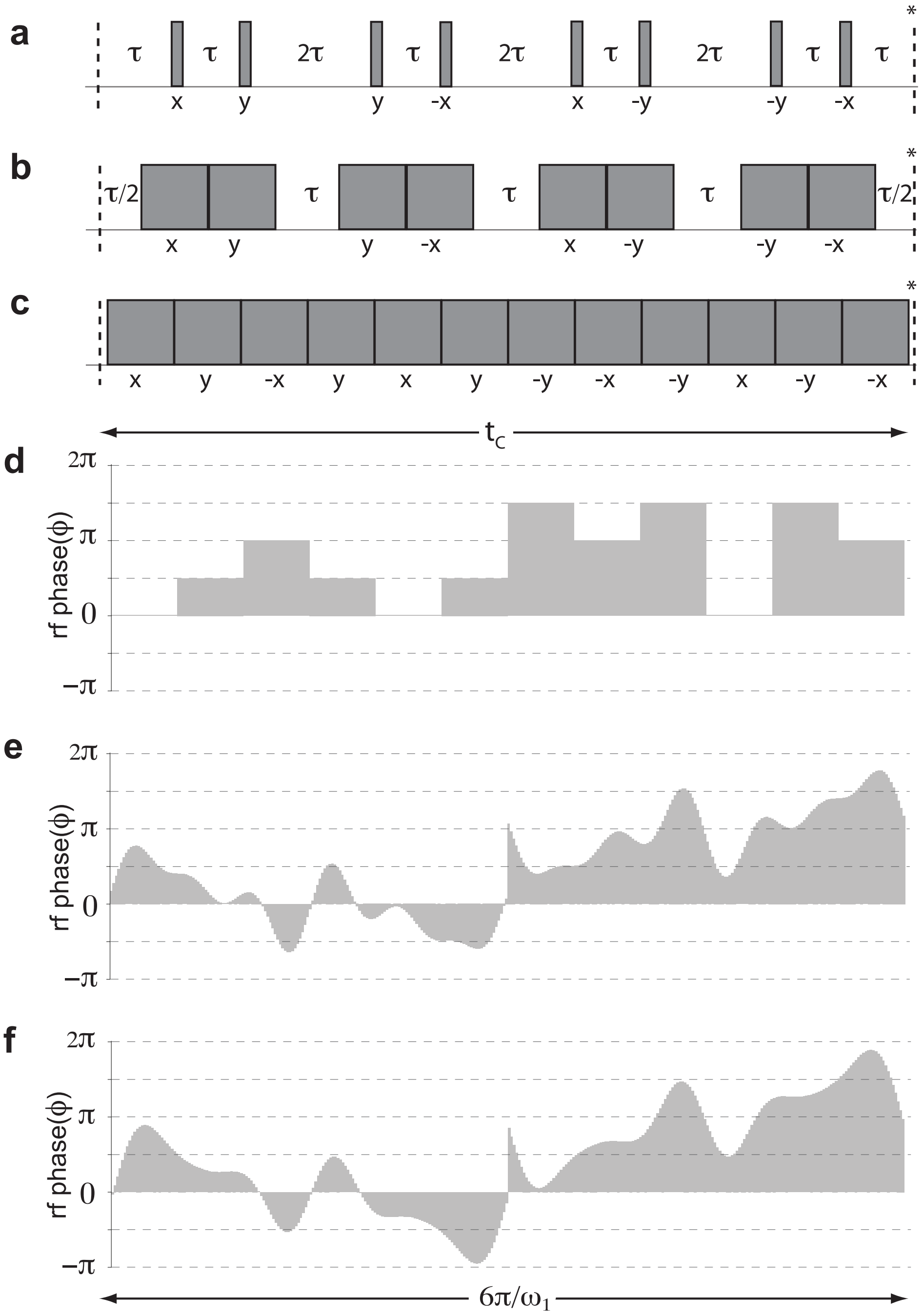

Figure 3.10. Multiple-pulse homonuclear decoupling sequences (a,b) MREV-8 [30] (a supercycled modification of WHH-4) and (c) BLEW-12 [125] in (a) original, windowed (b) semi-windowless and (c) windowless form, adapted from ref[125]. (d-f) Phase modulation of the (d) BLEW-12 (e) DUMBO-1 [34] (f) eDUMBO$_{22}$ [35] sequences. The DUMBO cycle time, t_c, and amplitude create a spin nutation with flip angle 6π (i.e., three complete revolutions about the effective field, B_{eff}). DUMBO-1 was originally developed as a 64-step sequence and later adapted to the 320 stepped phases shown, as used in this work.

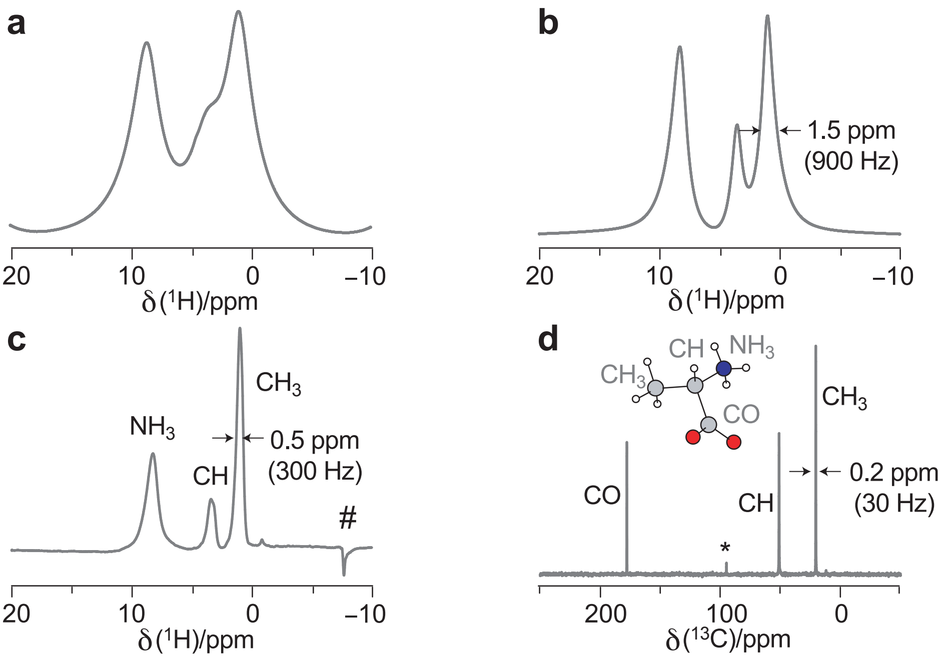

Figure 3.11. High-resolution (a-c) ^{1}H and (d) ^{13}C CP spectra of the amino acid *L*-alanine (inset), recorded at $\omega_0 = 600\,\text{MHz}$ and $\nu_r =$ (a,c,d) 12.5 kHz or (b) 30 kHz. *L*-alanine consists of three distinct ^{1}H and ^{13}C chemical sites, identified by their separate chemical shift frequencies. (a) At $\nu_r = 12.5\,\text{kHz}$ the ^{1}H sites are not clearly resolved, but resolution improves under (b) faster MAS or (c) CRAMPS, specifically, wDUMBO-1 decoupling with $\nu_1 = 100\,\text{kHz}$ amplitude. The scaling factor of (c) was 0.56 and # indicates the position of the central frequency artefact. (d) was recorded using $\nu_r = 100\,\text{kHz}$ TPPM decoupling during acquisition. (*) shows a spinning sideband due to the CO resonance.

θ, typically 0.5-1 µs in duration and are denoted by pale red pulses in the experimental sequences given in Fig. 3.9, and later in §3.3 and §3.4. The duration of the prepulse and initial phase of the DUMBO pulse (usually 160-230°) are optimised to give the smallest central frequency artefact in a one-dimensional (windowed) decoupled ^{1}H spectrum (see Fig. 3.11) recorded by a sequence as in Fig 3.9c. As such, it is often necessary to slightly offset the carrier frequency from the ^{1}H resonances for direct ^{1}H detection. The chemical shift axis is also scaled by the homonuclear decoupling sequence (see Eq. 3.22) - the scaling factor depends on the experimental parameters and is determined by a superposition of spectra carried out under CRAMPS and non-decoupled fast MAS.

A comparison of the ^{1}H line-narrowing achieved by CRAMPS and MAS is shown in Fig. 3.11 for the crystalline powder of *L*-alanine, where the resolution of the CH$_3$ resonance at $\nu_r = 12.5\,\text{kHz}$ is improved by a factor of 3 by CRAMPS (with wDUMBO-1 decoupling) compared to MAS alone. By comparison, the spectrum in Fig. 3.11d demonstrates the typical linewidths obtainable for ^{13}C CP MAS experiments.

3.3 NMR Experiments: Probing Connectivities

The J-coupling interaction between nuclei can be exploited by a variety of different NMR experiments to infer structural connectivities in materials. Considering the product operator description for a pair of 'weakly' coupled spins, it is possible to describe experiments that (a) measure J couplings for individual spin pairs, that can be a measure of the magnitude of specific bonding interactions and (b) correlate or transfer spin magnetization exclusively between pairs of bonded nuclei, identifing bonding environments based on associated chemical shifts.

3.3.1 Measuring J Couplings: The Heteronuclear Spin-Echo

During periods of free evolution, e.g., $\tau/2$, a coherence for a pair of $I = 1/2$ nuclei from two chemically-bonded atoms evolve under the effect of their isotropic chemical shifts and the isotropic J coupling (assuming that the dipolar interaction is zero under MAS, e.g., $\tau/2 = n\tau_r$). It is also assumed that the magnitude of the J coupling is significantly less than the difference in the isotropic chemical shifts of the two spins i.e., corresponding to the weak coupling limit, such that the evolution under $\hat{\mathscr{H}}_{CS}$ and $\hat{\mathscr{H}}_{J}$ can be considered separately. By analogy to the evolution under a chemical shift offset, given by product-operator notation in §2.2.3, the evolution of a transverse spin state (e.g., following a $90°_x$ pulse) of a nucleus, I, with a finite coupling to a heteronucleus, S, (J_{IS}) during $\tau/2$ is described:

$$I_z \xrightarrow{(90^\circ_x)_I} -I_y \xrightarrow{\pi J_{IS}\tau/2} -I_y \cos \pi J_{IS}\tau/2 + 2I_xS_z \sin \pi J_{IS}\tau/2 \tag{3.23}$$

where $2I_xS_z$ is the anti-phase spin operator described in Fig. 2.3. Under the secular approximation, $\hat{\mathscr{H}}_{CS}$ is linear in $\hat{I}_z$, such that the evolution under chemical shift gives rise to an inhomogeneous [25] broadening of the NMR linewidths resulting from inhomogeneities in the external field (along z) or small chemical changes within a sample. The *apparent* linewidth (from §3.1.1) observed in solids is given by $\Delta^* = 1/\pi {T_2}^*$, where ${T_2}^*$ is the dephasing time of the signal during acquisition. This linewidth is usually larger than J_{iso}, such that J couplings are not usually directly observed as a splitting of spectral peaks.

By performing a simple spin-echo experiment, $\tau/2-\pi-\tau/2$, it is possible to remove the effect of all terms which are linear in $\hat{I}_z$ and thus behave as offsets during the evolution period, such as field inhomogeneity effects or disorder. For this experiment, the expression given in Eq. 3.23 followed by a further $(180°)_I$ pulse on I and an identical evolution period $\tau/2$ results in:

$$\xrightarrow{(180^\circ_y)_I} -I_y \cos\pi J_{IS}\tau/2 - 2I_xS_z \sin\pi J_{IS}\tau/2 \xrightarrow{\pi J_{IS}\tau/2} -I_y \tag{3.24}$$

for a pulse along the y-axis. Therefore, the spin echo removes or *refocuses* the modulation of the signal caused by the J coupling. (An identical analysis is found for the simultaneous evolution under the chemical shift, Ω [107]). However, if the 180° pulses are applied simultaneously to the I and S channels (a *heteronuclear* spin echo), Eq. 3.24 becomes:

$$\begin{aligned} &\xrightarrow{(180^\circ_y)_I} && -I_y \cos\pi J_{IS}\tau/2 - 2I_xS_z \sin\pi J_{IS}\tau/2 \\ &\xrightarrow{(180^\circ_y)_S} && -I_y \cos\pi J_{IS}\tau/2 + 2I_xS_z \sin\pi J_{IS}\tau/2 \\ &\xrightarrow{\pi J_{IS}\tau/2} && -I_y \cos 2\pi J_{IS}\tau + 2I_xS_z \sin\pi J_{IS}\tau \end{aligned} \tag{3.25}$$

where the two (180°_y) pulses ensure that the $2I_xS_z \sin\pi J_{IS}\tau/2$ term i.e., the J-coupling modulation, is retained, whereas the chemical shift evolution will still have been refocused. This is also true for the case of a single (180°_y) pulse applied to a homonuclear pair of coupled spins, where I and S are of the same isotopic species, as the pulse will act on both I and S, individually, hence effectively, twice. In this case, the final expression in Eq. 3.25 takes into

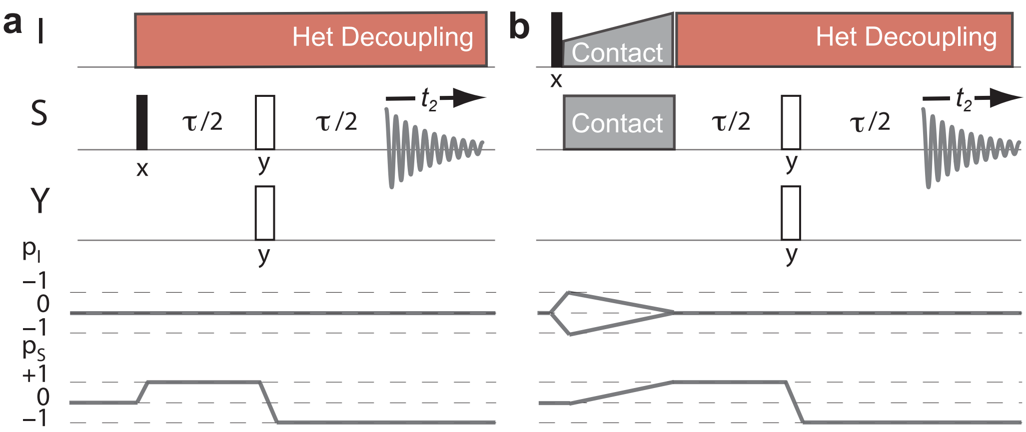

Figure 3.12. Heteronuclear Spin Echo sequences for determining J_{SY} in protonated systems. Initial transverse magnetization on S is generated by (a) direct S excitation (b) I-S cross polarization. Black solid and white open rectangles represent pulses with flip angles of 90° and 180°, respectively.

account that the sequence affects both spins identically:

$$-\left(I_y + S_y\right)\cos\pi J_{IS}\tau + \left(2I_xS_z + 2I_zS_x\right)\sin\pi J_{IS}\tau. \tag{3.26}$$

The spin-echo dephasing time, $T_2^{'}$, which is in effect during this sequence leads to refocused linewidths ($\Delta^{'} = 1/\pi T_2^{'}$) which are now sufficiently narrow such that the J splittings can be observed in the solid-state. Theoretical analyses of the J modulation observed in MAS spin-echo experiments, considering the effect of anisotropic interactions, have been presented [128, 129], including an extensive assessment of homonuclear J-coupled $I = 1/2$ pairs [130]. This work showed that the spin-echo modulation described could be accurately fitted to the $\cos\pi J_{IS}\tau$ modulation in Eq. 3.26 to extract the value of the J-coupling constant, even in the presence of large anisotropic interactions. This can be achieved by recording a series of spin-echo experiments whereby the evolution period is incremented and observing the integrated intensity of the absorptive resonance as a function of the total echo time (τ). By monitoring the integrated intensity of the NMR resonance, the anti-phase $\sin\pi J_{IS}\tau$ term in Eq. 3.26 (or 3.25, for heteronuclei) is effectively summed to zero, such that only the in-phase, cosine modulation is observed. Pham *et al.* have applied this methodology to pairs of homonuclear J-coupled $I = 1/2$ (^{15}N) nuclei [102], where, in the absence of zero-frequency peaks (see ref[130]) in the Fourier

Transformed spin-echo spectra, the integrated signal intensity of each resonance is fitted to the simple function

$$S(\tau) = A\cos(\pi J\tau)\exp(-\tau/T_2'), \tag{3.27}$$

or for the case of evolution under two J couplings

$$S(\tau) = A\cos(\pi J_1\tau)\cos(\pi J_2\tau)\exp(-\tau/T_2') \tag{3.28}$$

where the first data point is normalised ($\tau = 0$ is set to 1) and A, J (or J_1 and J_2, where $J = {}^{2h}J_{\mathrm{NN}}$, in [102]), and T_2 are free parameters. This and other studies also demonstrated the importance of efficient heteronuclear decoupling for the application of this technique to organic systems in order to remove the effects of the ^{1}H nuclei on the refocused linewidths detected.

In this thesis, the spin-echo sequences given in Fig. 3.12 are used to measure *heteronuclear* J couplings between S-Y pairs in the presence of $I = {}^1$H nuclei. Where S is a dilute $I = 1/2$ spin (^{13}C or ^{15}N), a cross polarization sequence is used to enhance the initial transverse magnetization state of S, otherwise, for $S = {}^{17}$O , direct excitation is achieved by a 90° pulse. A similar approach to that described in [102] is applied, whereby the normalised, integrated intensities of the resonances as a function of the total spin-echo evolution time ($S(\tau)$) are fitted to reveal the experimental J-coupling constants.

3.3.2 Heteronuclear Correlations: Refocused INEPT and MAS-J-HMQC

Evolution under a heteronuclear J coupling can also be manipulated by certain sequences of pulses to *transfer* magnetization between bonded pairs of nuclei. In the INEPT (Insensitive Nuclei Enhanced by Polarization Transfer) sequence [52], following on from a heteronuclear spin echo, $((90°_x)_I - \tau - (180°_y)_{IS} - \tau)$, given by Eq. 3.25, 90° pulses are applied to both I and S channels, simultaneously, such that:

$$\begin{aligned} &\xrightarrow{(90^\circ_y)_I} -I_y\cos 2\pi J_{IS}\tau - 2I_zS_z\sin 2\pi J_{IS}\tau \\ &\xrightarrow{(90^\circ_x)_S} -I_y\cos 2\pi J_{IS}\tau + 2I_zS_y\sin 2\pi J_{IS}\tau. \end{aligned} \tag{3.29}$$

Ideally, the evolution period is optimised for $\tau = 1/4J$, resulting in only the $2I_zS_y$ term, above, i.e., magnetization has been transferred from an initial I_y state to give anti-phase magnetization on S. The addition of another spin echo (τ'), for the Refocused INEPT sequence [50], converts this to in-phase S_x for absorptive lineshapes where the S signal acquired at this point contains only resonances from S nuclei with J couplings (i.e., bonded) to I. As a result of the selective magnetization transfer, the signal of the S nuclei is enhanced by a factor of γ_I/γ_S and the experimental recycle delay depends on the faster T_1 relaxation of I.

The sequence is applied as a two-dimensional correlation experiment by introducing a t_1 dimension, as described in Fig. 3.13a; t_1 is implemented directly after the first $(90°_x)_I$, where the system evolves only under the I chemical shift. This results in a 2D SQ$_{(I)}$-SQ$_{(S)}$ correlation experiment where peaks are only observed for J-coupled pairs I-S - a representive spectrum is shown in Fig. 3.14a.

An alternative J-mediated SQ-SQ heteronuclear correlation experiment is given in Fig. 3.13b; the MAS-J-HMQC (Heteronuclear Multiple Quantum Correlation) experiment [49], adapted from the equivalent J-HMQC sequence in the liquid state [51]. This experiment does not rely on a I-S magnetization transfer, thus can be preceded by a cross polarization sequence for the enhanced generation of initial S transverse magnetization. For example, following CP, the S spin is aligned along x, and the sequence follows:

$$\begin{aligned} S_x &\xrightarrow{\pi J_{IS}\tau} S_x\cos\pi J_{IS}\tau + 2I_zS_y\sin\pi J_{IS}\tau \\ &\xrightarrow{(90^\circ_y)_I} S_x\cos\pi J_{IS}\tau + 2I_xS_y\sin\pi J_{IS}\tau \\ &\xrightarrow{(90^\circ_{-y})_I} S_x\cos\pi J_{IS}\tau + 2I_zS_y\sin\pi J_{IS}\tau \end{aligned} \tag{3.30}$$

such that the heteronuclear double-quantum term ($2I_xS_y$) is present during t_1,

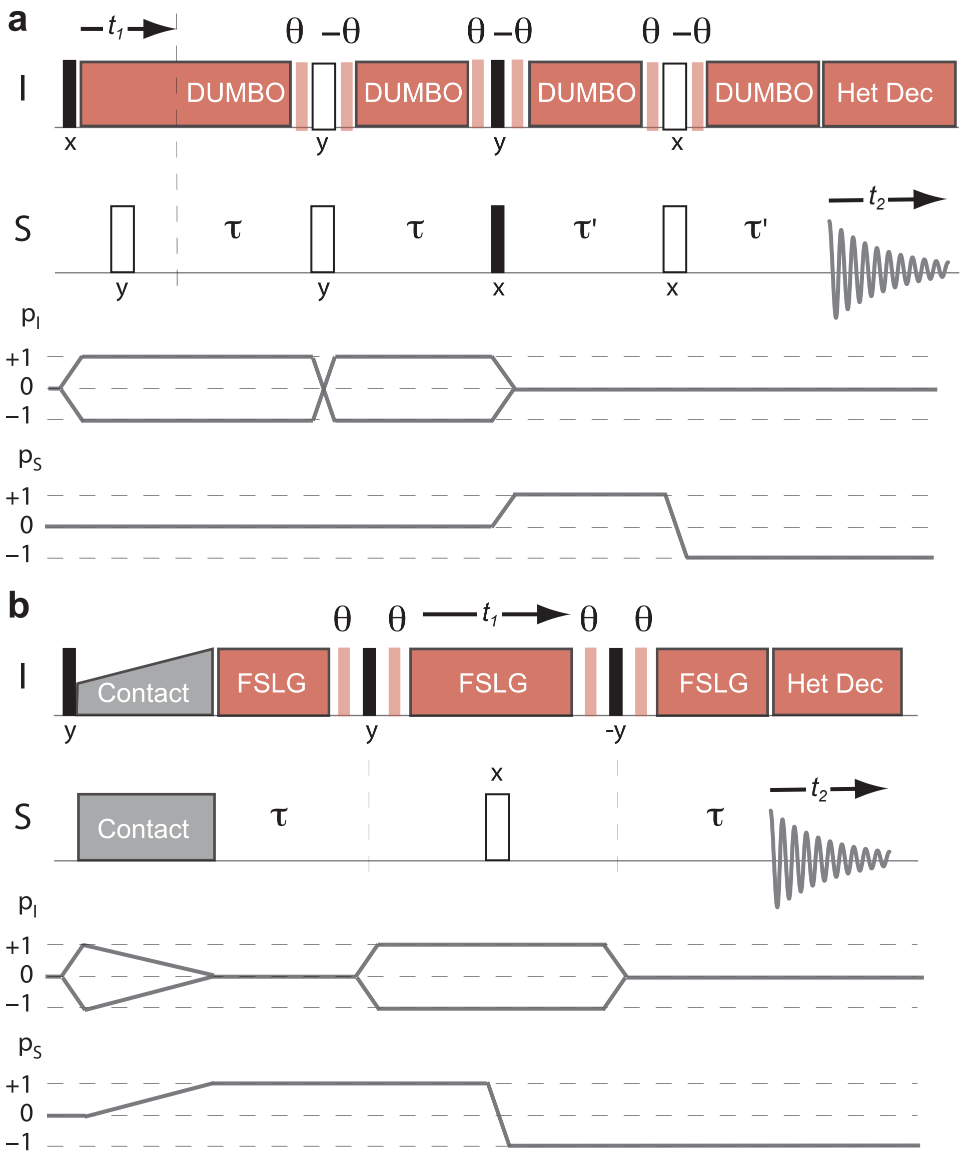

Figure 3.13. (a) Refocused INEPT [50] (b) MAS-J-HMQC [49] 2D heteronuclear correlation sequences with homonuclear ^{1}H decoupling (red blocks) during periods of free evolution and t_1 and prepulses, of flip angle θ (pale red). $(180°)_S$ pulses half-way through, t_1 refocus the S chemical shift.

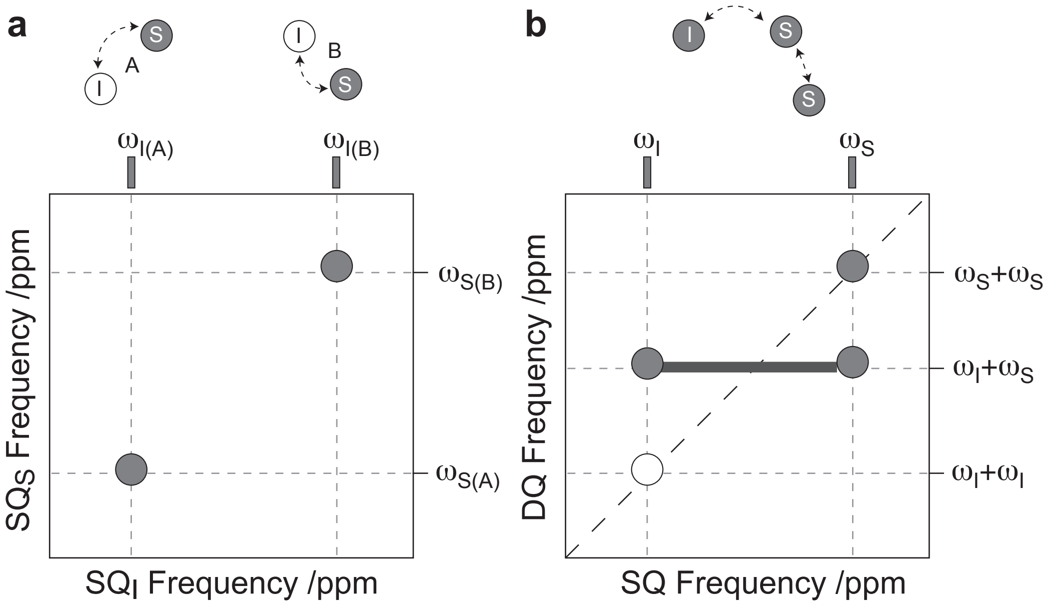

Figure 3.14. Schematic 2D (a) SQ-SQ and (b) DQ-SQ correlation spectra. (a) Heteronuclear SQ-SQ correlation where I and S are of different isotopic species. A peak on the spectrum correlates the I and S SQ frequencies (chemical shifts) for related spin groups. The examples shown in this work use J-mediated correlations such that an I-S peak indicates a directly bonded pair of heteroatoms. (b) A homonuclear DQ-SQ correlation whereby spins I and S are of the same isotopic species, with chemical shifts ω_I and ω_S, respectively. The DQ frequency, given in the indirect dimension, is the sum of SQ frequencies for a spin pair. A resonance peak due to DQC between nuclei of the same SQ chemical shift (S-S) appears along the diagonal of the spectrum, whereas peaks due to DQCs of nuclei with different SQ frequencies (I-S) appear equidistant from the diagonal. In this example, the lack of a peak at I-I indicates that no DQC exists between two spins of SQ frequency, ω_I.

where the system evolves under the I chemical shift (note that the 180° pulse in the middle of t_1 refocuses evolution under the S chemical shift). Antiphase magnetization on S is then generated by the second $(90)_I$ pulse. A phase cycle of ± 1 on the first 90° I causes only this antiphase term to be retained, whereby it evolves under the final τ period to the in-phase $-S_x$ state, such that the resulting 2D spectrum acquired is of the form given in Fig. 3.14a.

In this work, both heteronuclear correlation sequences are applied to organic systems where $I = {}^1$H. and so it is necessary to apply ^{1}H homonuclear decoupling throughout t_1, to improve resolution in the ^{1}H dimension, as well as throughout the τ evolution periods so as to ensure that the strong ^{1}H-^{1}H couplings do not interfere with the J_{IS} modulation. For the latter, τ is optimised as integer blocks of decoupling (FLSG or eDUMBO$_{22}$ to maximise the intensity of S signal detected. As part of the CRAMPS schemes, short pre-pulses, labelled by the flip-angle, θ, surround the decoupling blocks to align the magnetization perpendicular to the $< 111 >$ effective field axis during this time (see §3.2.2).

3.4 NMR Experiments: Interatomic Proximities

Due to the overriding spectral broadening arising from dipolar couplings in solid-state systems, much of the discussion has, so far, focussed upon the averaging or removal of this interaction by MAS or CRAMPS in order to obtain high-resolution spectra. However, as the magnitude of the dipolar coupling between a pair of nuclei, (given by d, see Eq. 2.97) is inherently related to the internuclear separation of the two spins, a controlled reintroduction of the dipolar interaction under MAS NMR (dipolar *recoupling* [53, 131]) can provide spectra containing quantitative information about interatomic distances in solids.

This work examines, in particular, dipolar couplings between ^{1}H nuclei by the generation of ^{1}H-^{1}H double-quantum coherences between coupled spin pairs [46, 54]. A variety of *r.f.* irradiation schemes exist for generating homonuclear, dipolar-driven DQCs, by reversing the dipolar averaging that occurs under MAS [117, 132–135]. Remembering that the dipolar coupling is completely averaged to zero over each period of MAS rotation, the application of *r.f.* pulses specifically synchronised with the rotor period, τ_r (and applied at intervals of less than τ_r), operate on the spin terms of the dipolar Hamiltonian to reintroduce the effect upon the spin system.

3.4.1 Double-Quantum Recoupling and the ^{1}H DQ-SQ Experiment

A simple *r.f.* irradiation scheme used for DQ dipolar recoupling is the homonuclear DRAMA (Dipolar Recoupling At the Magic Angle) sequence [133], consisting of two 90° pulses, 180° out of phase with one another, separated by

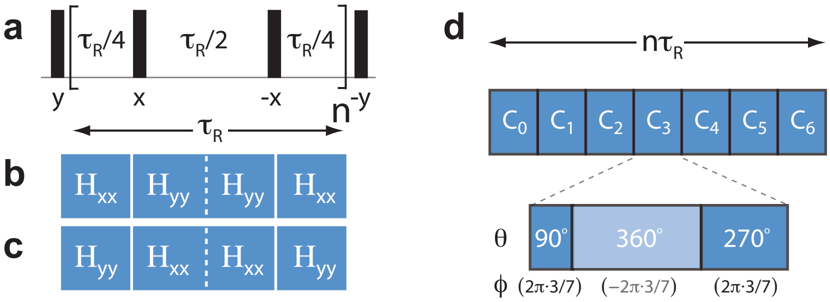

Figure 3.15. Pulse sequences for the generation of DQC using: (a) DRAMA [134], with the corresponding average homonuclear dipolar Hamiltonian in the toggling frame for (b) excitation and (c) (time reversal) reconversion; (d) symmetry-based POST-C7 [62].

$\tau_r/2$, as incorporated into the sequence given in Fig. 3.15a. An analysis of the homonuclear dipolar Hamiltonian, $\hat{\mathscr{H}}^D_{zz}$, in the toggling frame (as described in §3.2.2) is given in Fig. 3.15b, where the initial y pulse rotates this into $\hat{\mathscr{H}}^D_{xx}$ for the DQ recoupling. The DRAMA pulses are synchronised with the MAS rotation such that $\hat{\mathscr{H}}^D_{xx}$ and $\hat{\mathscr{H}}^D_{yy}$ each exist for $(n\tau_r/2)$. The average Hamiltonian throughout this time is then given by $\bar{\mathscr{H}}^0_D(n\tau_r) \propto (I_xS_x - I_yS_y)$, thus, double quantum spin terms are generated. The DQC generated in this case must be reconverted back to a population state ($p = 0$) before detection, which may be performed by repeating the DRAMA block in a time-reversed fashion, where the pulse phases are shifted by 90°, corresponding to the toggling frame Hamiltonians in Fig. 3.15c. An analysis of these terms reveals an inversion of the dipolar Hamiltonian to give $\bar{\mathscr{H}}^0_D(n\tau_r) \propto -(I_xS_x - I_yS_y)$.

In this work, a similar DQ dipolar recoupling sequence, BABA [117], is used with fast-MAS ($\nu_r = 30\,\mathrm{kHz}$) where 90° pulses are applied BAck-to-BAck at intervals of half the rotor period i.e., $90^\circ_x - \tau_r/2 - 90^\circ_{-x} - 90^\circ_y - \tau_r/2 - 90^\circ_{-y}$. This recoupling scheme has an amplitude dependence upon the rotor phase, such that non-rotor synchronised experiments lead to unusual spinning sideband patterns in 2D DQ spectra [38, 46]. The ^{1}H DQ MAS (BABA) spectra presented in this thesis were all recorded where $\Delta t_1 = \tau_r$ to avoid the observation of rotor-encoded spinning-sideband patterns.

Symmetry Based Recoupling: CN^ν_n Sequences

A particularly robust and efficient set of schemes for spin-interaction recoupling was introduced by Levitt *et al.* [53]. In §2.4.1, the spin interac-

Table 3.4. Spin and space rank and components for homonuclear spin interactions in the interaction frame of an applied rf field, under MAS. Notably the $m = 0$ term is not present due to rotational averaging. The selection rules given in Eq. 3.31 are applied for $C7_2^1$, $N = 7, n = 2, \nu = 1$ and satisfied for the $Z = 0$ condition for all interactions except CSA. Adapted from ref[53].

	Space		Spin		$C7_2^1$		
Interaction	j	m	λ	μ	m	μ	$m\lambda - \mu\nu$
CS$_{iso}$	0	0	1	-1,0,1	0	0	0
CS$_{aniso}$	2	-2,-1,1,2	1	-1,0,1	–	–	–
J	0	0	0	0	0	0	0
D	2	-2,-1,1,2	0	-2,-1,0,1,2	-1	-2	0
					1	2	0

tions were described in terms of spatial tensors with rank, j, and component, m, where $m = -j < -j + 1 < ... + j$, whereby a rotation between different axis frames, given in Eq. 2.75, causes a mixing of the m components. Similarly, the spin tensors can be defined by rank, λ, and component, μ, that also undergo a mixing of μ terms due to the spin rotations caused by *r.f.* irradiation. Rotor-synchronized *r.f.* schemes then establish periodic symmetry relationships between the spatial components, m, and spin components, μ, of the interaction, such that for specific sequences, only certain components are retained by the average Hamiltonian. Effectively, these sequences create a set of selection rules for each internal interaction and it is possible to control which spin interactions are able to evolve, and others that are suppressed by the *r.f.* scheme.

Specifically, the CN_n^ν class of symmetry-based recoupling sequences is defined where N, n and ν, the symmetry numbers, are integers. The *r.f.* sequence, of total duration n rotor periods (τ_r) is divided into N equal 'C$_\phi$' elements (see Fig. 3.15d), such that each element must induce a complete number of *r.f.* rotations i.e., 360°. The overall phase (ϕ) of each successive element is shifted by $2\pi\nu/N$. Therefore, over a complete cycle of N element, the spatial components have completed n full revolutions, and the phases have completed ν full rotations. Combining the spatial and spin dependences introduced by MAS and the CN_n^ν sequence leads to first order selection rules of the average Hamiltonian:

$$\bar{\mathscr{H}}^{(0)} = 0 \quad \text{if} \quad mn - \mu\nu \neq 0 \tag{3.31}$$

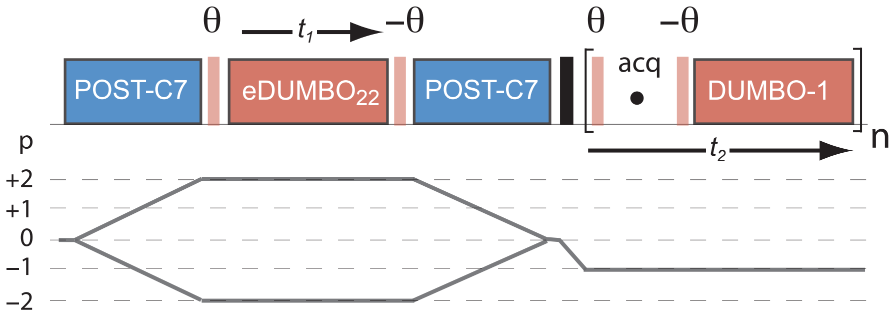

Figure 3.16. ^{1}H DQ-SQ (CRAMPS) correlation. Dipolar recoupling (blue) of DQC using the POST-C7 sequence. Homonuclear DUMBO decoupling (red) is applied in the both indirect and (windowed) direct dimension. Pale red pulses represent prepulses of flip angle θ.

where Z is any integer (including 0). For example, for the ($C7_2^1$) [136] scheme i.e., $N = 7, n = 2, \nu = 1$ the only spin interactions evolve where $2m - \mu = 7Z$ is satisfied. An examination of the space and spin components of the interaction Hamiltonians is given in Tab. 3.4, whereby the selection rules for ($C7_2^1$) are satisfied for the isotropic chemical shift, J, and the dipolar interaction, whereas the CSA interaction is suppressed.

In this work the Permutationally Offset Stabilized C7 (POST-C7) [62] sequence, given in Fig. 3.15d is used where the C$_\phi$ elements are divided into component pulses of flip angle, θ, and overall phase, ϕ, in degrees. The dipolar recoupling is used to generate ^{1}H-^{1}H DQC by incorporation into the two-dimensional DQ-SQ CRAMPS sequence given in Fig. 3.16 and employing a DQ phase cycle, such as that described in §3.1.4. Importantly, the C7 and POST-C7 sequences, unlike other DQ dipolar recoupling mechanisms, (e.g., BABA [117]) have a phase dependence upon the rotor phase, resulting in increased DQ efficiency and negating the need for rotor-synchronised 2D experiments.

As a result of the $C7_2^1$ symmetry condition, the nutation frequency of the DQ irradiation is given by $\omega_{1C7} = 7\omega_r$. The maximum amplitude of *r.f.* that can be applied without causing damage to the probe electronics is dependent upon the specific dimensions i.e., depends upon rotor size, but is typically in the limit of 100 kHz-120 kHz for the probes supporting rotors of diameter 4 mm-2.5 mm as used in this work. Therefore, for the use of $C7_2^1$ recoupling, the rotation speed is limited to approximately 15 kHz-18 kHz. In this work, experiments are typically carried out at $\nu_r = 12.5$ kHz corresponding to a recoupling amplitude of $\nu_1 = 87.5\,\text{kHz}$.

The number of C_ϕ elements used for excitation and reconversion (the recoupling time, τ_{rec}), is optimised to maximum DQC generation, where, in general 3 elements ($\tau_{rec} = 68.6\,\mu\text{s}$ at this spinning rate) is found to give maximum DQ intensity. High-resolution ^{1}H spectra are obtained in t_1 and t_2 by use of eDUMBO$_{22}$ and wDUMBO-1 homonuclear decoupling sequences, respectively. A schematic DQ-SQ spectrum is shown in Fig. 3.14b. In general, it has been shown that pairs of ^{1}H-^{1}H DQ peaks are generally observed in such 2D spectra for internuclear ^{1}H distances of approximately <3.5 Å [46].

3.5 Ab-Initio GIPAW Calculations

As introduced in §1.2, the GIPAW (Gauge Including Projector Augmented Waves) [77, 78] approach, which has been developed over the last decade, has proven to be a powerful technique for the calculation of NMR parameters using density functional theory (DFT). To complement the experimental work presented in this thesis, first-principles GIPAW chemical shift calculations were performed starting with X-ray or neutron diffraction crystal structures obtained from the Cambridge Chemical Database Service (CDS) [137]. All calculations used DFT within a generalized gradient approximation, specifically, the PBE exchange-correlation function [138] and the planewave pseudopotential approach [139]. Calculations were performed using the SGI Altix (56 x 1.6 GHz Intel Itanium2 processors) or IBM (96 x 3 GHz Intel Xeon 5160 processors) clusters at the University of Warwick and the AMD Opteron cluster at St. Andrews University, where some computations were carried out by Jonathan Yates and Anne-Christine Uldry.

It is common, in particular for crystal structures obtained by X-ray methods, that the positions of light elements (e.g., hydrogen atoms) are not determined from the experimental data, but rather are simply placed by the software. Therefore, before calculating NMR chemical shifts, all crystal structures were subject to a geometry optimization using the CASTEP DFT code [140, 141], where the positions of the atoms were allowed to move while the unit cell parameters remain fixed. Often, it is sufficient to relax only the ^{1}H atoms, however where large forces remain on the heavier elements following the optimization it is neccesary to allow further atomic species to relax. Where interatomic distances are quoted in this work (i.e., for identification of close ^{1}H-^{1}H proximities) these were taken from optimised structures following this approach, and derived using the DIAMOND [142] crystallographic viewing software.

NMR chemical shifts were calculated using either the PARATEC [143] or CASTEP codes [140, 141] employing GIPAW, which allows chemical shifts to be obtained with all-electron accuracy from calculations employing pseudopotentials. This approach uses a planewave basis set to expand the charge density and electronic wave functions, making it well suited to chemical shift calculations of periodic (crystalline) systems. The convergence of NMR parameters was analysed for each system whereby the cut off energy (eV) and sampling density of the Monkhorst-Pack grid [144] in reciprocal space (Å) were varied. The direct output of these ab-initio NMR calculations is the absolute shielding tensor, $\sigma(r)$, where, from §2.4.3

$$\sigma_{\text{iso}}(r) = {}^1\!/_3\text{Tr}\{\sigma(r)\} \tag{3.32}$$

To compare with experimentally determined chemical shifts, the expression

$$\delta_{\text{iso}}(r) = -\left[\sigma_{\text{iso}}(r) - \sigma_{\text{ref}}\right] \tag{3.33}$$

is used. In general, the shielding references, σ_{ref}, were determined (following the approach used in Ref.[80]) by a procedure that ensured that the mean of the calculated and experimental chemical shifts coincide. Values of σ_{ref} determined in this work were in a range which is consistent with other values in the literature [3, 80, 85, 145, 146].

J-coupling calculations presented here were carried out by Anne-Christine Uldry (St. Andrews, U.K. & Lausanne, Switzerland) as described by Joyce *et al.* [147], using a developer version of the CASTEP software package whereby Trouiller-Martins norm-conserving pseudopotentials [148] are used together with the projector augmented wave (PAW) [149] technique in order to recover the all-electron accuracy.

3.6 Further Experimental Details

Spectra presented in this thesis were recorded using various spectrometers operating at ^{1}H Larmor frequencies of 700 MHz (Bruker Avance II+, Lyon), 600 MHz (Bruker Avance II+ and Chemagnetics Infinity, Warwick), 500 MHz (Bruker Avance III, Lyon and Warwick; Bruker DSX, Lyon) and 300 MHz (Varian Infinity+, Warwick) using probes of diameter 2.5 mm, 3.2 mm and 4.0 mm and MAS frequencies in the range 8-30 kHz.

All experiments were performed (as accurately as possible) at the magic angle, which was adjusted by the observation of ^{79}Br MAS spectra of potassium bromide (KBr) where the number and amplitude of spinning sidebands were maximised as described in the literature [150]. Isotropic ^{1}H and ^{13}C chemical shifts were indirectly referenced to tetramethylsilane (TMS, $Si(CH_3))_4$), using the CH_3 resonance of *L*-alanine as a secondary reference ($\delta_{\text{iso}}(^1\text{H})= 3.6$ ppm $\delta(^{13}\text{C})= 51.0$ ppm). ^{15}N chemical shifts are referenced relative to neat liquid CH_33NO_2, using the ^{15}N resonance of [^{15}N]glycine at $\delta_{\text{iso}} =-347.4$ ppm as an external reference. To convert to the chemical shift scale frequently used in protein NMR, where the reference is liquid ammonia at −50 °C, it is necessary to add 379.5 ppm to the given values. The ^{17}O chemical shift scale was referenced to the ^{17}O signal of H_2O set to 0.0 ppm.

Errors in experimental chemical shifts are estimated at one quarter of the observed linewidth of each resonance. For ^{13}C/^{15}N and ^{1}H this approximates to ±0.1 and ±0.2 ppm, respectively, for the majority of chemical shift values discussed.

4

Better Resolution and Assignment of ^{1}H DQ Correlations by Through-Bond Refocused INEPT Transfer to ^{13}C

^{1}H nuclei are a very powerful probe of three-dimensional solid-state structures as they play a major role in many key intermolecular interactions. For example, π-π stacking and hydrogen-bonding interactions determine the self-assembly of many organic molecules in the solid-state, for which the ^{1}H chemical shift offers much information [46–48]. Also, the high natural abundance (and gyromagnetic ratio, γ) of ^{1}H nuclei causes proton experiments to be many times more sensitive ($\propto \gamma^3$) to the NMR technique than dilute (^{13}C, ^{15}N) organic spins, such that proton experiments can generally be recorded much more rapidly. This combination of factors, along with the typically short interproton distances observed in organic solids (e.g., < 2 Å for a CH_2 group), leads to large homonuclear dipolar couplings between pairs of ^{1}H nuclei. As the dipolar coupling between a spin pair has a very specific dependence upon their internuclear separation (as given in Eq. 2.97), this interaction potentially provides a particularly accurate mechanism for determining interatomic distances, both intra- and intermolecular, in solid structures.

Conflictingly, the same ^{1}H-^{1}H dipolar couplings result in marked broadening effects of NMR resonances such that fast MAS or combined MAS and homonuclear decoupling methodologies [40] are generally employed in order to sufficiently resolve ^{1}H spectra in the solid-state (see §2.4.5 and §3.2.2). By the very nature of these techniques, the homonuclear dipolar couplings are averaged out and so must be specifically reintroduced by the NMR experiment for H-H proximities to be determined[1]. As such, dipolar *recoupling* pulse sequences are necessary under MAS conditions to restore the dipolar coupling information, whereby the timings of the recoupling pulses are synchronised with the period of MAS rotation.

4.1 ^{1}H DQ Spectroscopy

A particularly robust mechanism for probing H-H proximities is double quantum (DQ) spectroscopy, where (as described in §2.2.2 and §3.4) double quantum coherences (DQCs) are generated between pairs of through-space coupled spins. In general, DQC can be created for both J-coupled and dipolar coupled pairs of $I = 1/2$ nuclei, however, the ^{1}H-^{1}H J couplings are many times smaller than the spin-echo proton linewidths (Δ', see §3.3.1), such that only dipolar-coupled protons have been shown to generate DQC in solids. Originally, Baum *et al.* demonstrated that multiple quantum (MQ) coherences could be used to estimate the size of ^{1}H spin clusters under static conditions [151, 152]. Since then, many recoupling sequences [53, 131] have been presented for the generation of homonuclear DQC under MAS, including DRAMA [133, 134], DRAWS [153], BABA [117], HORROR [135], C7 [136] and POST-C7 [62].

As described in §1.1, two-dimensional ^{1}H DQ MAS and DQ CRAMPS techniques have been presented for the study of structure and dynamics in many solid-state systems. However, the experimental application of ^{1}H DQ-SQ methods as an intermolecular probe is fundamentally restricted by the ^{1}H resolution achievable for any given system. As such, this is dependent upon the variation of chemical sites within the molecule i.e., the spread of ^{1}H resonances in an NMR spectrum. For example, hydrogen-bonded protons typically exhibit a downfield shift of their isotropic resonance to high ppm values, making such ^{1}H resonances and ^{1}H-^{1}H DQ coherences involving these nuclei relatively simple to identify under fast MAS alone. Conversely, ^{1}H resonances due to multiple aromatic or aliphatic proton environments (e.g., the two distinct protons in a CH_2 group), tend to fall within a much smaller

---

[1] Alternatively, NOESY-type ^{1}H-^{1}H spin-diffusion methods are also used to infer structural information, without the use of active recoupling [46, 66, 103]

spectral window and are hence more difficult to separate (see §5). To this end, ^{1}H DQ heteronuclear correlation experiments have been proposed, whereby the resolution of the ^{1}H DQ dimension is improved by the use of a high-resolution heteronucleus, such as ^{13}C or ^{15}N. Reif *et al.* [154] and Lesage *et al.* [155] have presented such experiments, where a cross polarization sequence is used to correlate the indirect (^{1}H DQ) and direct (^{15}N SQ, ^{13}C SQ) dimensions, for the case of a peptide and microcrystalline protein, respectively. In these studies, samples were fully ^{15}N, and ^{15}N, ^{13}C enriched, and partially deuterated to improve the resolution of proton resonances. Specifically, only certain proton sites were back or re-exchanged after deuteration such that limited transfer of ^{1}H DQ polarization to heteronuclei would be possible (given short contact times), thus reducing complications due to the generally non-selective nature of the CP transfer.

This chapter presents a new experiment where the ^{1}H DQ dimension is correlated with a ^{13}C SQ dimension using the refocused INEPT (§3.3.2) pulse-sequence element [50] to transfer magnetization *specifically via one-bond* ^{1}H-^{13}C *J couplings*. Thus, H-H proximities are unambiguously identified by their well-resolved ^{13}C-bonded neighbours, while the sensitivity of (*natural abundance*) ^{13}C (H) NMR signals is simultaneously enhanced by the INEPT transfer. This new technique is applied to the pharmaceutical compound, penicillin-G, for which the NMR resonances have previously been assigned [65], to establish its suitability as a structural probe of such organic solids. 'Close' proton-proton proximities are identified, by comparison to an optimised reference crystal structure, for both intra- and intermolecular spin distances, emphasising the potential of this technique as a means for determining three-dimensional packing arrangements. In the following chapter, this ^{1}H DQ-^{13}C CRAMPS experiment is presented for a more challenging organic system, namely, the disaccharide, β-maltose monohydrate. The work presented in this and the following chapter was carried out in collaboration with the Emsley group in Lyon, France.

4.2 Experimental Details

The K^+ salt of penicillin-G, **4-1**, was purchased from Aldrich and used without further purification or recrystallisation. Spectra were recorded at ENS, Lyon, France using a Bruker Avance II+ spectrometer operating at a ^{1}H Larmor frequency of 700 MHz, using a 3.2 mm probe at a MAS frequency of 18.5 kHz.

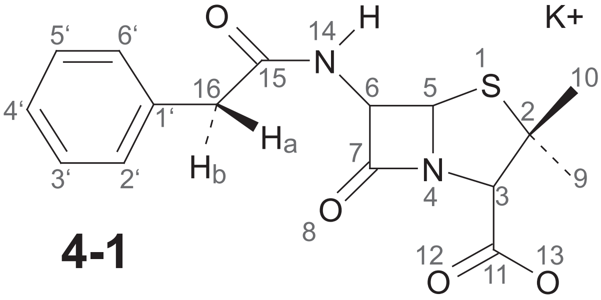

4-1

^{1}H DQ-^{13}C INEPT: The pulse sequence and coherence transfer pathway diagram is presented in Fig. 4.1. 7 basic POST-C7 [62] elements (total duration 108.1 µs, $\nu_1 = 129.5$ kHz) were used for excitation and reconversion of DQ coherence. Homonuclear ^{1}H dipolar decoupling with $\nu_1 = 100$ kHz was implemented using the windowless eDUMBO$_{22}$ [35] sequence during t_1 periods of free evolution, whereas heteronuclear SPINAL-64 [20] decoupling ($\nu_1 =$ 100 kHz, 4.7 µs pulse duration) was applied during a t_2 acquisition time of 20.0 ms. For eDUMBO$_{22}$, the 32 µs decoupling cycles were divided into 320 steps of 100 ns each and a pre-pulse $\theta = 1.1$ µs was used. The scaling factor in F_1 was 0.57. A $\tau = \tau' =$ evolution period of 1.12 ms was used to maximize the ^{1}H-^{13}C through-bond polarization transfer. For each of 256 t_1 slices (using the States-TPPI method with an increment of 64 µs), 192 transients were coadded with a recycle delay of 2.5 s (total experimental time of 34 h). The employed 64-step phase cycle is listed in Appendix A.1.

^{13}C CP MAS: ^{13}C magnetization was generated by cross polarization with a 50 to 100 % ramp on the ^{1}H channel for a contact time of 1 ms. SPINAL-64 [20] heteronuclear decoupling ($\nu_1 = 100$ kHz, 4.7 µs pulse duration) was applied during a t_2 acquisition time of 19.9 ms. 256 transients were co-added with a recycle delay of 2.5 s.

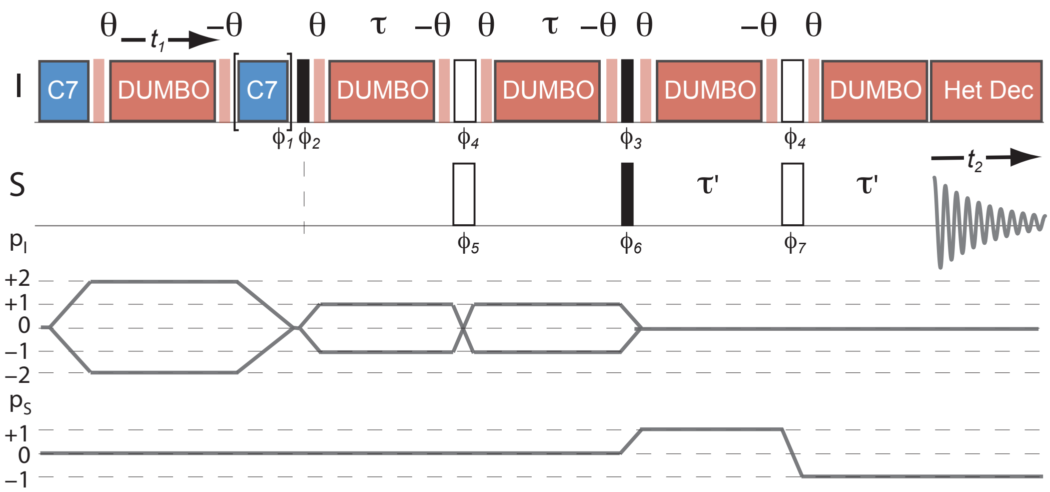

Figure 4.1. Pulse sequence and coherence pathway transfer diagram for the new ^{1}H (DQ DUMBO)-^{13}C (SQ) refocused INEPT experiment. The phase cycle used employed in this work is tabulated in Appendix A.1.

4.3 Results

The pulse sequence described in Fig. 4.1 was used to record a ^{1}H DQ (CRAMPS)-^{13}C refocused INEPT spectrum of penicillin-G (**4-1**), as shown in Fig. 4.2a. ^{1}H DQC between spin pairs evolves during t_1, and is transferred to ^{13}C SQC in t_2 for J-coupled C-H nuclei. A short spin-echo duration, $\tau = \tau' = 1.1\,\mathrm{ms}$, was used for the refocused INEPT transfer such that the spectrum in Fig. 4.2a correlates ^{13}C resonances with ^{1}H DQ resonances that involve the ^{1}H nucleus (or nuclei) that is (are) directly bonded to a specific ^{13}C nucleus.

High-resolution ^{1}H-^{1}H DQ-SQ CRAMPS and ^{1}H-^{13}C SQ-SQ refocused INEPT 2D NMR spectra have previously been presented for the K$^+$ salt of penicillin-G, **4-1**, in combination with first-principles (GIPAW) ^{1}H and ^{13}C chemical shift calculations [65]. In the preceding study, almost all ^{1}H resonances were assigned to individual protons by comparison of ^{1}H DQ correlations with the expected ^{1}H-^{1}H proximities predicted by the optimised crystal structure. A ^{1}H SQ-^{13}C SQ refocused INEPT correlation and chemical shift calculations performed upon the geometrically optimised crystal structure were then used to confirm assignments of ^{1}H and ^{13}C resonances from the C-H sites. The assigned experimental ^{1}H and ^{13}C chemical shift values are given in Tab. 4.1. Chemical shifts that could not be individually distinguished included the five aromatic protons and some doubt was also expressed regard-

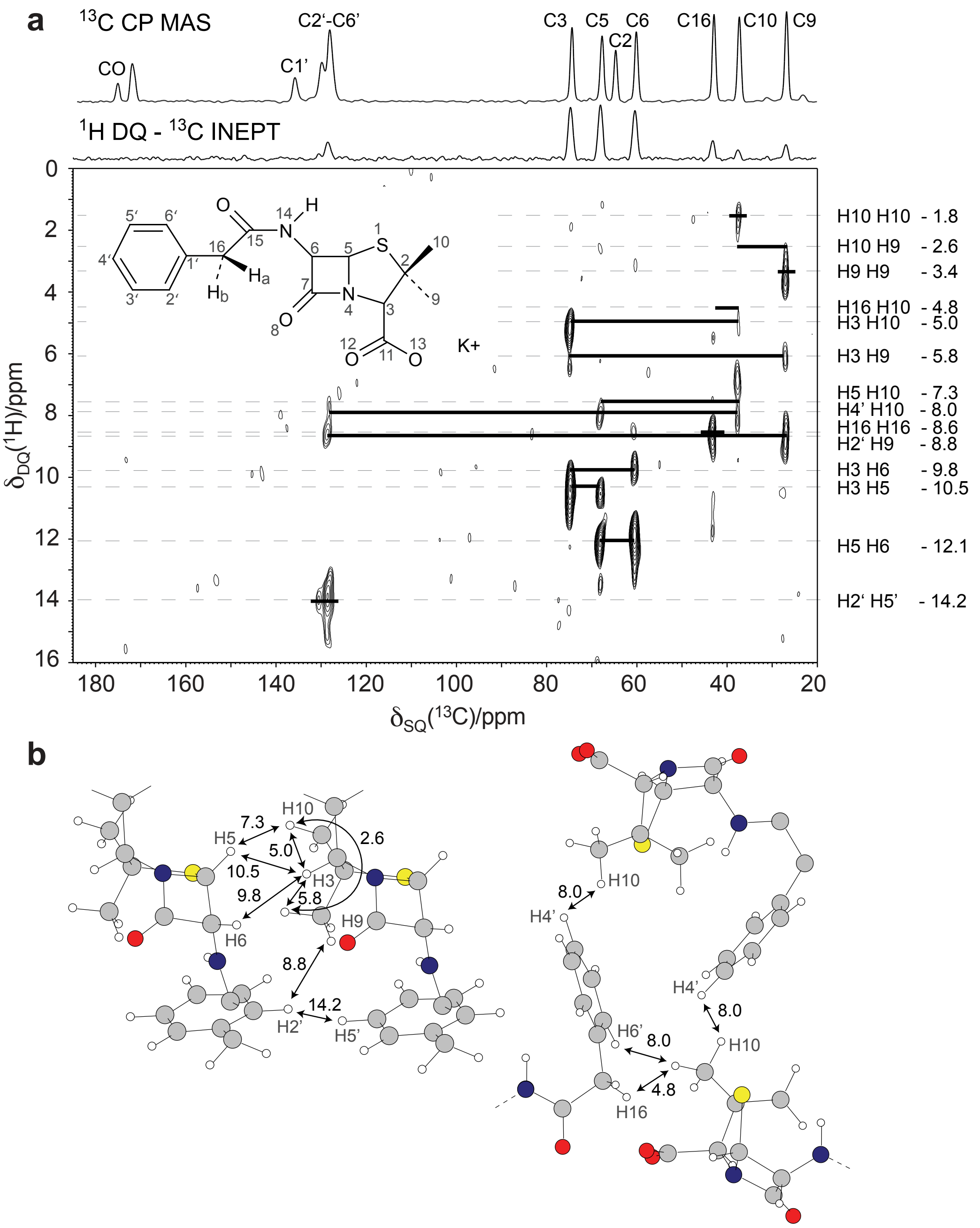

Figure 4.2. (a) A ^{1}H (700 MHz) (DQ DUMBO)-^{13}C (SQ) refocused INEPT spectrum of the K^{+} salt of penicillin-G, **4-1**, recorded at 18.5 kHz MAS and a bearing gas temperature of 298 K using the pulse sequence in Fig. 4.1. The base contour level is at 13 % of the maximum peak height. The ^{1}H DQ coherences are assigned in Tab. 4.2. Solid horizontal bars indicate specific DQ coherences between pairs of CH, CH$_2$ or CH$_3$ ^{1}H nuclei. The skyline projection onto the ^{13}C axis is compared to a ^{13}C CP MAS spectrum. (b) Representations of the geometrically optimised (GIPAW) crystal structure [65] showing H-H proximities that give rise to evident DQ peaks in (a), the H-H proximities are labelled by their corresponding ^{1}H DQ chemical shift in ppm (see Tab. 4.2).

Table 4.1. Experimental ^{13}C and ^{1}H chemical shifts of **4-1**, as assigned in ref[65] using ^{1}H DQ-SQ CRAMPS and ^{1}H-^{13}C refocused INEPT spectra.

Site	δ_{iso} /ppm (^{13}C)	(^{1}H)	Site	δ_{iso} /ppm (^{13}C)	(^{1}H)
7	176.1		3	74.9	4.1
11	172.9		5	68.2	6.4
15	172.3		2	65.2	
1’	136.4		6	60.5	5.7
4’	130.6	7.1	16a	43.3	4.7
6’	130.6	7.1	16b		3.9
2’	128.7	7.1	10	37.6	0.9
3’	128.7	7.1	9	27.1	1.7
5’	128.7	7.1	14		6.2

ing the assignment of the chemical shifts of the two diastereotopic protons of the CH_2 group.

In the work presented here, a similar approach was adopted whereby ^{1}H-^{1}H DQ correlations were assigned based on the close proton proximities given by the geometrically optimised diffraction data (Fig. 4.2b). The observed ^{1}H DQ frequencies involving the CH, CH_2 and CH_3 ^{1}H nuclei of penicillin-G are given as dashed horizontal lines in Fig. 4.2a (H-H distances < 2.9 Å, see Tab. 4.2). Solid black lines indicate the specific ^{1}H-^{1}H DQ coherences where the two ^{1}H nuclei are directly bonded to distinct ^{13}C nuclei. Notably, ^{1}H DQ peaks corresponding to *both intramolecular and intermolecular proximities are observed* e.g., (^{13}C) = 27.1 & 74.9 ppm, DQ(^{1}H) = 5.0 ppm (H3-H10, intramolecular); (^{13}C) = 37.6 & 74.9 ppm, DQ(^{1}H) = 5.8 ppm (H3-H9, intramolecular); (^{13}C) = 60.5 & 68.2 ppm, DQ(^{1}H) = 12.1 ppm (H5-H6, intramolecular); (^{13}C) = 27.1 & 130.6 ppm, DQ(^{1}H) = 8.0 ppm (H10-H4’, H10-H6’, intermolecular); (^{13}C) = 37.6 & 128.7 ppm, DQ(^{1}H) = 8.8 ppm (H9-H2’, intermolecular); (^{13}C) = 60.5 & 74.9 ppm, DQ(^{1}H) = 9.8 ppm (H3-H6, intermolecular); (^{13}C) = 68.2 & 74.9 ppm, DQ(^{1}H) = 10.5 ppm (H3-H5, intermolecular). Representations of the geometrically optimised (CASTEP) crystal structure [65] showing H-H proximities that give rise to these DQ peaks are shown in Fig. 4.2b.

In addition, single correlation peaks are observed for the DQ coherences among the two sets of CH_3 protons, (^{13}C) = 37.6 ppm, DQ(^{1}H) = 3.4 ppm

(H9) and (^{13}C) = 27.1 ppm, DQ(^{1}H) = 1.8 ppm (H10), between the two CH$_2$ protons, (^{13}C) = 43.3 ppm, DQ(^{1}H) = 8.6 ppm (H16a-H16b), and among the aromatic CH protons, (^{13}C) = 128.7 ppm, DQ(^{1}H) = 14.2 ppm (e.g., H2'-H5'). Therefore, ^{1}H DQ correlations involving the H9 and H10 CH$_3$ groups are now clearly identified individually by their ^{13}C chemical shift. It should be noted that, aside from the peak at (^{13}C) = 43.3 ppm, (DQ(^{1}H) = 8.6 = 4.7+3.9 ppm corresponding to the DQC between the two CH$_2$ protons (H16a + H16b), no other peaks are observed in the spectrum in Fig. 4.2a due to close proximities involving the CH$_2$ group (i.e., < 2.9 Å as given in Tab. 4.2) i.e., (^{13}C) = 43.3 & 128.7 ppm, DQ(^{1}H) = 11.8 ppm (H16a-H6', intramolecular), (^{13}C) = 43.3 & 128.7 ppm, DQ(^{1}H) = 11.0 ppm (H16b-H2', intramolecular), (^{13}C) = 43.3 & 27.1 ppm, DQ(^{1}H) = 4.8 ppm (H16b-H10a,b, intermolecular). However, weak, single peaks are observed at these DQ frequencies for the directly bonded ^{13}C resonances of H16 and H10 for the intra and intermolecular cases, respectively. This is not a surprising result, considering the ^{13}C signal intensity as a function of the INEPT τ evolution delay for a CH$_2$ group exhibits a distinctly faster dephasing than for CH or CH$_3$ resonances [50], and so the overall amount of magnetization transfered via J_{CH} for the H16 group is likely to be lower. Furthermore, the short H16a-H16b distance (1.75 Å), which leads to a prominent single DQ peak is likely to truncate the dipolar coupling between the individual H16 protons and other further away ($\geq$ 2.44 Å) ^{1}H nuclei [156], reducing the amount of ^{1}H DQ coherence generated for these correlations.

Table 4.2. ^{1}H DQ correlations$^{\mathrm{ab}}$ involving the CH, CH$_2$ and CH$_3$ ^{1}H nuclei (< 2.9 Å) in the K^{+} salt of penicillin-G, **4-1**.

	H-H /Å	$\delta_{\mathrm{SQ\_1}}$ (^{1}H) /ppm	$\delta_{\mathrm{SQ\_2}}$ (^{1}H) /ppm	δ_{DQ} (^{1}H) /ppm		H-H /Å	$\delta_{\mathrm{SQ\_1}}$ (^{1}H) /ppm	$\delta_{\mathrm{SQ\_2}}$ (^{1}H) /ppm	δ_{DQ} (^{1}H) /ppm
H9a					**H16b**				
H9c	1.78	1.7	1.7	3.4	H16a	1.75	3.9	4.7	8.6
H9b	1.78	1.7	1.7	3.4	H10b	2.49	3.9	0.9	4.8
H3	2.49	1.7	4.1	5.8	H2'	2.55	3.9	7.1	11.0

Continued on Next Page...

Table 4.2 – Continued

	H-H /Å	$\delta_{\mathrm{SQ\_1}}$ (^{1}H) /ppm	$\delta_{\mathrm{SQ\_2}}$ (^{1}H) /ppm	δ_{DQ} (^{1}H) /ppm		H-H /Å	$\delta_{\mathrm{SQ\_1}}$ (^{1}H) /ppm	$\delta_{\mathrm{SQ\_2}}$ (^{1}H) /ppm	δ_{DQ} (^{1}H) /ppm
H10b	2.61	1.7	0.9	2.6	H10a	2.84	3.9	0.9	4.8
H10c	2.65	1.7	0.9	2.6	**H6**				
H14	2.70	1.7	6.2	7.9	H5	2.51	5.7	6.4	12.1
H9b					H3	2.75	5.7	4.1	9.8
H9c	1.78	1.7	1.7	3.4	**H5**				
H9a	1.78	1.7	1.7	3.4	H3	2.38	6.4	4.1	10.5
H3	2.58	1.7	4.1	5.8	H6	2.51	6.4	5.7	12.1
H14	2.73	1.7	6.2	7.9	H10b	2.80	6.4	0.9	7.3
H9c					**H3**				
H9b	1.78	1.7	1.7	3.4	H5	2.38	4.1	6.4	10.5
H9a	1.78	1.7	1.7	3.4	H9a	2.49	4.1	1.7	5.8
H10c	2.51	1.7	0.9	2.6	H9b	2.58	4.1	1.7	5.8
H2’	2.74	1.7	7.1	8.8	H10b	2.73	4.1	0.9	5.0
H10a					H6	2.75	4.1	5.7	9.8
H10b	1.77	0.9	0.9	1.8	**H2’**				
H10c	1.81	0.9	0.9	1.8	H5’	2.13	7.1	7.1	14.2
H6’	2.13	0.9	7.1	8.0	H3’	2.48	7.1	7.1	14.2
H4’	2.38	0.9	7.1	8.0	H16b	2.55	7.1	3.9	11.0
H16b	2.84	0.9	3.9	4.8	H9c	2.74	7.1	1.7	8.8
					H6’	2.74	7.1	7.1	14.2
H10b					**H3’**				
H10a	1.77	0.9	0.9	1.8	H10c	2.33	7.1	0.9	8.0
H10c	1.77	0.9	0.9	1.8	H2’	2.48	7.1	7.1	14.2
H16b	2.49	0.9	3.9	4.8	H4’	2.51	7.1	7.1	14.2
H9a	2.61	0.9	1.7	2.6	H5’	2.73	7.1	7.1	14.2
H3	2.73	0.9	4.1	5.0	**H4’**				
H5	2.80	0.9	6.4	7.3	H10c	2.10	7.1	0.9	8.0

Continued on Next Page. . .

Table 4.2 – Continued

	H-H /Å	$\delta_{\mathrm{SQ\_1}}$ (^{1}H) /ppm	$\delta_{\mathrm{SQ\_2}}$ (^{1}H) /ppm	δ_{DQ} (^{1}H) /ppm		H-H /Å	$\delta_{\mathrm{SQ\_1}}$ (^{1}H) /ppm	$\delta_{\mathrm{SQ\_2}}$ (^{1}H) /ppm	δ_{DQ} (^{1}H) /ppm
H10c					H10a	2.38	7.1	0.9	8.0
H10b	1.77	0.9	0.9	1.8	H5’	2.46	7.1	7.1	14.2
H10a	1.81	0.9	0.9	1.8	H3’	2.51	7.1	7.1	14.2
H4’	2.11	0.9	7.1	8.0	**H5’**				
H3’	2.33	0.9	7.1	8.0	H2’	2.13	7.1	7.1	14.2
H9c	2.51	0.9	1.7	2.6	H4’	2.46	7.1	7.1	14.2
H9a	2.65	0.9	1.7	2.6	H6’	2.50	7.1	7.1	14.2
H16a					H3’	2.73	7.1	7.1	14.2
H16b	1.75	4.7	3.9	8.6	**H6’**				
H6’	2.44	4.7	7.1	11.8	H10a	2.12	7.1	0.9	8.0
					H16a	2.44	7.1	4.7	11.8
					H5’	2.50	7.1	7.1	14.2
					H2’	2.74	7.1	7.1	14.2

[a] Listed in order of corresponding ^{13}C chemical shift. Intermolecular proximities are highlighted in grey.

[b] H-H distances from the (CASTEP) geometrically optimised neutron diffraction crystal structure (see §4.2 and ref.[65]).

4.4 Summary and Outlook

With advances in ^{1}H line-narrowing methodologies, ^{1}H DQ CRAMPS experiments are becoming increasingly popular for determining three-dimensional structures and packing arrangements of crystalline powders. This chapter has presented a ^{1}H (DQ DUMBO)-^{13}C (SQ) refocused INEPT NMR spectrum for the pharmaceutical compound, penicillin-G. In such a spectrum, the separation of the ^{1}H DQ coherences by means of the resolved ^{13}C resonances allows a ^{1}H DQ coherence due to two ^{1}H nuclei that are directly bonded to two distinct (directly bonded) carbon atoms to be identified. By following such ^{1}H DQ peaks, for directly bonded carbon atoms, such a spectrum would hence allow, in principle, the carbon skeleton of an organic molecule to be mapped out in an analogous fashion to the case of a ^{13}C-^{13}C correlation spectrum recorded with, e.g., the refocused INADEQUATE [157] or DQ-filtered COSY [158–160] experiments. An important distinction, however, is that, at natural abundance, correlation peaks in a ^{13}C-^{13}C spectrum are only observed where there are two adjacent ^{13}C nuclei (with probability 1 in 10,000 considering a single ^{13}C-^{13}C pair) often demanding experimental times of around one week to record. For example, application of the refocused INADEQUATE sequence for the identification of two polymorphs of non-enriched testosterone, required 5 days of measurement time [85]. By comparison, in a ^{1}H (DQ DUMBO)-^{13}C (SQ) refocused INEPT NMR spectrum, significant enhancement is provided by exploiting the ^{1}H nuclei, with signal being observed for all molecules with at least one ^{13}C nucleus. There is currently much interest in the ability of experimental methods to characterise organic materials at natural abundance, most notably, for the distinction of polymorphs in pharmaceutical materials, for which the ^{1}H-^{1}H DQ-SQ CRAMPS technique has already been demonstrated [67]. It is envisaged that the new experiment presented here, as well as allowing the better resolution of ^{1}H DQ peaks via the ^{13}C chemical shift, will provide a more sensitive alternative to ^{13}C-^{13}C experiments for the intra and intermolecular 'mapping' of such systems, and will hence emerge as a valuable additional tool in the NMR crystallography toolkit.

5

Complete ^{1}H Resonance Assignment of a Disaccharide from ^{1}H DQ CRAMPS and First-Principles Calculations

As introduced in the previous chapter, the identification of intermolecular proton-proton proximities in high-resolution double-quantum (DQ) spectra provides valuable information regarding three-dimensional molecular structures. An obvious precursor to this is the resolution and assignment of ^{1}H chemical shifts in the solid state, which can prove a particularly demanding task for certain materials, such as sugars. This chapter presents the first full ^{1}H resonance assignment of a disaccharide, and as such, opens the way for further applications of solid-state NMR to the important class of biological molecules, oligosaccharides.

5.1 Solid-State NMR of Saccharides

In comparison to the many applications of solid-state NMR to peptides and proteins [161, 162], there are relatively few reports of applications of solid-state NMR to saccharides, even at the level of disaccharides [80, 163, 164]. Obtaining high resolution ^{1}H solid-state NMR spectra of saccharides presents a particular challenge because of the large numbers of distinct protons confined to a small chemical shift range. Nevertheless, saccharides are vital constituents of many biological molecules, for example, the raffinose family are believed to stabilize plant cell membranes during freezing and dehydration

[165], whereas other saccharides also find numerous applications as stabilizers and cryoprotectants in many biological systems and foods [166–168]. More notably, oligosaccharides are known to bind to the plasma membranes of animal cells, acting as chemical markers for many cell recognition processes such as blood group specificity and immune system regulation. As such, the binding of a pentasaccharide to the membrane protein DC-SIGN is involved in HIV infection [169], while the biosynthesis of peptidoglycans is a major target of antibiotics [170] and cyclodextrin complexes are also being much investigated for use in drug delivery [171].

Results are presented here for the disaccharide β-maltose monohydrate, for which ^{1}H-^{1}H DQ-SQ CRAMPS spectra are shown together with ^{1}H (DQ)-^{13}C correlation spectra obtained with the new pulse sequence introduced in the previous chapter. Compared to the observation of only a single broad peak in a ^{1}H DQ spectrum recorded at 30 kHz magic-angle spinning (MAS), the use of DUMBO ^{1}H homonuclear decoupling in the ^{1}H DQ CRAMPS experiment allows the resolution of distinct DQ correlation peaks which, in combination with chemical shift calculations from first principles based on the GIPAW plane-wave pseudopotential approach, enables the assignment of *all* ^{1}H resonances due to the 24 distinct protons in β-maltose monohydrate, notably, including the hydroxyl protons. In addition, variable-temperature ^{1}H-^{1}H DQ CRAMPS spectra reveal small increases in the ^{1}H chemical shifts of the OH resonances upon decreasing the temperature from 348 K to 248 K. The work presented in this chapter (including the ^{1}H DQ-^{13}C INEPT experiment introduced in chapter §4) has recently been accepted for publication [1].

5.2 Experimental and Computational Details

5.2.1 Sample Preparation

A paramagnetic doped sample of β-maltose monohydrate, **5-1**, was prepared by the Lyon group, so as to reduce the T_1 relaxation time, by recrystallisation of 615 mg of β-maltose monohydrate (95%+, Sigma Aldrich) with the minimum amount of water required to dissolve, plus a 1 ml pipette full of glacial acetic acid and a spatula tip (< 5 mg) of $MnCl_2 \cdot 4H_2O$. The crystals that formed initially overnight were filtered after allowing evaporation to occur for 2 days. After washing with acetic acid, and further evaporation for 2 days, the final sample was obtained after being placed in an oven at 60 °C for 36 hours.

5-1

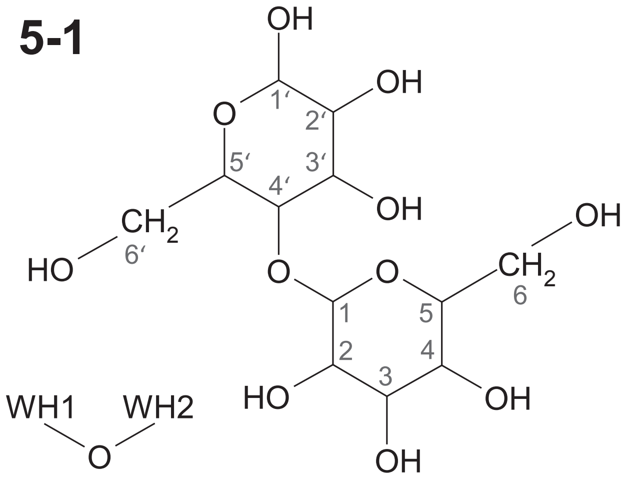

5.2.2 Solid-State NMR

Spectra were recorded on Bruker Avance III spectrometers in either Lyon or Warwick, both operating at a ^{1}H Larmor frequency of 500 MHz. A ^{1}H DQ MAS spectrum was recorded using a 2.5 mm probe at Warwick at 30 kHz MAS. All other experiments were performed using 4 mm triple resonance probes, operating in double-resonance mode, (variable temperature experiments at Warwick, other experiments at Lyon) at a MAS frequency of 12.5 kHz. In all experiments, ^{1}H 90° pulses were of duration 2.5 µs.

^{1}H DQ MAS: One rotor period of the BABA [117] recoupling sequence was used for excitation and reconversion of DQ coherence. The recycle delay was 2 s. For each of the 100 t_1 slices (using the States-TPPI [115] method with a rotor-synchronised increment of 33.3 s), 16 transients were co-added.

^{1}H DQ CRAMPS: The ^{1}H DQ CRAMPS pulse sequence employed is detailed in ref[64]. The experiment was performed using 3 basic POST-C7 [62] elements (total duration 68.6 µs, $\nu_1 = 87.5$ kHz) for excitation and reconversion of DQ coherence. Homonuclear ^{1}H dipolar decoupling with $\nu_1 = 100$ kHz was implemented using the windowless eDUMBO$_{22}$ [35] sequence during t_1 and windowed DUMBO-1 (wDUMBO-1 [34, 41]) for CRAMPS acquisition in

t_2. For both eDUMBO$_{22}$ and wDUMBO-1, the 32 µs decoupling cycles were divided into 320 steps of 100 ns each (Lyon) or the 24 µs decoupling cycles were divided into 320 steps of 75 ns each (Warwick). Small pre-pulses, $\theta_1 = 1.0$ µs and $\theta_2 = 0.5$ µs, rotate the magnetization from a plane perpendicular to the effective decoupling field to the detection plane (x, y). For acquisition, a short detection window was inserted after every three (Lyon) or two (Warwick) DUMBO-1 cycles in order to acquire a complex point. Including the detection window and θ_2 pre-pulses, the effective t_2 dwell time was 100.3 µs corresponding to a total acquisition time of 17.4 ms (Lyon) or 53.8 µs corresponding to a total acquisition time of 10.3 ms (Warwick). For each of the 192 (Lyon) or 288 (Warwick) t_1 slices, (using the States-TPPI method with an increment of 96 µs), 32 (Lyon) or 16 (Warwick) transients were coadded with a recycle delay of 5 s (Lyon) or 2.5 s (Warwick), corresponding to a total experimental time of 8.5 h (Lyon) or 3.2 h (Warwick). The scaling factors were 0.57 in F$_1$ and 0.56 in F$_2$ (Lyon) and 0.63 in F$_1$ and 0.57 in F$_2$ (Warwick).

^{13}C CP MAS: ^{13}C magnetization was generated by cross polarization with a 50 to 100 % ramp (Lyon) or 90 to 100 % ramp (Warwick, variable temperature) on the ^{1}H channel for a contact time of 2 ms (Lyon) or 1 ms (Warwick). SPINAL-64 [20] heteronuclear decoupling ($\nu_1 = 100$ kHz, 4.7 µs (Lyon), 4.6 µs (Warwick) pulse duration) was employed throughout a t_2 acquisition time of 34.9 ms (Lyon) or 20.5 ms (Warwick). 128 transients (Lyon) or 32 transients (Warwick) were co-added, with a recycle delay of 4 s (Lyon) or 3 s (Warwick).

^{1}H DQ - ^{13}C INEPT: The pulse sequence and coherence transfer pathway diagram is presented in Fig. 4.1. 3 basic POST-C7 elements (total duration 68.6 µs, $\nu_1 = 87.5$ kHz) were used for excitation and reconversion of DQ coherence. Homonuclear ^{1}H dipolar decoupling with $\nu_1 = 100$ kHz was implemented using the windowless eDUMBO$_{22}$ sequence during t_1 periods of free evolution, whereas heteronuclear SPINAL-64 decoupling ($\nu_1 = 100$ kHz, 4.7 µs pulse duration) was applied during a t_2 acquisition time of 25.0 ms. For eDUMBO$_{22}$, the 32 µs decoupling cycles were divided into 320 steps of 100 ns each and a pre-pulse $\theta = 1.1$ µs was used. The scaling factor in F$_1$ was 0.54. A $\tau = \tau' =$ evolution period of 1.12 ms was used to maximize the ^{1}H-^{13}C through-bond polarization transfer. For each of 160 t_1 slices (using the States-TPPI method with an increment of 64 µs), 256 transients were coadded with a recycle delay of 4 s (total experimental time of 46 h). The employed 64-step phase cycle is listed in Appendix A.1.

5.2.3 First-Principles NMR Chemical Shift Calculations

Calculations of the NMR chemical shifts from first principles for β-maltose monohydrate were performed by Jonathan Yates, Oxford, using the methods and computational parameters described in ref[80]. A partial geometry optimization was first carried out using the CASTEP code [140, 141] starting with the neutron diffraction crystal structure (MALTOS11 [172]) and allowing the positions of the hydrogen atoms to move. The distances listed in this chapter are for the geometry optimised crystal structure, available as Supporting Information with ref[80].

The NMR chemical shifts were computed using the PARATEC [143] code and the GIPAW method [77, 78], as described in §3.5. Calculated chemical shieldings were referenced using Eq. 3.33, where reference shieldings were determined as $\sigma_{\text{ref}}(^1\text{H}) = 30.17$ ppm, $(^{13}\text{C}) = 167.1$ ppm (following the approach used in ref[80]), such that the mean of the calculated and experimental ^{1}H chemical shifts (the extrapolated to 0K OH ^{1}H chemical shifts and the CH protons) and ^{13}C chemical shifts (extrapolated to 0K) for all sites in β-maltose monohydrate coincide. It should be noted that the calculated ^{13}C chemical shifts presented in Table 1 of ref[80] used $\sigma_{\text{ref}}(^{13}\text{C}) = 168.1$ ppm, as determined using the experimental chemical shifts at 298 K.

5.3 Results

5.3.1 ^{1}H DQ CRAMPS

Figs. 5.1a and 5.1b compare ^{1}H-^{1}H (500 MHz) DQ-SQ correlation spectra of β-maltose monohydrate obtained under fast MAS alone (Fig. 5.1a, 30 kHz MAS) and by the CRAMPS approach (Fig. 5.1b, employing ^{1}H DUMBO homonuclear decoupling at a MAS frequency of 12.5 kHz). The observation of a single broad peak in the ^{1}H-^{1}H DQ-SQ MAS spectrum is representative of the insufficient line narrowing achieved by 30 kHz MAS; by comparison, the enhanced resolution provided by the ^{1}H-^{1}H DQ-SQ CRAMPS technique enables the observation of distinct DQ correlation peaks. In addition, Fig. 5.1c presents a ^{1}H (DQ-DUMBO) - ^{13}C (SQ) correlation spectrum of β-maltose monohydrate obtained using the pulse sequence shown in Fig. 4.1, where the refocused INEPT pulse-sequence element ensures that magnetization is transferred from ^{1}H to ^{13}C via through-bond J_{CH} couplings [50]. A short spin-echo duration, $\tau = \tau' =$ 1.1 ms, was used for the refocused INEPT transfer such that the spectrum in Fig. 5.1c correlates ^{13}C resonances with ^{1}H DQ resonances that involve the ^{1}H nucleus (or nuclei) that is (are) directly bonded to the specific ^{13}C nucleus. The following describes how all OH ^{1}H resonances can be assigned on the basis of the ^{1}H DQ CRAMPS spectra in Fig. 5.1 together with first-principles calculations, as well as the knowledge of the ^{13}C and ^{1}H chemical shifts of the CH moieties as determined from combined experimental and computational studies based on a ^{1}H-^{13}C MAS-J-HMQC spectrum [80] and the determination of the ^{13}C chemical shift anisotropies [94].

Fig. 5.2a shows an expanded view of the ^{1}H-^{1}H DQ-SQ CRAMPS spectrum of β-maltose monohydrate that highlights the DQ correlation peaks among CH and between CH and OH ^{1}H nuclei, as assigned in Tabs. 5.1 and 5.2, respectively. The H-H proximities corresponding to the eight DQ coherences due to the intramolecular proximities of CH and OH protons associated with the same carbon are shown in Fig. 5.2b. For example, a particularly prominent DQ correlation is that corresponding to the 2.13 Å proximity between CH1' and OH1' at a DQ frequency of DQ = 4.2 + 7.2 = 11.4 ppm. All but one of these eight DQ coherences correspond to a H-H distance of less than 2.35 Å. The exception is the OH2 proton, where there is a considerably longer distance (2.85 Å) to the CH2 proton attached to the same carbon. In this case, there are closer (intermolecular) proximities to the CH6a (2.50 Å) and CH3 (2.63 Å) ^{1}H nuclei that have the same ^{1}H chemical shift as OH2 and thus the same DQ frequency, DQ = 3.7 + 5.1 = 8.8 ppm. These proximities as well as those between CH4 and OH3' (2.35 Å, DQ = 3.1 + 5.6 = 8.7 ppm) and between CH1 and OH2 (2.85 Å, DQ = 4.8 + 5.1 = 9.9 ppm) that give rise

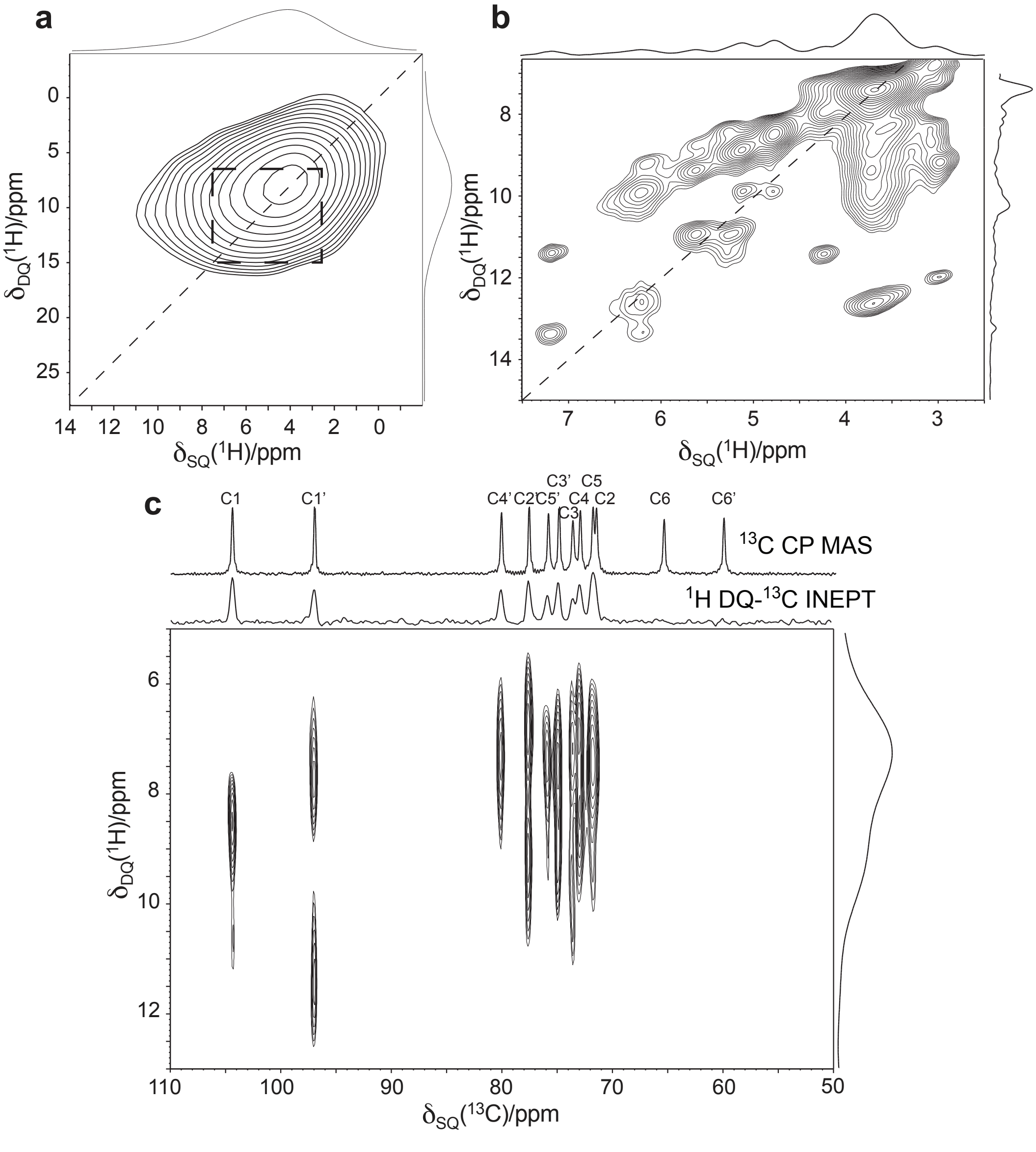

Figure 5.1. ^{1}H (500 MHz) DQ NMR spectra (with skyline projections) of *β*-maltose monohydrate, **5-1**, doped with $MnCl_2$, with the bearing gas temperature regulated at 298 K: (a) a ^{1}H-^{1}H DQ-SQ MAS spectrum recorded at 30 kHz MAS, (b) a ^{1}H-^{1}H DQ (DUMBO)-SQ (DUMBO) CRAMPS spectrum recorded at 12.5 kHz MAS using the pulse sequence described in ref[64], (c) a ^{1}H (DQ DUMBO) - ^{13}C (SQ) refocused INEPT spectrum recorded at 12.5 kHz MAS using the pulse sequence shown in Fig. 4.1. The base contour level is at (a) 8 %, (b) 7 % and (c) 20 % of the maximum peak height in each spectrum. In (a) and (b), the $F_1 = 2F_2$ diagonal is shown as a short-dashed line. The region within the long-dashed rectangle in (a) corresponds to that shown in (b). In (c), the skyline projection onto the ^{13}C axis is compared to a ^{13}C CP MAS spectrum, also recorded with the bearing gas temperature regulated at 298 K.

Table 5.1. ^{1}H DQ correlations[a] among CH ^{1}H nuclei[b] (< 2.9 Å) in β-maltose monohydrate, **5-1**.

CH proton	$\delta_{\mathrm{SQ\_1}}(^{1}\mathrm{H})$ /ppm	CH proton	$\delta_{\mathrm{SQ\_2}}(^{1}\mathrm{H})$ /ppm	Separation[c] /Å	$\delta_{\mathrm{DQ}}(^{1}\mathrm{H})$ /ppm
CH2’	3.0	CH4’	3.4	2.61	6.4
CH4	3.1	CH6a	3.7	2.48	6.8
CH4	3.1	CH2	3.7	2.50	6.8
CH4’	3.4	CH5’	3.7	2.36	7.1
CH4’	3.4	CH3’	3.7	2.49	7.1
CH2’	3.0	CH1’	4.2	2.57	7.2
CH5	3.6	CH2	3.7	2.23	7.3
CH5	3.6	CH6b	3.7	2.49	7.3
CH5	3.6	CH3	3.7	2.63	7.3
CH6a	3.7	CH6b	3.7	1.77	7.4
CH6’a	3.7	CH6’b	3.7	1.78	7.4
CH2	3.7	CH3	3.7	2.12	7.4
CH5’	3.7	CH6’b	3.7	2.41	7.4
CH5’	3.7	CH6’a	3.7	2.43	7.4
CH5’	3.7	CH3’	3.7	2.53	7.4
CH4’	3.4	CH1’	4.2	2.66	7.6
CH5’	3.7	CH1’	4.2	2.37	7.9
CH3’	3.7	CH1’	4.2	2.67	7.9
CH4’	3.4	CH1	4.8	2.06	8.2
CH5	3.6	CH1	4.8	2.49	8.4
CH5’	3.7	CH1	4.8	2.45	8.5
CH2	3.7	CH1	4.8	2.47	8.5

[a] Intermolecular proximities are highlighted in grey.

[b] ^{1}H chemical shifts for the CH resonances have been determined and assigned previously from combined experimental and computational studies based on a ^{1}H-^{13}C MAS-J-HMQC spectrum [80] and the determination of the ^{13}C chemical shift anisotropies [94].

[c] H-H distances from the (CASTEP) optimised neutron diffraction crystal structure (see §5.2 and ref[80]).

to evident DQ peaks in Fig. 5.2a are shown in Fig. 5.2c.

Fig. 5.3a presents an expanded view of the ^{1}H-^{1}H DQ-SQ CRAMPS spectrum given in Fig. 5.1b, showing the DQ correlations among the OH protons. The assignments are illustrated in Fig. 5.3b and tabulated in Tab. 5.3. Consider the OH3’ proton that has close proximities to the OH4 (2.01 Å) and OH2 (2.46 Å) protons, corresponding to DQ = 5.3 + 5.6 = 10.9 ppm and DQ = 5.1 + 5.6 = 10.7 ppm, respectively. From an analysis of experimental and calculated (for 8-spin clusters using SPINEVOLUTION) ^{1}H DQ build-up curves for the dipeptide β-AspAla, it has been observed that the relative intensity of

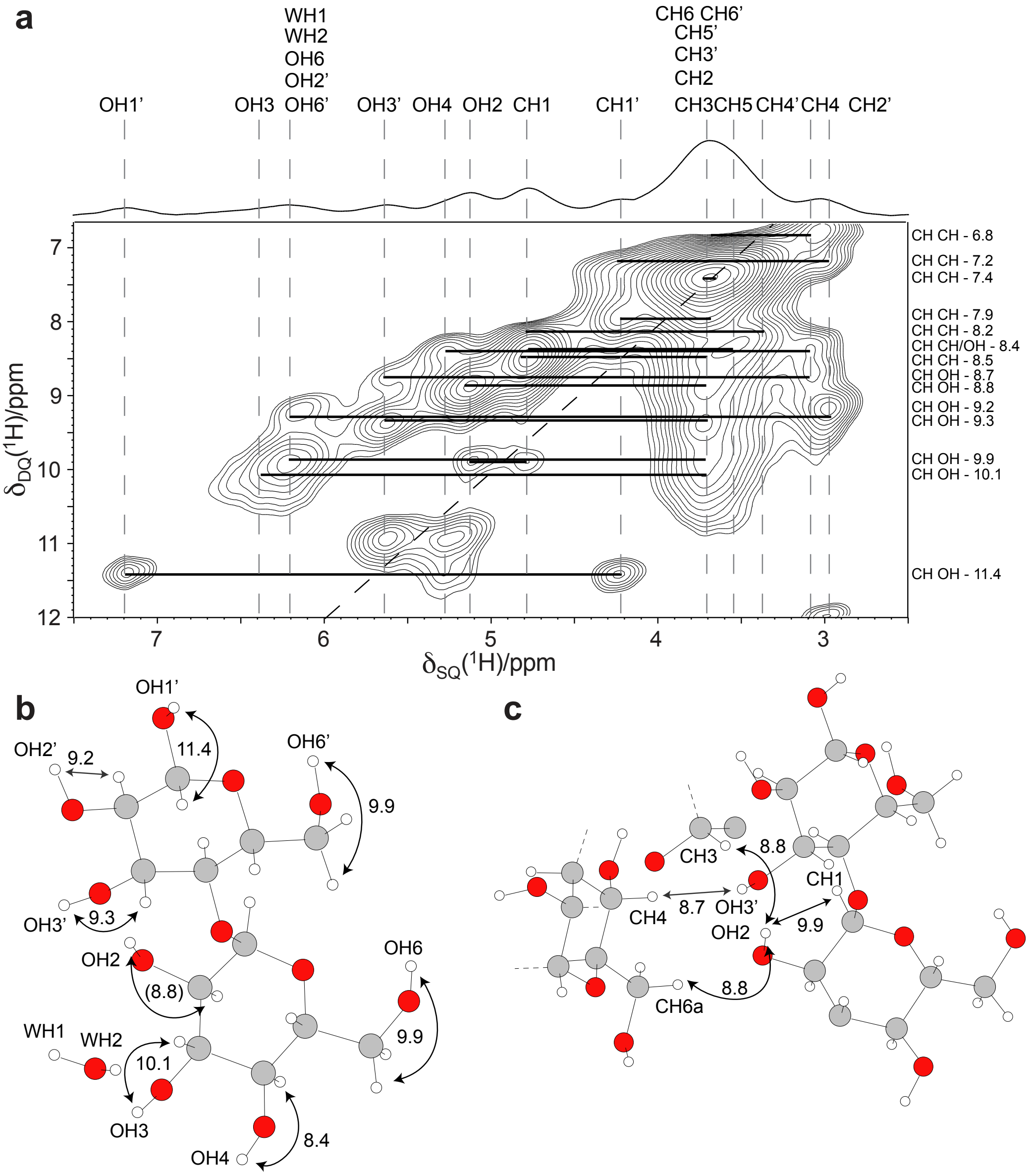

Figure 5.2. (a) An expanded region of the ^{1}H-^{1}H (500 MHz) DQ-SQ CRAMPS NMR spectrum of β-maltose monohydrate, **5-1**, doped with MnCl$_2$, with the bearing gas temperature regulated at 298 K (see Fig. 5.1b), showing DQ correlation peaks among CH and between CH and OH ^{1}H nuclei, as assigned in Tabs. 5.1 and 5.2, respectively. Solid horizontal bars indicate specific DQ coherences between pairs of CH & CH or CH & OH ^{1}H nuclei. The base contour is shown at 7 % of the maximum peak height. (b, c) Representations of the geometrically optimised (CASTEP) crystal structure [80] showing H-H proximities between CH and OH protons corresponding to (b) the eight intramolecular DQ coherences between CH and OH protons associated with the same carbon and (c) other DQ coherences that give rise to evident DQ peaks in (a). In (b) and (c), H-H proximities are labelled by their corresponding ^{1}H DQ chemical shift (see Tab. 5.2).

Table 5.2. ^{1}H DQ correlations[a] between CH and OH ^{1}H nuclei[b] ($<$ 2.9 Å) in β-maltose monohydrate, **5-1**.

CH proton	$\delta_{\mathrm{SQ\_1}}(^{1}\mathrm{H})$ /ppm	OH proton	$\delta_{\mathrm{SQ\_2}}(^{1}\mathrm{H})$ /ppm	Separation[c] /Å	$\delta_{\mathrm{DQ}}(^{1}\mathrm{H})$[d] /ppm
CH4	**3.1**	**OH4**	**5.3**	**2.32**	**8.4**
CH4’	3.4	OH2	5.1	2.80	8.5
CH4	3.1	OH3’	5.6	2.35	8.7
CH6a	3.7	OH2	5.1	2.50	8.8
CH3	3.7	OH2	5.1	2.63	8.8
CH2	**3.7**	**OH2**	**5.1**	**2.85**	**8.8**
CH2’	**3.0**	**OH2’**	**6.2**	**2.25**	**9.2**
CH3’	**3.7**	**OH3’**	**5.6**	**2.23**	**9.3**
CH6b	3.7	OH3’	5.6	2.48	9.3
CH6a	**3.7**	**OH6**	**6.2**	**2.28**	**9.9**
CH6’b	**3.7**	**OH6’**	**6.2**	**2.29**	**9.9**
CH5’	3.7	OH6’	6.2	2.57	9.9
CH6a	3.7	WH1	6.2	2.63	9.9
CH6’b	3.7	OH2’	6.2	2.64	9.9
CH6b	3.7	WH1	6.2	2.67	9.9
CH2	3.7	WH2	6.2	2.69	9.9
CH6’a	3.7	OH6	6.2	2.69	9.9
CH6’b	3.7	OH2’	6.2	2.79	9.9
CH1	4.8	OH2	5.1	2.85	9.9
CH6’a	3.7	OH6’	6.2	2.87	9.9
CH6b	3.7	OH6	6.2	2.87	9.9
CH6’a	3.7	OH2’	6.2	2.89	9.9
CH3	**3.7**	**OH3**	**6.4**	**2.10**	**10.1**
CH6’b	3.7	OH3	6.4	2.70	10.1
CH1’	4.2	WH1	6.2	2.90	10.4
CH6b	3.7	OH1’	7.2	2.88	10.9
CH1’	**4.2**	**OH1’**	**7.2**	**2.13**	**11.4**

[a] Intermolecular proximities are highlighted in grey.

[b] ^{1}H chemical shifts for the CH resonances have been determined and assigned previously from combined experimental and computational studies based on a ^{1}H-^{13}C MAS-*J*-HMQC spectrum [80] and the determination of the ^{13}C chemical shift anisotropies [94].

[c] H-H distances from the (CASTEP) optimised neutron diffraction crystal structure (see §5.2 and ref[80]).

[d] The H-H proximities corresponding to the eight DQ coherences due to the intramolecular proximities of CH and OH protons associated with the same carbon are shown in bold.

Table 5.3. ^{1}H DQ correlations[a] between OH ^{1}H nuclei (< 2.9 Å) in β-maltose monohydrate, **5-1**.

OH proton	$\delta_{\mathrm{SQ\_1}}(^1\mathrm{H})$ /ppm	OH proton	$\delta_{\mathrm{SQ\_2}}(^1\mathrm{H})$ /ppm	Separation[b] /Å	$\delta_{\mathrm{DQ}}(^1\mathrm{H})$ /ppm
OH2	5.1	OH3'	5.6	2.46	10.7
OH4	5.3	OH3'	5.6	2.01	10.9
OH4	5.3	OH2'	6.2	2.45	11.5
OH4	5.3	OH3	6.4	2.59	11.7
WH1	6.2	WH2	6.2	1.59	12.4
OH2'	6.2	OH6'	6.2	2.14	12.4
WH2	6.2	OH6'	6.2	2.14	12.4
WH1	6.2	OH6	6.2	2.26	12.4
WH1	6.2	OH6'	6.2	2.27	12.4
WH1	6.2	OH3	6.4	2.34	12.6
WH2	6.2	OH3	6.4	2.42	12.6
WH2	6.2	OH3	6.4	2.47	12.6
OH6'	6.2	OH3	6.4	2.79	12.6
OH6	6.2	OH1'	7.2	2.43	13.4
OH6	6.2	OH1'	7.2	2.47	13.4
WH1	6.2	OH1'	7.2	2.71	13.4

[a] Intermolecular proximities are highlighted in grey.

[b] H-H distances from the (CASTEP) optimised neutron diffraction crystal structure (see §5.2 and ref[80]).

DQ peaks is a quantitative measure of relative H-H distances in a multi-spin dipolar coupled ^{1}H network [156]. To a first approximation, the analysis of ref[39, 173] predicts that the different rates of build-up are in the ratio of the dipolar coupling squared, and hence the internuclear distance to the inverse sixth power, i.e., 2.466 / 2.016 = 3.4 for the DQ peaks at 10.9 and 10.7 ppm. This is consistent with a clear pair of DQ peaks at $5.3 + 5.6 = 10.9$ ppm, with a shoulder evident at the OH2 ^{1}H chemical shift of 5.1 ppm corresponding to the $5.1 + 5.6 = 10.7$ ppm DQ coherence. A diagonal peak is also observed at DQ $= 6.2 + 6.2 = 12.4$ ppm that corresponds to the DQ correlations among and to the two protons of the monohydrate water molecule, while a pair of DQ peaks is observed at DQ $= 6.2 + 7.2 = 13.4$ ppm that corresponds to the proximities of OH1' and OH6 (2.43 Å and 2.47 Å).

A ^{1}H (DQ-DUMBO)-^{13}C (SQ) correlation spectrum of β-maltose monohydrate obtained using the pulse sequence in Fig. 4.1 is presented in Fig. 5.1c. As noted above, the refocused INEPT pulse-sequence element ensures that magnetization is transferred from ^{1}H to ^{13}C via through-bond J_{CH} couplings

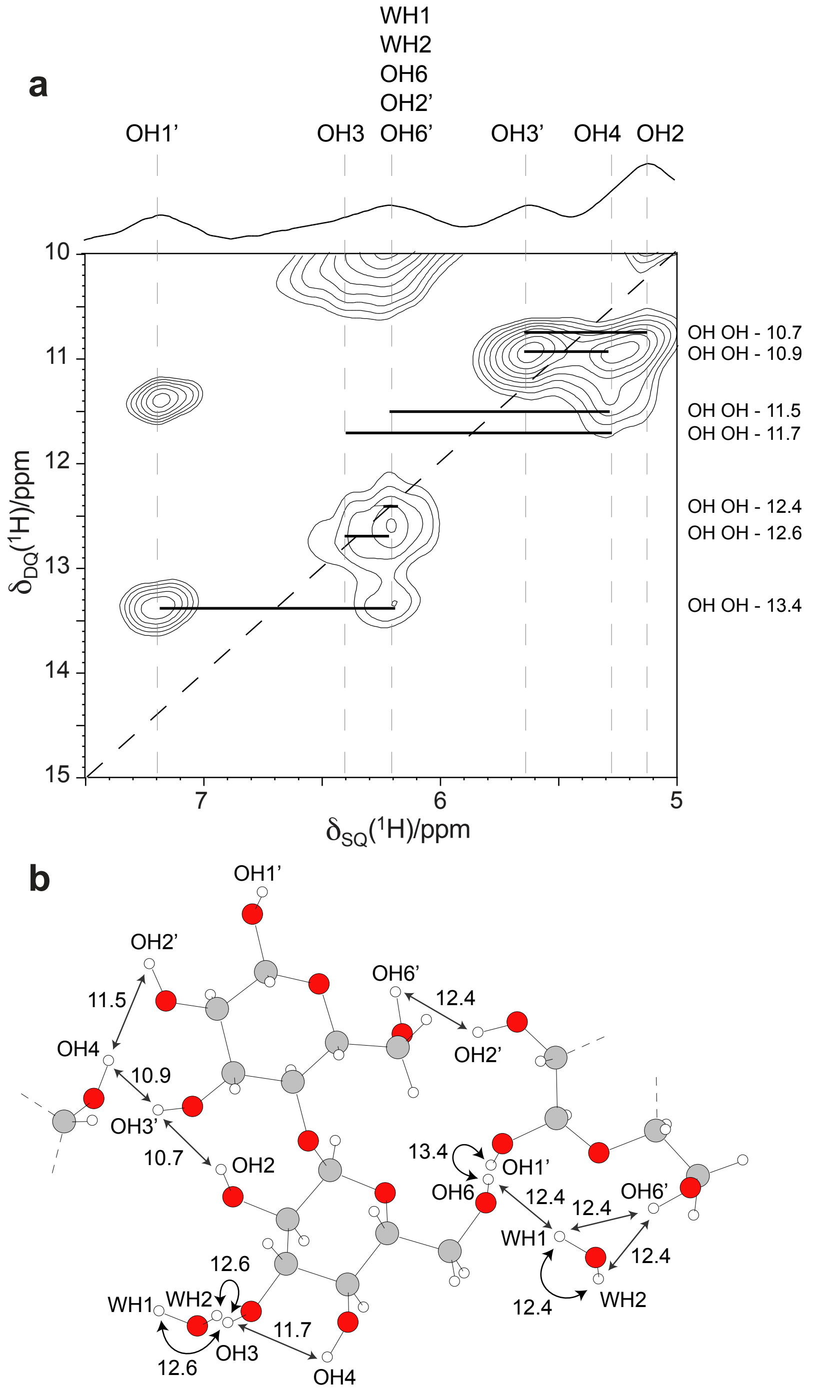

Figure 5.3. (a) An expanded region of the ^{1}H-^{1}H (500 MHz) DQ-SQ CRAMPS NMR spectrum (see Fig. 5.1b) of β-maltose monohydrate, **5-1**, doped with $MnCl_2$, with the bearing gas temperature regulated at 298 K, displaying DQ correlation peaks among the OH ^{1}H nuclei, as assigned in Tab. 5.3. Solid horizontal bars indicate specific DQ coherences between pairs of OH ^{1}H nuclei. The base contour is shown at 7 % of the maximum peak height. (b) A representation of the geometrically optimised (CASTEP) crystal structure [80] showing the H-H proximities corresponding the assigned DQ peaks - the H-H proximities are labelled with their ^{1}H DQ chemical shift (see Tab. 5.3).

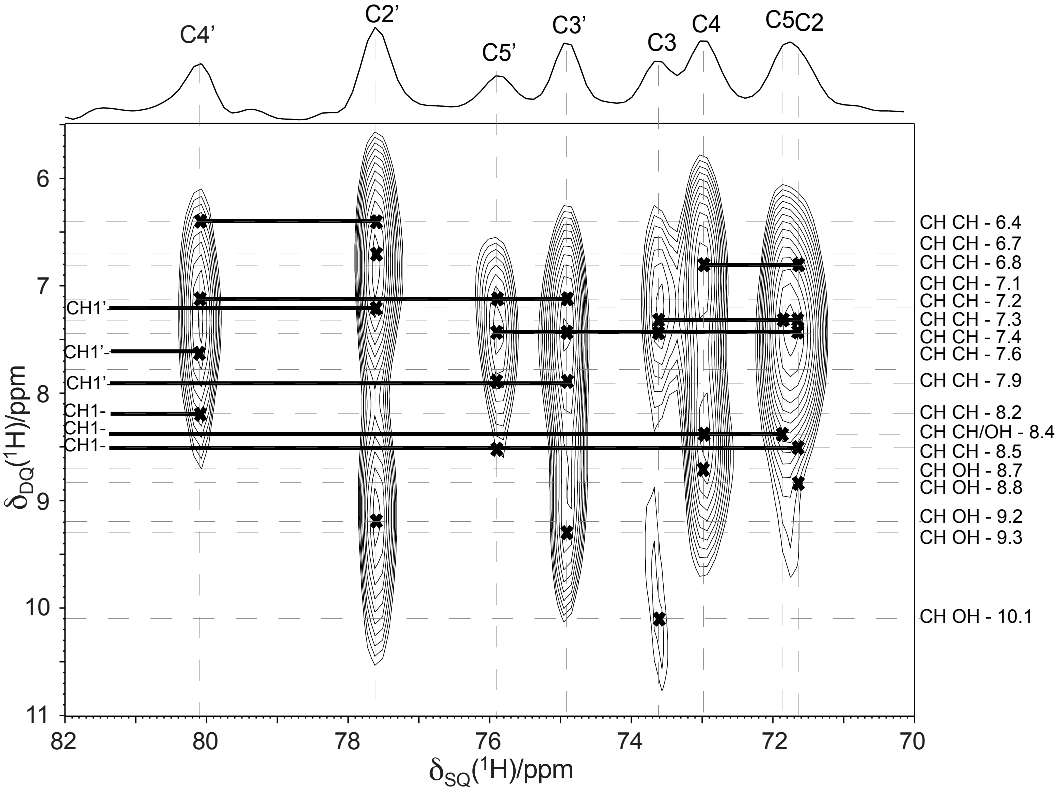

Figure 5.4. An expanded region of the ^{1}H (500 MHz) (DQ DUMBO)-^{13}C (SQ) refocused INEPT NMR spectrum of β-maltose monohydrate, **5-1**, doped with MnCl$_2$, with the bearing gas temperature regulated at 298 K, shown in Fig. 5.1c. The base contour level is at 20 % of the maximum peak height. The ^{1}H DQ coherences are assigned in Tab. 5.4. Solid horizontal bars indicate specific DQ coherences between pairs of CH ^{1}H nuclei.

[50]. A short spin-echo duration, $\tau = \tau' = 1.1$ ms, was used for the refocused INEPT transfer such that the ^{13}C resonances are correlated with ^{1}H DQ resonances that involve the ^{1}H nucleus that is directly bonded to a specific ^{13}C nucleus. Comparing the ^{13}C projection with a ^{13}C CP MAS spectrum (see top of Fig. 5.1c), it is observed that correlations are only evident for the CH ^{13}C resonances: no signal is seen for the CH$_2$ resonances (C6 and C6') - this is a consequence of the faster dephasing of the ^{1}H and ^{13}C transverse magnetization for a CH$_2$ as compared to a CH group. (Greater intensity for the CH$_2$ peaks, at the expense of reduced intensity of the CH peaks, would be expected if shorter spin-echo durations, τ and τ', and shorter ^{1}H DQ recoupling times were used.)

A zoomed-in region of the ^{1}H (DQ-DUMBO) - ^{13}C (SQ) correlation spectrum corresponding to the ^{13}C resonances between 70 and 82 ppm is shown in Fig. 5.4 (this includes all CH ^{13}C resonances except C1 and C1'). Dashed horizontal lines correspond to the ^{1}H DQ coherences involving the CH ^{1}H nuclei (H-H distances < 2.9 Å, see Tab. 5.4). Note that, of the H-H proximities tabulated in Tabs. 5.1 to 5.3, only ^{1}H DQ peaks corresponding to those in Tabs. 5.1 and 5.2 involving at least one CH ^{1}H nucleus are observed in Fig. 5.4. For DQ coherences involving a CH and an OH proton, a single ^{1}H DQ - ^{13}C SQ correlation peak is observed at the ^{13}C chemical shift of the CH group: for example, correlations are observed at: (^{13}C) = 73.0 ppm, DQ(^{1}H) = 8.4 ppm (CH4-OH4); (^{13}C) = 73.8 ppm, DQ(^{1}H) = 10.1 ppm (CH3-OH3); (^{13}C) = 75.0 ppm, DQ(^{1}H) = 9.3 ppm (CH3'-OH3'); (^{13}C) = 77.7 ppm, DQ(^{1}H) = 9.2 ppm (CH2'-OH2'); (^{13}C) = 97.0 ppm, DQ(^{1}H) = 11.4 ppm (CH1'-OH1') for the five intramolecular proximities (< 2.35 Å) between a CH and an OH proton associated with the same carbon.

Considering the CH-CH DQ coherences (see Tab. 5.1), in the ^{1}H-^{1}H DQ-SQ CRAMPS spectrum (see Fig. 5.2a), it is possible only to resolve separate DQ peaks for the CH1, CH1', CH4 and CH2' protons whose ^{1}H chemical shifts (4.8, 4.2, 3.1 and 3.0 ppm) are significantly different from the other 8 CH or CH2 protons whose chemical shifts lie between 3.4 and 3.7 ppm. DQ coherences among these latter 8 protons give rise to a large diagonal peak centred at DQ = 3.7 + 3.7 = 7.4 ppm in the ^{1}H-^{1}H DQ-SQ CRAMPS spectrum. In the ^{1}H (DQ-DUMBO)-^{13}C (SQ) correlation spectrum in Fig. 5.4, the separation of the ^{1}H DQ coherences by means of the resolved ^{13}C resonances allows separate ^{1}H DQ coherences to be identified for this very crowded region of the ^{1}H-^{1}H DQ-SQ CRAMPS spectrum. Specific DQ coherences between pairs of CH ^{1}H nuclei are highlighted by means of solid horizontal bars in Fig. 5.4, e.g., (^{13}C) = 71.6 & 73.8 ppm, DQ(^{1}H) = 7.4 ppm (CH2-CH3); (^{13}C) = 75.0 & 80.2 ppm, DQ(^{1}H) = 7.1 ppm (CH3'-CH4'); (^{13}C) = 75.0 & 75.9 ppm, DQ(^{1}H) = 7.4 ppm (CH3'-CH5').

5.3.2 Variable Temperature Experiments and First-Principles Calculations

Fig. 5.5 presents ^{1}H-^{1}H 2D DQ-SQ CRAMPS spectra of β-maltose monohydrate recorded at bearing gas temperatures of (a) 348 K, (b) 323 K, (c) 298 K,

Table 5.4. ^{1}H DQ correlations[ab] involving CH ^{1}H nuclei (< 2.9 Å) in β-maltose monohydrate, **5-1**.

	H-H /Å	δ_{SQ_1} (^{1}H) /ppm	δ_{SQ_2} (^{1}H) /ppm	δ_{DQ} (^{1}H) /ppm
CH2				
CH3	2.12	3.7	3.7	7.4
CH5	2.23	3.7	3.6	7.3
CH1	2.47	3.7	4.8	8.5
CH4	2.50	3.7	3.1	6.8
WH2	2.67	3.7	6.2	9.9
OH2	2.86	3.7	5.1	8.8
CH5				
CH2	2.23	3.6	3.7	7.3
CH6b	2.49	3.6	3.7	7.3
CH1	2.49	3.6	4.8	8.4
CH3	2.63	3.6	3.7	7.3
CH4				
OH4	2.32	3.1	5.3	8.4
OH3’	2.35	3.1	5.6	8.7
CH6a	2.48	3.1	3.7	6.8
CH2	2.50	3.1	3.7	6.8
CH3				
OH3	2.10	3.7	6.4	10.1
CH2	2.12	3.7	3.7	7.4
CH5	2.63	3.7	3.6	7.3
OH2	2.63	3.7	5.1	8.8
CH3’				
OH3’	2.23	3.7	5.6	9.3
OH4’	2.50	3.7	3.4	7.1
CH5’	2.53	3.7	3.7	7.4
CH1’	2.67	3.7	4.2	7.9
CH5’				
CH4’	2.36	3.7	3.4	7.1
CH1’	2.37	3.7	4.2	7.9
CH6’b	2.41	3.7	3.7	7.4
CH6’a	2.43	3.7	3.7	7.4
CH1	2.45	3.7	4.8	8.5
CH3’	2.53	3.7	3.7	7.4
OH6’	2.57	3.7	6.2	9.9
CH2’				
OH2’	2.25	3.0	6.2	9.2
CH2’	2.57	3.0	4.2	7.2
CH4’	2.61	3.0	3.4	6.4
CH4’				
CH1	2.06	3.4	4.8	8.2
CH5’	2.36	3.4	3.7	7.1
CH3’	2.49	3.4	3.7	7.1
CH2’	2.61	3.4	3.0	6.4
CH1’	2.67	3.4	4.2	7.6
OH2	2.80	3.4	5.1	8.5
CH1’				
OH1’	2.13	4.2	7.2	11.4
CH5’	2.037	4.2	3.7	7.9
CH2’	2.57	4.2	3.0	7.2
CH4’	2.67	4.2	3.4	7.6
CH3’	2.67	4.2	3.7	8.9
CH1				
CH4’	2.06	4.8	3.4	8.2
CH5’	2.45	4.8	3.7	8.5
CH2	2.47	4.8	3.7	8.5
CH5	2.49	4.8	3.6	8.4
OH2	2.85	4.8	5.1	9.9

[a] Listed in order of corresponding ^{13}C chemical shift. Intermolecular proximities are highlighted in grey.

[b] H-H distances from the (CASTEP) optimised neutron diffraction crystal structure (see §5.2 and ref[80]).

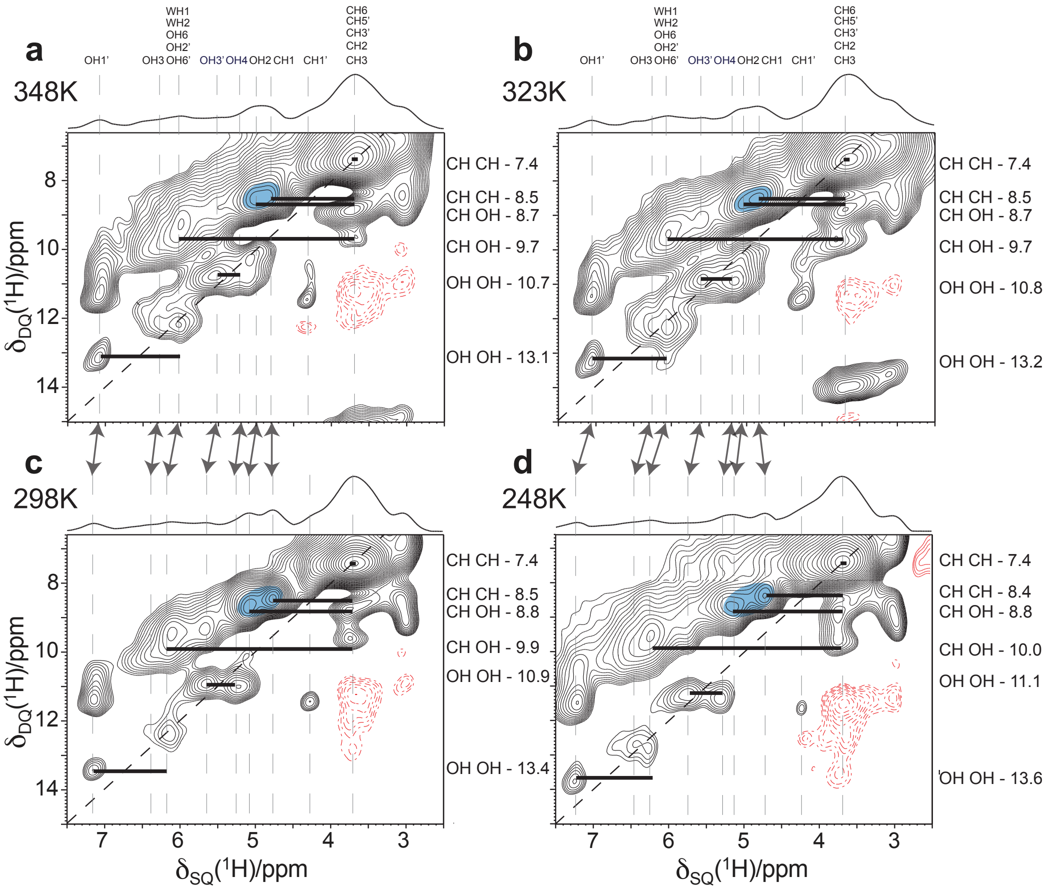

Figure 5.5. ^{1}H-^{1}H (500 MHz) DQ-SQ CRAMPS NMR spectra of β-maltose monohydrate, **5-1**, doped with MnCl$_2$, recorded at 12.5 kHz MAS, whereby the bearing gas temperature is regulated at (a) 348 K, (b) 323 K, (c) 298 K, (d) 248 K. The base contour level is at 6 % of the maximum peak height in each spectrum. The $F_1 = 2F_2$ diagonal is shown as a short-dashed line and negative contours are shown in red. Solid horizontal bars indicate specific DQ coherences, for which rows from the 2D spectra are shown in Fig. 5.6. The temperature-dependent change in the ^{1}H chemical shift of the OH protons is indicated by the arrows that link the vertical lines in (a) & (c) and (b) & (d). The region of the 2D spectra corresponding to the DQ coherences between CH1 & CH2 and between OH2 and CH2 is highlighted; the two distinct DQ peaks become increasingly more resolved as the temperature is decreased due to the significant increase in the OH2 ^{1}H chemical shift, while the CH1 ^{1}H chemical shift only changes slightly.

(d) 248 K, while Fig. 5.6 displays rows extracted from the four spectra at the labelled ^{1}H DQ frequencies in Fig. 5.5. All four spectra were recorded in the same experimental session and processed using the same F_1 and F_2 scaling factors (see §5.2). (Note that the ^{1}H-^{1}H DQ-SQ CRAMPS spectra in Fig. 5.5 were recorded on a different spectrometer as compared to the spectrum presented above (Figs. 5.1b, 5.2a and 5.3a): while the resolution is observed to be slightly reduced in Fig. 5.5, the distinct DQ resonances noted above are clearly resolved.) A careful inspection of the 2D spectra in Fig. 5.5 and the extracted rows in Fig. 5.6 reveals that while the ^{1}H SQ frequencies of the CH protons are essentially unchanged, there is a small decrease in the ^{1}H SQ frequencies of the OH protons upon increasing the temperature. This is particularly evident for the highlighted (in blue) regions of the 2D spectra shown in Fig. 5.5 that correspond to the DQ coherences between CH1 & CH2 and between OH2 and CH2; the two distinct DQ peaks are not resolved at 348 K and become increasingly more resolved as the temperature is decreased due to the significant increase in the OH2 ^{1}H chemical shift, while the CH1 ^{1}H chemical shift only changes slightly.

The temperature-dependent changes in ^{1}H chemical shifts of the OH protons are tabulated in Tab. 5.5. Such changes have been noted previously for ^{1}H chemical shifts of other hydrogen-bonded resonances in organic solids: Figure 6a of ref[174] shows the decrease by over 1.5 ppm in the ^{1}H chemical shift of a hexabenzocoronene carboxylic acid derivative upon heating from 320 K to 410 K; the ^{1}H chemical shift of the carboxylic acid OH and lactam NH protons in ^{1}H (700 MHz) MAS (30 kHz) spectra of bilirubin were observed to decrease by 0.5 and 0.3 ppm, respectively, upon heating from 320 K to 410 K (see figure S3 in ref[56]); the ^{1}H chemical shift of the carboxylic acid OH in the dipeptide β-AspAla was observed to increase by 0.12 ppm upon cooling from 295 K to 255 K [79, 175]. Tab. 5.5 also lists the ^{1}H chemical shifts of the OH protons as calculated by the GIPAW method [77, 78] (see §3.5). Note that two distinct ^{1}H chemical shifts of 5.6 and 6.9 ppm are calculated for the two protons of the water molecule. However, at room temperature, the water molecule is expected to undergo a fast motion that interchanges the position of the two protons. This corresponds to both protons exhibiting an average

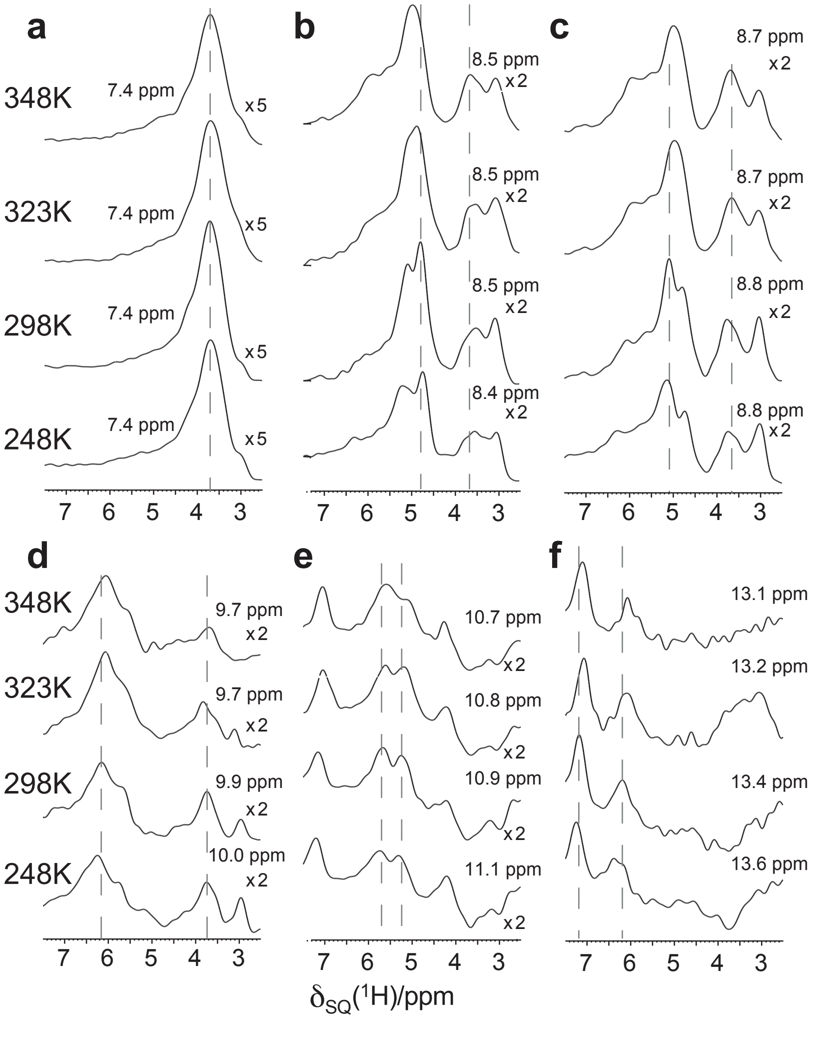

Figure 5.6. Rows extracted from the variable temperature ^{1}H-^{1}H (500 MHz) DQ-SQ CRAMPS NMR 2D spectra of β-maltose monohydrate, **5-1**, doped with $MnCl_2$ shown in Fig. 5.5. Dashed vertical lines indicate the positions of the ^{1}H (SQ) chemical shifts at 298 K corresponding to the DQ frequency of the extracted row.

Table 5.5. ^{1}H chemical shifts of the OH protons and ^{13}C chemical shifts of β-maltose monohydrate, **5-1**, as determined from variable-temperature ^{1}H-^{1}H DQ-SQ CRAMPS NMR spectra (see Fig. 5.5), ^{13}C CP MAS NMR spectra (see [1]) and first-principles (GIPAW) calculations

Site	Experimental $\delta_{\mathrm{iso}}(^{1}\mathrm{H}, ^{13}\mathrm{C})$ /ppm					Calculated[b] $\delta_{\mathrm{iso}}(^{1}\mathrm{H}, ^{13}\mathrm{C})$ /ppm
	348 K	323 K	298 K	248 K	0 K[a]	
OH1’	7.1	7.1	7.2	7.3	7.5	7.6
OH3	6.3	6.3	6.4	6.5	6.9	7.0
OH2’	6.0	6.1	6.2	6.3	6.7	6.7
OH6’	6.0	6.1	6.2	6.3	6.7	6.7
OH6	6.0	6.1	6.2	6.3	6.7	6.6
WH[c]	6.0	6.1	6.2	6.3	6.7	6.3
OH3’	6.0	5.6	5.6	5.6	5.8	6.1
OH4	5.5	5.2	5.3	5.3	5.6	5.6
OH2	5.0	5.0	5.1	5.1	5.4	5.1
C1	104.7	104.6	104.6	104.3	103.3	106.0
C1’	97.3	97.2	97.1	96.9	95.9	98.3
C4’	80.5	80.4	80.3	80.1	79.1	79.2
C2’	77.9	77.9	77.8	77.6	76.9	76.5
C5’	76.3	76.2	76.1	75.8	74.6	74.7
C3’	75.3	75.2	75.1	74.9	73.9	74.0
C3	74.1	73.9	73.8	73.6	72.4	71.4
C4	73.4	73.3	73.2	73.0	72.0	71.4
C5	72.1	72.0	71.9	71.7	70.7	70.6
C2	72.1	72.0	71.9	71.7	70.7	70.5
C6	65.7	65.7	65.6	65.5	65.0	63.2
C6’	60.4	60.2	60.2	60.0	59.0	57.5

[a] Determined from a linear extrapolation to 0 K using the experimental ^{1}H and ^{13}C chemical shifts at 348 K, 323 K, 298 K and 248 K.

[b] $\sigma_{\mathrm{ref}}(^{1}\mathrm{H}) = 30.17$ ppm, $(^{13}\mathrm{C}) = 167.1$ ppm (see Eq. 3.33 in §3.5); determined by a procedure that ensured that the mean of the calculated and experimental ^{1}H chemical shifts (the extrapolated to 0K OH ^{1}H chemical shifts and the CH protons) and ^{13}C chemical shifts (extrapolated to 0K) for all sites in β-maltose monohydrate coincide. NB: The calculated ^{13}C chemical shifts presented in Table 1 of ref[80] used $\sigma_{\mathrm{ref}}(^{13}\mathrm{C}) = 168.1$ ppm, as determined using the experimental chemical shifts at 298 K.

[c] Average of the calculated ^{1}H chemical shifts (5.6 and 6.9 ppm) for the two protons in the water molecule.

chemical shift, i.e., $(5.6 + 6.9)/2 = 6.3$ ppm, as stated in Tab. 5.5.

Comparing the calculated and room-temperature ($T = 298\,K$) ^1H chemical shifts in Tab. 5.5, it is observed that the calculated ^1H chemical shifts are consistently higher than the experimental ^1H chemical shifts (the same reference shielding was used as in ref[80], where the calculated and experimental ^1H chemical shifts for the CH and CH_2 groups were shown to be in agreement within 0.3 ppm). This discrepancy has been noted previously by Pickard *et al.* who showed that better agreement between calculation and experiment is obtained for hydrogen-bonded protons by comparing to an extrapolated experimental ^1H chemical shift at 0 K [79]. This improvement is understandable given that the chemical shifts are calculated for a structure that is obtained by a geometry optimization at 0 K, starting with an experimental single-crystal structure determined at a finite temperature.

Recently, Dumez and Pickard have considered the effect of vibrational averaging on calculated ^1H chemical shifts [175], building on a previous study of the temperature dependence of ^{17}O and ^{25}Mg chemical shifts in solid MgO [176]. Specifically, NMR shielding calculations were performed for a series of configurations that take into account the curvature of the potential energy surface around the equilibrium geometry of each vibrational mode, with shielding values being obtained by averaging over the entire set. For the carboxylic acid OH in the dipeptide β-AspAla, where a temperature-dependent change in the ^1H chemical shift had been observed experimentally, ^1H chemical shifts were calculated as 14.72 ppm (single geometrically-optimised ”static” geometry), 14.38 ppm (vibrational averaging, at 0 K), and 13.91 ppm (vibrational averaging, at 293 K) [175]. The room-temperature ^1H chemical shift has been measured experimentally as 12.9 ppm [79], thus the consideration of vibrational averaging reduces the discrepancy between experiment and calculation. It is noted that Ruud *et al.* have previously presented Hartree-Fock level gas-phase calculations showing corrections of 0.5 to 0.7 ppm due to zero-point vibrational motion for ^1H chemical shifts in small organic molecules [177]. Importantly, in agreement with the increase in the ^1H chemical shift observed experimentally for decreasing temperatures, the calculations show an increase of 0.5 ppm when comparing the consideration of vibrational averaging at 293 K

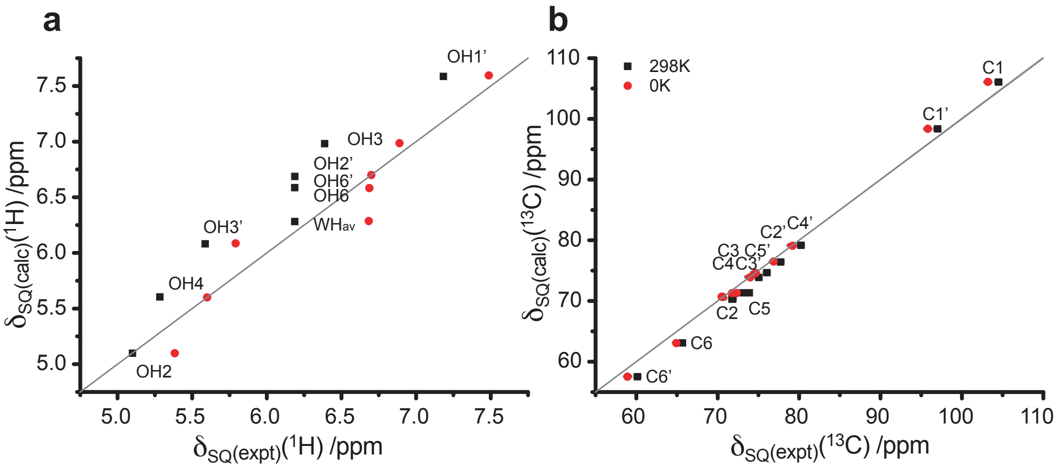

Figure 5.7. A graphical comparison of the experimental and calculated chemical shifts for β-maltose monohydrate for (a) the ^{1}H chemical shifts of the OH protons and (b) the ^{13}C chemical shifts (see Tab. 5.5). Black squares and red circles correspond to the experimental chemical shifts as measured at 298 K and those extrapolated to 0 K, respectively.

and 0 K [175].

In the context of Refs.[79, 175], Tab. 5.5 also lists ^{1}H chemical shifts for β-maltose monohydrate extrapolated to 0 K assuming a linear change with respect to temperature based on the experimental trend observed for the ^{1}H chemical shifts measured between T =248 K and 348 K. Good agreement (0.4 ppm) is evident in Tab. 5.5 between the experimental ^{1}H chemical shifts extrapolated to 0 K and the calculated ^{1}H chemical shifts, for the case here of the OH protons in β-maltose monohydrate.

Variable-temperature ^{13}C CP MAS spectra of β-maltose monohydrate were also recorded at bearing gas temperatures of 348 K, 323 K, 298 K and 248 K (not shown, see Supporting Information of ref[1]). Experimental values are listed in Tab. 5.5, together with values obtained by linear extrapolation to 0 K as well as calculated (GIPAW) chemical shifts for the geometrically optimised crystal structure, as presented previously in ref[80]. A graphical comparison of the experimental and calculated chemical shifts for β-maltose monohydrate is presented in Fig. 5.7 for (a) the ^{1}H chemical shifts of the OH protons and (b) the ^{13}C chemical shifts. Black squares and red circles correspond to the experimental chemical shifts as measured at 298 K and those extrapolated to 0 K, respectively. It is apparent that, in contrast to the case of the ^{1}H SQ frequencies of the OH protons discussed above (see Tab. 5.5 and

Fig. 5.7a), the ^{13}C chemical shifts are observed to consistently increase with increasing temperature (see Tab. 5.5 and Fig. 5.7b). In this context, it is noted that the chemical shift calculations (GIPAW) in ref[80] reveal positive and negative isolated molecule to crystal changes, δ_{iso}, in the ^{1}H and ^{13}C chemical shifts, respectively, (see Tables 2 and 3 of ref[80]) for CH moieties in the most favourable CH$\cdots$O weak hydrogen-bonding environments.

5.4 Summary and Outlook

The disaccharide β-maltose monohydrate represents a challenging case for high-resolution ^{1}H solid-state NMR because of the 24 distinct protons (14 aliphatic and 10 OH) having ^{1}H chemical shifts that all fall within a narrow range of approximately 3 to 7 ppm. Only with the significantly enhanced resolution afforded by ^{1}H-^{1}H DQ-SQ CRAMPS and ^{1}H (DQ DUMBO)- ^{13}C (SQ) refocused INEPT spectra was it possible to observe distinct DQ correlation peaks that allowed, in combination with first-principles GIPAW NMR chemical shift calculations, the *first* full ^{1}H resonance assignment of a disaccharide. In particular, the new ^{1}H DQ heteronuclear correlation experiment (introduced in §4) enabled the unambiguous identification of ^{1}H DQ peaks that could not be distinguished in the traditional ^{1}H DQ-SQ CRAMPS spectrum, and hence constitutes an important component of the analysis presented. This demonstrates the potential of this experiment, therefore, to assist with difficult solid-state analyses.

In particular, with this combination of advanced analytical methods, it has been possible for the hydroxyl ^{1}H chemical shifts of a sugar molecule, which have been previously inaccessible by solid-state NMR, to be experimentally determined. Indeed, it is these OH moieties that are responsible for the vital hydrogen bonding interactions that not only stablise the self-assembly of saccharides, but also enable the binding of these molecules to peptides and proteins within cell membranes and so determines the many biological functions carried out by sugars. Thus, solid-state NMR has much to offer potential investigations into hydrogen-bonding interactions and hence the establishment of structure-function relationships.

It is also observed that, while the experimental CH ^{1}H resonances are essentially unchanged over temperature range 248 K to 348 K, the OH ^{1}H resonances show a clear shift to higher ppm values as the temperature is decreased, i.e., generally towards the computationally determined chemical shift value calculated for an optimised (0 K) crystal structure. Similar changes in ^{1}H chemical shifts of hydrogen bonded resonances have been noted previously for the carboxylic acid OH protons in bilirubin (and also the lactam NH proton) [56], a hexabenzocoronene carboxylic acid derivative [174] and the dipeptide β-AspAla [79, 175]. Therefore, as the combined use of experimental NMR and chemical shift calculations becomes more widespread, it is crucial that potential perturbations (e.g., temperature and vibrational effects, highlighted here) are considered, in order to improve the agreement between experimentally and computationally determined chemical shifts.

Moreover, it is emphasised that the resonance assignment presented here was carried out using a sample at natural abundance, i.e., there was no need for isotopic labeling. The dream of the NMR crystallography approach is the ability to go ‘from spectrum to structure’ in a procedure that involves identifying the actual exhibited three-dimensional structure from an ensemble generated by a crystal structure prediction approach, by comparing experimental and calculated NMR parameters. To improve the success of such ‘spectrum to structure’ methodologies as much experimental NMR data as possible should be used; the ability to determine ^{1}H chemical shifts via high-resolution DQ CRAMPS experiments is, thus, of much importance for the further development of NMR crystallography.

6

Self-Assembly of Guanosine Derivatives: Distinguishing the G-quartet and G-Ribbon at Natural Abundance

Molecules that are observed to *self-assemble* into ordered three-dimensional structures are of much interest in supramolecular chemistry for the design of functional, often nanoscale, devices. A notable compound within this area is guanosine [178], the sugar derivative of the (DNA/RNA) nucleobase guanine, which is known to exhibit a variety of modes of self-recognition. Specifically, the guanine headgroup contains distinct complementary hydrogen-bond donor and acceptor sites, such that under different conditions, various combinations of Watson-Crick or Hoogsteen base-pairing interactions direct the formation of dimeric [179], ribbon-like [180], tetrameric [181] or helical-type [182, 183] structures. In particular, the planar tetramer, i.e., the G-*quartet*, has undergone extensive research after having been associated with key biological functions [184], notably, in the action of telomeres in chromosomal DNA, which are vital for controlling cell division and hence preventing the growth of cancerous cells [185]. Self-assembled quartet and *quadruplex* structures have also shown much promise as building blocks for functional applications across chemical biology and nanoelectronics, including synthetic ion transporters [186], nanowires [187] and organic semiconductors, many of which are reviewed in refs.[188, 189]. Similarly, ribbon-type self-assemblies of guanosine materials have been shown to form a completely new class of gel-like liquid crystals [180, 190], often possessing photoconductive [191] properties suitable for molecular electronic devices e.g., biophotonic sensors [192], rectifiers [193] and field effect transistors

[194].

The vast majority of work carried out on guanosine materials, to date, has focussed upon the use of single-crystal diffraction techniques or solution-based methods, which are not always appropriate for full characterisations of these new materials. This work exploits the sensitive structure determining properties of solid-state NMR to accurately identify and *distinguish* different three-dimensional structures, notably, the G-quartet and G-ribbon assemblies, in naturally abundant guanosine derivatives.

6.1 Guanosine Derivatives and G-Quartets

The G-quartet was first observed in 1962 by fibre diffraction studies of 3'- and 5'-guanosine monophosphate (GMP), where (according to the labelling given throughout this chapter, and in Fig. 6.1a) N2H$\cdots$N7 and N1H$\cdots$O6 hydrogen bonds were formed between four neighbouring molecules to produce planar macrocycles with a characteristic central cavity [195]. Further diffraction studies of guanosine analogues revealed that the polar nature of the aromatic guanine rings caused these tetramers to stack forming columnar polymers, or helical-type structures [196]. This stacking mechanism also explained previous observations of guanosines forming gels in aqueous solution [195]. Moreover, the assembly of long 'G-*quadruplex*' structures, seemed to be stablized by the presence of alkali metal cations (e.g., K^+ Na^+), which inhabit the central cavity to create a more electronically favourable environment for the clustered oxygens (O6) atoms [197]. There has since been much work upon the characterization of cation-templated quadruplex assemblies, with diffraction crystal structures showing the insertion of the ion species between the G-quartets [198]. Notably, guanosine tetramer structures have displayed properties of ion selectivity, whereby only sufficiently small cations are incorporated into the quadruplex [197]. As such, considerable work has gone into examining guanosine materials, in particular, *lipophilic* derivatives, for the design of ion-selective ionophores and various other synthetic devices [188].

Gottarelli *et al.* have extensively studied lipophilic G-derivatives with and without alkali ions, including the deoxygenated, long-chained derivative,

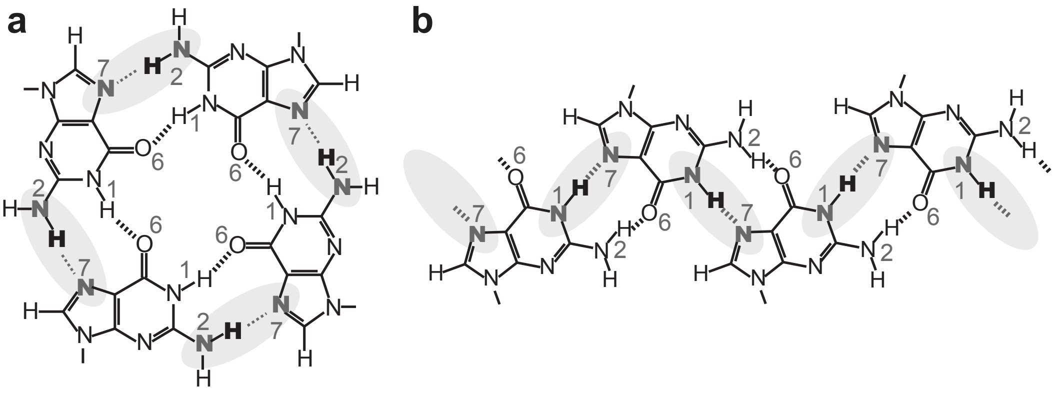

Figure 6.1. G-Quartet and (solid-state) G-Ribbon hydrogen bonding structures discussed in this work.

6-1. By a combination of ^{1}H solution-state NMR and circular dichroism (CD) methods, it was shown that, in the presence of ions (e.g., K^{+}), **6-1** forms stacked G-quartets (octamers or columnar aggregates, depending on the concentration) in $CDCl_3$ solution [186, 199, 200]. However, in the absence of ions, **6-1** assembles instead into ribbon-like structures to produce a lyotropic liquid-crystalline phase in chloroform or hydrocarbon solvents [180], and at the solid-liquid interface [201]. In fact, two distinct types of ribbon were observed in solution and on solid surfaces, characterised by N1H$\cdots$O6, N2H$\cdots$N3 and N1H$\cdots$N7, N2H$\cdots$O6 intermolecular hydrogen-bonds, respectively, where ^{1}H solution-state NMR measurements were able to directly observe the structural change on dissolution [201]. Although it has not been possible to obtain a single-crystal diffraction structure for **6-1**, Giorgi *et al.* later presented the crystal structure for the shorter-chain derivative, **6-2**, clearly showing the appearance of N1H$\cdots$N7, N2H$\cdots$O6 stablising hydrogen bonds [190] (see Fig. 6.2d). These initial papers supported the previous assumption that alkali cations were necessary for the stabilization of G-quadruplexes, and that otherwise, ribbon-type structures would be exhibited in both solid and liquid phase.

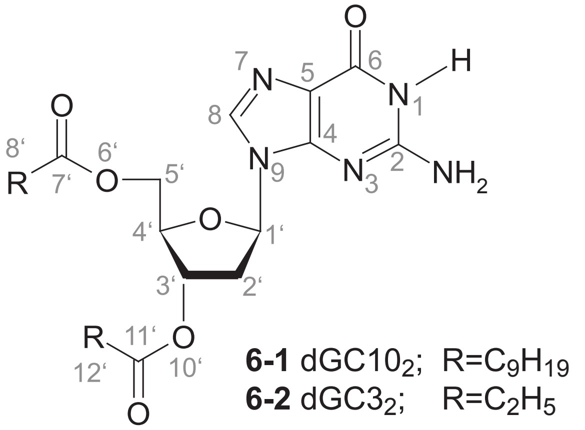

6-1 dGC10_2; R=C_9H_{19}
6-2 dGC3_2; R=C_2H_5

However, it was shown that modifications to the C8 position of a guanosine derivative could force the assembly back into quartet formation without the need for templating cations, as demonstrated in both chlorinated organic solvents and the solid state [202]. Later, further C8 substituted derivatives were examined by Giorgi *et al.* and Lena *et al.* [203] in solution and on solid surfaces using ^{1}H solution-state NMR and CD measurements, and X-ray diffraction measurements, respectively [204]. It was also concluded that, in general, 8-substituted guanosines formed G-quartets more readily. In particular, 8-oxo substituted guanosines provided additional hydrogen-bond donor and acceptor arrangements that could result in further new types of quartet and helical assemblies. Therefore, the issue of quartet formation in non-cation templated guanosines was not, it seemed, as simple as was first observed.

In 2005, Pham *et al.* provided new insight into this problem whereby, using solid-state NMR techniques, the specific intermolecular NH$\cdots$N hydrogen bonds that characterised the different modes of guanosine self-assembly could be directly determined. The observation of correlation peaks due to hydrogen-bond-mediated J couplings in ^{15}N refocused INADEQUATE [157] spectra identified the intermolecular N1H$\cdots$N7 J couplings associated with the ribbon structures formed by **6-2** and a polymorph of **6-1**, in the solid state [205]. A third 2D spectrum was presented that showed that a different polymorph of an un-8-substituted G-derivative, **6-1**, and indeed the polymorph that formed most readily, assembled into a quartet-like arrangement as indicated by an intermolecular N2H$\cdots$N7 J coupling (in the absence of cations).

While the results presented by Pham *et al.* [102, 205] demonstrated the structural sensitivity of solid-state NMR for this aim, it should be noted that the 2D ^{15}N experiments were feasible only for fully isotopically ^{15}N labeled samples. The aim of the work presented in this chapter is to investigate the structural information that can be obtained by high-resolution solid-state NMR techniques applied at *natural isotopic abundance*. Firstly, multidimensional ^{1}H and ^{13}C spectra are presented for the well characterised systems **6-1** and **6-2**, along with GIPAW chemical shift calculations of the geometrically optimised crystal structure of **6-2**, in order to accurately assign the 'signature' ^{1}H and ^{13}C solid-state chemical shifts of both the G-quartet and G-ribbon structures. Following this, the same experimental techniques are applied to a range of further derivatives, **6-3** to **6-6** (see §6.4) for which diffraction-based single crystal structures are not available, and by comparison to spectra obtained for **6-1** and **6-2**, the mode of solid-state self-assembly is predicted for these materials.

6.2 Experimental Details

6.2.1 Sample Preparation

This work has been carried out in collaboration with Gottarelli, Spada *et al.*, Bologna, who are gratefully acknowledged for synthesizing the materials discussed, according to the procedures described in refs[190, 204]. The full chemical names of the studied guanosine derivatives are: **6-1** (dGC10) 2'-deoxy-3',5'-O-didecanoylguanosine; **6-2** (dCG3) 2'-deoxy-3',5'-O-dipropanoylguanosine; **6-3** (GC3) 2',3',5'-O-tripropanoylguanosine; **6-4** (GC10) 2',3',5'-O-tridecanoylguanosine; **6-5** (8BrGC10) 2',3',5'-O-tridecanoyl-8-bromoguanosine; **6-6** (G-ace-C10) 2',3'-O-isopropylidene-5'-decanoylguanosine.

6.2.2 Solid-State NMR

The majority of spectra presented in this chapter were recorded on a Bruker Avance II+ spectrometer operating at a ^{1}H Larmor frequency of 600 MHz. ^{1}H fast-MAS and DQ MAS spectra were recorded using a 2.5 mm probe at

30 kHz MAS. All other experiments on this spectrometer were performed using a 4 mm triple resonance probe, operating in double-resonance mode at a MAS frequency of 12.5 kHz. ^{13}C CP MAS spectra shown for **6-2** were recorded on a Chemagnetics Infinity spectrometer operating at a ^{1}H Larmor frequency of 600 MHz using a 4 mm probe spinning at 8 kHz, while those shown for **6-3**, **6-4**, and **6-6** were recorded on a Varian Infinity+ console operating at a ^{1}H Larmor frequency of 300 MHz using a double resonance 4 mm probe at 8.5 kHz. In all experiments, ^{1}H 90° pulses were of duration 2.5 µs.

^{13}C CP MAS: ^{13}C magnetization was generated by cross polarization with a ramp of (**6-1**, **6-5**) 80 to 100 %, (**6-2**) 50 to 100 % or (**6-3**, **6-4**, **6-6**) 40 to 100 % on the ^{1}H channel for a contact time of 1 ms. TPPM [19] ^{1}H heteronuclear decoupling with $\nu_1 = 100$ kHz, $\Delta\phi_p = 15°$ and pulse duration (**6-1**) 4.85 µs, (**6-2**, **6-5**) 4.8 µs or (**6-3**, **6-4**, **6-6**) 4.67 µs was employed throughout a t_2 acquisition time of (**6-1**, **6-5**) 20 ms or (**6-2** to **6-4**, **6-6**) 40 ms. (**6-1**) 256, (**6-2**) 1024, (**6-3**) 19200, (**6-4**) 22800, (**6-5**) 512 or (**6-6**) 20400 transients were co-added, with a recycle delay of (**6-1**) 2 s, (**6-2**) 6 s, (**6-3**, **6-4**, **6-6**) 3 s or (**6-5**) 2.5 s.

^{1}H fast MAS: All direct ^{1}H excitation experiments were performed using 90° pulses of duration 2.5 µs and a t_2 acquisition time of 10 ms. (**6-1** - **6-3**) 4 or (**6-4** - **6-6**) 16 transients were co-added, with a recycle delay of (**6-1** - **6-2**) 2 s or (**6-3** - **6-6**) 3 s.

^{1}H DQ MAS: One rotor period of the BABA [117] recoupling sequence was used for excitation and reconversion of DQ coherence. The recycle delay was 2 s. For each of the 128 t_1 slices (using the States [113] method with a rotor-synchronised increment of 33.3 µs), 16 transients were co-added corresponding to a total experimental time of ≈1 h.

^{1}H CRAMPS: Windowed (wDUMBO-1 [41]) homonuclear decoupling cycles of $\nu_1 = 100$ kHz and duration 24 µs (320 steps of 75 ns each) were employed throughout detection along with pre-pulses, $\theta = 0.7$ µs. For acquisition, a detection window was inserted after each DUMBO-1 cycle to give an effective t_2 dwell time (including the pre-pulses) of 29.8 µs, corresponding to a total acquisition time of 11.7 ms. The recycle delay was 3 s and (**6-1**, **6-2**) 32 or (**6-3** - **6-6**) 128 transients were co-added. The scaling factor in F_2 was (**6-1**,

6-3) 0.55 or (**6-2**, **6-4** - **6-6**) 0.57.

^{1}H DQ CRAMPS: 3 basic POST-C7 [62] elements (total duration 68.6 µs, $\nu_1 = 87.5$ kHz) were used for the excitation and reconversion of DQ coherence. Homonuclear ^{1}H dipolar decoupling with $\nu_1 = 100$ kHz was implemented using the windowless eDUMBO$_{22}$ [35] sequence during t_1 and windowed DUMBO-1 (wDUMBO-1 [41]) for CRAMPS acquisition in t_2. For both eDUMBO$_{22}$ and wDUMBO-1, the 24 µs decoupling cycles were divided into 320 steps of 75 ns each and pre-pulses of θ_1 equal to (**6-1**, **6-4**, **6-6**) 0.75 µs, (**6-2**, **6-5**) 0.7 µs or (**6-3**) 0.8 µs and θ_2 of (**6-1**, **6-4**, **6-6**) 0.75 µs, (**6-2**, **6-5**) 0.7 µs or (**6-3**) 0.86 µs were used. For acquisition, a detection window was inserted after each DUMBO-1 cycle to give an effective t_2 dwell time (including the pre-pulses) of 29.8 µs, corresponding to a total acquisition time of (**6-1**) 10.5 ms, (**6-2**, **6-6**) 10.7 ms, (**6-3**, **6-4**) 7.2 ms or (**6-5**) 11.1 ms. For each of the 100 t_1 slices, (using the States-TPPI [115] method with an increment of 48 µs), (**6-3**) 32 or (otherwise) 16 transients were coadded with a recycle delay of 2.5 s corresponding to a total experimental time of (**6-3**) 2 h or (otherwise) 1 h. The scaling factors were (**6-1**) 0.60, (**6-2**, **6-3**, **6-6**) 0.61, (**6-4**) 0.62 or (**6-5**) 0.64 in F$_1$ and (**6-1**, **6-2**, **6-3**) 0.55, (**6-4**, **6-6**) 0.56 or (**6-5**) 0.58 in F$_2$.

^{1}H-^{13}C Refocused INEPT: ^{13}C 90° pulses were of duration 4 µs and an evolution period, $\tau = \tau'$ of (**6-1**) 0.64 ms, (**6-2**) 1.44 ms, (**6-3**, **6-6**) 1.28 ms or (**6-4**, **6-5**) 0.96 ms was used to maximize the ^{1}H-^{13}C through-bond polarization transfer. Homonuclear ^{1}H dipolar decoupling with $\nu_1 = 100$ kHz was implemented using the windowless eDUMBO$_{22}$ [35] sequence during t_1 and periods of free evolution (τ, τ'), whereas heteronuclear TPPM [19] decoupling ($\nu_1 = 100$ kHz, $\Delta\phi_p = 15°$ and 4.85 µs pulse duration) was applied during a t_2 acquisition time of 20.5 ms. For eDUMBO$_{22}$, the 32 µs decoupling cycles were divided into 320 steps of 100 ns each and a pre-pulse $\theta = 0.5$ µs was used. The scaling factor in F$_1$ was (**6-1**, **6-2**) 0.50, (**6-3**, **6-4**) 0.58, (**6-5**) 0.51 or (**6-6**) 0.62. For each of 60 t_1 slices (using the States-TPPI [115] method with an increment of 64 µs), (**6-1**, **6-5**) 512, (**6-2**, **6-3**) 576, (**6-4**) 416 or (**6-6**) 432 transients were coadded with a recycle delay of 2 s (total experimental time of (**6-1**, **6-5**) 17 h, (**6-2**, **6-3**) 19 h or (**6-4**, **6-6**) 14 h.

6.2.3 Computational Details

The crystal structure of **6-2** was obtained from the crystallographic database (reference code MOFBUE [190]) and geometry optimisations were performed using the density functional theory (DFT) code CASTEP. Initial efforts to relax only the ^{1}H atoms resulted in large forces remaining on some of the heavier elements, in particular the carbon atoms of the alkyl chains, such that all atoms were then allowed to relax. Ultrasoft pseudopotentials with a maximum planewave cutoff of 800 eV were used, along with a Monkhorst-Pack grid with a minimum sample spacing of 0.08 Å^{-1}. NMR chemical shifts were also computed using the CASTEP code (and GIPAW approach) with a planewave basis set of maximum cut off energy of 800 eV. Integrals over the Brillouin zone were performed using a similarly dense Monkhorst-Pack grid. Geometry optimization calculations took 8.5 h on 32 nodes of 3 GHz Intel Xeon 5160 processors (IBM cluster, University of Warwick) and shielding tensor calculations, 3.5 h.

Absolute shieldings were converted to chemical shifts using Eq. 3.33 such that the mean of the calculated and experimental ^{13}C and ^{1}H chemical shifts of **6-2** coincide; $\sigma_{\text{ref}}(^{13}\text{C}) = 168.1$ ppm, $(^1\text{H}) = 29.97$ ppm.

6.3 Results: dGC10 and dGC3

6.3.1 1D ^{13}C and ^{1}H MAS and GIPAW Calculations

Figs. 6.2a and 6.2b compare the ^{13}C CP MAS spectra of deoxyguanosine derivatives dGC10 (**6-1**) and dGC3 (**6-2**). Most notably, a simple counting of peaks shows that the spectrum in (b) exhibits a doubling of resonances in comparison to that shown in (a). This crystallographic splitting of ^{13}C resonances is indicative of multiple, specifically two, distinct molecules in the asymmetric unit cell of **6-2**. This is in agreement with the ribbon-like crystal structure [190] obtained for **6-2**, shown in Fig. 6.2d (geometrically optimised), where the two independent molecules (Z'= 2, see §7, labelled **A** and **B**) are identified. An analysis of the two distinct molecules from the diffraction structure reveals differences in molecular conformation and environment, which would hence be

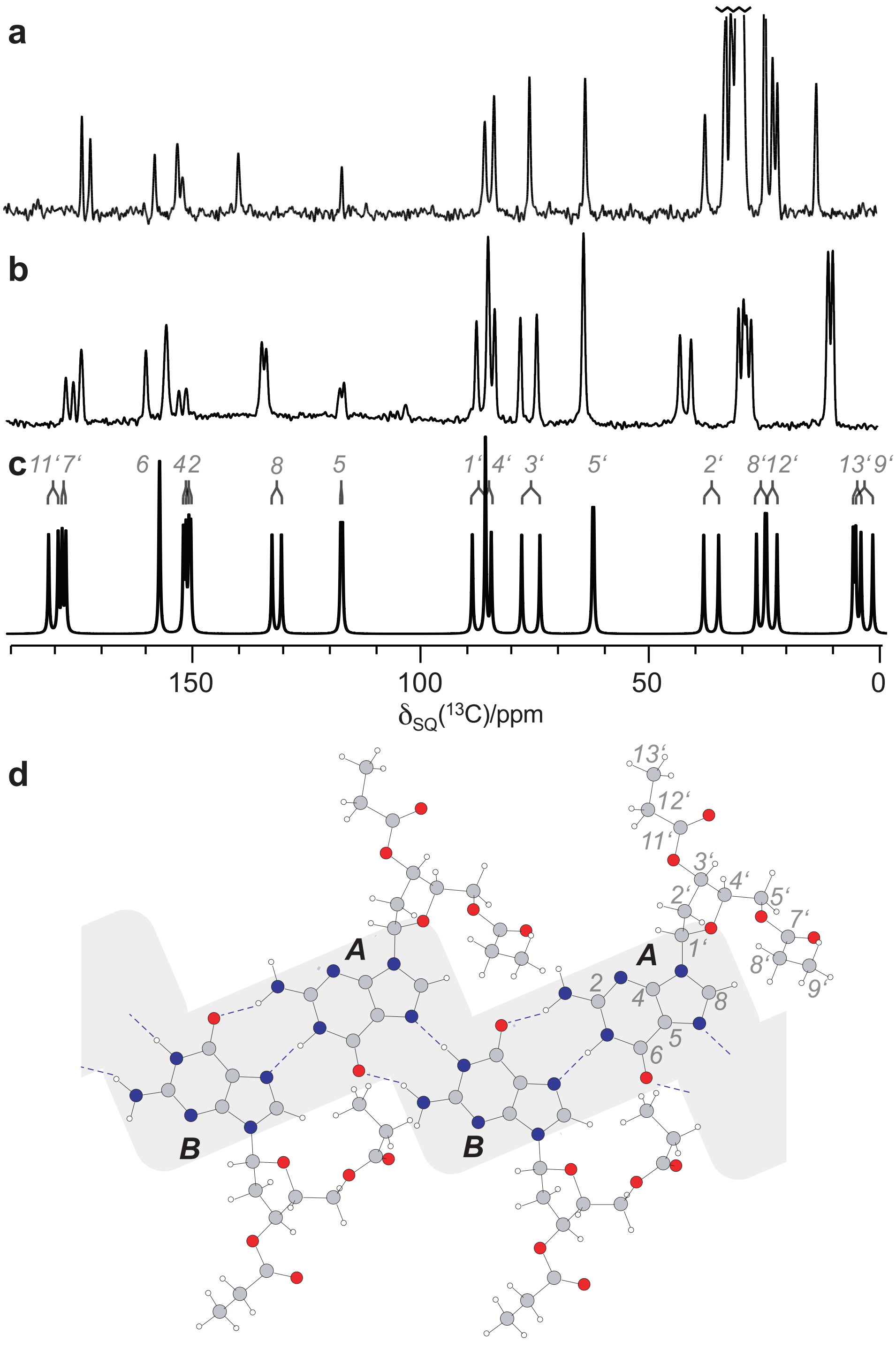

Figure 6.2. ^{13}C NMR spectra of deoxyguanosine compounds (a) **6-1** and (b,c) **6-2**. (a,b) ^{13}C CP MAS NMR spectra recorded at a Larmor frequency of 150 MHz and at a MAS frequency of 12.5 kHz. The overlapped resonances of the multiple CH$_2$ groups around 20-30 ppm in (a) have been truncated, so as to emphasise the resonances at larger chemical shift values. (c) Computed GIPAW ^{13}C chemical shifts taken from the CASTEP optimised structure, as shown in (d), convoluted with 50 Hz Lorentzian linebroadening and with site assignments shown. (d) Geometrically optimised (CASTEP) crystal structure of **6-2** with dashed lines indicating the N1H···N7, N2H···O6 hydrogen-bonding interactions of the ribbon structure. The two distinct molecules of the asymmetric unit cell (**A**, **B**) are identified along with ^{13}C site labels.

expected to give rise to different chemical shieldings. Indeed, the chemical shifts for the optimised structure were computed using the GIPAW method, and are presented in spectral form in Fig. 6.2c (see Tab. 6.1 for tabulated values). Good agreement between the experimental and calculated ^{13}C chemical shifts of the CASTEP optimised crystal structure is noted, although, as is commonly observed with the GIPAW technique, experimental chemical shifts with low ppm values (here, alkyl CH_2 and CH_3 ^{13}C resonances) are often underestimated by calculation, and conversely those with high ppm values (e.g., carbonyl resonances) are overestimated. This can be seen throughout the calculated chemical shifts presented in this thesis, for example in the following chapter for ^{1}H and ^{13}C values of campho[2,3-c]pyrazole (see §7.3.3). This is discussed in more detail for dGC3 later in this chapter, along with a graphical comparison provided in Fig. 6.7. In conclusion, by examination of the ^{13}C CP MAS spectrum of **6-2**, it is clear that this sample exists in ribbon-like guanosine form, moreover, the doubling of experimental resonances observed in this spectrum acts as a signature for this crystallographic structure. Accordingly, the lack of peak splitting in Fig. 6.2a, suggests that **6-1** adopts a distinctly different solid-state structure.

Considering the work of Pham *et al.* [205] using ^{15}N -labeled compounds, a doubling of peaks was also observed in the ^{15}N CP MAS spectra of the ribbon-like structures of **6-1** and **6-2** (confirmed by the doubling of peaks in a 2D refocused INADEQUATE spectrum due to intermolecular N1H$\cdots$N7 hydrogen-bond-mediated J couplings). Conversely, ^{15}N NMR spectra of the quartet-like form of **6-1** (indicated by an intermolecular N2H$\cdots$N7 hydrogen-bond-mediated J coupling) showed no such peak splitting. Therefore, the spectrum presented in Fig. 6.2a is indicative that the **6-1** compound studied here is quartet-like in nature, where the single, narrow linewidths also suggest that a single, well-ordered molecular species exists throughout the three-dimensional structure.

An important distinction should be made at this point regarding the stereochemistry of the derivatives. It has been well documented that in the various architectures adopted by guanosines, the molecules exist in either *syn* or *anti* conformations with respect to the glycosidic bond (N9-C1'), as is sketched

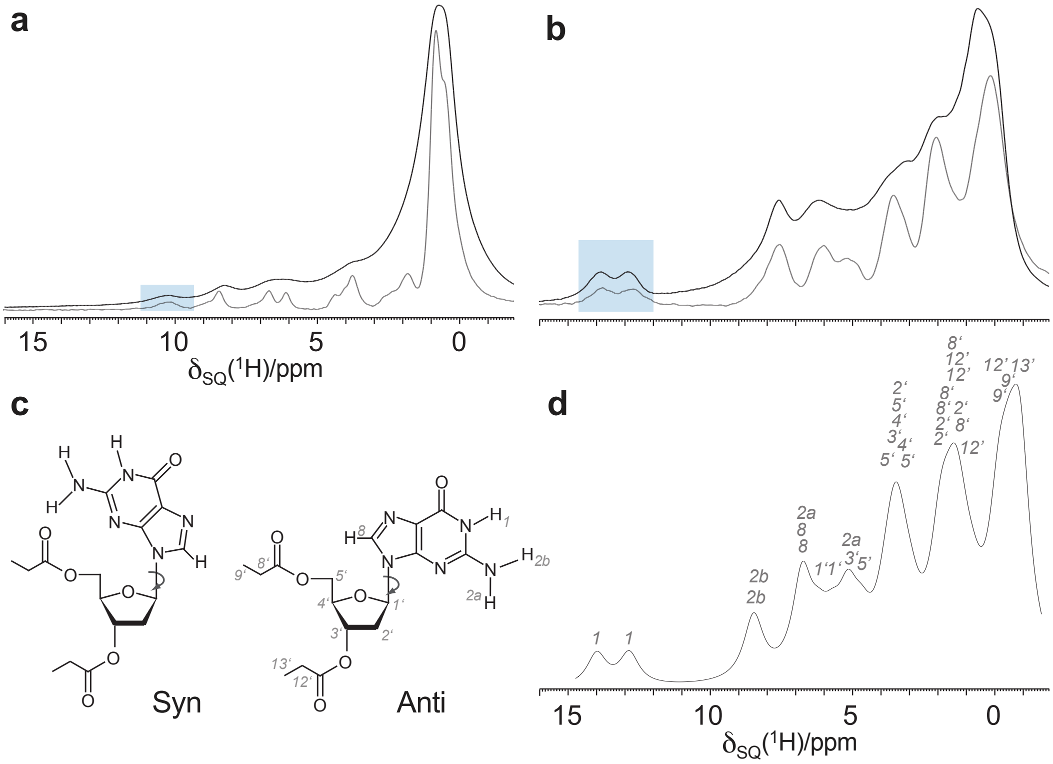

Figure 6.3. ^{1}H NMR spectra of deoxyguanosine compounds (a) **6-1** and (b,d) **6-2**. (a,b) ^{1}H fast MAS (black) and homonuclear (DUMBO) decoupled (grey) NMR spectra recorded at 600 MHz and rotation frequencies of 30 kHz and 12.5 kHz, respectively. Areas highlighted in blue are attributed to the hydrogen bonded NH sites. (d) Computed GIPAW ^{1}H chemical shifts taken from the CASTEP optimised structure, as shown in Fig. 6.2d, convoluted with 500 Hz Lorentzian linebroadening. The site assignments given here specifically distinguish between the two NH_2 protons due to the hydrogen bonding exhibited in the ribbon structure(see Fig. 6.2d), but not the CH_2 protons. (c) A sketch of syn and anti conformations of **6-2**. Only the anti orientation is observed for **6-2** in the single-crystal X-ray diffraction (ribbon) structure [190], for which the ^{1}H site labels are given.

in Fig. 6.3c for **6-2**. The conformation adopted, which solid-state NMR chemical shift values could potentially identify, is also thought to be closely linked to the three-dimensional self-assembly mechanisms. Indeed, many solution-state NMR studies of guanosine architectures (including of dGC10, **6-1**) use the ^{1}H chemical shifts to characterise three-dimensional structure on the basis of predicted NH$\cdots$ hydrogen bonds [180, 186, 199, 200, 202] and syn, anti orientations of molecules [186]. This will be discussed further in §6.4.

Fig. 6.3a,b present ^{1}H NMR spectra of **6-1** and **6-2** recorded under fast MAS (30 kHz, black) and CRAMPS (with DUMBO decoupling, grey), along with the computed GIPAW ^{1}H chemical shifts of **6-2**. The resolution afforded by 30 kHz MAS is not sufficient to resolve the majority of ^{1}H chemical shifts, but provides a convenient envelope with which to accurately scale the chemical shift axes of DUMBO decoupled ^{1}H spectra (scaling factors of 0.55 and 0.57 were applied in (a) and (b), respectively). The ^{1}H resonances of the hydrogen bonded NH protons, indicated by blue highlighting of the spectra, can be identified based on their uniquely shielded nuclear environments (and by comparison with the calculated shifts of **6-2**). In this region in (b), a clear doubling of peaks is, once again, evident for the ribbon architecture of **6-2**. These resonances are also shifted downfield by roughly 3-4 ppm with respect to the highest ^{1}H resonance of (a), indicating a distinctly different hydrogen-bonding arrangement between the two compounds. The computed ^{1}H chemical shifts of **6-2** are presented in Fig. 6.3d, (see also Tab. 6.1) with an applied line broadening of 500 Hz, and show good agreement with the ^{1}H DUMBO spectrum given in Fig. 6.3b. Hence, the accuracy of the GIPAW method allows a tentative ^{1}H assignment to be made for **6-2** at the experimental ^{1}H resolution shown here.

6.3.2 ^{1}H-^{13}C SQ-SQ and ^{1}H-^{1}H DQ-SQ 2D Correlations

Fig. 6.4a and Fig. 6.4b present ^{1}H-^{13}C heteronuclear correlation spectra of **6-1** and **6-2**, respectively, recorded (at 12.5 kHz MAS) using the refocused INEPT [50] pulse sequence with DUMBO homonuclear decoupling applied to achieve high-resolution in the indirect (^{1}H) dimension. DUMBO (specifically, eDUMBO$_{22}$ homonuclear decoupling) was also applied throughout the evolution periods, where short (< 1.5 ms) $\tau = \tau'$ periods were used for the refocused INEPT transfer such that correlation peaks were observed for directly bonded pairs of ^{1}H-^{13}C nuclei. The through-bond transfer of ^{1}H magnetization to the well-resolved ^{13}C nuclei allows the ^{1}H chemical shifts of carbon-bonded protons to be assigned for **6-1** and **6-2**, as tabulated in Tab. 6.1. Exceptions to this are the ^{1}H resonances of the CH$_2$ groups in the sugar ring, CH2' and CH5' for which correlations peaks are weak or not visible at the contour level shown in Fig. 6.4b. As discussed in §5.3 and ref.[50], this can be attributed to the faster dephasing of ^{1}H, ^{13}C magnetization for a CH$_2$ group with respect to a

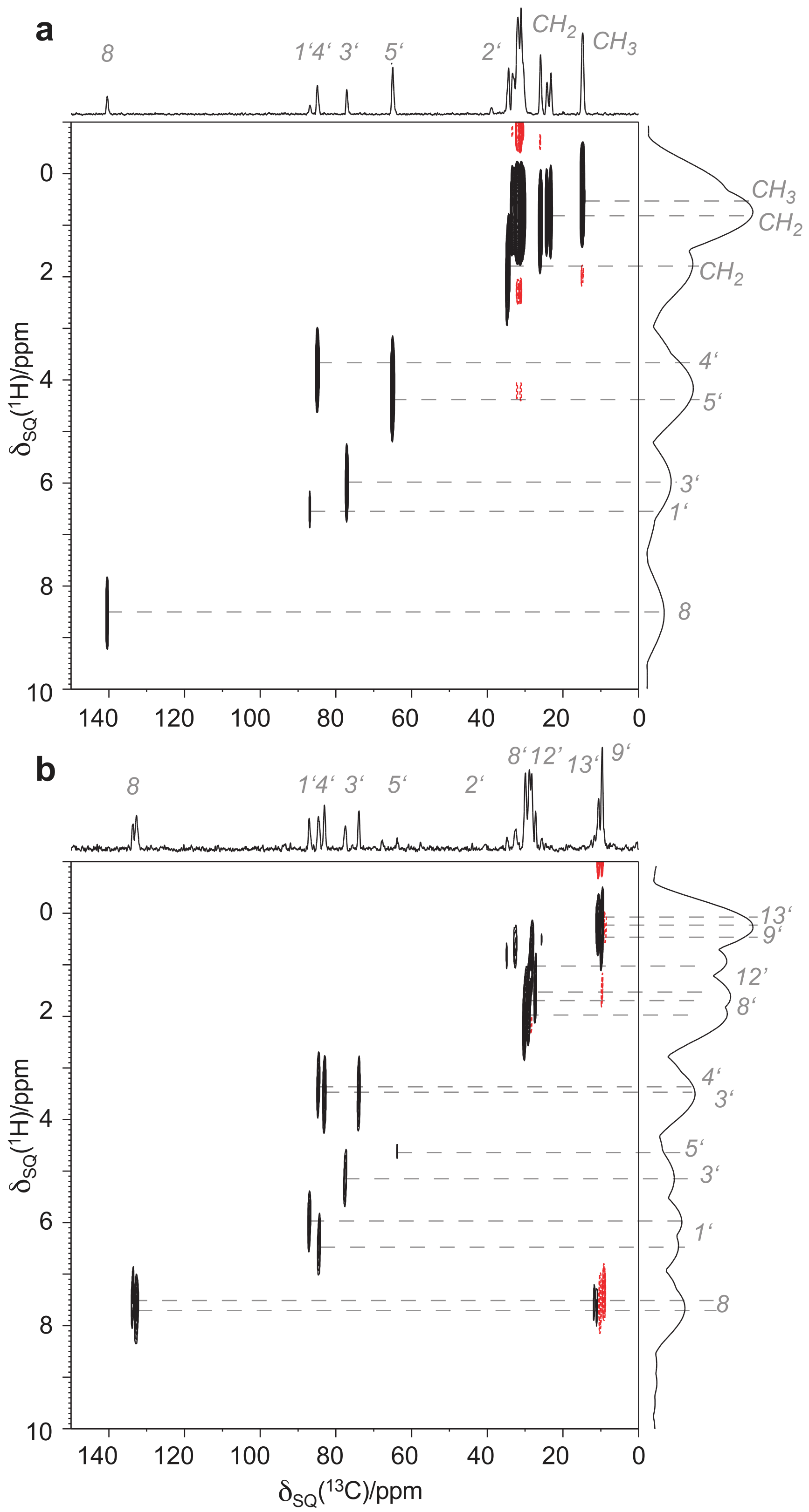

Figure 6.4. ^{1}H (DUMBO)-^{13}C refocused INEPT spectra of (a) **6-1** and (b) **6-2**, recorded at Larmor frequencies of (^{1}H) 600 MHz and (^{13}C) 150 MHz, 12.5 kHz MAS and using the pulse sequence described in Fig. 3.13a and ref[50], along with skyline ^{1}H and ^{13}C projections. Assignments of ^{13}C and ^{1}H chemical shifts are based on calculated shieldings determined for **6-2**, as given in Figs. 6.2c, 6.3d and Tab. 6.1. The base contour level is at (a) 9% or (b) 15% of the maximum peak height in each spectrum and negative contours are shown in red.

CH group.

Correlations resulting from the alkyl CH_2 resonances (CH8' CH12' in Fig. 6.4b), however, are observed for these compounds. It should be noted that, while the CH_2 and CH_3 resonances (CH8', CH9' CH12' CH13') can be separately identified (and chemical shifts assigned by comparison to computed values) for **6-2**, the multiple sites of the long alkyl chain in **6-1** result in many ^{1}H and ^{13}C resonances between $\delta_{SQ}(^{13}C)$ = 20−35 ppm in Fig. 6.4a. No attempt is made here to distinguish each of the ^{13}C chemical shifts of in this region, and as such they are collectively referred to as the CH_2 and CH_3 resonances of the alkyl chain in Fig. 6.4a.

Table 6.1. ^{13}C and ^{1}H chemical shifts of dGC10 (**6-1**) and dGC3 (**6-2**), as determined from ^{13}C CP MAS, ^{1}H (DUMBO), ^{1}H (DUMBO)-^{13}C refocused INEPT, ^{1}H DQ(DUMBO)-SQ(DUMBO) spectra (see Figs. 6.2- 6.6), and first-principles (GIPAW) calculations^{ab} of **6-2**.

Site	Mol	$\delta_{iso}(^{13}C)$ /ppm			$\delta_{iso}(^{1}H)$ /ppm		
		Expt		Calc^a	Expt		Calc^{ab}
		dGC10	dGC3	dGC3	dGC10	dGC3	dGC3
NH1	A				10.2	13.2	13.0
	B					14.0	14.1
NH2a	A				6.8	5.6	5.3
	B					6.1	6.9
NH2b	A				8.8	7.5	8.6
	B					8.0	8.5
C11'	A	174.3	176.6	178.8			
	B		177.1	180.8			
C7'	A	172.6	174.9	171.1			
	B		175.4	177.9			
C6	A	158.5	154.6	156.8			
	B		154.6	156.7			
C2	A	153.6	154.6	150.4			
	B		154.6	151.0			

Continued on Next Page. . .

Table 6.1 – Continued

Site	Mol	$\delta_{\text{iso}}(^{13}\text{C})$ /ppm			$\delta_{\text{iso}}(^{1}\text{H})$ /ppm		
		Expt		Calc[a]	Expt		Calc[ab]
		dGC10	dGC3	dGC3	dGC10	dGC3	dGC3
C4	A	152.4	150.2	150.0			
	B		151.9	151.6			
CH8	A	140.4	132.9	130.3	8.5	7.7	6.8
	B		134.3	132.4		7.5	6.9
CH5	A	117.8	116.2	117.5			
	B		115.3	117.1			
CH1’	A	86.7	87.0	88.9	6.6	6.0	5.8
	B		84.5	86.1		6.2	6.3
CH4’	A	84.9	84.5	86.1	3.6	3.5	3.5
	B		83.1	84.8		3.3	3.3
CH3’	A	77.0	77.5	78.2	6.0	5.2	5.2
	B		73.9	74.3		3.5	3.7
CH5’a	A	64.9	63.7	62.6	4.3	4.8	4.8
	B		63.7	62.9		3.5	3.7
CH5’b	A					3.0	3.0
	B					3.7	4.0
CH2’a	A	39.0	42.7	38.8	4.0	2.2	2.1
	B		40.2	35.5		1.4	1.4
CH2’b	A				2.2	2.2	2.0
	B					3.5	3.5
CH12’a	A	23.2-34.6[c]	27.1	25.4	2.5[c]	1.5	1.5
	B		28.2	27.3		1.0	0.0
CH12’b	A				1.8[c]	1.5	1.4
	B					1.0	0.9
CH8’a	A		28.8	22.8	0.8[c]	2.0	1.8
	B		29.9	25.1		1.7	1.5
CH8’b	A				0.8[c]	2.0	1.2

Continued on Next Page…

Table 6.1 – Continued

Site	Mol	$\delta_{\mathrm{iso}}(^{13}C)$ /ppm			$\delta_{\mathrm{iso}}(^{1}H)$ /ppm		
		Expt		Calc[a]	Expt		Calc[ab]
		dGC10	dGC3	dGC3	dGC10	dGC3	dGC3
	B					2.0	1.9
CH9’	A	15.0	10.3	4.7	0.5	0.5	−0.1
	A			6.3		0.2	−0.4
CH13’	A	14.6	9.4	2.1	0.5	0.2	−0.8
	A			5.8		0.0	−0.8

[a] $\sigma_{\mathrm{ref}}(^{1}H) = 29.97$ ppm, $(^{13}C) = 168.1$ ppm (see Eq. 3.33 in §3.5); determined by a procedure that ensured that the mean of the calculated and experimental ^{13}C and ^{1}H chemical shifts for all sites in dGC3 coincide.

[b] Average of the calculated ^{1}H chemical shifts for the CH_3 protons CH9’ and CH13’.

[c] Range of alkyl CH_2 resonances (*cf* CH8’, CH12’) observed for **6-1**, ^{13}C chemical shifts not individually assigned. ^{1}H chemical shifts identified based on ^{1}H-^{1}H proximities given in Fig. 6.6c and Tab. 6.5 but not necessarily assigned to sites shown.

Importantly, as no correlations peaks are observed for ^{1}H nuclei that are not directly bonded to ^{13}C nuclei, the ^{1}H (DUMBO)-^{13}C refocused INEPT experiment does not provide insight into the ^{1}H chemical shifts of the NH and NH_2 protons of the guanosine compounds.

Figs. 6.5 and 6.6 present high-resolution ^{1}H DQ-SQ correlation spectra of **6-2** and **6-1**, respectively, recorded under fast (30 kHz) MAS alone (6.5a, 6.6a) and CRAMPS (6.5b-d, 6.6b-d), specifically, DUMBO decoupling applied at a MAS frequency of 12.5 kHz. For both samples, the contours of the ^{1}H DQ-SQ spectra recorded under fast-MAS take the same outline appearance as those recorded under CRAMPS, particularly regarding correlation peaks appearing at $\delta_{\mathrm{DQ}}(^{1}H)$ frequencies > 11 ppm. Nevertheless, it is clear that the resolution of the CRAMPS spectra is superior in both cases, as is immediately obvious from a comparison of the skyline projections in (a) and (b). In particular, the enhanced resolution provided by this experiment allows the assignment of experimental ^{1}H NH chemical shifts as shown in (d) (specifically, using NH–H proximities, indicated in (e)) and tabulated in Tab. 6.1 alongside the calculated ^{1}H NH chemical shifts of **6-2**.

The expanded regions in (c) and (d) of Figs. 6.5 and 6.6 show the ^{1}H

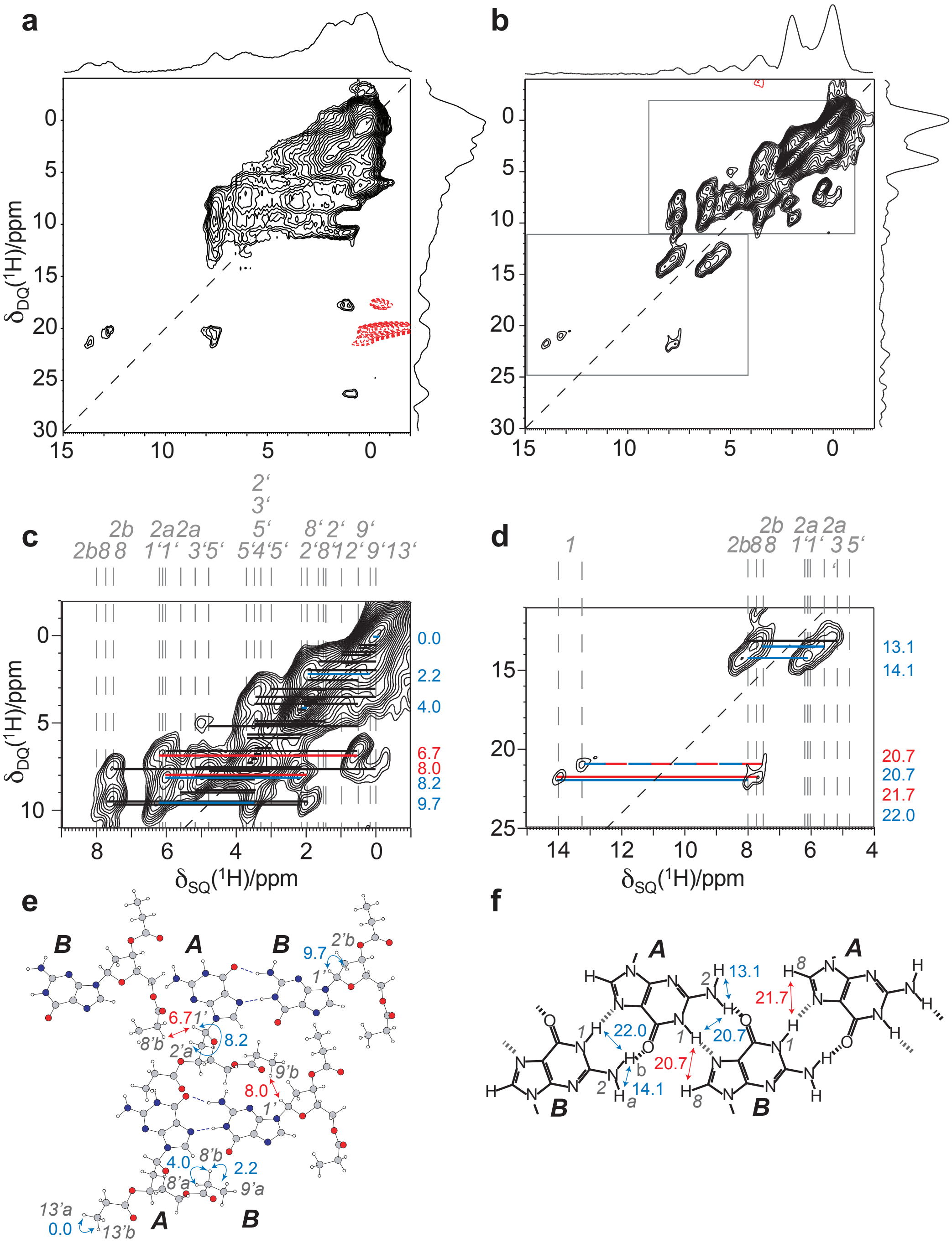

Figure 6.5. ^{1}H (600 MHz) DQ NMR spectra of dGC3, **6-2**: (a) a ^{1}H-^{1}H DQ-SQ MAS spectrum recorded at 30 kHz MAS, (b) a ^{1}H-^{1}H DQ (DUMBO)-SQ (DUMBO) CRAMPS spectrum recorded at 12.5 kHz MAS. The base contour level is at (a) 2 % or (b-d) 3 % of the maximum peak height in each spectrum, negative contours are given in red and skyline projections are shown for (a,b). In all spectra, the $F_1 = 2F_2$ diagonal is shown as a dark dashed line. The regions within the rectangles in (b) correspond to those expanded in (c,d), where site assignments are shown and DQ correlations are indicated by solid horizontal bars. Blue and red bars in (c, d) highlight DQ coherences arising from pairs of intra and inter-molecular ^{1}H nuclei, respectively, which are discussed in the text. (e,f) Representations of ribbon-like structure of **6-2** showing the H-H proximities corresponding to the assigned DQ peaks in (c,d) - the H-H proximities are labelled with their ^{1}H DQ chemical shift (see Tabs. 6.2- 6.4).

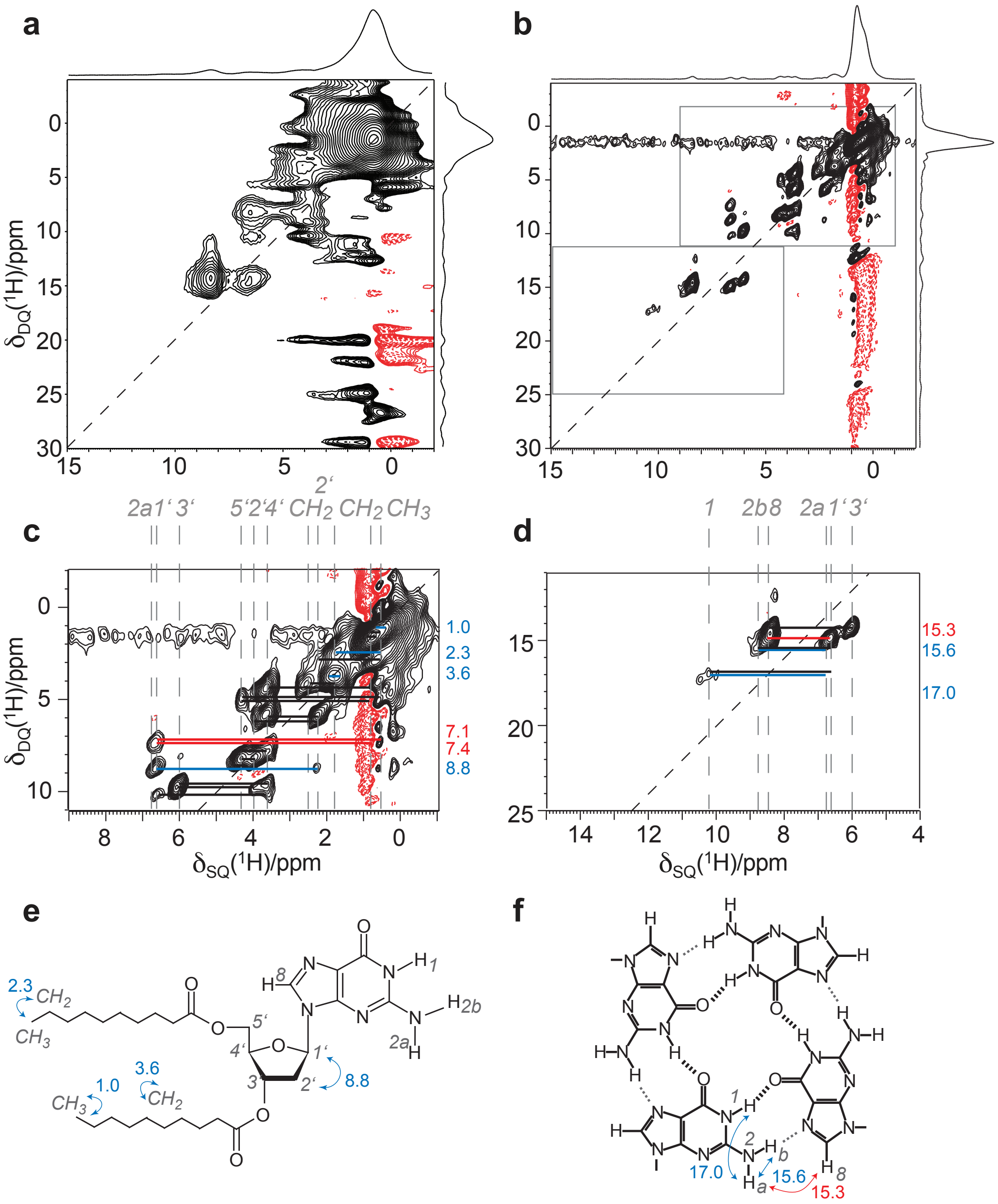

Figure 6.6. ^{1}H (600 MHz) DQ NMR spectra of dGC10, **6-1**: (a) a ^{1}H-^{1}H DQ-SQ MAS spectrum recorded at 30 kHz MAS, (b) a ^{1}H-^{1}H DQ (DUMBO)-SQ (DUMBO) CRAMPS spectrum recorded at 12.5 kHz MAS. The base contour level is at (a) 4 % or (b-d) 1 % of the maximum peak height in each spectrum, negative contours are given in red and skyline projections are shown for (a,b). In all spectra, the $F_1 = 2F_2$ diagonal is shown as a dark dashed line. The regions within the rectangles in (b) correspond to those expanded in (c,d), where site assignments are shown and DQ correlations are indicated by solid horizontal bars. Blue and red bars in (c,d) highlight DQ coherences arising from pairs of intra and inter-molecular ^{1}H nuclei, respectively, which are discussed in the text. (e,f) Schematic and representation of quartet-like structure of **6-1** showing the H-H proximities corresponding to the assigned DQ peaks in (c,d) - the H-H proximities are labelled with their ^{1}H DQ chemical shift (see Tab. 6.5).

DQ-SQ (CRAMPS) correlation peaks in more detail for two regions of the spectrum highlighted in (b). The areas shown in (c) display large, relatively broad contours for both samples between ^{1}H(DQ) 0-5 ppm due to the many overlapping peaks for the DQ coherences between and among the alkyl chain groups, listed in Tab. 6.2 for **6-2** (along with distances from the (CASTEP) geometrically optimised crystal structure) and Tab. 6.5 for **6-1**. For example, peaks corresponding to DQ coherences among CH_3 protons (**6-2**: H13a'A-H13b'A, 0.0 + 0.0 = 0.0 ppm (1.78 Å), **6-1**: CH_3-CH_3, 0.5 + 0.5 = 1.0 ppm), and CH_2 protons (**6-2**: H8a'A-H8b'A, 2.0 + 2.0 = 4.0 ppm (1.77 Å), **6-1**: CH_2-CH_2, 1.8 + 1.8 = 3.6 ppm) of the same chemical site are observed as well as those between intramolecular alkyl sites e.g., between CH_3 and CH_2 groups of the chain (**6-2**: H9a'B-H8b'B, 0.2 + 2.0 = 2.2 ppm (2.50 Å), **6-1**: CH_3-CH_2, 0.5 + 1.8 = 2.3 ppm). These regions also highlight correlations involving ^{1}H nuclei of the sugar ring (listed in Tabs. 6.3 and 6.5 for **6-2** and **6-1** respectively), notably prominent pairs of peaks are observed in both spectra arising from the same intramolecular H1'-H2' proximities (**6-2**: H1A-H2a'A, 6.0 + 2.2 = 8.2 ppm (2.44 Å), H1B-H2b'B, 6.2 + 3.5 = 9.7 ppm (2.44 Å), **6-1**: 6.6 + 2.2 = 8.8 ppm). The intramolecular proximities evident from Figs. 6.5c and 6.6c are indicated in blue in Figs. 6.5e and 6.6e and are labelled with the corresponding ^{1}H DQ chemical shifts.

Interestingly, Fig. 6.5c also shows pairs of peaks assigned to DQ coherences for intermolecular proximities (shown in red) between one ^{1}H nucleus on the sugar ring and others on the alkyl chains (**6-2**: H1'B-H9'bA, 6.2 + 0.5 = 6.7 ppm (2.24 Å), H1'A-H8'bB, 6.0 + 2.0 = 8.0 ppm (2.49 Å), see Tab. 6.3). Fig. 6.5e shows a representation of the optimised crystal structure of **6-2** (where the H-H proximities are labelled according to their ^{1}H DQ chemical shifts) from which it can be seen that these proximities between the two distinct molecules (**A,B**) of **6-2** arise due to the stacking of the planar ribbon structures.

Moreover, similar proximities are observed for **6-1**: H1'-CH_3, 0.5 + 6.6 = 7.1 ppm, H1'-CH_2, 0.8 + 6.6 = 7.4 ppm, (see Tab. 6.5) which are highlighed by red horizontal bars on Fig. 6.6c. As pairs of DQ peaks are generally only observed for H-H proximities less than 3.5 Å, such proximities provide insight into the molecular arrangements of dGC10 molecules in solids. The traditionally observed geometries of guanosine, either in syn or anti orientations are unlikely to result in these particular moieties being in close proximity with one another unless, for example, the alkyl chains are folded (about e.g., CH4' position). Otherwise, these DQ coherences can be attributed to close proximities of ^{1}H of different molecules and could also, for example, indicate a stacking of quartets or a helical arrangement. Therefore, the ^{1}H-^{1}H correlations observed in this manner provide structural constraints for modelling three-dimensional arrangements of atoms. These constrains could be compared to similar information obtained from known quartet or quadruplex crystal structures or solution-state constraints (i.e., from NOESY type data) to infer similarities to a particular structural model.

The expanded regions given in Figs. 6.5d and 6.6d also highlight H-H proximities involving the NH protons that give rise to evident pairs of ^{1}H DQ correlation peaks. The internal geometry of the NH and NH$_2$ protons of the guanine head group gives rise to close intramolecular proximities among NH(1)-NH(2) (**6-2**: H1A-H2bA, 13.2 + 7.5 = 20.7 ppm (2.36 Å), H1B-H2bB, 14.0 + 8.0 = 22.0 ppm (2.34 Å), **6-1**: H1-H2a, 10.2 + 6.8 = 17.0 ppm) and between the NH(2a)-NH(2b) (**6-2**: H2aA-H2bA, 5.6 + 7.5 = 13.1 ppm (1.75 Å), H2aB-H2bB, 6.1 + 8.0 = 14.1 ppm (1.75 Å), **6-1**: H2a-H2b, 6.8 + 8.8 = 15.6 ppm) for both samples (see Tabs. 6.4 and 6.5).

Tab. 6.1 shows that the chemical shift of the CH8 proton is similar to that of an NH2 proton. Considering Tab. 6.4, the closest H-H for CH8 are to NH1: 7.5 + 13.2 = 20.7 ppm and 7.7 + 14.0 = 21.7 ppm. However, the distances of 2.88 Å and 2.80 Å are significantly longer than the closer distances between NH1 and NH2, thus these DQ peaks are expected to be of low intensity [156].

A graphical comparison of experimental and calculated ^{13}C and ^{1}H chemical shifts for **6-2** is presented in Fig. 6.7. A common observation of GIPAW calculations is an overestimation of the paramagnetic contribution to the chemical shift, such that the slope of such a plot deviates from unity, as is also observed in Figs. 7.5 and 5.7 in this thesis. An obvious consequence is the underestimation of ^{13}C and ^{1}H chemical shifts for the alkyl resonances in

Table 6.2. ^{1}H DQ correlations[a] among alkyl ^{1}H nuclei(< 3.0 Å) in dGC3, **6-2**, taken from Fig. 6.5c.

CH proton	$\delta_{SQ\_1}(^1H)$ /ppm	CH proton	$\delta_{SQ\_2}(^1H)$ /ppm	Separation[b] /Å	$\delta_{DQ}(^1H)$ /ppm
H13'a A	0.0	H13'b A	0.0	1.78	0.0
H13'b A	0.0	H9'a A	0.5	2.74	0.5
H9'a B	0.2	H9'b B	0.5	1.78	0.7
H9'b A	0.5	H9'c A	0.5	1.78	1.0
H13'a B	0.0	H12'b B	1.0	2.47	1.0
H9'a B	0.2	H12'a B	1.0	2.66	1.2
H13'a A	0.0	H12'a A	1.5	2.47	1.5
H9'b B	0.5	H12'a B	1.0	2.89	1.5
H9'a B	0.2	H12'b A	1.5	2.65	1.7
H9'a B	0.2	H8'a B	1.7	2.53	1.9
H13'b A	0.0	H8'b A	2.0	2.15	2.0
H12'a B	1.0	H12'b B	1.0	1.78	2.0
H9'a B	0.2	H8'b B	2.0	2.50	2.2
H9'a A	0.5	H8'b A	2.0	2.48	2.5
H12'a A	1.5	H12'b A	1.5	1.75	3.0
H12'a A	1.5	H8'b B	2.0	2.40	3.5
H8'a A	2.0	H8'b A	2.0	1.77	4.0

[a] Intermolecular proximities are highlighted in grey.

[b] H-H distances from the (CASTEP) geometrically optimised crystal structure. Where multiple H-H proximities involving the same chemical sites and ^{1}H chemical shifts exist, only the pair with the shortest distance is quoted.

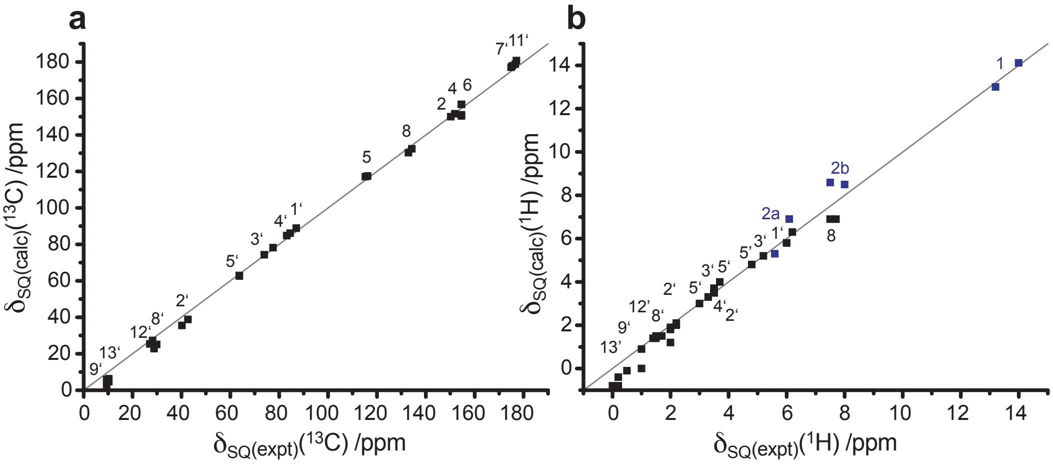

Figure 6.7. A graphical comparison of the experimental and calculated (a) ^{13}C (b) ^{1}H chemical shifts of **6-2**, with NH ^{1}H chemical shifts highlighted in blue (see Tab. 6.1).

Table 6.3. ^{1}H DQ correlations[a] involving sugar ^{1}H nuclei(< 3.0 Å) in dGC3, **6-2**, taken from Fig. 6.5c.

CH proton	$\delta_{\text{SQ-1}}(^1\text{H})$ /ppm	CH proton	$\delta_{\text{SQ-2}}(^1\text{H})$ /ppm	Separation[b] /Å	$\delta_{\text{DQ}}(^1\text{H})$ /ppm
H13’a B	0.0	H5’b A	3.0	2.70	3.0
H2’a B	1.4	H8’a B	1.7	2.25	3.1
H13’a A	0.0	H5a’ B	3.5	2.29	3.5
H13’a B	0.0	H4’ A	3.5	2.46	3.5
H9’b B	0.5	H5’b A	3.0	2.69	3.5
H2’a B	1.4	H2’a A	2.2	2.06	3.6
H8’a B	1.7	H2’a A	2.2	2.57	3.9
H9’c A	0.5	H2’b A	3.5	2.29	4.0
H12’a B	1.0	H5’b A	3.0	2.84	4.0
H8’a A	2.0	H2’b A	2.2	2.75	4.2
H2’a A	2.2	H2’b A	2.2	1.80	4.4
H2’a B	1.4	H2’b B	3.5	1.77	4.9
H2’a B	1.4	H3’ B	3.5	2.36	4.9
H8’a B	1.7	H2’b B	3.5	2.98	5.2
H9’b B	0.5	H5’a A	4.8	2.51	5.3
H8’a A	2.0	H5’b B	3.7	2.98	5.7
H2’b A	2.2	H5’b B	3.7	2.25	5.9
H5’b A	3.0	H4’ A	3.5	2.46	6.5
H9’b A	0.5	H1’ A	6.0	2.73	6.5
H9’b A	0.5	H1’ B	6.2	2.24	6.7
H4’ B	3.3	H5’a B	3.5	2.46	6.8
H3’ B	3.5	H5’a B	3.5	2.56	7.0
H2’b B	3.5	H3’ B	3.5	2.79	7.0
H5’a B	3.5	H5’b B	3.7	1.79	7.2
H3’ B	3.5	H5’b B	3.7	2.55	7.2
H2’b A	2.2	H3’ A	5.2	2.44	7.4
H8’a B	1.7	H1’ A	6.0	2.80	7.7
H5’b A	3.0	H5’a A	4.8	1.79	7.8
H8’b B	2.0	H1’ A	6.0	2.49	8.0
H4’ B	3.3	H5’a A	4.8	2.82	8.1
H5’b A	3.0	H3’ A	5.2	2.58	8.2
H2’a A	2.2	H1’ A	6.0	2.44	8.2
H4’ A	3.5	H5’a A	4.8	2.52	8.3
H4’ A	3.5	H3’ A	5.2	2.80	8.7
H2’b B	3.5	H1’ B	6.2	2.44	9.7
H4’ A	3.5	H1’ B	6.2	2.75	9.7

[a] Intermolecular proximities are highlighted in grey.

[b] H-H distances from the (CASTEP) geometrically optimised crystal structure.

Table 6.4. ^{1}H DQ correlations[a] involving NH, NH$_2$ and CH8 ^{1}H nuclei(< 3.0 Å) in dGC3, **6-2**, taken from Fig. 6.5d.

CH proton	$\delta_{\mathrm{SQ\_1}}(^1\mathrm{H})$ /ppm	CH proton	$\delta_{\mathrm{SQ\_2}}(^1\mathrm{H})$ /ppm	Separation[b] /Å	$\delta_{\mathrm{DQ}}(^1\mathrm{H})$ /ppm
H13’c B	0.0	H2b A	7.5	2.97	7.5
H8’b B	2.0	H2a B	6.1	2.83	8.1
H4’ B	3.5	H2a A	5.6	2.85	8.9
H2’a B	1.4	H8 B	7.5	2.92	8.9
H2’b B	3.5	H2a A	5.6	2.56	9.1
H5’a B	3.5	H2a A	5.6	2.84	9.1
H8’b A	2.0	H8 A	7.7	2.52	9.7
H2’a A	2.2	H8 B	7.5	2.53	9.7
H2a A	5.6	H2b A	7.5	1.75	13.1
H3’ A	5.2	H2b B	8.0	2.70	13.2
H13’b B	0.0	H1 A	13.2	2.83	13.2
H13’b A	0.0	H1 B	14.0	2.88	14.0
H2a B	6.1	H2b B	8.0	1.75	14.1
H12’b A	1.5	H1 A	13.2	2.90	14.7
H12’b B	1.0	H1 B	14.0	2.90	15.0
H8 B	7.5	H1 A	13.2	2.88	20.7
H2b A	7.5	H1 A	13.2	2.36	20.7
H8 A	7.7	H1 B	14.0	2.84	21.7
H2b B	8.0	H1 B	14.0	2.34	22.0

[a] Intermolecular proximities are highlighted in grey.

[b] H-H distances from the (CASTEP) geometrically optimised crystal structure.

Table 6.5. ^{1}H DQ correlations involving all ^{1}H nuclei in dGC10, **6-1** taken from Fig. 6.6c,d.

CH proton	$\delta_{\mathrm{SQ\_1}}(^1\mathrm{H})$ /ppm	CH proton	$\delta_{\mathrm{SQ\_2}}(^1\mathrm{H})$ /ppm	$\delta_{\mathrm{DQ}}(^1\mathrm{H})$ /ppm
CH_3	0.5	CH_3	0.5	1.0
CH_3	0.5	CH_2	0.8	1.3
CH_2	0.8	CH_2	0.8	1.6
CH_3	0.5	CH_2	1.8	2.3
CH_3	0.5	H2'	2.2	2.7
CH_2	1.8	CH_2	1.8	3.6
CH_2	1.8	CH_2	2.5	4.3
CH_2	0.8	H4'	3.6	4.4
CH_3	0.5	H5'	4.3	4.8
CH_2	0.8	H5'	4.3	5.1
H2'	2.2	H4'	3.6	5.8
H2'	2.2	H2'	4.0	6.2
CH_3	0.5	H1'	6.6	7.1
CH_2	0.8	H1'	6.6	7.4
H4'	3.6	H5'	4.3	7.9
H2'	4.0	H5'	4.3	8.3
H5'	4.3	H5'	4.3	8.6
H2'	2.2	H1'	6.6	8.8
H4'	3.6	H3'	6.0	9.6
H2'	4.0	H3'	6.0	10.0
H4'	3.6	H1'	6.6	10.2
H3'	6.0	H8	8.5	14.5
H1'	6.6	H8	8.5	15.1
H2a	6.8	H8	8.5	15.3
H1'	6.6	H2b	8.8	15.4
H2a	6.8	H2b	8.8	15.6
H1'	6.6	H1	10.2	16.8
H2a	6.8	H1	10.2	17.0

particular. However, the calculated chemical shift values of the sugar ring sites (CH1'-CH5') show excellent agreement with those determined experimentally for both ^{13}C and ^{1}H nuclei, such that these chemical shifts are assigned with confidence. In the following section, the ^{13}C resonances assigned here to these sites for **6-2** (and, similarly, **6-1**) are compared with those observed from a range of new guanosine derivatives in order to infer structural information (see Fig. 6.8 and Tab. 6.6).

6.4 Results: Synthetic RNA Guanosine Derivatives

6.4.1 1D ^{13}C and ^{1}H MAS

For the synthetic materials **6-3** to **6-6** discussed in this section, it has not been possible to obtain single crystals suitable for diffraction studies and hence no existing diffraction structures are available. However, it is shown here that structural information can be extracted from *natural abundance* solid-state NMR spectra.

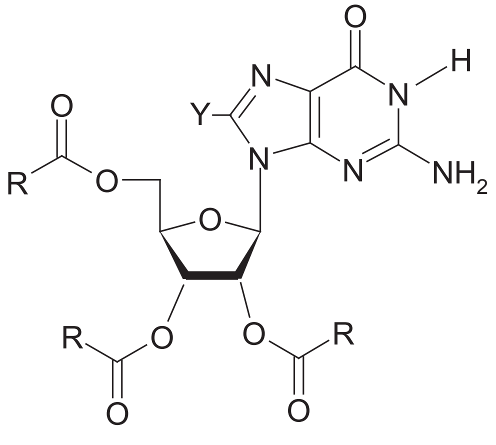

6-3 GC3$_3$; R=C_2H_5 Y=H
6-4 GC10$_3$; R=C_9H_{19} Y=H
6-5 8BrGC10$_3$; R=C_9H_{19} Y=Br

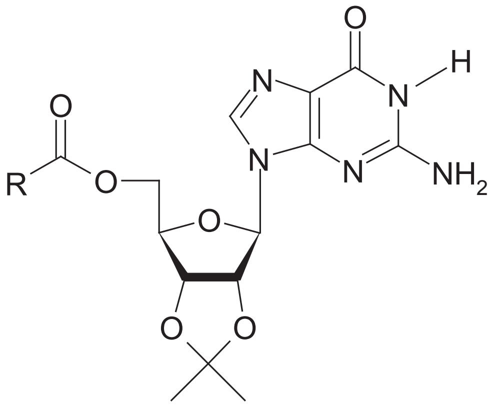

6-6 GaceC10; R=C_9H_{19}

Fig. 6.8 presents ^{13}C CP MAS spectra for guanosine derivatives **6-1** to **6-6**, showing ^{13}C resonances of the sugar ring sites, C5 and C8 nuclei, where peaks in **6-1** (a) and **6-2** (b) are assigned from the previous section. The four new materials discussed in this section are no longer deoxygenated

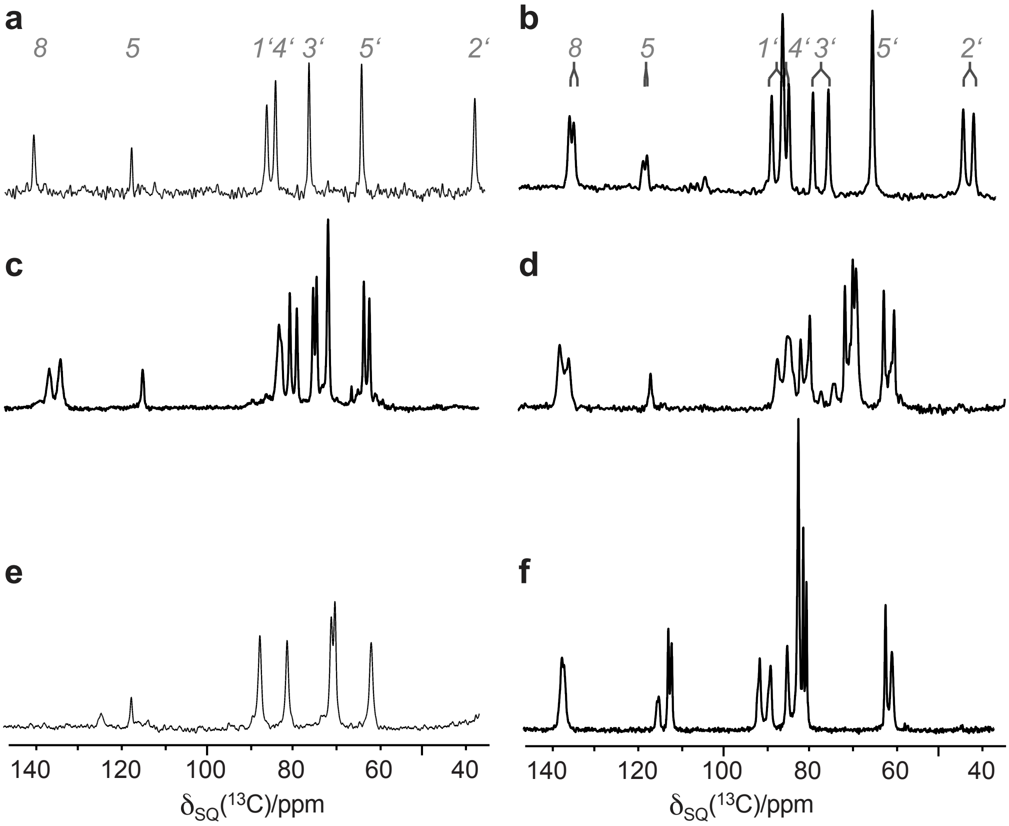

Figure 6.8. ^{13}C CP MAS spectra of guanosine derivatives (a) **6-1** (b) **6-2** (c) **6-3** (d) **6-4** (e) **6-5** (f) **6-6**, expanded to show the ^{13}C resonances around the sugar and CH8 region. Spectra were recorded at Larmor and MAS frequencies of (a) 175 MHz, 8.5 kHz (b,e) 150 MHz, 12.5 kHz (c-d,f) 75 MHz, 8.5 kHz, respectively. Site assignments are labelled for **6-1** and **6-2** from Tab. 6.1.

derivatives, as they have substituted groups at the C2' position of the sugar ring, either an identical alkyl chain to that at C3' (**6-3** to **6-5**) or an acetyl group joining the oxygen atoms directly bonded to the C2' and C3' sites (**6-6**). Thus, none of the four spectra shown in (c-f) contain ^{13}C resonances at approximately 40 ppm, where the (CH$_2$) C2' site appears in (a-b), as this peak now appears at approximately 70 ppm i.e., in a similar position as C3'. Notably, only Figs. 6.8a and 6.8e display one ^{13}C peak per atomic site, which immediately suggests that of the new materials only **6-5** assembles to form quartet-like structures in the solid state. The spectra given in Fig. 6.8c and Fig. 6.8d, corresponding to **6-3** and **6-4** are remarkably similar, and have many features in common with the ^{13}C resonances observed in (b) for the established ribbon structure of **6-2**. Also in common with **6-2**, the ^{13}C chemical shifts of the C8 resonances of **6-3**, **6-5** and **6-6** all appear below 140 ppm, noting that the 8-bromine substitution in **6-5** shifts this peak the furthest upfield to generate a small, broad resonance around 125 ppm.

A comparison of ^{1}H fast-MAS (black) and CRAMPS (DUMBO - grey) NMR spectra is given in Fig. 6.9(a-f) for compounds **6-1** to **6-6**, respectively. The multiple CH$_2$ resonances of the additional long alkyl chains in **6-4** and **6-5** cause many overlapping resonances in the range 0.5-1.0 ppm which reduce the relative intensity of resonances at higher ppm valuesd. With the line narrowing provided in the ^{1}H CRAMPS spectra it is possible to resolve further ^{1}H peaks as compared to under MAS alone - resonance assignments are labelled above the spectra. Most notably, the hydrogen bonded NH1 ^{1}H chemical shifts (highlighted in blue) are assigned at approximately 10.8 ppm for **6-5** and between 14.0-15.0 ppm for the remaining three new derivatives (see Tab. 6.7). By analogy with the ^{1}H chemical shifts of **6-1** and **6-2** this suggests that N1H$\cdots$N7 hydrogen bonds (i.e., quartet-like structures) are present for **6-5**, as compared to N1H$\cdots$O6 (ribbons), in other cases.

6.4.2 ^{1}H-^{13}C SQ-SQ and ^{1}H-^{1}H DQ-SQ 2D Correlations

Expanded regions of ^{1}H-^{13}C heteronuclear correlation spectra of **6-1** to **6-6** are presented in Fig. 6.10, that show ^{13}C-^{1}H chemical shifts of the sugar and CH8

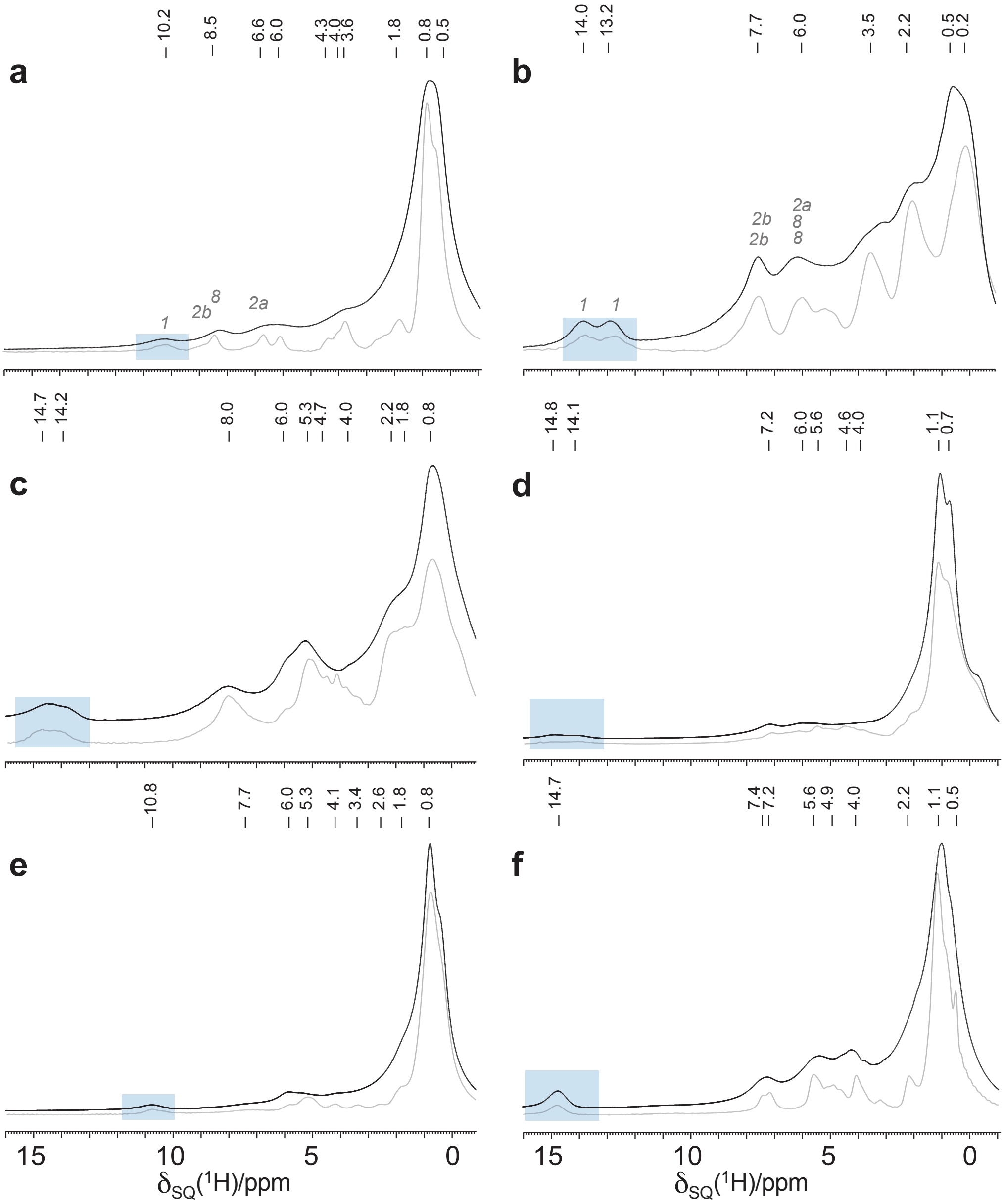

Figure 6.9. ^{1}H NMR spectra of deoxyguanosine compounds (a) **6-1** (b) **6-2** (c) **6-3** (d) **6-4** (e) **6-5** (f) **6-6**. ^{1}H fast MAS (black) and homonuclear (DUMBO) decoupled (grey) NMR spectra recorded at 600 MHz and MAS frequencies of 30 kHz and 12.5 kHz, respectively. Regions highlighted in blue are attributed to the hydrogen bonded NH sites. Chemical shift values resolved from CRAMPS spectra are identified. Site assignments of NH, NH_2 and CH8 resonances are labelled for **6-1** and **6-2** from Tab. 6.1.

Table 6.6. Comparison of experimentally determined ^{13}C chemical shifts of CH8 and sugar carbons for **6-1** to **6-6** (shown in this chapter, from Figs. 6.8 and 6.10) with solution-state chemical shifts reported in ref.[186] for **6-1**.

Site	$\delta_{\text{iso}}(^{13}\text{C})$ /ppm [a]						$\delta_{\text{iso}}(^{13}\text{C})$ /ppm [b]	
	dGC3	GC3	GC10	G-ace-C10	8BrGC10	dGC10	dGC10 (K^+)	
	6-2	**6-3**	**6-4**	**6-6**	**6-5**	**6-1**		
	Anti	Anti?	Anti?	Anti?	Syn?	Syn?	Syn	Anti
CH8	134.3	136.8	139.2	139.3	125.6	140.4	137.7	134.9
	132.9	134.7	137.1	138.8				
CH1’	87.0	84.0	88.8	93.5	88.4	86.7	86.6	82.4
	84.5	83.8	86.4	91.0				
CH4’	84.5	81.5	83.4	87.1	82.1	84.9	82.6	83.1
	83.1	79.9	81.3	84.5				
CH3’	77.5	76.4	73.1	84.5	72.0	77.0	74.4	74.5
	73.9	75.3	71.3	83.4				
CH5’	63.7	64.5	64.1	64.3	62.8	64.9	64.2	64.8
	63.7	63.1	61.7	62.8				
CH2’	42.7	73.8	70.5	83.4	71.1	39.0	31.8	31.8
	40.2	72.7	70.2	82.6				

[a] Experimental values taken from spectra shown in this chapter. Where chemical shifts corresponding to two distinct molecules are shown/predicted no specific assignments (i.e., to **A,B**) are made. The assignments of CH2’ and CH3’ ^{13}C chemical shifts for **6-3** - **6-6** are arbitrary.

[b] From ref[186] NB: CH2’-CH5’ ^{13}C nuclei are not assigned to specific syn anti conformations and listed only for comparison.

region. Spectra were recorded under similar conditions as to those described in §6.3.1 (see §6.2.2), such that correlation peaks are only visible for directly bonded pairs of ^{1}H-^{13}C nuclei. Similarly, correlation peaks resulting from CH_2 (CH5’) groups are weak or not visible in many of Fig. 6.10c-f. Based on experimentally (and calculated) chemical shift values determined for **6-1** and **6-2**, and correlation peaks visible in Fig. 6.10c-f, ^{13}C and ^{1}H assignments were made for **6-3** to **6-6** in this region, as listed in Tabs. 6.6 and 6.7. In these tables, predictions have been made for **6-3** to **6-6** regarding modes of self assembly i.e., G-quartet and G-ribbon structures and also molecular conformation (syn, anti) based on the ^{13}C and ^{1}H chemical shifts determined from Figs. 6.8 - 6.10 by analogy with those shown in §6.3.1. A comparison is also made with the solution state chemical shifts presented by Marlow *et al.*, where detailed NOESY analyses were used to identify the syn and anti arrangements of two G-quartets observed for K^+ templated octamers of dGC10 (**6-1**) in $CDCl_3$ [186]. This is discussed further below.

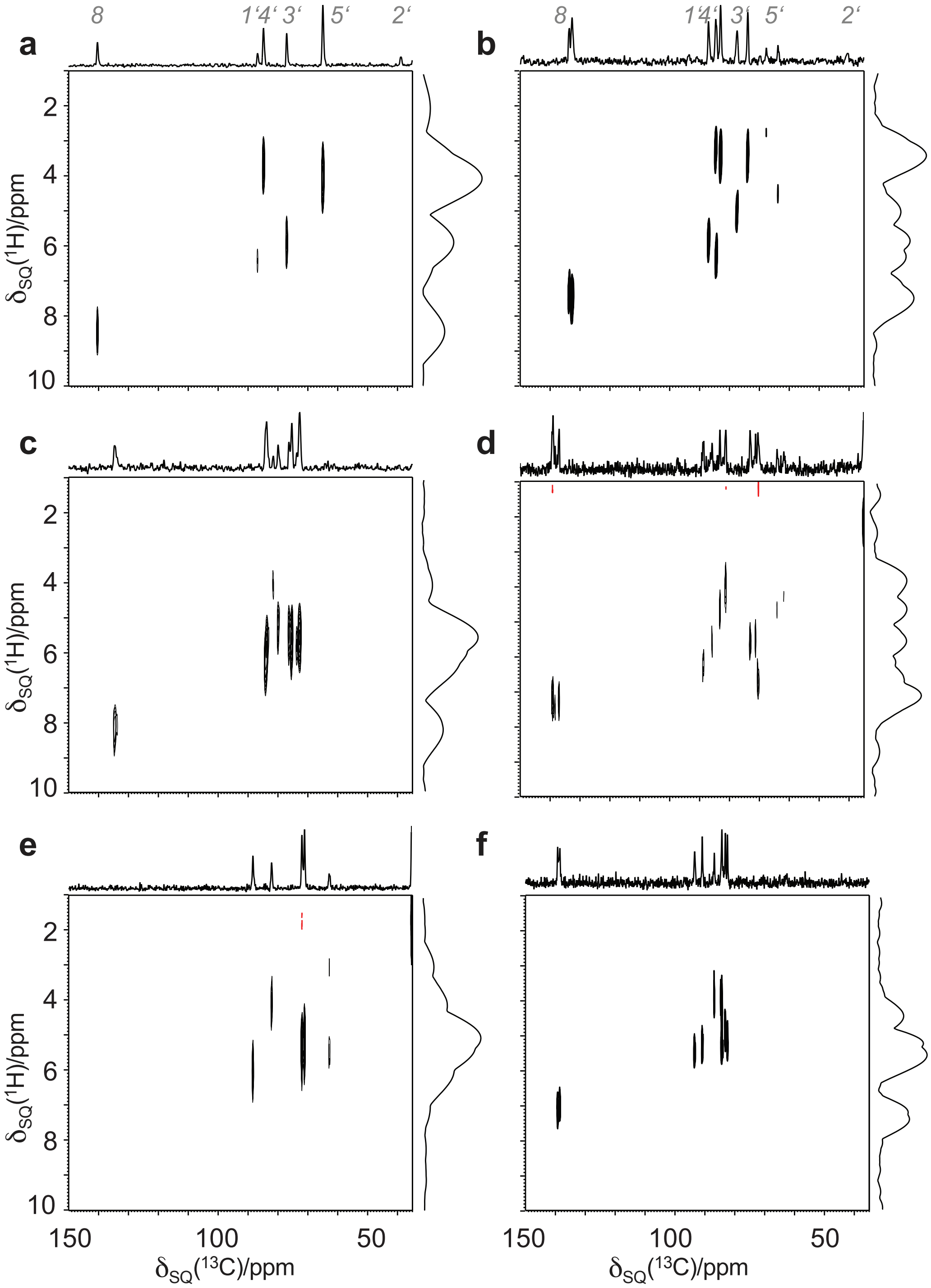

Figure 6.10. ^{1}H (DUMBO)-^{13}C refocused INEPT spectra of (a) **6-1** (b) **6-2** (c) **6-3** (d) **6-4** (e) **6-5** (f) **6-6**, recorded at Larmor frequencies of (^{1}H) 600 MHz and (^{13}C) 150 MHz and 12.5 kHz MAS, with skyline ^{1}H and ^{13}C projections. Spectra show expanded regions containing ^{13}C and ^{1}H chemical shifts assigned to the CH8 sites and sugar ring atoms. Assignments of ^{13}C chemical shifts of **6-1 6-2** are indicated, taken from Tab. 6.1. The base contour level is at (a) 9%, (b) 15%, (c) 14%, (d) 6%, (e) 4% or (f) 18% of the maximum peak height in each spectrum and negative contours are shown in red.

The ^{1}H NH and NH$_2$ chemical shifts of **6-3** to **6-6** are assigned using the ^{1}H DQ(DUMBO)-SQ(DUMBO) spectra shown in Fig. 6.11 and listed in Tab. 6.7. As was revealed using one-dimensional ^{1}H MAS and CRAMPS, the resolvable NH1 ^{1}H chemical shift also offers immediate insight into the hydrogen bonding exhibited and thus the structural arrangement. As a consequence, pairs of ^{1}H-^{1}H peaks appear in this region of the spectra resulting from DQ coherences involving the NH proton at approximately $\delta_{\mathrm{DQ}}(^1\mathrm{H})= 17$ ppm and 22 ppm for quartet and ribbon structures, respectively. These correlation peaks are particularly weak (and as such are only observed at contour levels around 1% of the maximum peak height) suggesting that they arise due to relatively long H-H proximities, nevertheless, the high sensitivity of ^{1}H experiments allows these correlations to be identified.

6.4.3 Syn & Anti Conformations

Many G-quartet-based structures (formed in the presence of ions) including octamers or stacked columnar aggregates have been observed by solution-state NMR or single-crystal diffraction to contain both syn and anti conformations, often alternating between them, as the base may be free to rotate with respect to the planar quartet such that stacked quartets or helical quadruplex structures are formed [186, 198, 200, 206]. A study by Marlow *et al.* of dGC10 (K$^+$) in CDCl$_3$ solution, assigned various ^{13}C and ^{1}H resonances to the syn and anti conformations present, as given in Tabs. 6.6 and 6.7, respectively. It is observed that in solution, the differences in ^{13}C chemical shift between the two conformations of dGC10 (K$^+$) quartets are significant for the CH8 and CH1', and similarly the ^{1}H chemical shift of the CH8 site.

For **6-2**, it is known that both distinct molecules of the ribbon-like architecture exist in an *anti* orientation of the base [190, 201]. Therefore, in this work, all samples displaying crystallographic splittings of ^{13}C of ^{1}H resonances are assumed to adopt ribbon structures (and hence anti conformations, in Tabs. 6.6 and 6.7).

Materials assigned as ‘quartet-like’ here (**6-1**, **6-5**) reveal well resolved, single resonances in ^{13}C and ^{1}H spectra, that indicate single species of quartets.

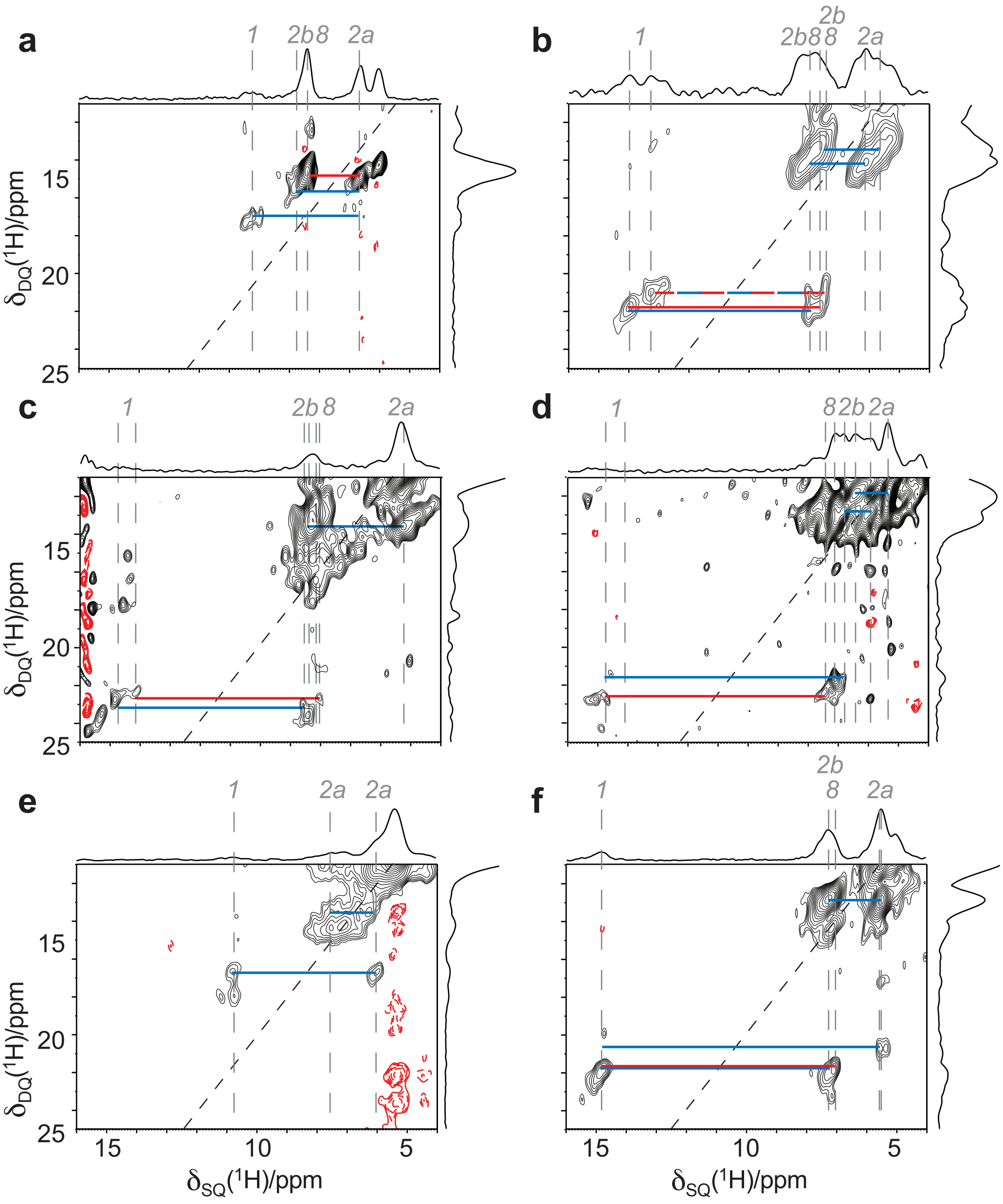

Figure 6.11. ^{1}H (600 MHz) DQ (DUMBO)-SQ (DUMBO) CRAMPS spectra of (a) **6-1**, (b) **6-2**, (c) **6-3**, (d) **6-4**, (e) **6-5**, (f) **6-6** recorded at 12.5 kHz MAS. The base contour level is at (a, d-f) 1 %, (b) 2 % or (c) 3 % of the maximum peak height in each spectrum, negative contours are given in red and skyline projections are shown. Spectra show expanded regions corresponding to those presented in Figs. 6.5d and 6.6d, to identify pairs of peaks resulting from DQ coherences between NH, NH_2 and CH8 protons. Assignments of ^{1}H chemical shifts (shown in grey, listed in Tab. 6.7) are tentative in some cases, as discussed in the text. In all spectra, the $F_1 = 2F_2$ diagonal is shown as a dark dashed line. Blue and red horizontal bars in (d) highlight DQ coherences arising from (in c-f, predicted) pairs of intra and inter-molecular ^{1}H nuclei, respectively.

Table 6.7. Comparison of experimentally determined ^{1}H chemical shifts of NH, NH$_2$, CH8 and sugar protons for **6-1** to **6-6** (from Figs. 6.9- 6.11) with solution-state chemical shifts reported in ref.[186] for **6-1**.

Site	$\delta_{\text{iso}}(^1\text{H})$ /ppm [a]						$\delta_{\text{iso}}(^1\text{H})$ /ppm [b]	
	dGC3	GC3	GC10	G-ace-C10	8BrGC10	dGC10	dGC10 (K$^+$)	
	6-2	**6-3**	**6-4**	**6-6**	**6-5**	**6-1**		
	Anti	Anti	Anti	Anti	Syn	Syn	Syn	Anti
NH1	14.1	14.7	14.8	14.7	10.8	10.2	12.0	12.0
	13.2	14.2	14.1	14.7				
NH2a[c]	6.1	5.3	5.4	5.6	6.1	6.8	5.2	5.0
	5.6		6.0					
NH2b[c]	8.0	8.6	6.4	7.4	7.5	8.8	9.3	9.5
	7.5	8.4	6.8					
CH8	7.5	8.0	7.2	7.2	–	8.5	7.4	8.0
	7.7	8.2	7.4	7.0				
CH1'	6.0	6.3	6.2	5.5	6.0	6.6	6.2	6.4
	6.2	6.0	5.6	5.3				
CH4'	3.5	4.0	4.7	4.3	4.1	3.6	4.4	4.4
	3.3	5.3	4.0	4.0				
CH3'[c]	5.2	5.5	5.6	5.2	5.3	6.0	5.6	5.3
	3.5	5.6	5.5	4.0				
CH5'	4.8	5.3	4.6		5.5	4.3	4.7	4.8
	3.5	4.4	4.3		3.0		4.4	4.2
	3.0	4.7						
	3.7							
CH2'[c]	2.2	5.8	6.6	4.9	5.1	4.0	3.6	3.1
	1.4	5.5	6.8	5.2		2.2	2.4	2.6
	2.2			3.7				
	3.5							

[a] Experimental values taken from spectra shown in this chapter. Where chemical shifts corresponding to two distinct molecules are shown/predicted no specific assignments (i.e., to **A,B**) are made. CH and CH$_2$ ^{1}H chemical shifts are ordered according to the rows given in in Tab. 6.6 for their directly bonded ^{13}C nuclei. Assignments of CH2' and CH3' ^{1}H chemical shifts for **6-3** - **6-6** are arbitrary.

[b] From ref[186]. NB: CH2'-CH5' ^{1}H nuclei are *not* assigned to specific syn anti conformations and listed only for comparison.

[c] Tentative assignments made for **6-3** to **6-6**, see Fig. 6.10 and 6.11.

Previous studies of 8-substituted derivatives also concluded that single syn conformations were most likely, specifically that sterically large substituents at the C8 position force the derivative away from ribbon (anti) formation into a syn position to drive quartet assemblies [202], while the syn conformation of bromine subsitituents is also well documented in the crystalline state [207, 208]. A comparison of ^{13}C chemical shifts of the CH8 site shows that (some, predicted) syn arrangements tend to produce higher chemical shift values for this position as compared to anti arrangements, with (**6-5** being the exception due to the effect of the bromine substitution). However, the ^{1}H chemical shift values at this site (see Tab. 6.7) appear to be much more varied between the structures and conformations such that a specific trend can not be isolated for this group of materials. Therefore, solid-state effects on chemical shifts seem to be more important than solely the influence of syn/anti conformation, as compared to solution studies.

6.5 Summary and Outlook

Solid-state NMR has previously been shown to be an extremely powerful probe of guanosine polymorphism using ^{15}N labeled compounds to identify and quantitatively measure through-hydrogen-bond mediated J couplings of G-quartet and G-ribbon structures [102, 205]. The work presented in this chapter demonstrates that advanced ^{1}H and ^{13}C experiments can be applied to these materials at *natural isotopic abundance* to identify specific modes of self-assembly of G-derivatives.

With the assistance of first-principles GIPAW chemical shift calculations, ^{1}H and ^{13}C chemical shifts are assigned with a high degree of accuracy, and are shown to be sensitive probes of local molecular environments as well as intermolecular arrangements. As such, ‘signature’ features in NMR spectra (in particular ^{1}H-^{13}C through-bond correlations and ^{1}H-^{1}H DQ-SQ dipolar correlations) can be identified, and a ‘spectrum to structure’ methodology can be applied to systems where it proves not possible to obtain single-crystals suitable for diffraction studies. The collection of techniques presented here constitute a robust and versatile experimental approach for crystallographic characterisation with important implications for the distinction of organic polymorphs, not least for the broad range of applications being sought from self assembled and guanosine based materials [188, 189].

7

Identifying Molecules Within the Asymmetric Unit: Campho[2,3-c]Pyrazole

7.1 Independent Molecules in The Asymmetric Unit

Crystallographic systems containing multiple molecules in the asymmetric unit cell ($Z' > 1$)[1] can be particularly challenging to characterise [209]. Advances in experimental and computational techniques have alleviated some of the extra demands imposed by these materials, yet the relative proportion of solved structures for $Z' > 1$ materials in the rapidly expanding crystal structure database (CSD) has remained at a relatively low percentage ($\approx 11\%$ [210]) for the last forty years. This is quite surprising considering the valuable information contained within these systems regarding the mechanisms of crystallisation and intermolecular interactions. The reasons for some molecules assembling with many different independent molecules in their most favourable crystallographic arrangements has much to teach crystal engineers (who aim to predict and control the assembly of ordered materials) regarding distinctive packing arrangements and the factors that govern this [211].

Some groups have taken a particular interest in $Z' > 1$ crystal structures in organic systems, e.g., alcohols and phenols [212], and it has been suggested that dominant hydrogen bonds (in this case chains formed by hydroxyl groups O-H$\cdots$O-H) can play a key role in high Z' formations. The campho[2,3-c]pyrazole system (**7-1**) has also been studied in a variety of contexts (see

---

[1] Z' is defined as the number of formula units divided by the number of general positions

[213]) and, interestingly, the X-ray diffraction crystal structure reveals that it crystallizes into two cyclic trimers (Z'=6) directed by approximately linear NH$\cdots$N hydrogen bonds, while ^{13}C CP MAS solid-state NMR spectra show a well-resolved sixfold multiplicity of resonances for most carbon atoms [214]. This work provides a clear example of the value of NMR as a sensitive probe of local molecular structure in these cases, however, it also highlights the difficulty encountered when assigning the NMR chemical shifts to the many independent molecules of the asymmetric unit. Recently, Yap *et al.* have employed the use of first-principles chemical shifts calculations based on the Gauge Invariant Atomic Orbital (GIAO) method [215] (specifically the GIAO/B3LYP/6-31G(d) developed by Ditchfield [216]), so as to make a tentative assignment of the ^{13}C chemical shifts [213] based on a single 'best fit' approach.

The work presented in this chapter demonstrates that the assignment of solid-state NMR chemical shifts is possible where mutiple resonances are observed due to (Z' > 1) crystallographic splittings, using a *multinuclear* (^{13}C and ^{1}H) approach in combination with ab-initio GIPAW chemical shift calculations. Specifically, through-bond heteronuclear correlation experiments performed at natural isotopic abundance provide *associated* (i.e., ^{13}C and ^{1}H) chemical shift values which can be compared with those calculated using the geometrically optimised X-ray crystal structure for each of the independent molecules to improve the accuracy of the resonance assignment and probe effects of crystallographic packing.

7.2 Experimental Details

7.2.1 Sample Preparation

The (4S,7R)-7,8,8-trimethyl-4,5,6,7-tetrahydro-4,7-methano-2H-indazole enantiomer of campho[2,3-c]pyrazole (**7-1**) was synthesized according to the procedure described in ref[214] in the group of Rosa Claramunt (Madrid, Spain).

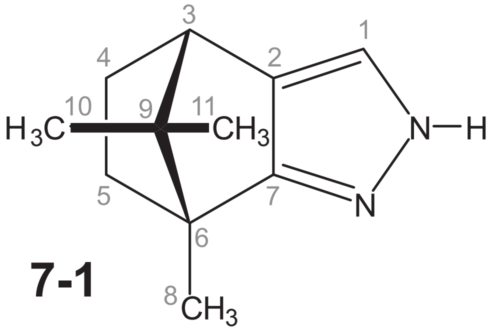

7-1

7.2.2 Solid-State NMR

Spectra were recorded in Lyon by Steven Brown on a Bruker DSX spectrometer, operating at a ^{1}H Larmor frequency of 500 MHz, and using a Bruker 4 mm double-resonance probe. For all ^{13}C detected experiments, the MAS frequency was 12.5 kHz, ^{1}H 90° pulses were of duration 2.5 s, and a 100 - 50% ramped cross polarization pulse was used on the ^{1}H channel. TPPM [19] heteronuclear decoupling of $\nu_1 = 100$ kHz, pulse duration 4.6 µs and phase increment $\Delta\phi = 15°$ was employed throughout a t_2 acquisition time of 40 ms.

^{13}C CP MAS: ^{13}C magnetization was generated by cross polarization for a contact time of 1 ms. 1024 transients were co-added, with a recycle delay of 3 s.

^{1}H-^{13}C MAS-J-HMQC: ^{13}C magnetization was generated by cross polarization for a contact time of 2 ms, ^{13}C 90° pulses were of duration 7.4 µs and evolution periods of $\tau = 2.384$ ms and 0.928 ms were used to maximize the ^{1}H-^{13}C through-bond polarization transfer for CH/CH$_3$ and CH$_2$ sites, respectively. Homonuclear ^{1}H decoupling of $\nu_1 = 100$ kHz was implemented during the J evolution periods and t_1 using the FSLG [27] technique, with cycled blocks of duration 16 µs and magic pulses of 1.52 µs. For each of the 200 t_1 slices (using the States [113] method with an increment of 64 µs), 32 and 112 transients were co-added with recycles delays of 4.5 s and 5.2 s corresponding to total experimental times of 8 h and 32 h, respectively. The scaling factor was 0.61 in F$_1$ for both spectra.

^{1}H DQ-SQ MAS: A Bruker 2.5 mm probe was used at a MAS frequency of 30 kHz. ^{1}H 90° pulses were of duration 2 s and the BABA [117] recoupling sequence of one complete rotor period was used for excitation and reconversion of DQ coherence. The recycle delay was 3 s. For each of the 64 t_1 slices (using the States-TPPI [115] method with a rotor-synchronised increment of 33.3 µs), 16 transients were co-added corresponding to a total experimental time of approximately 50 minutes.

7.2.3 Computational Details

An X-ray diffraction crystal structure of **7-1** was obtained from the crystallographic database (LABHEB [214]) and geometry optimisations were performed using the density functional theory (DFT) code CASTEP. It is well known that crystal structures determined from X-ray diffraction tend to have large errors regarding the positions of the hydrogen atoms, such that an optimization of the H positions, at least, gives better agreement with ^{1}H NMR chemical shifts. In this case, with the heavy atoms fixed during the geometry optimization, large forces were still observed on many of the carbon atoms such that all (348) atoms in the complete unit cell were allowed to relax. Ultrasoft pseuodopotentials with a maximum planewave cutoff of 800 eV were used, along with a Monkhorst-Pack grid with a minimum sample spacing of 0.08 Å^{-1}. All distances stated in this work are for the full geometry optimised crystal structure.

NMR chemical shifts were computed for the 'complete' crystal structure, also using the CASTEP code (and GIPAW approach) with a planewave basis set and maximum cut off energy of 1000 eV. Integrals over the Brillouin zone were performed using a similarly dense Monkhorst-Pack grid. Calculation of the shielding tensors for all nuclei in the full crystal took 27 h on 32 nodes of 3 GHz Intel Xeon 5160 processors (using 125 GB of memory, IBM cluster, University of Warwick). Further calculations were performed for each of the six independent molecules of the asymmetric unit cell in an 'isolated' environment, whereby each complete molecule was extracted from the geometry-optimised structure and placed into a supercell with simple cubic (P1) periodicity. The size of the unit cell was increased until the calculated parameters for the molecule converged (i.e., intermolecular interactions were assumed to be negligible) where the cell dimensions were found to be 10 x

10 x 10 Å. NMR chemical shielding values were then also computed for the three separate instances whereby the isolated structure was (i) not further optimised, (ii) optimised with all atoms allowed to relax, (iii) optimised with only the hydrogen atoms allowed to relax. For each of these cases, all geometry optimizations and NMR shielding calculations used a planewave basis set with a maximum energy of 1000 eV, with integrals taken over the Brillouin zone using a minimum sample spacing 0.05 $Å^{-1}$. Calculations of the shielding tensors for nuclei in the isolated molecules took up to 9 h real time using 8 nodes and 32 GB of memory on the resource noted above.

Absolute shieldings were converted to chemical shifts using Eq. 3.33 such that the mean of the calculated and experimental ^{13}C and ^{1}H chemical shifts of **7-1** coincide; $\sigma_{\mathrm{ref}}(^{13}\mathrm{C})$ = 172.2 ppm, (^{1}H) = 30.7 ppm. However the local agreement of calculated and experiments chemical shifts for each atom of the independent molecules was much better using referencing values which were adjusted for separate atoms of the molecule i.e., such that the mean of the calculated and experimental shifts *for each site* coincide. The individual referencing values used appear in the range $\sigma_{\mathrm{ref}}(^{13}\mathrm{C})$= 166.3 - 173.2 ppm and $\sigma_{\mathrm{ref}}(^{1}\mathrm{H})$= 29.2 - 30.9 ppm and can be found in the captions for Tabs. 7.1- 7.4.

7.3 Results

In the solid state, **7-1** crystallizes with six independent molecules in the asymmetric unit cell by the formation of two cyclamers [214], labelled **A-B-C, D-E-F**, as is shown for the geometrically optimised crystal structure in Fig. 7.1a. The variations in chemical environment of each of these independent molecules gives rise to a distinct multiplicity of resonances in the ^{13}C CP MAS spectrum, as can be seen in Fig. 7.1b. An initial assignment of the ^{13}C spectral regions is made on the basis of previous solid-state NMR work [214]. For certain carbon atoms within the molecule exactly six individually resolved resonances can be distinguished (e.g., an expansion of the C5 region of the spectrum can be seen in the inset of Fig. 7.1b).

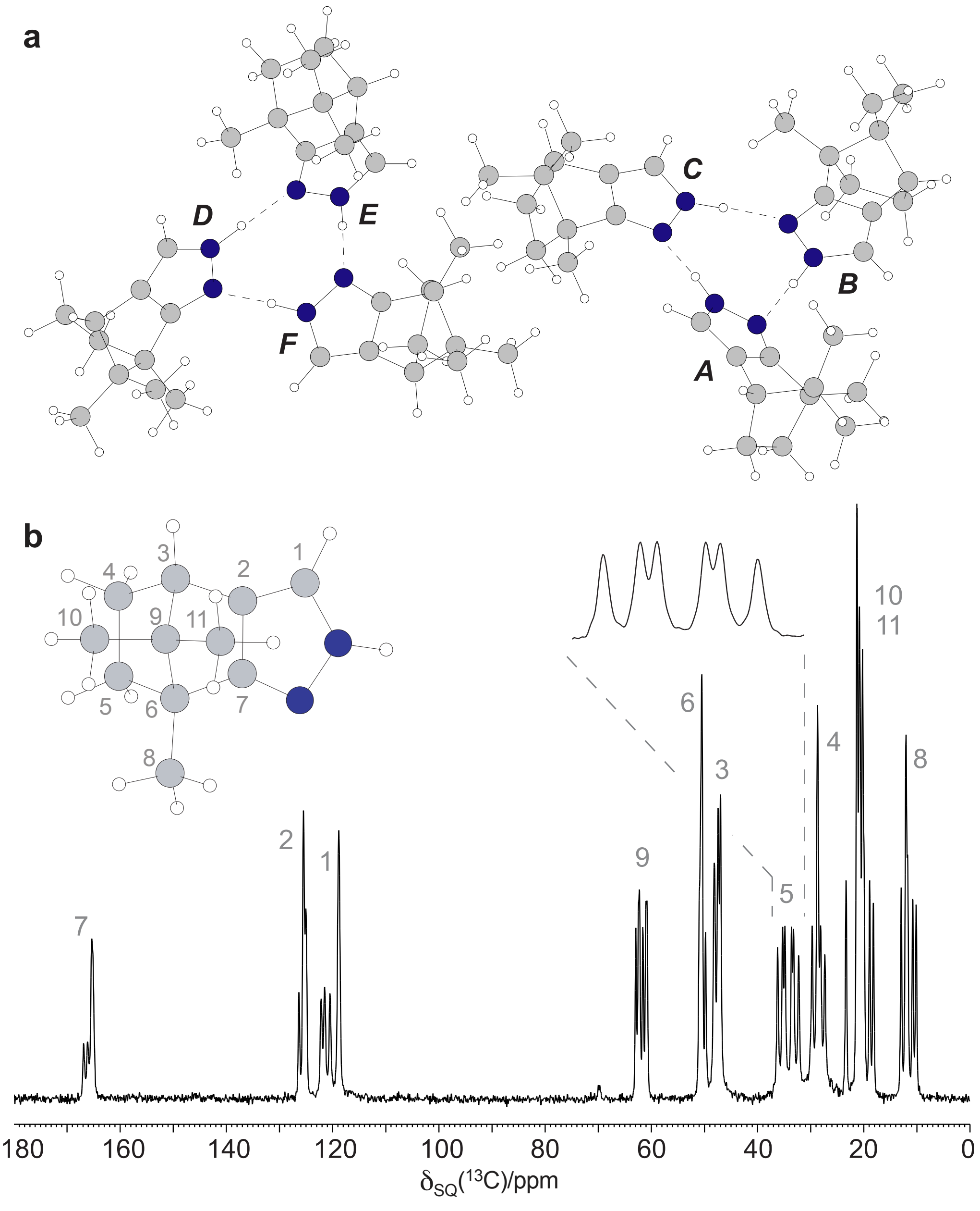

Figure 7.1. (a) Representation of the geometrically optimised crystal structure of **7-1** showing the six independent molecules in the unit cell (Z' = 6) **A-F**. (b) A ^{13}C CP MAS NMR spectrum recorded at a Larmor frequency of 125 MHz and a MAS frequency of 12.5 kHz, with the 11 carbon atoms per molecule labelled according to the schematic molecule shown (inset). A region showing the ^{13}C peaks assigned to the C5 atom is expanded and displayed (inset) showing the six ^{13}C resonances corresponding to this one atomic site.

7.3.1 ^{1}H-^{13}C 2D SQ-SQ Correlation

Fig. 7.2 presents high-resolution ^{1}H-^{13}C correlation spectra of **7-1**, obtained using the MAS-J-HMQC sequence [49] with FSLG [27] homonuclear decoupling applied to achieve high resolution in the indirect (^{1}H) dimension at a MAS frequency of 12.5 kHz. FSLG was also applied throughout the evolution periods where (Fig. 7.2a) $\tau = 2.4$ ms was optimal for the observation of correlation peaks for directly bonded pairs of ^{1}H-^{13}C nuclei of CH or CH_3. More intense correlation peaks for CH_2 sites were observed at the shorter dephasing time of $\tau = 0.9$ ms as shown in Fig. 7.2b.

The areas highlighted in grey in Fig. 7.2 are expanded in Fig. 7.3, corresponding to the chemical shift regions of the protonated carbon atoms. Black crosses are used to indicate the positions of the ^{13}C and ^{1}H chemical shifts calculated for the full geometrically optimised crystallographic structure, as listed in Tabs. 7.1 and 7.2. For each of the carbon atoms shown in (a-d), six two-dimensional peaks are identified i.e., one per independent molecule in the asymmetric unit cell. Resonances originating from C10 and C11 atoms fall within the same ^{13}C chemical shift range (approx. 18-24 ppm) causing many of the twelve carbon signals to overlap, however by correlation with the ^{1}H dimension (Fig. 7.3c), better resolution of the chemical shifts from each of the independent molecules is achieved. For the CH_2 moieties C5 and C4 given in Figs. 7.3e and 7.3f, respectively, two distinct ^{1}H chemical shifts are identified for each of the six independent carbons.

A complete list of ^{1}H and ^{13}C chemical shifts determined from the MAS-J-HMQC spectra presented in Figs. 7.2 and 7.3 can be found in Tab. 7.1 (CH and CH_3) and Tab. 7.2 (CH_2), along with their calculated counterparts as determined by GIPAW chemical shift calculations. As described in §5.3.2 and §6.3, it is commonly observed for the computation of NMR chemical shifts that the slope of experimental vs. calculated values deviates consistently from unity, such that the calculated and experimental chemical shifts are "misaligned" for the distinct chemical sites. To allow clear comparison between experiment and calculation for the six distinct molecules, the calculated values given here have been referenced such that $\sigma_{\text{ref}}(^{13}\text{C})$ and $\sigma_{\text{ref}}(^1\text{H})$ have been separately

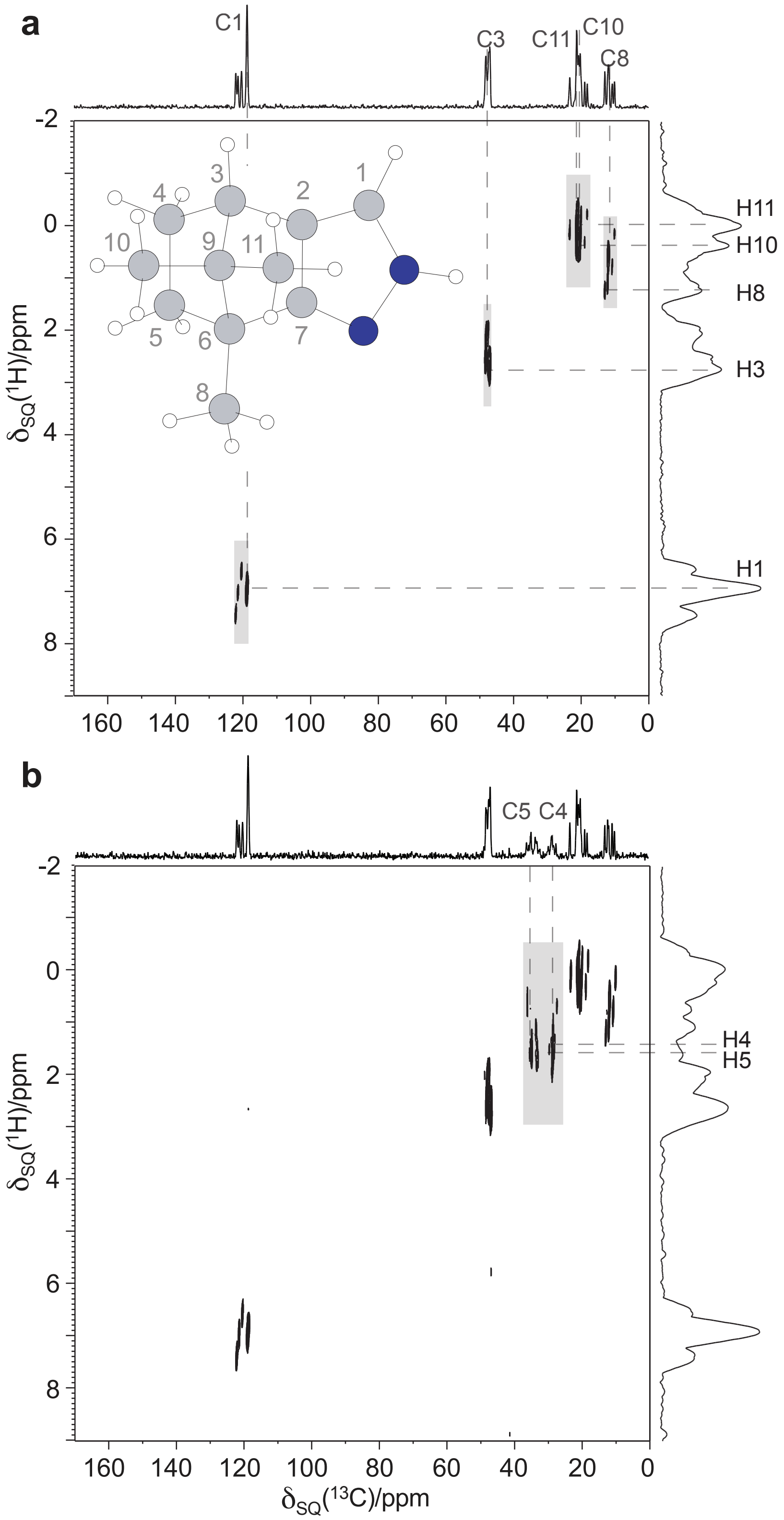

Figure 7.2. ^{1}H-^{13}C MAS-J-HMQC spectra of **7-1** recorded at Larmor frequencies of (^{1}H) 500 MHz and (^{13}C) 125 MHz, 12.5 kHz MAS and using the pulse sequence described in Fig. 3.13b with τ = (a) 2.4 ms or (b) 0.9 ms. The base contour level is at (a) 20% (b) 18% of the maximum peak height in each spectrum and skyline ^{1}H and ^{13}C projections are shown. Through-bond ^{1}H-^{13}C correlations are indicated by dashed lines, labelled according to the scheme shown (see inset). Areas highlighted in grey are shown as expanded regions in Fig. 7.3, where chemical shift correlations of individual resonance peaks are given.

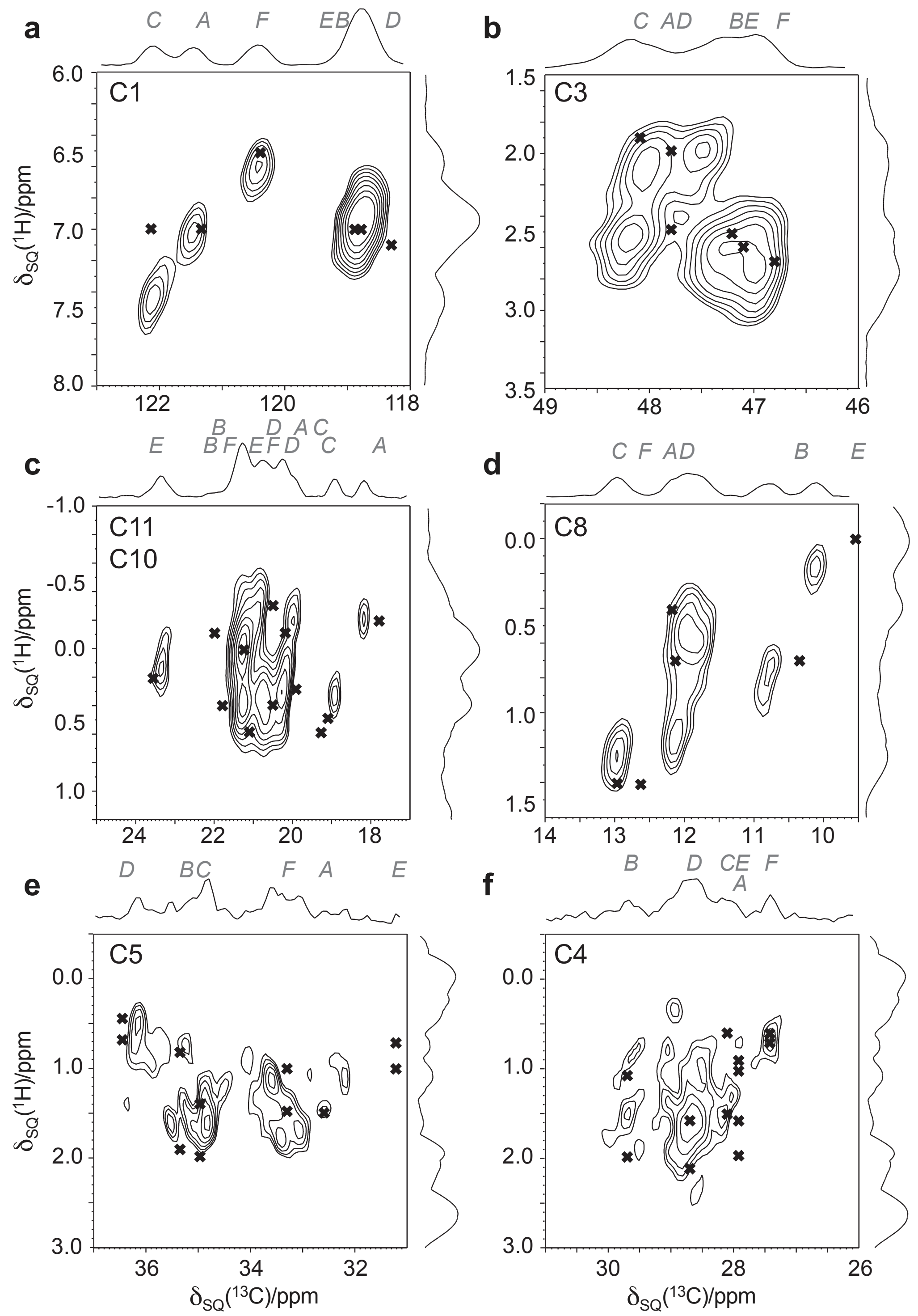

Figure 7.3. Expanded regions of the MAS-*J*-HMQC spectra shown in Fig. 7.2 highlighting the ^{13}C and ^{1}H chemical shifts associated with the protonated carbon atoms of **7-1**. Taken from Fig. 7.2a: CH; (a) C1, (b) C3, CH_3; (c) C11 & C10, (d) C8, taken from Fig. 7.2b: CH_2; (e) C5 and (f) C4. The base contour level is shown at (a-d) 23% or (e-f) 13% of the maximum peak height in each spectrum and skyline ^{1}H and ^{13}C projections are shown. Black crosses indicate the positions of the ^{1}H and ^{13}C chemical shifts calculated using the (complete) geometrically optimised crystal structure of **7-1** (see Fig. 7.1a). **A-F** labels above the ^{13}C skyline projection denote the specific molecule in the asymmetric unit corresponding to the crosses in the 2D spectra below.

determined for each of the individual carbon and proton atoms.

Calculated ^{1}H and ^{13}C chemical shift values for the complete geometrically optimised crystal structure which are referenced individually (values of σ_{ref} can be found in Tabs. 7.1- 7.4) show a good agreement with those determined from the ^{1}H-^{13}C experiment (also shown graphically, later, in Fig. 7.5). Hence this methodology offers a two-fold identification of specific independent molecules, by correlation of pairs of ^{1}H, ^{13}C chemical shifts from the MAS-*J*-HMQC spectra. The ^{1}H chemical shifts as determined from the MAS-*J*-HMQC experiment as shown in Figs. 7.2 and 7.3 benefit from enhanced resolution resulting from the CRAMPS (FSLG decoupling) technique applied, with linewidths of the order of 0.3 ppm/170 Hz (H1), and the correlation peaks on this spectrum are limited to directly bonded CH resonances for such short τ evolution times.

7.3.2 ^{1}H 2D DQ-SQ MAS

For the case of **7-1**, where only one of the proton atoms is not directly bonded to a carbon, it is straightforward to distinguish the NH ^{1}H chemical shift as it is shifted downfield due to intermolecular hydrogen-bonding interactions, such that a ^{1}H experiment carried out at a MAS frequency of 30 kHz is sufficient to resolve the isotropic chemical shift. This is illustrated by the ^{1}H DQ-SQ (fast-MAS) correlation experiment shown in Fig. 7.4a. Solid lines and crosses along the horizontal axis indicate DQ correlation peaks between pairs of protons within close proximity, i.e., less than 3.5 Å apart. These are highlighted, along with H-H distances (in Å) as determined for the geometrically optimised crystal structure, for which one of the two trimers is presented in Fig. 7.4b. The autopeak present at the NH $\delta_{\text{SQ}}(^1\text{H})=$ 13.6 ppm, $\delta_{\text{DQ}}(^1\text{H})=$ 27.2 ppm provides confirmation of the cyclic intermolecular NH$\cdots$N hydrogen bonding geometry, with H-H distances predicted at 2.81 Å, 2.91 Å, 2.99 Å for the CASTEP optimised trimer shown. The calculated NH chemical shifts are compared to the experimental values in Tab. 7.4.

Fig. 7.4a also demonstrates the lower resolution achieved by fast-MAS for the CH protons compared to that achieved by the ^{1}H-^{13}C (CRAMPS) ap-

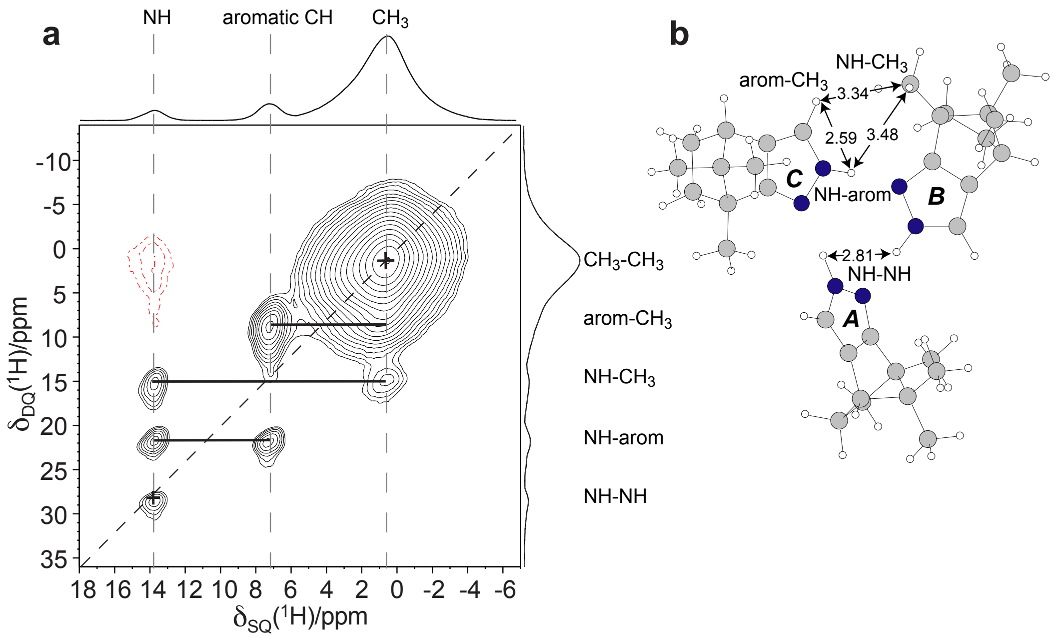

Figure 7.4. (a) ^{1}H (500MHz) DQ MAS spectrum (with skyline projections) of **7-1** recorded at 30 kHz MAS, using the BABA recoupling sequence. The base contour level is at 5% and the $F_1 = 2F_2$ diagonal is shown as a short-dashed line. Solid horizontal bars or crosses indicate specific DQ coherences between pairs of ^{1}H nuclei. (b) Representation of the geometrically optimised (CASTEP) crystal structure [214] showing one of the two trimers, with H-H proximities (given in Å) that give rise to evident DQ peaks in (a). Distances including CH_3 proximities are shown relative to the central carbon atom.

proach, shown in Figs. 7.2 and 7.3. For example, linewidths of the aromatic CH proton H1, (1.5 ppm, 730 Hz) are approximately 5 times broader than those observed under FSLG at a MAS frequency of 12.5 kHz as given above. The large broad peak at $\delta_{SQ}(^1H)<6$ ppm obscures the chemical shift resolution between CH_2 and CH_3 protons, but nevertheless, key proton-proton proximities are identified using the ^{1}H DQ method.

Table 7.1. ^{13}C and ^{1}H chemical shifts of CH and CH_3 atoms of **7-1** as determined from ^{13}C CP MAS and MAS-J-HMQC ($\tau = 2.4$ ms) NMR spectra and first-principles (GIPAW) calculations.

Site	Mol	δ_{iso}(Expt) /ppm		δ_{iso}(Calc)^{a} /ppm							
		^{13}C	^{1}H	^{13}C^{b}	^{13}C^{c}	^{13}C^{d}	^{13}C^{e}	^{1}H^{b}	^{1}H^{c}	^{1}H^{d}	^{1}H^{e}
C1 (H1)	**C**	122.2	7.4	122.2	115.1	115.9	115.4	7.0	6.5	6.6	6.6
	A	121.5	7.0	121.3	115.0	115.7	114.7	7.0	6.5	6.6	6.6
	F	120.5	6.6	120.4	114.8	115.3	114.3	6.5	6.5	6.6	6.6
	E	118.8	6.9	118.9	115.5	115.5	114.7	7.0	6.5	6.6	6.6
	B	118.8	6.9	118.8	115.1	115.6	114.7	7.0	6.6	6.6	6.6
	D	118.8	7.0	118.3	115.3	115.6	115.3	7.1	6.6	6.6	6.6
C3 (H3)	**A**	48.2	2.5	47.8	47.5	47.7	47.7	2.5	2.3	2.3	2.3
	C	48.1	2.1	48.1	47.8	47.9	48.0	1.9	2.3	2.3	2.3
	B	47.4	2.6	47.2	47.5	47.8	47.6	2.5	2.3	2.3	2.3
	D	47.4	1.9	47.8	48.2	47.8	48.1	2.0	2.3	2.3	2.3
	F	46.9	2.7	46.8	47.4	47.7	47.5	2.7	2.1	2.2	2.2
	E	46.9	2.5	47.1	47.2	48.0	47.2	2.6	2.2	2.2	2.2
C11 (H11 a-c)^{f}	**E**	23.4	0.2	23.6	17.6	17.9	17.8	0.2	0.1	0.2	0.1
	B	21.3	0.0	22.0	17.4	18.1	17.7	−0.1	0.4	0.3	0.4
	F	21.3	0.0	21.2	18.3	18.1	18.3	0.0	0.3	0.3	0.4
	A	20.2	0.3	19.9	17.6	17.9	17.9	0.3	0.1	0.2	0.1
	C	20.2	0.3	19.3	16.6	17.4	17.1	0.6	0.2	0.2	0.2
	D	20.0	−0.2	20.2	17.7	18.1	17.8	−0.1	0.4	0.3	0.4
C10 (H10 a-c)^{f}	**B**	21.3	0.4	21.8	17.6	17.6	17.8	0.4	0.6	0.5	0.6
	E	20.9	0.3	21.1	17.2	17.4	17.4	0.6	0.5	0.5	0.5
	D	20.9	−0.3	20.5	17.7	17.6	17.7	−0.3	0.6	0.5	0.5
	F	20.7	0.4	20.5	17.6	17.4	17.7	0.4	0.6	0.6	0.6
	C	18.9	0.3	19.1	17.0	17.4	17.3	0.5	0.5	0.5	0.5
	A	18.2	−0.2	17.8	17.0	17.3	17.5	−0.2	0.5	0.5	0.5

Continued on Next Page…

Table 7.1 – Continued

Site	Mol	δ_{iso}(Expt) /ppm		δ_{iso}(Calc)[a] /ppm							
		^{13}C	^{1}H	^{13}C[b]	^{13}C[c]	^{13}C[d]	^{13}C[e]	^{1}H[b]	^{1}H[c]	^{1}H[d]	^{1}H[e]
C8	**C**	13.0	1.2	13.0	7.5	7.6	7.6	1.4	0.7	0.7	0.7
(H8	**F**	12.1	1.1	12.6	8.0	7.8	7.9	1.4	0.8	0.8	0.8
a-c)[f]	**A**	12.0	0.5	12.2	7.8	7.7	7.7	0.4	0.7	0.7	0.7
	D	11.8	0.6	12.1	7.7	7.6	7.7	0.7	0.8	0.8	0.8
	B	10.8	0.8	10.3	7.3	7.6	7.5	0.7	0.8	0.8	0.8
	E	10.1	0.2	9.5	7.4	7.7	7.6	0.0	0.7	0.7	0.7

[a] Calculated chemical shift references are adjusted for individual atoms: $\sigma_{\mathrm{ref}}(^{13}\mathrm{C})/\mathrm{ppm} =$ 170.0 (C1), 169.3 (C3), 172.9 (C11), 173.2 (C10), 173.2 (C8). $\sigma_{\mathrm{ref}}(^{1}\mathrm{H})/\mathrm{ppm} = 29.9$ (H1), 30.4 (H3), 30.7 (H11a-c), 30.6 (H10a-c), 30.7 (H8a-c).

[b] Full crystal structure, geometrically optimised with all atoms allowed to relax.

[c] Isolated molecule with no further optimization.

[d] Isolated molecule with all atoms allowed to relax.

[e] Isolated molecule with only H atoms allowed to relax.
(All isolated molecules were extracted from the geometrically optimised crystal structure)

[f] Average calculated chemical shift of CH_3 protons.

Table 7.2. ^{1}H and ^{13}C chemical shifts of CH_2 atoms of **7-1** as determined from ^{13}C CP MAS and MAS-J-HMQC ($\tau = 0.9\,\mathrm{ms}$) NMR spectra and first-principles (GIPAW) calculations.

Site	Mol	δ_{iso}(Expt) /ppm		δ_{iso}(Calc)[a] /ppm							
		^{13}C	^{1}H	^{13}C[b]	^{13}C[c]	^{13}C[d]	^{13}C[e]	^{1}H[b]	^{1}H[c]	^{1}H[d]	^{1}H[e]
C5	**D**	36.2	0.5	36.5	33.7	32.8	33.6	0.4	0.5	0.1	−0.1
(H5a,			0.7					0.7	1.1	−0.1	0.0
H5b)	**B**	35.3	0.7	35.3	32.4	32.8	32.5	0.8	0.1	0.1	−0.2
			1.6					1.9	−0.2	0.0	0.0
	C	34.9	1.3	35.0	33.0	33.2	33.2	1.4	−0.4	0.0	0.0
			1.6					2.0	−0.2	0.0	0.0
	F	33.6	1.2	33.3	32.8	32.9	32.8	1.0	0.0	0.0	0.0

Continued on Next Page...

Table 7.2 – Continued

Site	Mol	δ_{iso}(Expt) /ppm		δ_{iso}(Calc)^{a} /ppm							
		^{13}C	^{1}H	^{13}C^{b}	^{13}C^{c}	^{13}C^{d}	^{13}C^{e}	^{1}H^{b}	^{1}H^{c}	^{1}H^{d}	^{1}H^{e}
			1.8					1.5	0.3	0.0	0.0
	A	33.2	1.4	32.5	32.6	32.8	32.8	1.5	−0.4	0.0	0.1
			1.6					1.5	0.4	−0.1	0.0
	E	32.2	0.9	31.2	32.1	33.0	32.3	0.7	0.4	−0.1	0.1
			1.1					1.0	0.9	−0.1	0.0
C4 (H4a, H4b)	**B**	29.7	0.9	29.7	27.4	26.9	27.6	1.1	−0.4	0.1	−0.1
			1.5					2.0	−0.1	−0.1	0.0
	D	28.9	0.4	28.1	26.7	26.9	26.8	0.6	0.2	0.0	−0.1
			1.9					1.5	0.3	0.0	0.0
	C	28.7	1.6	28.7	26.3	26.7	26.5	1.6	−0.7	0.0	0.1
			2.4					2.2	−0.3	0.0	0.0
	E	28.6	0.9	27.9	26.4	27.0	26.6	1.0	0.0	−0.1	0.1
			2.3					2.0	−0.1	0.1	0.0
	A	28.2	1.1	27.9	26.2	26.7	26.5	0.9	0.1	0.0	0.1
			1.5					1.6	0.4	0.0	0.0
	F	27.4	0.6	27.4	26.8	26.8	26.9	0.6	0.3	−0.1	0.1
			0.7					0.7	1.2	0.0	0.0

[a] Calculated chemical shift references adjusted for individual atoms. σ_{ref} (^{13}C)/ppm = 167.9 (C5), 171.6 (C4). σ_{ref}(^{1}H)/ppm = 30.9 (H5a), 30.8 (H5b), 30.8 (H4a), 30.5 (H4b).

[b] Full crystal structure, geometrically optimised with all atoms allowed to relax.

[c] Isolated molecule with no further optimization.

[d] Isolated molecule with all atoms allowed to relax.

[e] Isolated molecule with only H atoms allowed to relax.
(All isolated molecules were extracted from the geometrically optimised crystal structure)

Table 7.3. ^{13}C chemical shifts non-protonated carbon atoms of **7-1** as determined from ^{13}C CP MAS and first-principles (GIPAW) calculations.

Site	Mol	δ_{iso}(Expt) /ppm	δ_{iso}(Calc)^{a} /ppm			
		^{13}C	^{13}C^{b}	^{13}C^{c}	^{13}C^{d}	^{13}C^{e}
C7	**A**	166.9	167.2	166.3	166.3	166.8
	B	166.1	166.2	165.5	166.3	166.0
	E	165.5	165.4	165.7	166.5	166.0
	F	165.3	165.1	165.2	166.2	165.8
	D	165.2	165.0	164.9	166.3	165.3
	C	165.0	164.7	165.5	166.2	165.7
C2	**D**	126.3	126.7	124.4	124.6	124.8
	E	125.6	125.6	124.7	124.9	125.1
	A	125.4	125.5	124.2	124.9	124.7
	F	125.3	125.3	124.3	125.1	124.8
	B	125.0	125.0	123.7	124.6	124.1
	C	124.9	124.7	123.9	124.8	124.5
C9	**E**	62.9	63.2	59.5	59.5	60.0
	F	62.4	62.5	59.7	59.6	59.6
	A	62.2	62.4	59.9	59.8	60.0
	C	61.6	61.5	58.9	58.9	58.8
	D	61.0	60.8	58.1	59.1	58.0
	B	60.8	60.5	57.8	59.1	57.9
C6	**A**	51.0	51.2	49.6	49.6	49.5
	C	50.8	50.4	48.7	49.4	48.8
	B	50.6	50.3	48.9	49.3	48.9
	E	50.4	50.3	49.3	49.5	49.2
	D	49.8	49.6	49.1	49.3	49.1
	F	49.7	49.5	49.5	49.4	49.4

Continued on Next Page...

Table 7.3 – Continued

Site	Mol	δ_{iso}(Expt) /ppm	δ_{iso}(Calc)[a] /ppm			
		^{13}C	^{13}C[b]	^{13}C[c]	^{13}C[d]	^{13}C[e]

[a] Calculated chemical shift references adjusted for individual atoms. $\sigma_{\text{ref}}(^{13}\text{C})$/ppm = 167.8 (C7), 166.5 (C2), 166.3 (C9), 167.9 (C6).

[b] Full crystal structure, geometrically optimised with all atoms allowed to relax.

[c] Isolated molecule with no further optimization.

[d] Isolated molecule with all atoms allowed to relax.

[e] Isolated molecule with only H atoms allowed to relax. (All isolated molecules were extracted from the geometrically optimised crystal structure.)

Table 7.4. ^{1}H chemical shifts of NH atom of **7-1** as determined from ^{1}H DQ MAS NMR and first-principles (GIPAW) calculations.

Site	Mol	δ_{iso}(Expt) /ppm	δ_{iso}(Calc)[a] /ppm			
		^{1}H	^{1}H[b]	^{1}H[c]	^{1}H[d]	^{1}H[e]
NH	**A**	13.6	14.1	8.4	7.8	7.8
	D		13.7	8.5	7.8	7.9
	E		13.6	8.3	7.8	7.8
	C		13.5	8.4	7.8	7.9
	B		13.4	8.4	7.8	7.9
	F		13.3	8.4	7.8	7.8

[a] Calculated values are referenced such that the mean of the experimental and calculated values of the ^{1}H chemical shifts for the NH proton coincide; $\sigma_{\text{ref}}(^1\text{H})$/ppm = 29.2.

[b] Full crystal structure, geometrically optimised with all atoms allowed to relax.

[c] Isolated molecule with no further optimization.

[d] Isolated molecule with all atoms allowed to relax.

[e] Isolated molecule with only H atoms allowed to relax. (All isolated molecules were extracted from the geometrically optimised crystal structure.)

7.3.3 The Effect of Intermolecular Interactions on ^{1}H & ^{13}C Chemical Shifts

Fig. 7.5 demonstrates in graphical form the agreement between experimentally and computationally determined ^{13}C and ^{1}H chemical shifts, with black squares representing the individually referenced calculated values taken from the full crystal structure, and red circles those taken from isolated molecules where all atoms were further allowed to relax. It can be seen that, whereas calculations for the full crystal structure fit well, with black squares lying mostly along the linear diagonal, chemical shifts resulting from the relaxed isolated molecules have little variation in calculated values between the independent molecules. This is particularly prominent for the isolated NH ^{1}H value, as well as the CH_2 values signified by the horizontal clusters of red circles around 0-3 ppm.

A comparison of the different calculated chemical shift values in Fig. 7.5 and Tabs. 7.1- 7.4 highlights the sensitivity of the NMR chemical shift, in particular, to (i) intermolecular interactions and crystalline packing and (ii) molecular geometry. The most significant difference between the ^{1}H and ^{13}C calculated chemical shifts for all atoms is between those of the complete crystal structure, and those of the independent molecules being placed individually into a supercell (where the nearest equivalent molecule is 10 Å away) where chemical shifts are recalculated with no further optimization. This chemical shift difference acts as quantitive measure of the effect of nearby molecules and intermolecular interactions on each independent molecule. For ^{13}C nuclei, the largest average differences between these values are observed (compare columns with ‘b’ and ‘c’ footnotes in Tab. 7.1) for the CH (C1; average $\Delta\delta_{\text{iso}}^{\text{cryst-mol}}(^{13}\text{C})$=4.9 ppm) and for the CH_3 atoms (C8, C10, C11; average $\Delta\delta_{\text{iso}}^{\text{cryst-mol}}(^{13}\text{C})$=3.4 ppm) on the extremeties of the molecule, although when considered as a fraction of the observed ^{13}C chemical shift range, these differences are less than 3%.

The difference in ^{1}H chemical shift between these two calculated quantities, is much more significant for the NH proton (average $\Delta\delta_{\text{iso}}^{\text{cryst-mol}}(^1\text{H})$= 5.2 ppm, see Tab. 7.4), where the experimental ^{1}H chemical shift range is ap-

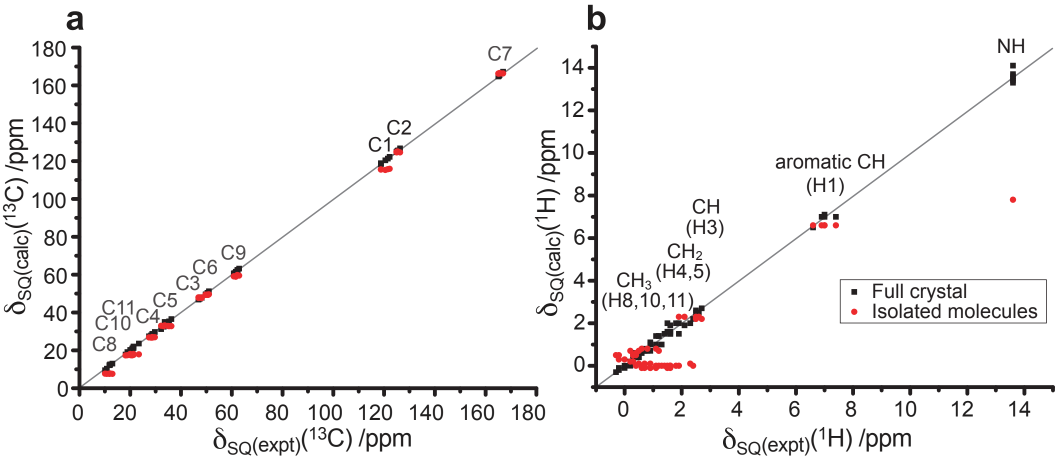

Figure 7.5. A graphical comparison of the experimental and calculated (a) ^{13}C (b) ^{1}H chemical shifts of **7-1**. Black squares and red circles correspond to the chemical shifts calculated for the complete (geometrically optimised) crystal structure of **7-1** and the those of the isolated independent molecules (after a further geometry optimization where all atoms were allowed to relax), respectively, where individual shift references (σ_{ref}) are used (see Tabs. 7.1- 7.4).

proximately 20 ppm. This is a direct consequence of the NH$\cdots$N hydrogen bonds stabilizing the cyclamers of the complete (geometrically optimised) crystal structure where (N)H$\cdots$N distances are, on average, 1.81 Å with close to linear angles (174°-179°). The effect of hydrogen bonding on ^{1}H chemical shifts is well documented [38] and previous work by Schmidt *et al.* and Uldry *et al.* has presented a similar result for $\Delta\delta_{\text{iso}}^{\text{cryst-mol}}(^{1}\text{H})\approx 5$ ppm for NH$\cdots$O hydrogen bonds in L-histidine·HCl [100] and uracil [3] along with the weaker effect of CH…O hydrogen bonds $\Delta\delta_{\text{iso}}^{\text{cryst-mol}}(^{1}\text{H})\approx 2$ ppm in uracil [3] and β-maltose monohydrate [80].

Table 7.5. Spread of experimental and calculated ^{13}C, ^{1}H chemical shifts for **7-1** as determined from ^{13}C CP MAS, ^{1}H-^{13}C MAS-J-HMQC and ^{1}H DQ MAS NMR and first-principles (GIPAW) calculations.

Site	$\Delta_{\text{A-F}}\delta_{\text{iso}}$(Expt) /ppm		$\Delta_{\text{A-F}}\delta_{\text{iso}}(\text{Calc})^{\text{a}}$ /ppm							
	^{13}C	^{1}H	^{13}C$^{\text{b}}$	^{13}C$^{\text{c}}$	^{13}C$^{\text{d}}$	^{13}C$^{\text{e}}$	^{1}H$^{\text{b}}$	^{1}H$^{\text{c}}$	^{1}H$^{\text{d}}$	^{1}H$^{\text{e}}$
C1, H1	3.4	0.8	3.9	0.7	0.6	1.1	0.6	0.1	0.0	0.0
C3, H3	1.3	0.8	1.3	1.0	0.3	0.9	0.8	0.2	0.1	0.1
C11, H11a-c	3.4	0.5	4.3	1.7	0.7	1.2	0.7	0.3	0.1	0.3

Continued on Next Page…

Table 7.5 – Continued

Site	$\Delta_{\text{A-F}}\delta_{\text{iso}}$(Expt) /ppm		$\Delta_{\text{A-F}}\delta_{\text{iso}}$(Calc)[a] /ppm							
	^{13}C	^{1}H	^{13}C^{b}	^{13}C^{c}	^{13}C^{d}	^{13}C^{e}	^{1}H^{b}	^{1}H^{c}	^{1}H^{d}	^{1}H^{e}
C10, H10a-c	3.1	0.7	4.0	0.6	0.3	0.5	0.9	0.1	0.1	0.1
C8, H8a-c	2.9	1.0	3.5	0.7	0.2	0.4	1.4	0.1	0.1	0.1
C5, H5a,b	4.0	0.8	5.3	1.6	0.4	1.3	1.1	0.9	0.2	0.3
		1.1					1.3	1.3	0.1	0.0
C4, H4,b	2.3	1.2	2.3	1.2	0.3	1.1	1.0	1.0	0.2	0.2
		1.7					1.5	1.5	0.2	0.0
C7	1.9		2.5	1.4	0.3	1.5				
C2	1.4		2.0	1.0	0.5	1.0				
C9	2.1		2.7	2.1	0.9	2.1				
C6	1.3		1.7	0.9	0.3	0.7				
NH		0.0[f]					0.8	0.2	0.0	0.1

[a] Calculated chemical shift references adjusted for individual atoms: σ_{ref} values are given in captions to Tabs. 7.1- 7.4.

[b] Full crystal structure, geometrically optimised with all atoms allowed to relax.

[c] Isolated molecule with no further optimization.

[d] Isolated molecule with all atoms allowed to relax.

[e] Isolated molecule with only H atoms allowed to relax.
(All isolated molecules were extracted from the geometrically optimised crystal structure)

[f] Only one value of $\delta_{\text{iso}}(^{1}\text{H})$ is resolved for this site (see Fig. 7.4).

The sensitivity of the ^{1}H chemical shift to such small variations in chemical environment means that it can provide further insight into molecular geometry as well as intermolecular effects. Tab. 7.5 shows the range of chemical shifts observed across the six independent molecules ($\Delta_{\text{A-F}}\delta_{\text{iso}}$) as determined by experiment and calculation. Clearly, for the majority of ^{13}C and ^{1}H sites, the largest calculated chemical shift ranges are observed for the full crystal structure (see columns marked footnote 'b') calculations, and show good agreement with the ranges observed experimentally. As the molecules are placed into 'isolated' environments (without further geometrical optimization) the ranges of calculated values drops sharply (see columns; footnote 'c' compared to ‘b’), for the CH and CH_3 sites in particular. Interestingly, this is not the case for ^{1}H ranges of the CH_2 sites.

As expected, when the isolated molecules are relaxed (columns ‘d’ and ‘e’), and thus the geometries of molecules **A-F** become more alike, the differences in calculated chemical shifts are minimized. For ^{13}C, the difference in $\Delta_{\text{A-F}}\delta_{\text{iso}}$ values is small when only H atoms are allowed to move i.e., columns ‘c’ and ‘e’ are compared with, as expected, a more marked difference being observed when C atoms are also relaxed (i.e., ‘c’ compared to ‘d’). For ^{1}H values, $\Delta_{\text{A-F}}\delta_{\text{iso}}$ of relaxed isolated molecules (H atoms are relaxed in both ‘d’ and ‘e’) is very small at $\approx 0.0-0.2$ ppm for most ^{1}H resonances. This is in agreement with the observations made in ref[3], where the change in ^{1}H chemical shifts between isolated molecules with and without relaxation of atoms shows a direct relation to the N-H and C-H bond lengths within the molecule. For **7-1**, the N-H bond lengths are 1.046 to 1.050 Å in the full geometrically optimised crystal structure, while all bond lengths are the same (1.013 Å within ± 0.0005 Å and 1.014 Å within ± 0.0003 Å) after optimization of atomic positions (for H only, and all atom positions, respectively) for the 6 extracted isolated molecules.

7.4 Summary and Outlook

The assignment of solid-state NMR resonances for systems with multiple molecules in the asymmetric unit cell is often far from trivial. This chapter has presented a high-resolution, multinuclear (^{1}H-^{13}C) NMR approach for one such system where Z'=6, which allows better identification and assignment of crystallographically split ^{13}C peaks when applied in combination with first-principles (GIPAW) chemical shift calculations. Unlike experimental information from only one nuclear species, the additional C-H bonding constraint provided by the use of the MAS-J-HMQC experiment aids the assignment of each of the (Z'= 6) independent molecules of the campho[2,3-c]pyrazole system.

An alternative, commonly used approach in the context of ^{13}C assignment is the refocused INADEQUATE [157] correlation experiment which can explicitly determine ^{13}C backbone connectivities of molecules, provided that sufficient resolution of overlapped resonances (Z'$>$ 1) is possible. However, as discussed in §4.4, this experiment will take considerably longer experimental times (5 days in [85]) to sufficiently observe correlation peaks due to the statistical likelihood of pairs of bonded ^{13}C-^{13}C nuclei at natural abundance (1 in 10,000).

This study has shown the importance of considering computed chemical shifts for the *complete* unit cell (348 atoms, here) as opposed to isolated molecules, for an accurate resonance assignment of multiple independent molecules. ^{1}H chemical shifts are particularly sensitive to crystallographic packing arrangements and intermolecular interactions as well as differences in geometry between the distinct molecules. While such calculations are inherently more computationally demanding, much insight is to be gained from complete unit cell calculations, and also from the differences in calculated chemical shift values when compared to those computed for isolated molecules. Establishing the factors that direct crystalline packing, and also cause materials to order with multiple, distinct molecules in the asymmetric unit is particularly relevant for the understanding of solids and of much interest in crystal engineering [217].

8

Measuring J Couplings Across Intermolecular $^{15}N^{1}H\cdots{}^{17}O$ & $^{13}C^{1}H\cdots{}^{15}N$ Hydrogen Bonds

8.1 Probing Hydrogen Bonding Interactions

Hydrogen bonds play a major role in directing the assembly of organic molecules into large supramolecular structures, and as such are a key theme throughout this thesis. These donor-acceptor interactions are most commonly encountered between covalently bonded NH or OH sites with other N or O sites, with $NH\cdots O$ bonds being a prominently observed interaction in biological chemistry e.g., Watson-Crick base pairing of DNA or in protein structures. When studied by X-ray diffraction techniques, hydrogen-bonded sites are well characterised by close proximities (i.e., $H\cdots N$, $H\cdots O$ distances $< 2.2\,\text{Å}$) and near linear arrangements of atoms.

Over recent years, there has been an increasing discussion of 'weak' hydrogen bonds also forming between less electronegative atoms, such as the CH donor in $CH\cdots O$ or $CH\cdots N$ interactions [218, 219]. Observations of such close proximities in many crystal structures have shown longer distances (i.e., $H\cdots N$, $H\cdots O < 3.0\,\text{Å}$) and wider distributions of angles (90-180°) in these cases. It has been debated as to whether such three-dimensional arrangements are indeed structure directing, or are simply secondary consequences of other stronger intermolecular interactions which are also present in the material [220].

Solid-state NMR parameters are particularly sensitive to the effects of chemical bonding, thus this technique has much to offer the study of hydrogen-bonded systems in organic solids. In particular the proton chemical shift provides direct insight into hydrogen-bonded moieties in organic molecules (see chapters 5-7) and many combined experimental and computational studies have investigated the effect of intermolecular interactions on the ^{1}H (and ^{13}C) chemical shifts [5, 58, 100, 146, 221–223]. For example, a comparison of the ^{1}H chemical shifts of isolated molecules and the full crystal structure (i.e., without and with intermolecular interactions) provides quantitative information regarding the hydrogen-bonding interactions present [3, 100] (see also chapter 7). Observations of similar (smaller) ^{1}H chemical shifts changes in CH$\cdots$O and CH$\cdots$N systems has also further solidified the evidence for the existence of 'weak' hydrogen-bonding interactions [3, 80].

Recently, building upon solution-state NMR observations [224, 225], it has been shown that solid-state NMR is able to directly detect the presence of scalar couplings across (strong) hydrogen bonds by the excitation of through-bond double-quantum coherence (as observed using the solid-state INADEQUATE [226] and refocused INADEQUATE [157] experiments [205, 227]). Furthermore, a simple homonuclear spin-echo ($\tau/2 - \pi - \tau/2$) sequence allows the size of the J coupling constants across intermolecular NH$\cdots$N hydrogen bonds to be determined quantitatively [101, 102]. In combination with this, the CASTEP DFT code has recently been adapted to compute the scalar J couplings between pairs of atoms using a similar approach to the GIPAW method for calculating chemical shifts, with good agreement being observed between experimentally and computationally determined J values [147]. Specifically, CASTEP calculations have been shown to provide excellent accuracy for hydrogen-bond mediated $^{2h}J_{\mathrm{NN}}$ couplings determined experimentally using ^{15}N spin-echo MAS experiments [81].

Prior to ref[2], however, there had been no such investigation into NH$\cdots$O hydrogen-bond-mediated J couplings ($^{2h}J_{\mathrm{NO}}$) by solid state NMR, despite the biological relevance of these interactions. The NMR active nucleus ^{17}O possesses $I = {}^5\!/_2$ and thus an electric quadrupole moment ($Q = -2.6 \times 10^{-30}\,\mathrm{m}^2$), moreover it has a low sensitivity due to its very low natural abundance (0.0037%) and low resonance frequency ($\gamma = -3.628 \times 10^7\,\mathrm{rad\,T^{-1}\,s^{-1}}$). However, with the commercial availability of ^{17}O enriched water, and advances in sensitivity enhancement and high-resolution sequences for quadrupolar nuclei, ^{17}O solid-state NMR is being increasingly used in the study of biological (as well as inorganic [228]) materials [229]. Whereas a small number of ^{17}O heteronuclear experiments have been presented (see refs in [2]), no ^{15}N-^{17}O experiments appear in the literature (prior to ref[2]) as the proximate Larmor frequencies of these nuclei, in combination with their low sensitivity, present significant challenges for solid-state NMR.

This chapter presents (^{17}O/^{15}N and ^{15}N/^{17}O) heteronuclear spin-echo experiments applied to isotopically labelled [^{15}N$_2$, ^{17}O$_2$]uracil for the determination of $^{2h}J_{\mathrm{NO)}}$ couplings across intermolecular NH$\cdots$O hydrogen bonds. This work has recently been published along with similar ^{17}O and ^{17}O/^{13}C investigations of [^{2}H(NH$_3$), 1-^{13}C, ^{15}N, ^{17}O$_2$]glycine$\cdot^2$HCl and dipolar coupling measurements in the two systems [2]. A similar methodology is also applied for the direct measurement of $^{2h}J_{\mathrm{NC}}$ and $^{3h}J_{\mathrm{NC}}$ values across CH$\cdots$N hydrogen bonds in [^{15}N, ^{13}C$_2$]4-cyano-4'-ethynylbiphenyl.

8.2 Experimental Details

8.2.1 Sample Preparation

[^{15}N$_2$, ^{17}O$_2$]uracil (**8-1**) was synthesized by Ivan Hung (Warwick) using [1,3-^{15}N]uracil (Sigma-Aldrich, UK) and enriching with [70%-^{17}O]H$_2$O according to the literature protocol [230, 231] (see also [2]). [^{15}N, ^{13}C$_2$]4-cyano-4'-ethynylbiphenyl (**8-2**) was synthesized in the group of Rosa Claramunt (Madrid, Spain) using the three-step procedure described in ref[3].

8-1

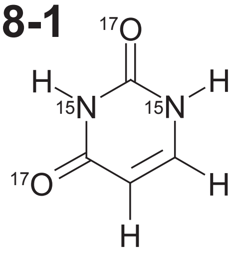

8-2

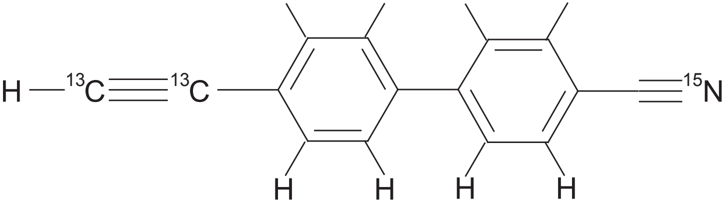

8.2.2 Solid-State NMR

Experiments on **8-1** were performed using a Bruker Avance II+ NMR spectrometer, operating at ^{1}H , ^{15}N and ^{17}O Larmor frequencies of 600, 61 and 81 MHz, respectively, using a Bruker 3.2 mm triple-resonance MAS probe spinning at 20 kHz. This study was carried out in cooperation with Ivan Hung and Johanna Becker-Baldus at the University of Warwick.

^{17}O/^{15}N and ^{15}N/^{17}O heteronuclear spin-echo experiments were performed using the pulse sequences given in Fig. 3.12a and Fig. 3.12b, respectively. 'Central-transition selective' $\pi/2$-pulses of 5.0 µs were used for ^{17}O, corresponding to $\nu_1 = 16.7$ kHz (i.e., taking into account the scaling by $(I + {}^{1}\!/_{2})^{-1}$) and $\pi/2$-pulses of 5.0 µs were used for ^{15}N, corresponding to $\nu_1 = 50$ kHz. For the ^{15}N detected experiment, ^{15}N magnetization was generated by cross polarization with a ramp of 80 to 100 % on the ^{1}H channel for a contact time of 1 ms. SPINAL-64 heteronuclear decoupling [20] with $\nu_1(^{1}\text{H}) = 100$ kHz and pulse duration 4.85 µs was employed throughout a t_2 acquisition time of (^{15}N/^{17}O) 15 ms or (^{17}O/^{15}N) 5 ms. ^{17}O and ^{15}N homonuclear spin-echo experiments were performed by omitting the π pulse on the non-observe (i.e., ^{15}N and ^{17}O, respectively) channel. In total, 1152 and 256 transients were coadded for each τ increment for ^{17}O/^{15}N and ^{15}N/^{17}O experiments, respectively, and a recycle delay of 7.5 s was used to minimize the duty cycle of the NMR probe.

Experiments on **8-2** were performed using a Bruker Avance III NMR spectrometer, operating at ^{1}H , ^{15}N and ^{13}C Larmor frequencies of 500, 50 and 125 MHz, respectively, using a Bruker 3.2 mm triple-resonance MAS probe spinning at 10 kHz. ^{13}C CP MAS: ^{13}C magnetization was generated by cross polarization with a ramp of 90 to 100 % on the ^{1}H channel for a contact time of 1 ms. SPINAL-64 heteronuclear decoupling of $\nu_1 = 100$ kHz and pulse duration 4.6 µs was employed throughout a t_2 acquisition time of 10 ms. 8 transients were co-added, with a recycle delay of 48 s. In all experiments, ^{1}H 90° pulses were of duration 2.5 µs.

^{15}N/^{13}C heteronuclear spin-echo experiments were performed using the pulse sequence given in Fig. 3.12b. ^{15}N magnetization was generated by cross polarization with a ramp of 40 to 60 % on the ^{1}H channel for a contact time of 5 ms and π-pulses of 10.0 µs and 8.0 µs were used (corresponding to $\nu_1 = 50$ kHz and $\nu_1 = 62.5$ kHz) for ^{15}N and ^{13}C, respectively. SPINAL-64 heteronuclear decoupling [20] with $\nu_1(^1\mathrm{H}) = 100$ kHz and pulse duration 4.9 µs was employed throughout a t_2 acquisition time of 10 ms. ^{15}N homonuclear spin-echo experiments were performed by omitting the π pulse on the non-observe (i.e., ^{13}C) channel. In total, 768 transients were coadded for each τ increment and a recycle delay of 16 s was used.

For all spin-echo experiments, the $\tau/2$ evolution periods were set equal to integer multiples of the rotor period, τ_r. Where data corresponding to the quotient $S_\mathrm{Q}(\tau) = S_\mathrm{HET}(\tau)/S_\mathrm{HOM}(\tau)$ are presented, the homonuclear and heteronuclear spin-echo spectra were recorded consecutively for each evolution interval. $S_\mathrm{HET}(\tau)$ and $S_\mathrm{HOM}(\tau)$ integrals were taken over the respective resolved peaks after Fourier transformation with respect to t_2. Errors in $S_\mathrm{Q}(\tau)$ were determined using

$$\frac{\Delta S_\mathrm{Q}}{S_\mathrm{Q}} = \sqrt{\left(\frac{\Delta S_\mathrm{HET}}{S_\mathrm{HET}}\right)^2 + \left(\frac{\Delta S_\mathrm{HOM}}{S_\mathrm{HOM}}\right)^2} \tag{8.1}$$

where ΔS_HET and ΔS_HOM were the errors determined for the integrated intensities of the peak regions, based on the signal-to-noise ratio observed at $\tau = 0$ for the heteronuclear and homonuclear experiments, respectively. Fitting of parameters was performed using MATLAB routines provided by Paul Hodgkinson, with errors on these parameters as well as the correlation coefficients determined using the covariance method as described in detail in ref.[102].

8.2.3 Computational Details

J-coupling calculations were carried out by Anne-Christine Uldry (St. Andrews, U.K. & Lausanne, Switzerland) on geometrically optimised crystal structures (URACIL [232] and JOQSEN [233] taken from the Cambridge crystal structure database [137]) for which details have previously been described [3]. A plane-wave cutoff of 1100 eV or 800 eVand a k-point sampling grid density of 0.08 (**8-1**) or 0.07 (**8-2**) Å^{-1} was used. The J couplings are computed by considering one nucleus as a perturbation, and it is therefore necessary to

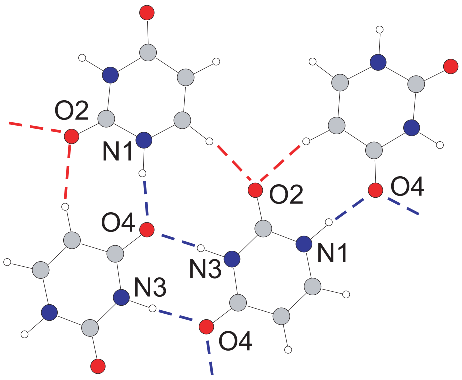

Figure 8.1. Representations of the geometrically optimised crystal structure of **8-1** showing the NH$\cdots$O and CH$\cdots$O hydrogen bonding arrangements, indicated by the blue and red dashed lines, respectively.

multiply the size of the original crystal unit cell until the values of the couplings are converged. A 2 x 2 x 2 supercell (384 atoms) and 1 x 1 x 1 (200 atoms) were found to be sufficient for the J couplings to be well converged (within 0.1 Hz) for **8-1** and **8-2**, respectively. For uracil, the calculation time for the J couplings varied between 27 and 41 h on 24 nodes of the AMD Opteron cluster at St. Andrews University, depending on the perturbing nucleus. Calculations on 4-cyano-4'-ethynylbiphenyl took less than 6 h on 12 nodes of the SGI Altix cluster at the University of Warwick.

8.3 Results

8.3.1 ^{15}N^{1}H$\cdots$^{17}O Hydrogen Bonding in Uracil

Fig. 8.1 illustrates the arrangement of uracil molecules in the geometrically optimised (CASTEP) crystal structure of **8-1**. O4 takes part in NH$\cdots$O hydrogen-bonding with *both* N1(H) and N3(H) sites (with O-N distances of 2.83 Å and 2.84 Å, respectively), whereas O2 forms weak CH$\cdots$O hydrogen bonds, as discussed in ref[3].

One-dimensional ^{17}O and ^{1}H-^{15}N CP MAS spin-echo (see pulse sequences in Fig. 3.12) spectra of [$^{15}N_2$, $^{17}O_2$]uracil are presented in Fig 8.2a and Fig 8.2b, respectively, recorded using $\tau = 0$. The ^{15}N CP MAS spectrum (Fig. 8.2b) shows two resonances at -244.2 and -222.2 ppm which are assigned to the N1 and N3 sites, respectively [3]. The two oxygen sites of **8-1** cannot

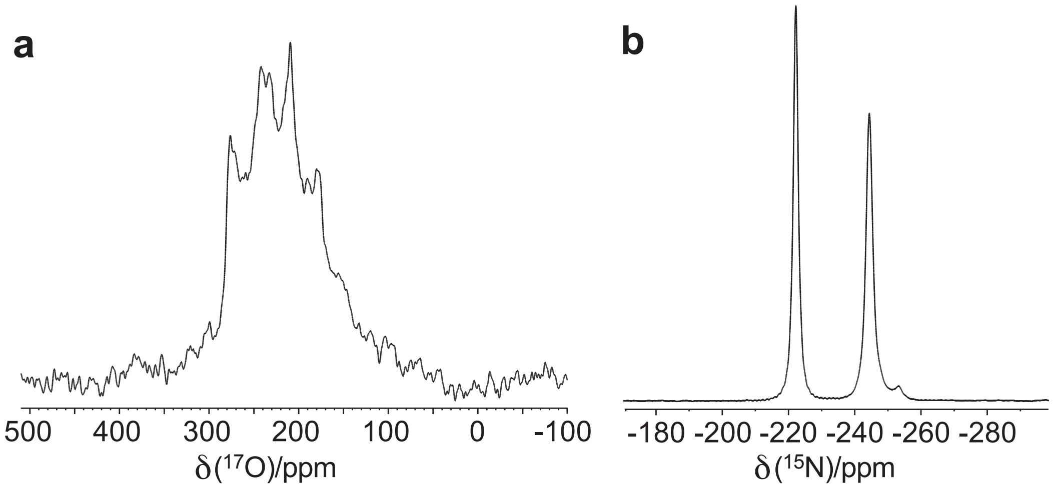

Figure 8.2. (a) Homonuclear ^{17}O and (b) ^{1}H-^{15}N spin-echo spectra obtained for $\tau = 0$ for **8-1** at ^{1}H , ^{17}O and ^{15}N Larmor frequencies of 600, 81 and 61 MHz and 20 kHz MAS. The noise level is calculated as (a) 4 % and (b) 0.08 %.

be resolved at the field strength (14.1 T) shown in Fig 8.2a, primarily, due to the similar chemical shift values and quadrupolar parameters of O2 and O4 (which have previously been determined by ^{17}O MQMAS studies [230]), thus a single, broad lineshape is observed at approximately 230 ppm. Due to this overlap of the two ^{17}O resonances, for which only the O4 site takes part in NH$\cdots$O intermolecular hydrogen bonding to the N1 and N3 atoms, the spin-echo analysis must take into account the contribution from ^{17}O nuclei *with* and *without* hydrogen-bond mediated $^{2h}J_{\mathrm{NO}}$ couplings. The quantity p is defined, therefore, as the fraction of ^{17}O for which an O-N J coupling exists.

Homonuclear ^{17}O (open diamonds) and heteronuclear ^{17}O/^{15}N (filled diamonds) spin-echo ($\tau/2 - \pi - \tau/2$) intensities as a function of the evolution time τ are presented for **8-1** in Fig. 8.3a, obtained using the pulse sequence in Fig. 3.12a (without and with the ^{15}N π pulse). This pulse sequence has also been used to determine J couplings between ^{27}Al-^{31}P [234, 235] and ^{71}Ga-^{31}P [236] spin pairs. Best fits (see Tab. 8.1) are shown as solid lines for the homonuclear spin-echo data fit to the simple decaying exponential function of Eq. 8.2, and the heteronuclear spin-echo data (for J_1 set equal to J_2, and T'_{2a} set equal to T'_{2b}) fit to Eq. 8.3

$$S(\tau) = A \exp(-\tau/T'_{2a}) \tag{8.2}$$

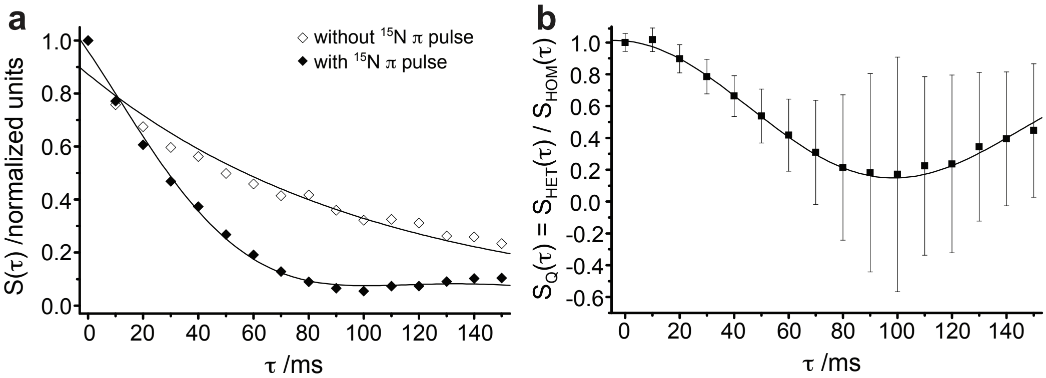

Figure 8.3. (a) ^{17}O homonuclear (open diamonds) and ^{17}O/^{15}N heteronuclear (filled diamonds) spin-echo ($\tau/2 - \pi - \tau/2$) intensities for **8-1** as a function of the evolution time together with best-fits to Eqs. 8.2 and 8.3, respectively (solid lines, see Tab. 8.1). Experiments were carried out at 14.1 T ($\omega_0(^1\mathrm{H}) =$ 600 MHz) and a MAS frequency of 20.0 kHz. The error bars for the experimental intensities were determined to be ±0.04 and are omitted for clarity. (b) The quotient $S_\mathrm{Q}(\tau) = S_\mathrm{HET}(\tau)/S_\mathrm{HOM}(\tau)$ for **8-1** together with the best-fit to Eq. 8.4 (solid line, see Tab. 8.1). $S_\mathrm{Q}(\tau)$ has been normalized such that $S_\mathrm{Q}(\tau = 0) = 1.00$: experimentally the ratio of the integrated intensities $S_\mathrm{HET}(\tau = 0)/S_\mathrm{HOM}(\tau = 0)$ equalled 1.02.

$$S(\tau) = A[p\cos(\pi J_1\tau)\cos(\pi J_2\tau)\exp(-\tau/T'_{2a}) + (1-p)\exp(-\tau/T'_{2b})] \qquad (8.3)$$

Fig. 8.3b shows the quotient $S_\mathrm{Q}(\tau) = S_\mathrm{HET}(\tau)/S_\mathrm{HOM}(\tau)$, where $S_\mathrm{HET}(\tau)$ and $S_\mathrm{HOM}(\tau)$ refer to the ^{17}O/^{15}N heteronuclear and ^{17}O homonuclear spin-echo data presented in Fig. 8.3a. $S_\mathrm{Q}(\tau)$ is given as

$$S_\mathrm{Q}(\tau) = A[p\cos(\pi J_1\tau)\cos(\pi J_2\tau)\exp(-\tau/\Delta T'_2) + (1-p)] \qquad (8.4)$$

where

$$1/\Delta T'_2 = (1/T'_{2(\mathrm{HET})}) - (1/\Delta T'_{2(\mathrm{HOM})}) \qquad (8.5)$$

A good fit (for J_1 set equal to J_2, see Tab. 8.1) to Eq. 8.4 is observed in Fig. 8.3b. The $^{2h}J_\mathrm{NO}$ couplings as determined from the fits of $S_\mathrm{HET}(\tau)$ and $S_\mathrm{Q}(\tau)$, namely 5.8 ± 0.6 and 5.1± 0.6 Hz, respectively, are in agreement with each other. Smaller correlation coefficients involving J are found for the fit of $S_\mathrm{Q}(\tau)$, although those for $S_\mathrm{HET}(\tau)$ are still reasonable ($J, p = 0.52$; $J, T'_{2a} = -0.41$; $J, A = 0.37$ for $S_\mathrm{HET}(\tau)$ and $J, p = -0.25$; $J, T'_{2a} = -0.01$; $J, A = 0.15$ for $S_\mathrm{Q}(\tau)$). The experimental average $^{2h}J_\mathrm{NO}$ couplings are in good agreement with those determined by a CASTEP [147] calculation (see §8.2.3 and ref[2]), namely $^{2h}J_\mathrm{N1,O4} = 6.1$ and $^{2h}J_\mathrm{N3,O4} = 4.6$ Hz. As shown in the

Table 8.1. Parameters extracted from the fits of the ^{17}O and ^{17}O/^{15}N spin-echo ($\tau/2 - \pi - \tau/2$) intensities for **8-1** in Fig. 8.3

Data Set	A	T'_{2a} /ms	p^{a}	$^{2h}J_{\mathrm{NO}}{}^{\mathrm{b}}$/Hz	$[\epsilon^2]^{\mathrm{c}}$
$S_{\mathrm{HOM}}{}^{\mathrm{de}}$	0.87±0.03	102±7			0.0075
$S_{\mathrm{HET}}{}^{\mathrm{ef}}$	0.96±0.04	62^{g}±10	0.66±0.14	5.8±0.6	0.0026
$S_{\mathrm{Q}}{}^{\mathrm{eh}}$	1.01±0.05	550^{i}±1479	0.85±0.20	5.1±0.6	0.0019

[a] The relatve contribution of O4 ^{17}O nuclei to the ^{17}O resonance (overlapping O2 and O4).
[b] J_1 was set equal to J_2 (otherwise correlation coefficients greater than 0.99 were obtained).
[c] $\epsilon^2 = \sum [I_{\mathrm{fit}}(n) - I_{\mathrm{exp}}(n)]^2 / \sum I_{\mathrm{exp}}(n)^2$.
[d] Fit to Eq. 8.2.
[e] One or more correlation coefficients are greater than 0.7 (see SI of ref[2]).
[f] Fit to Eq. 8.3.
[g] T'_{2a} was set equal to T'_{2b} otherwise correlation coefficients of greater than 0.99 were obtained.
[h] Fit of $S_{\mathrm{Q}}(\tau) = S_{\mathrm{HET}}(\tau)/S_{\mathrm{HOM}}(\tau)$ to Eq. 8.4.
[i] $1/\Delta T'_2 = (1/T'_{2(\mathrm{HET})}) - (1/\Delta T'_{2(\mathrm{HOM})})$

Supporting Information of ref[2] all other ^{15}N-^{17}O J couplings (both inter- and intramolecular) are calculated to be of magnitude 0.5 Hz or less.

Figs. 8.4a and 8.4c compare homonuclear ^{15}N (open diamonds) and heteronuclear ^{15}N/^{17}O (filled diamonds) spin-echo ($\tau/2 - \pi - \tau/2$) data obtained using the pulse sequence in Fig. 3.12b (without and with the ^{17}O π pulse) for the (a) N1 and (c) N3 resonances. In both cases, there is a small yet significant difference between the homonuclear and heteronuclear spin-echo data. Figs 8.4b and 8.4d show the quotient $S_{\mathrm{Q}}(\tau) = S_{\mathrm{HET}}(\tau)/S_{\mathrm{HOM}}(\tau)$ for the (b) N1 and (d) N3 resonances, where $S_{\mathrm{HET}}(\tau)$ and $S_{\mathrm{HOM}}(\tau)$ refer to the ^{15}N/^{17}O heteronuclear and ^{15}N homonuclear spin-echo data presented in Figs. 8.4a and 8.4c. $S_{\mathrm{Q}}(\tau)$ is given as

$$S_{\mathrm{Q}}(\tau) = A[p\cos(\pi J \tau)\exp(-\tau/\Delta T'_2) + (1-p)] \tag{8.6}$$

where p now corresponds to the proportion of ^{15}N nuclei with a J coupling to a ^{17}O (specifically, O4) nucleus. Good fits (see Tab. 8.2) to Eq. 8.6 are observed in Figs. 8.4b and 8.4d. Although there is a very high correlation between p and J (the p, J correlation coefficient equals -0.98 and -0.99 for N1 and N3, respectively, as given in the Supporting Information of ref[2]), the fitted J couplings of 6.7± 0.4 Hz (N1) and 4.8± 0.5 Hz (N3) are in remarkably good agreement with those determined by the CASTEP [147] calculation, namely $^{2h}J_{\mathrm{N1,O4}} = 6.1$ and $^{2h}J_{\mathrm{N3,O4}} = 4.6$ Hz.

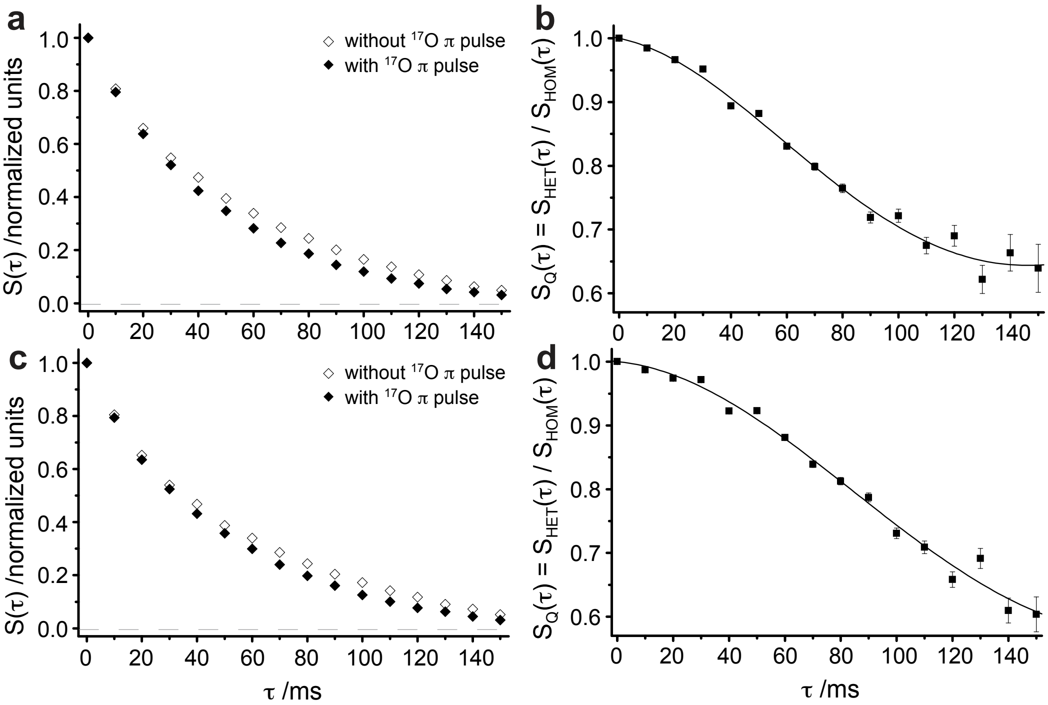

Figure 8.4. (a, c) ^{15}N homonuclear (open diamonds) and ^{15}N/^{17}O heteronuclear (filled diamonds) spin-echo ($\tau/2-\pi-\tau/2$) intensities for the (a) N1 and (c) N3 resonances of **8-1** as a function of the evolution time. Experiments were carried out at 14.1 T ($\omega_0(^1H)$ = 600 MHz) and a MAS frequency of 20.0 kHz. The error bars for the experimental intensities were determined to be ±0.0008 and are omitted for clarity. (b, d) The quotient $S_Q(\tau) = S_{HET}(\tau)/S_{HOM}(\tau)$ for the (b) N1 and (d) N3 resonances of **8-1** together with the best-fits (solid line, see Tab. 8.2) to Eq. 8.4. $S_Q(\tau)$ has been normalized such that $S_Q(\tau = 0) = 1.00$: experimentally the ratio of the integrated intensities $S_{HET}(\tau = 0)/S_{HOM}(\tau = 0)$ equalled 1.001 and 0.999 for the (b) N1 and (d) N3 resonances, respectively.

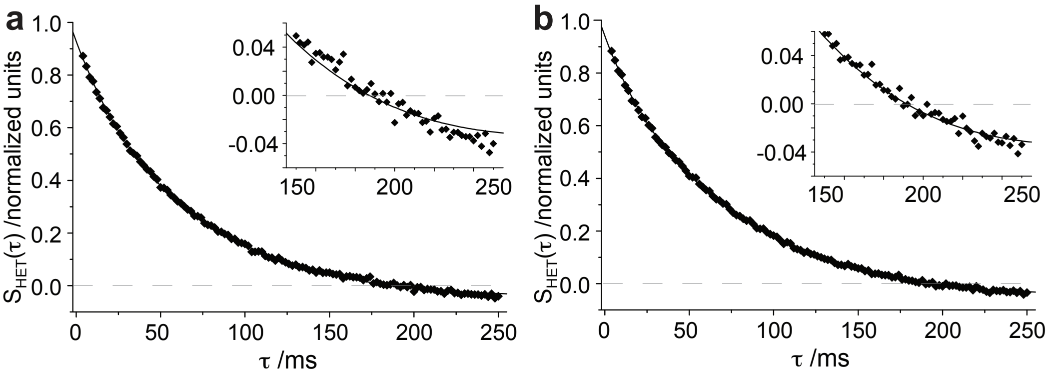

Figure 8.5. ^{15}N/^{17}O heteronuclear spin-echo ($\tau/2 - \pi - \tau/2$) intensities for the (a) N1 and (b) N3 resonances of **8-1** as a function of the evolution time together with the best fits (black curves) to Eq. 8.4 (see Tab. 8.2). The error bars for the experimental ^{15}N data points of both sites were determined to be ±0.003 and are omitted for clarity (16 transients were coadded for each τ increment). Expansions for τ =160-250 ms are shown as insets. Experiments were carried out at 14.1 T ($\omega_0(^1H)$ = 600 MHz) and a MAS frequency of 20.0 kHz.

Table 8.2. Parameters extracted from the fits of the ^{15}N and ^{15}N/^{17}O spin-echo ($\tau/2-\pi-\tau/2$) intensities of **8-1** in Figs. 8.4 and 8.5.

Data Set	A	p^{a}	J_{NO} /Hz	J_{NN} /Hz	T'_{2a} /ms	T'_{2b} /ms	$[\epsilon^2]^{\mathrm{b}}$
S_{Q} N1-O4 $^{\mathrm{cd}}$	1.00±0.01	0.22±0.01	6.7±0.4		294$^{\mathrm{e}}$±38		0.0003
S_{Q} N3-O4 $^{\mathrm{cd}}$	1.00±0.01	0.27±0.03	4.8±0.5		585$^{\mathrm{e}}$±98		0.0003
S_{HET} N1-O4 $^{\mathrm{df}}$	0.93±0.01	0.51±0.15	0.0±67	2.7±0.1	121±4	33.7±4.6	0.0005
S_{HET} N3-O4 $^{\mathrm{df}}$	0.94±0.01	0.69±0.071	0.0±1775	2.6±0.1	110±2	25.4±3.1	0.0003

[a] The proportion of ^{15}N nuclei with a J coupling to an ^{17}O nucleus, corresponding to the degree of ^{17}O labeling at the O4 site.

[b] $\epsilon^2 = \sum\left[I_{\mathrm{fit}}(n) - I_{\mathrm{exp}}(n)\right]^2 / \sum I_{\mathrm{exp}}(n)^2$.

[c] Fit of $S_{\mathrm{Q}}(\tau) = S_{\mathrm{HET}}(\tau)/S_{\mathrm{HOM}}(\tau)$ to Eq. 8.6, J corresponds to $^{2h}J_{\mathrm{NO}}$.

[d] One or more correlation coefficients are greater than 0.7 (see SI of ref[2]).

[e] $1/\Delta T'_2 = (1/T'_{2(\mathrm{HET})}) - (1/\Delta T'_{2(\mathrm{HOM})})$.

[f] Fit to Eq. 8.7.

Fig. 8.5 presents ^{15}N/^{17}O heteronuclear spin-echo ($\tau/2-\pi-\tau/2$) data for the (a) N1 and (b) N3 uracil resonances for a spin-echo duration up to 250 ms (obtained in a separate experiment to that corresponding to the data presented in Fig. 8.4). The CASTEP [147] calculation (see §8.2.3 and ref[2]) predicts an intramolecular J_{NN} coupling in **8-1**, $^2J_{\mathrm{N1,N3}} = 2.7$ Hz. This is consistent with the observation of zero crossings at long spin-echo durations (≈200 ms) and the good fits (see Tab. 8.2) to

$$S(\tau) = A\cos(\pi J_1\tau)[p\cos(\pi J_2\tau)\exp(-\tau/T'_{2a}) + (1-p)\exp(-\tau/T'_{2b})] \quad (8.7)$$

(where $J_1 = {}^2J_{\mathrm{NN}}$, $J_2 = {}^{2h}J_{\mathrm{NO}}$). Specifically, the correlation coefficients involving $^2J_{\mathrm{NN}}$ are reasonable (maximum magnitude 0.59 and 0.62 for the N1 and N3 data, respectively), and the experimental values of $^2J_{\mathrm{NN}} = 2.7\pm\ 0.1$ Hz and $2.6\pm\ 0.1$ Hz are in perfect agreement with the calculated value of $^2J_{\mathrm{N1,N3}} = 2.7$ Hz. Tab. 8.2 shows that it is, however, not possible to determine $^{2h}J_{\mathrm{NO}}$ from the fit to the heteronuclear spin-echo data. In this respect, note that the modulation under the homonuclear $^2J_{\mathrm{N1,N3}}$ coupling will be present for both the ^{15}N homonuclear and ^{15}N/^{17}O heteronuclear spin-echo experiments. It is removed by taking the quotient $S_{\mathrm{Q}}(\tau) = S_{\mathrm{HET}}(\tau)/S_{\mathrm{HOM}}(\tau)$, hence allowing the observation in Figs. 8.4b and 8.4d of the modulation due to the proportion of ^{15}N with a hydrogen-bond mediated J coupling to a ^{17}O nucleus.

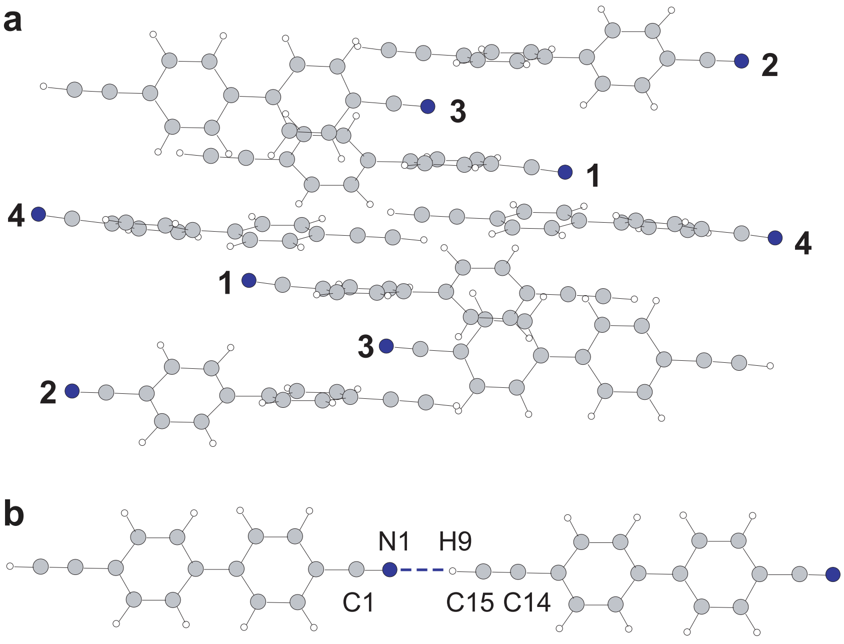

Figure 8.6. Representations of the geometrically optimised crystal structure of **8-2** showing (a) the four independent molecules of the unit cell and (b) the 'weak' CH···N hydrogen bonding which takes place between adjacent (like) molecules, indicated by the blue dashed line.

8.3.2 ^{13}C^{1}H$\cdots$^{15}N Hydrogen Bonding in 4-Cyano-4'-Ethynylbiphenyl

Representations of the geometrically optimised (CASTEP) crystal structure of **8-2** are presented in Fig. 8.6, where the four independent molecules in the asymmetric unit are identified (Fig. 8.6a) and the intermolecular hydrogen-bonding interactions (^{13}C$\equiv$^{13}CH$\cdots$^{15}N$\equiv$C) between the C15H9$\cdots$N1 sites of similar distinct molecules are given. The one-dimensional MAS NMR spectra of **8-2** are shown in Fig. 8.7; (a) presents ^{15}N CP MAS spin-echo spectra of [^{15}N, $^{13}C_2$]4-cyano-4'-ethynylbiphenyl recorded using $\tau = 0$, showing a single ^{15}N resonance at -126.7 ppm which corresponds to the ^{15}N$\equiv$C labeled site, N1. Fig. 8.7b displays the ^{13}C CP MAS spectrum of **8-2** which contains a broad resonance at ≈ 84 ppm due to the overlapped resonances of the (^{13}C$\equiv$^{13}CH) C14 and C15 sites (see also Figures 3 and 4 of ref[3] for further details of the molecular geometries and ^{13}C, ^{15}N MAS NMR spectra).

Homonuclear ^{15}N (open diamonds) and heteronuclear ^{15}N/^{13}C (filled diamonds) spin-echo ($\tau/2 - \pi - \tau/2$) data obtained using the pulse sequence in Fig. 3.12b (without and with the ^{13}C π pulse) is presented for **8-2** in Fig. 8.8a.

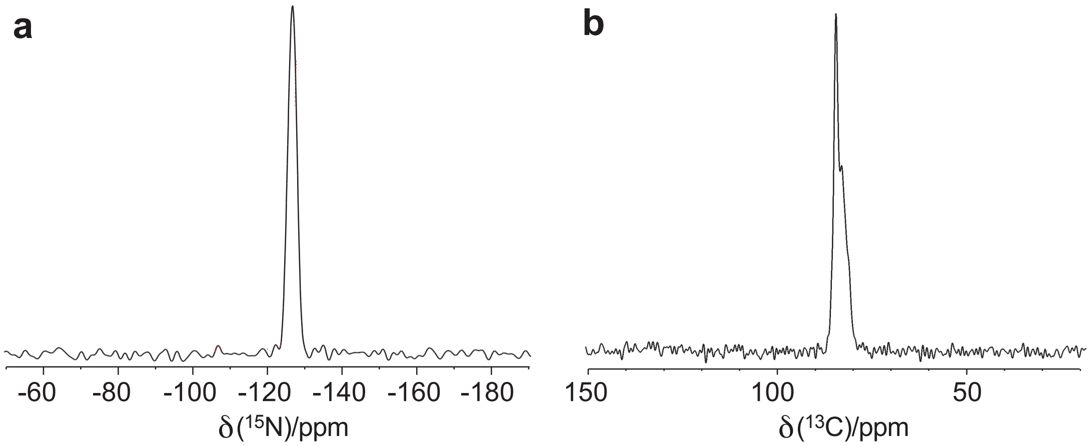

Figure 8.7. (a) Homonuclear ^{15}N CP MAS spin-echo spectrum obtained for $\tau = 0$ and (b) ^{13}C CP MAS spectra of **8-2** at ^{1}H , ^{15}N and ^{13}C Larmor frequencies of 500, 50 and 125 MHz and MAS of 10 kHz. The noise level in (a) is calculated as 0.9 %.

Table 8.3. Parameters extracted from the fit of the quotient $S_{\mathrm{Q}}(\tau)$ of ^{15}N and ^{15}N/^{13}C spin-echo ($\tau/2 - \pi - \tau/2$) intensities for **8-2** in Fig. 8.8 to Eq. 8.8.

Data Set	A	$\Delta T_2'$ /ms	J_1 /Hz	J_2 /Hz	$[\epsilon^2]$[a]
S_{Q} [b]	1.024±0.008	– [c]	4.7±0.4	2.9±0.8	0.0010

[a] $\epsilon^2 = \sum \left[I_{\mathrm{fit}}(n) - I_{\mathrm{exp}}(n)\right]^2 / \sum I_{\mathrm{exp}}(n)^2$.

[b] Fit of $S_{\mathrm{Q}}(\tau) = S_{\mathrm{HET}}(\tau)/S_{\mathrm{HOM}}(\tau)$ to Eq. 8.8 where $J_1 = {}^{2h}J_{\mathrm{N1C15}}$ and $J_2 = {}^{3h}J_{\mathrm{N1C14}}$

[c] $1/\Delta T_2' = (1/T'_{2(\mathrm{HET})}) - (1/\Delta T'_{2(\mathrm{HOM})})$, $\exp(-\tau/\Delta T_2')$ was set to 1 (otherwise correlation coefficients greater than 0.99 were obtained).

There is a distinct difference in modulation between the spin-echo intensities recorded in the homonuclear and heteronuclear cases. Fig 8.8b shows the quotient $S_{\mathrm{Q}}(\tau) = S_{\mathrm{HET}}(\tau)/S_{\mathrm{HOM}}(\tau)$, where $S_{\mathrm{HET}}(\tau)$ and $S_{\mathrm{HOM}}(\tau)$ refer to the ^{15}N/^{13}C heteronuclear and ^{15}N homonuclear spin-echo data presented in Fig. 8.8a. $S_{\mathrm{Q}}(\tau)$ is given as

$$S_{\mathrm{Q}}(\tau) = A\cos(\pi J_1 \tau)\cos(\pi J_2 \tau)\exp(-\tau/\Delta T_2') \tag{8.8}$$

As compared to §8.3.1 it can be assumed here that the ^{15}N and ^{13}C isotopic labeling of the hydrogen-bonding sites ($^{13}\mathrm{C}\equiv{}^{13}\mathrm{CH}\cdots{}^{15}\mathrm{N}\equiv\mathrm{C}$) is close to 100 % such that, to a good approximation, all the ^{15}N signal intensity detected for both the homonuclear and heteronuclear spin-echo experiments will be for ^{15}N (N1) sites which take part in hydrogen bonding with ^{13}C (C15) nuclei.

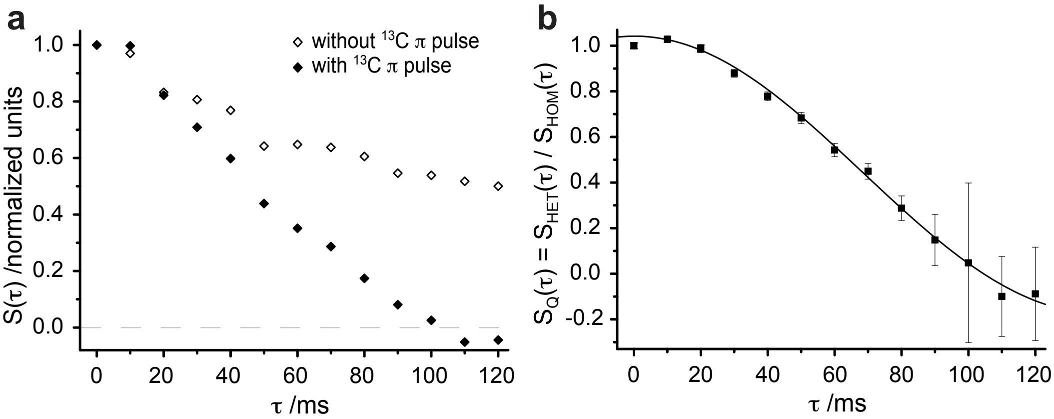

Figure 8.8. ^{15}N homonuclear (open diamonds) and ^{15}N/^{13}C heteronuclear (filled diamonds) spin-echo ($\tau/2{-}\pi{-}\tau/2$) intensities for **8-2** as a function of the evolution time recorded at 11.8 T ($\omega_0(^1\mathrm{H})$ = 500 MHz) and a MAS frequency of 10.0 kHz. The error bars for the experimental intensities were determined to be ± 0.009 and are omitted for clarity. (b) The quotient $S_\mathrm{Q}(\tau) = S_\mathrm{HET}(\tau)/S_\mathrm{HOM}(\tau)$ for **8-2**, together with the best-fits (solid line, see Tab. 8.3) to Eq. 8.8. $S_\mathrm{Q}(\tau)$ has been normalized such that $S_\mathrm{Q}(\tau = 0) = 1.00$: experimentally the ratio of the integrated intensities $S_\mathrm{HET}(\tau = 0)/S_\mathrm{HOM}(\tau = 0)$ equalled 0.998.

A good fit (see Tab. 8.3) to Eq. 8.8 is observed for $S_\mathrm{Q}(\tau)$ in Fig. 8.8b (where $\Delta T_2'$ is set to zero). Despite the high correlation between J_1 and J_2 (-0.95) the fitted J couplings of 4.7± 0.4 Hz (C15) and 2.9± 0.8 Hz (C14) are in reasonable agreement with the average of those determined by a CASTEP [147] calculation for the four independent molecules of the asymmetric unit cell, $^{2h}J_\mathrm{N1,C15(av)} = -8.6$ and $^{3h}J_\mathrm{N1,C14(av)} = -1.4$ Hz (a complete list of calculated J coupling values for the four N1 sites of **8-2** can be found in Tab. 8.4). As described in refs[81, 147], the CASTEP calculations also allow a determination of the sign of J-coupling constants, which is not determined experimentally due to the cosine modulation of the spin-echo experiment. The calculated $^{2h}J_\mathrm{NO}$ couplings presented in §8.3.1 are positive, as expected for a XH$\cdots$Y hydrogen bond in which the gyromagnetic ratios of X and Y have the same sign ($\gamma(^{15}\mathrm{N})$ and $\gamma(^{17}\mathrm{O})$ are -2.7×10^7 and -3.6×10^7 rad T^{-1} s^{-1}, respectively) [237, 238], whereas the positive $\gamma(^{13}\mathrm{C})$=6.7×10^7 rad T^{-1} s^{-1} results in negative values of J_NC being computed.

While the calculated values of the hydrogen-bond mediated ($^{2,3h}J_\mathrm{NC}$) couplings do not lie within the estimated error range of those determined by the fitting of experimental spin-echo data it is evident that the heteronuclear (^{15}N/^{13}C) and homonuclear (^{15}N) experiments reveal distinctly different mod-

Table 8.4. Calculated (CASTEP) J couplings for N1 ($|J| > 1\,\text{Hz}$) in **8-2**.

	Mol	$K_{ij}{}^{\text{a}}$	$J_{ij}{}^{\text{b}}$/Hz				
			Tot	FC	SD	Para	Dia
N1-C1	1	54.91	-16.82	-13.64	-4.29	1.15	-0.04
	2	54.97	-16.84	-13.62	-4.34	1.15	-0.03
	3	55.41	-16.98	-13.75	-4.32	1.13	-0.03
	4	55.99	-17.15	-13.92	-4.32	1.12	-0.04
N1-C15	1	28.3	-8.68	-8.58	-0.03	-0.04	-0.03
	2	24.01	-7.36	-7.26	-0.04	-0.04	-0.03
	3	27.89	-8.54	-8.44	-0.04	-0.04	-0.03
	4	32.06	-9.82	-9.68	-0.07	-0.05	-0.03
N1-C2	1	-9.15	2.80	2.13	0.09	0.58	0.01
	2	-9.24	2.83	2.16	0.09	0.58	0.00
	3	-9.15	2.80	2.13	0.09	0.58	0.01
	4	-9.15	2.80	2.12	0.10	0.58	0.00
N1-C14	1	4.49	-1.38	-1.32	0.00	-0.05	0.00
	2	5.54	-1.70	-1.65	0.00	-0.01	-0.03
	3	4.47	-1.37	-1.32	0.00	-0.05	0.00
	4	4.96	-1.52	-1.47	0.00	-0.05	0.00

[a] K_{ij}, is given in units of 10^{19} kg m^{-2} s^{-2} Å^{-2}.

[b] The J_{ij} terms (given in Hz) are computed from K where the total isotopic J is given by $J_{ij}(\text{Tot}) = K_{ij}\gamma_i\gamma_j\hbar/2\pi$. The different contributions to J_{ij}(Tot) are given; Fermi-Contact, Spin-Dipole, Paramagnetic and Diamagnetic terms, respectively (see ref[147]).

ulations, for which the quotient ($S_{\text{Q}}(\tau) = S_{\text{HET}}(\tau)/S_{\text{HOM}}(\tau)$) can be fitted to a function which describes the presence of two, small ($< 10\,\text{Hz}$) intermolecular J coupling constants. As discussed in ref[3], the paper presenting the utilised crystal structure reports significant orientational disorder, with this, together with the complication that the observed experimental data is an average over the 4 distinct molecules in the asymmetric unit cell, being a potential explanation for the poorer agreement between experiment and calculcation as compared to **8-1** above.

Due to the ^{13}C labeling scheme of **8-2**, the largest (intramolecular) J_{NC} coupling between the directly bonded N1-C1 sites is not observed which (averaged over Z'=4) is calculated as $-16.9\,\text{Hz}$. It is significant, however, that a hydrogen-bond-mediated J coupling is also detected *via* another covalently bonded atom (i.e., a *three*-bond, hydrogen-bond mediated coupling). From the geometrically optimised crystal structure of **8-2**, the N1-C15 distances across N1$\cdots$HC15 intermolecular hydrogen bonds are on average 3.28 Å, as opposed to 2.83 Å and 2.84 Å separations determined for O4-N1, O4-N3 sites in **8-1**. Thus it is expected that the magnitude of the J interactions are weaker in this case. It should be noted that the J coupling constant (J_{ij}) is defined as a function of the gyromagnetic ratios (γ_i, γ_j) of the coupled spin pair, i and j, and thus it is not surprising that the $J_{\mathrm{N1,C15(av)}} > J_{\mathrm{NO}}$ despite the longer N-C distances. The reduced spin coupling constant K_{ij}, defined as $K_{ij} = 2\pi J_{ij}/\hbar\gamma_i\gamma_j$, allows the scalar couplings to be compared independent of the nuclear species, with K_{NC} values for **8-2** listed in Tab. 8.4. Interestingly, comparing the (average over Z'=4) K_{NC} values (given in units of 10^{19} kg m^{-2} s^{-2} Å^{-2}) computed for **8-2**; $^{2h}K_{\mathrm{N1,C15(av)}} = 28.1$ with the K_{NO} of **8-1**; (given in the Supporting Information of ref[2]) $^{2h}K_{\mathrm{N1,O4}} = 36.8$ and $^{2h}K_{\mathrm{N1,O3}} = 28.1$ i.e., the N-O, N-C J-coupling interactions are computed to be of a similar magnitude, despite the longer interatomic distances across the hydrogen bond.

8.4 Summary and Outlook

As presented in ref[2], this chapter shows the determination of ^{15}N-^{17}O J couplings in the solid-state. Heteronuclear ^{15}N-^{17}O J couplings are experimentally determined from fits of the quotient of the integrated intensity obtained in a heteronuclear and a homonuclear spin-echo experiment, $S_{\mathrm{Q}}(\tau) = S_{\mathrm{HET}}(\tau)/S_{\mathrm{HOM}}(\tau)$. Importantly, for $S_{\mathrm{Q}}(\tau)$, there is only a small damping of the signal that is fit to a decaying exponential corresponding to the difference in the dephasing times for the heteronuclear and homonuclear spin-echo experiments. Excellent agreement is observed between the experimentally determined J couplings and those calculated using the first principles CASTEP code [147].

^{17}O solid-state NMR is being increasingly employed as a probe of biological molecules [229–231, 239–242]. Given the importance of NH$\cdots$O hydrogen bonding, e.g., in proteins and nucleic acids, there is evidently much potential to further apply the through-hydrogen bond ^{15}N-^{17}O solid-state NMR experiments demonstrated here, so as to unambiguously identify specific structure-determining interactions.

In addition, the heteronuclear spin-echo experiment presented in this chapter also gives the direct determination of J couplings across weak intermolecular CH$\cdots$N hydrogen bonds. The modulation of $S_{\mathrm{Q}}(\tau)$, derived from heteronuclear (^{15}N/^{13}C) and homonuclear ^{15}N spin-echo measurements, is fitted to a function depending on two hydrogen-bond J couplings across two and three bonds, in agreement with J couplings calculated by CASTEP. This is believed to be the first solid-state determination of J couplings across a weak (CH$\cdots$N) hydrogen bond.

9

Summary and Outlook

The work contained in this thesis has presented a collection of new results where advanced multinuclear MAS NMR experiments are applied to a range of systems so as to provide structural insight. Specifically, 2D ^{1}H-^{13}C heteronuclear and ^{1}H-^{1}H homonuclear spectra that utilize and probe through-bond connectivities and through-space proximities, together with 1D ^{13}C CP MAS and ^{1}H MAS and CRAMPS spectra, have been presented in combination with first-principles (GIPAW) calculations. In addition, heteronuclear (^{15}N-^{17}O and ^{15}N-^{13}C) spin-echo experiments demonstrate the first quantitative measurement of hydrogen-bond mediated J couplings for intermolecular NH$\cdots$O and NH$\cdots$C hydrogen-bonding bonding interactions. Hydrogen bonds (in particular, NH$\cdots$O) are known to play a crucial role in the formation of many important biological structures such as proteins and DNA, therefore, the direct measurement of $^{2h}J_{\mathrm{NO}}$ couplings should be of much interest for the ever increasing number solid-state NMR studies of peptides and proteins.

The ^{1}H, ^{13}C techniques presented have, in the first instance, allowed full resonance assignments of ^{1}H and ^{13}C NMR chemical shifts to be made for challenging solid-state systems including a disaccharide, a DNA derivative and a chiral pyrazole containing six molecules in the asymmetric unit cell. Furthermore, the ^{1}H DQ (CRAMPS) techniques employed here yield high-resolution ^{1}H spectra that allow the determination of close H-H proximities and hence the identification of key intermolecular interactions in organic solids. In particular, a new ^{1}H DQ (CRAMPS)-^{13}C (refocused INEPT) experiment is presented that combines a ^{1}H DQ dimension with a through-bond heteronuclear transfer sequence such that better resolution is obtained via selective transfer to

^{13}C nuclei. As applied to β-maltose monohydrate, this new experiment, together with GIPAW calculations, has enabled the first complete ^{1}H chemical shift assignment of a simple sugar, including the hydroxyl resonances, which have previously been inaccessible by solid-state NMR. Therefore, it is envisaged that this high resolution ^{1}H DQ-^{13}C technique will be well suited to the study of H-H proximities in organic solids where traditional ^{1}H DQ spectra are not sufficiently resolved by the use of fast-MAS or CRAMPS. Importantly, the methods outlined above have been used to predict the different crystallographic packing arrangements of a range of synthetic RNA derivatives, for which no single crystals suitable for diffraction studies could be obtained. It is to be emphasised that these experimental methods were applied to samples at natural isotopic abundance. This demonstrates the potential of NMR for determining the solid-state assembly and packing for many important systems where it is not possible to prepare single crystals for diffraction, e.g., pharmaceutical polymorphs. This is one of the key aims of the NMR crystallography approach and, thus, the techniques and applications presented here represent significant development in this field.

A

Supplementary Information

Matrix Representations of Two-Spin Product Operators

$$\hat{S}_x = \begin{pmatrix} 0 & \frac{1}{2} & 0 & 0 \\ \frac{1}{2} & 0 & 0 & 0 \\ 0 & 0 & 0 & \frac{1}{2} \\ 0 & 0 & \frac{1}{2} & 0 \end{pmatrix} \qquad \hat{S}_y = \begin{pmatrix} 0 & -\frac{1}{2}i & 0 & 0 \\ \frac{1}{2}i & 0 & 0 & 0 \\ 0 & 0 & 0 & -\frac{1}{2}i \\ 0 & 0 & \frac{1}{2}i & 0 \end{pmatrix} \qquad \hat{S}_z = \begin{pmatrix} \frac{1}{2} & 0 & 0 & 0 \\ 0 & -\frac{1}{2} & 0 & 0 \\ 0 & 0 & \frac{1}{2} & 0 \\ 0 & 0 & 0 & -\frac{1}{2} \end{pmatrix}$$

$$2\hat{I}_x\hat{S}_x = \begin{pmatrix} 0 & 0 & 0 & \frac{1}{2} \\ 0 & 0 & \frac{1}{2} & 0 \\ 0 & \frac{1}{2} & 0 & 0 \\ \frac{1}{2} & 0 & 0 & 0 \end{pmatrix} \qquad 2\hat{I}_x\hat{S}_y = \begin{pmatrix} 0 & 0 & 0 & -\frac{1}{2}i \\ 0 & 0 & \frac{1}{2}i & 0 \\ 0 & -\frac{1}{2}i & 0 & 0 \\ \frac{1}{2}i & 0 & 0 & 0 \end{pmatrix} \qquad 2\hat{I}_x\hat{S}_z = \begin{pmatrix} 0 & 0 & \frac{1}{2} & 0 \\ 0 & 0 & 0 & -\frac{1}{2} \\ \frac{1}{2} & 0 & 0 & 0 \\ 0 & -\frac{1}{2} & 0 & 0 \end{pmatrix}$$

$$2\hat{I}_y\hat{S}_x = \begin{pmatrix} 0 & 0 & 0 & -\frac{1}{2}i \\ 0 & 0 & -\frac{1}{2}i & 0 \\ 0 & \frac{1}{2}i & 0 & 0 \\ \frac{1}{2}i & 0 & 0 & 0 \end{pmatrix} \qquad 2\hat{I}_y\hat{S}_y = \begin{pmatrix} 0 & 0 & 0 & -\frac{1}{2} \\ 0 & 0 & \frac{1}{2} & 0 \\ 0 & \frac{1}{2} & 0 & 0 \\ -\frac{1}{2} & 0 & 0 & 0 \end{pmatrix} \qquad 2\hat{I}_y\hat{S}_z = \begin{pmatrix} 0 & 0 & -\frac{1}{2}i & 0 \\ 0 & 0 & 0 & \frac{1}{2}i \\ \frac{1}{2}i & 0 & 0 & 0 \\ 0 & -\frac{1}{2}i & 0 & 0 \end{pmatrix}$$

$$2\hat{I}_z\hat{S}_x = \begin{pmatrix} 0 & \frac{1}{2} & 0 & 0 \\ \frac{1}{2} & 0 & 0 & 0 \\ 0 & 0 & 0 & -\frac{1}{2} \\ 0 & 0 & -\frac{1}{2} & 0 \end{pmatrix} \qquad 2\hat{I}_z\hat{S}_y = \begin{pmatrix} 0 & -\frac{1}{2}i & 0 & 0 \\ \frac{1}{2}i & 0 & 0 & 0 \\ 0 & 0 & 0 & -\frac{1}{2} \\ 0 & 0 & -\frac{1}{2}i & 0 \end{pmatrix} \qquad 2\hat{I}_z\hat{S}_z = \begin{pmatrix} \frac{1}{2} & 0 & 0 & 0 \\ 0 & -\frac{1}{2} & 0 & 0 \\ 0 & 0 & -\frac{1}{2} & 0 \\ 0 & 0 & 0 & \frac{1}{2} \end{pmatrix}$$

$$ZQ_x = \begin{pmatrix} 0 & 0 & 0 & 0 \\ 0 & 0 & \frac{1}{2} & 0 \\ 0 & \frac{1}{2} & 0 & 0 \\ 0 & 0 & 0 & 0 \end{pmatrix} \qquad ZQ_y = \begin{pmatrix} 0 & 0 & 0 & 0 \\ 0 & 0 & -\frac{1}{2}i & 0 \\ 0 & \frac{1}{2}i & 0 & 0 \\ 0 & 0 & 0 & 0 \end{pmatrix}$$

$$DQ_x = \begin{pmatrix} 0 & 0 & 0 & \frac{1}{2} \\ 0 & 0 & 0 & 0 \\ 0 & 0 & 0 & 0 \\ \frac{1}{2} & 0 & 0 & 0 \end{pmatrix} \qquad DQ_y = \begin{pmatrix} 0 & 0 & 0 & -\frac{1}{2}i \\ 0 & 0 & 0 & 0 \\ 0 & 0 & 0 & 0 \\ \frac{1}{2} & 0 & 0 & 0 \end{pmatrix}$$

Table A.1. Phases used for ^{1}H DQ-^{13}C INEPT pulse sequence given in Fig. 4.1.

ϕ_1	x, y, −x, −y
ϕ_2	{x, x, x, x, x, x, x, x}*4{−x, −x, −x, −x, −x, −x, −x, −x}*4
ϕ_3	y, y, y, y, y, y, y, y, −y, −y, −y, −y, −y, −y, −y, −y
ϕ_4	x, x, x, x, −x, −x, −x, −x
ϕ_5	x, x, x, x, −x, −x, −x, −x
ϕ_6	{x, x, x, x}*4 {y, y, y, y}*4 {−x, −x, −x, −x}*4 {−y, −y, −y, −y}*4
ϕ_7	{x, x, x, x, −x, −x, −x, −x}*2 {y, y, y, y, −y, −y, −y, −y}*2
ϕ_{rec}	{x, −x, x, −x}*2 {−x, x, −x, x}*2 {y, −y, y, −y}*2 {−y, y, −y, y}*2

References

[1] A. L. Webber, B. Elena, J. M. Griffin, J. R. Yates, T. N. Pham, F. Mauri, C. J. Pickard, A. M. Gil, R. S. Stein, A. Lesage, L. Emsley, and S. P. Brown, "Solid-State NMR Spectroscopy of Saccharides: Complete ^{1}H Resonance Assignment of -Maltose from ^{1}H-^{1}H DQ-SQ CRAMPS and ^{1}H (DQ-DUMBO)-^{13}C SQ Refocused INEPT 2D Spectra and First Principles GIPAW Calculations," Phys. Chem. Chem. Phys., *accepted* (2010).

[2] I. Hung, A. C. Uldry, J. Becker-Baldus, A. L. Webber, A. Wong, M. E. Smith, S. A. Joyce, J. R. Yates, C. J. Pickard, R. Dupree, and S. P. Brown, "Probing Heteronuclear ^{15}N-^{17}O and ^{13}C-^{17}O Connectivities and Proximities by Solid-State NMR Spectroscopy," J. Am. Chem. Soc. **131,** 1820–34 (2009).

[3] A. C. Uldry, J. M. Griffin, J. R. Yates, M. Pérez-Torralba, M. D. Santa-María, A. L. Webber, M. L. L. Beaumont, A. Samoson, R. M. Claramunt, C. J. Pickard, and S. P. Brown, "Quantifying Weak Hydrogen Bonding in Uracil and 4-Cyano-4'-Ethynylbiphenyl: A Combined Computational and Experimental Investigation of NMR Chemical Shifts in the Solid State," J. Am. Chem. Soc. **130,** 945–54 (2008).

[4] Z. D. Zujovic, C. Laslau, G. A. Bowmaker, P. A. Kilmartin, A. L. Webber, S. P. Brown, and J. Travas-Sejdic, "Role of Aniline Oligomeric Nanosheets in the Formation of Polyaniline Nanotubes," Macromolecules **43,** 662–70 (2010).

[5] R. K. Harris, "NMR Crystallography: The Use of Chemical Shifts," Solid State Sci. **6,** 1025–37 (2004).

[6] F. Taulelle, "NMR Crystallography: Crystallochemical Formula and Space Group Selection," Solid State Sci. **6,** 1053–57 (2004).

[7] B. Elena, G. Pintacuda, N. Mifsud, and L. Emsley, "Molecular Structure Determination in Powders by NMR Crystallography from Proton Spin Diffusion," J. Am. Chem. Soc. **128,** 9555–60 (2006).

[8] R. K. Harris, R. E. Wasylishen, and M. J. Duer, *NMR Crystallography* (Wiley, 2009).

[9] F. Bloch, W. W. Hansen, and M. Packard, "The Nuclear Induction Experiment," Phys. Rev. **70,** 474 (1946).

[10] E. M. Purcell, H. C. Torrey, and R. V. Pound, "Resonance Absorption by Nuclear Magnetic Moments in a Solid," Phys. Rev. **69,** 37 (1946).

[11] R. R. Ernst, G. Bodenhausen, and A. Wokaun, *Principles of Nuclear Magnetic Resonance in One and Two Dimensions* (1987).

[12] E. R. Andrew, A. Bradbury, and R. G. Eades, "Nuclear Magnetic Resonance Spectra from a Crystal Rotated at High Speed," Nature **182,** 1659–59 (1958).

[13] E. R. Andrew, A. Bradbury, and R. G. Eades, "Removal of Dipolar Broadening of

Nuclear Magnetic Resonance Spectra of Solids by Specimen Rotation," Nature **183,** 1802–03 (1959).

[14] I. J. Lowe, "Free Induction Decays of Rotating Solids," Phys. Rev. Lett. **2,** 285 (1959).

[15] S. R. Hartmann and E. L. Hahn, "Nuclear Double Resonance in the Rotating Frame," Phys. Rev. **128,** 2042–53 (1962).

[16] M. Mehring, A. Pines, W. K. Rhim, and J. S. Waugh, "Spin-Decoupling in Resolution of Chemical Shifts in Solids by Pulsed NMR," J. Chem. Phys. **54,** 3239–40 (1971).

[17] A. Pines, M. G. Gibby, and J. S. Waugh, "Proton-Enhanced Nuclear Induction Spectroscopy. A Method for High Resolution NMR of Dilute Spins in Solids," J. Chem. Phys. **56,** 1776–77 (1972).

[18] J. Schaefer and E. O. Stejskal, "^{13}C Nuclear Magnetic-Resonance of Polymers Spinning at Magic Angle," J. Am. Chem. Soc. **98,** 1031–32 (1976).

[19] A. E. Bennett, C. M. Rienstra, M. Auger, K. V. Lakshmi, and R. G. Griffin, "Heteronuclear Decoupling in Rotating Solids," J. Chem. Phys. **103,** 6951–58 (1995).

[20] B. M. Fung, A. K. Khitrin, and K. Ermolaev, "An Improved Broadband Decoupling Sequence for Liquid Crystals and Solids," J. Magn. Reson. **142,** 97–101 (2000).

[21] F. Castellani, B. van Rossum, A. Diehl, M. Schubert, K. Rehbein, and H. Oschkinat, "Structure of a Protein Determined by Solid-State Magic-Angle-Spinning NMR Spectroscopy," Nature **420,** 98–102 (2002).

[22] S. G. Zech, A. J. Wand, and A. E. McDermott, "Protein Structure Determination by High-Resolution Solid-State NMR Spectroscopy: Application to Microcrystalline Ubiquitin," J. Am. Chem. Soc. **127,** 8618–26 (2005).

[23] A. Lange, K. Giller, S. Hornig, M. F. Martin-Eauclaire, O. Pongs, S. Becker, and M. Baldus, "Toxin-Induced Conformational Changes in a Potassium Channel Revealed by Solid-State NMR," Nature **440,** 959–62 (2006).

[24] A. T. Petkova, Y. Ishii, J. J. Balbach, O. N. Antzutkin, R. D. Leapman, F. Delaglio, and R. Tycko, "A Structural Model for Alzheimer's β-Amyloid Fibrils Based on Experimental Constraints from Solid State NMR," Proc. Natl. Acad. Sci. U. S. A. **99,** 16742–47 (2002).

[25] M. M. Maricq and J. S. Waugh, "NMR in Rotating Solids," J. Chem. Phys. **70,** 3300–16 (1979).

[26] M. Lee and W. I. Goldburg, "Nuclear-Magnetic-Resonance Line Narrowing by a Rotating Rf Field," Phys. Rev. **140,** A1261 (1965).

[27] A. Bielecki, A. C. Kolbert, and M. H. Levitt, "Frequency-Switched Pulse Sequences - Homonuclear Decoupling and Dilute Spin NMR in Solids," Chem. Phys. Lett. **155,** 341–46 (1989).

[28] E. Vinogradov, P. K. Madhu, and S. Vega, "High-Resolution Proton Solid-State NMR Spectroscopy by Phase-Modulated Lee-Goldburg Experiment," Chem. Phys. Lett. **314,** 443–50 (1999).

[29] J. S. Waugh, L. M. Huber, and U. Haeberlen, "Approach to High-Resolution NMR in Solids," Phys. Rev. Lett. **20,** 180 (1968).

[30] W. K. Rhim, D. D. Elleman, and R. W. Vaughan, "Analysis of Multiple Pulse NMR in Solids," J. Chem. Phys. **59,** 3740–49 (1973).

[31] B. C. Gerstein, R. G. Pembleton, R. C. Wilson, and L. M. Ryan, "High-Resolution NMR in Randomly Oriented Solids with Homonuclear Dipolar Broadening - Combined Multiple Pulse NMR and Magic Angle Spinning," J. Chem. Phys. **66,** 361–62 (1977).

[32] C. Filip and S. Hafner, "Analysis of Multiple-Pulse Techniques under Fast MAS Conditions," J. Magn. Reson. **147,** 250–60 (2000).

[33] E. Vinogradov, P. K. Madhu, and S. Vega, "Phase Modulated Lee-Goldburg Magic

Angle Spinning Proton Nuclear Magnetic Resonance Experiments in the Solid State: A Bimodal Floquet Theoretical Treatment," J. Chem. Phys. **115,** 8983–9000 (2001).

[34] D. Sakellariou, A. Lesage, P. Hodgkinson, and L. Emsley, "Homonuclear Dipolar Decoupling in Solid-State NMR Using Continuous Phase Modulation," Chem. Phys. Lett. **319,** 253–60 (2000).

[35] B. Elena, G. de Paepe, and L. Emsley, "Direct Spectral Optimisation of Proton-Proton Homonuclear Dipolar Decoupling in Solid-State NMR," Chem. Phys. Lett. **398,** 532–38 (2004).

[36] M. Hohwy, P. V. Bower, H. J. Jakobsen, and N. C. Nielsen, "A High-Order and Broadband CRAMPS Experiment Using Z-Rotational Decoupling," Chem. Phys. Lett. **273,** 297–303 (1997).

[37] P. K. Madhu, X. Zhao, and M. H. Levitt, "High-Resolution ^{1}H NMR in the Solid State Using Symmetry-Based Pulse Sequences," Chem. Phys. Lett. **346,** 142–48 (2001).

[38] S. P. Brown and H. W. Spiess, "Advanced Solid-State NMR Methods for the Elucidation of Structure and Dynamics of Molecular, Macromolecular, and Supramolecular Systems," Chem. Rev. **101,** 4125–55 (2001).

[39] I. Schnell and H. W. Spiess, "High-Resolution ^{1}H NMR Spectroscopy in the Solid State: Very Fast Sample Rotation and Multiple-Quantum Coherences," J. Magn. Reson. **151,** 153–227 (2001).

[40] P. K. Madhu, "High-Resolution Solid-State NMR Spectroscopy of Protons with Homonuclear Dipolar Decoupling Schemes under Magic-Angle Spinning," Solid State Nucl. Magn. Reson. **35,** 2–11 (2009).

[41] A. Lesage, D. Sakellariou, S. Hediger, B. Elena, P. Charmont, S. Steuernagel, and L. Emsley, "Experimental Aspects of Proton NMR Spectroscopy in Solids Using Phase-Modulated Homonuclear Dipolar Decoupling," J. Magn. Reson. **163,** 105–13 (2003).

[42] V. E. Zorin, B. Elena, A. Lesage, L. Emsley, and P. Hodgkinson, "On the Orientational Dependence of Resolution in ^{1}H Solid-State NMR, and Its Role in MAS, CRAMPS and Delayed-Acquisition Experiments," Magn. Reson. Chem. **45,** S93–S100 (2007).

[43] M. Leskes, P. K. Madhu, and S. Vega, "Supercycled Homonuclear Dipolar Decoupling in Solid-State NMR: Toward Cleaner ^{1}H Spectrum and Higher Spinning Rates," J. Chem. Phys. 128 (2008).

[44] M. Leskes, S. Steuernagel, D. Schneider, P. K. Madhu, and S. Vega, "Homonuclear Dipolar Decoupling at Magic-Angle Spinning Frequencies up to 65 kHz in Solid-State Nuclear Magnetic Resonance," Chem. Phys. Lett. **466,** 95–99 (2008).

[45] E. Salager, R. S. Stein, S. Steuernagel, A. Lesage, B. Elena, and L. Emsley, "Enhanced Sensitivity in High-Resolution ^{1}H Solid-State NMR Spectroscopy with DUMBO Dipolar Decoupling under Ultra-Fast MAS," Chem. Phys. Lett. **469,** 336–41 (2009).

[46] S. P. Brown, "Probing Proton-Proton Proximities in the Solid State," Prog. Nucl. Magn. Reson. Spectrosc. **50,** 199–251 (2007).

[47] S. P. Brown, "Recent Advances in Solid-State MAS NMR Methodology for Probing Structure and Dynamics in Polymeric and Supramolecular Systems," Macromol. Rapid Commun. **30,** 688–716 (2009).

[48] A. Lesage, "Recent Advances in Solid-State NMR Spectroscopy of Spin 1/2 Nuclei," Phys. Chem. Chem. Phys. **11,** 6876–91 (2009).

[49] A. Lesage, D. Sakellariou, S. Steuernagel, and L. Emsley, "Carbon-Proton Chemical Shift Correlation in Solid-State NMR by through-Bond Multiple-Quantum Spectroscopy," J. Am. Chem. Soc. **120,** 13194–201 (1998).

[50] B. Elena, A. Lesage, S. Steuernagel, A. Bockmann, and L. Emsley, "Proton to ^{13}C INEPT in Solid-State NMR Spectroscopy," J. Am. Chem. Soc. **127,** 17296–302 (2005).

[51] A. Bax, R. H. Griffey, and B. L. Hawkins, "Correlation of Proton and ^{15}N Chemical-

Shifts by Multiple Quantum NMR," J. Magn. Reson. **55,** 301–15 (1983).

[52] G. A. Morris and R. Freeman, "Enhancement of Nuclear Magnetic-Resonance Signals by Polarization Transfer," J. Am. Chem. Soc. **101,** 760–62 (1979).

[53] M. H. Levitt, "Symmetry-Based Pulse Sequences in Magic-Angle Spinning Solid-State NMR," Encyclopedia of Nuclear Magnetic Resonance **9,** 165–96 (2002).

[54] I. Schnell, "Dipolar Recoupling in Fast-MAS Solid-State NMR Spectroscopy," Prog. Nucl. Magn. Reson. Spectrosc. **45,** 145–207 (2004).

[55] I. Schnell, A. Lupulescu, S. Hafner, D. E. Demco, and H. W. Spiess, "Resolution Enhancement in Multiple-Quantum MAS NMR Spectroscopy," J. Magn. Reson. **133,** 61–69 (1998).

[56] S. P. Brown, X. X. Zhu, K. Saalwächter, and H. W. Spiess, "An Investigation of the Hydrogen-Bonding Structure in Bilirubin by ^{1}H Double-Quantum Magic-Angle Spinning Solid-State NMR Spectroscopy," J. Am. Chem. Soc. **123,** 4275–85 (2001).

[57] S. P. Brown, I. Schnell, J. D. Brand, K. Mullen, and H. W. Spiess, "An Investigation of $\pi - \pi$ Packing in a Columnar Hexabenzocoronene by Fast Magic-Angle Spinning and Double-Quantum ^{1}H Solid-State NMR Spectroscopy," J. Am. Chem. Soc. **121,** 6712–18 (1999).

[58] S. P. Brown, T. Schaller, U. P. Seelbach, F. Koziol, C. Ochsenfeld, F. G. Klarner, and H. W. Spiess, "Structure and Dynamics of the Host-Guest Complex of a Molecular Tweezer: Coupling Synthesis, Solid-State NMR, and Quantum-Chemical Calculations," Angew. Chem., Int. Ed. Engl. **40,** 717–20 (2001).

[59] V. Percec, M. Glodde, T. K. Bera, Y. Miura, I. Shiyanovskaya, K. D. Singer, V. S. K. Balagurusamy, P. A. Heiney, I. Schnell, A. Rapp, H. W. Spiess, S. D. Hudson, and H. Duan, "Self-Organization of Supramolecular Helical Dendrimers into Complex Electronic Materials (Vol 419, Pg 384, 2002)," Nature **419,** 862–62 (2002).

[60] T. M. Alam, M. Nyman, B. R. Cherry, J. M. Segall, and L. E. Lybarger, "Multinuclear NMR Investigations of the Oxygen, Water, and Hydroxyl Environments in Sodium Hexaniobate," J. Am. Chem. Soc. **126,** 5610–20 (2004).

[61] F. Rataboul, A. Baudouin, C. Thieuleux, L. Veyre, C. Coperet, J. Thivolle-Cazat, J. M. Basset, A. Lesage, and L. Emsley, "Molecular Understanding of the Formation of Surface Zirconium Hydrides Upon Thermal Treatment under Hydrogen of [(Sio)Zr(Ch(2)Tbu)(3)] by Using Advanced Solid-State NMR Techniques," J. Am. Chem. Soc. **126,** 12541–50 (2004).

[62] M. Hohwy, H. J. Jakobsen, M. Edén, M. H. Levitt, and N. C. Nielsen, "Broadband Dipolar Recoupling in the Nuclear Magnetic Resonance of Rotating Solids: A Compensated C7 Pulse Sequence," J. Chem. Phys. **108,** 2686–94 (1998).

[63] P. K. Madhu, E. Vinogradov, and S. Vega, "Multiple-Pulse and Magic-Angle Spinning Aided Double-Quantum Proton Solid-State NMR Spectroscopy," Chem. Phys. Lett. **394,** 423–28 (2004).

[64] S. P. Brown, A. Lesage, B. Elena, and L. Emsley, "Probing Proton-Proton Proximities in the Solid State: High-Resolution Two-Dimensional ^{1}H-^{1}H Double-Quantum CRAMPS NMR Spectroscopy," J. Am. Chem. Soc. **126,** 13230–31 (2004).

[65] N. Mifsud, B. Elena, C. J. Pickard, A. Lesage, and L. Emsley, "Assigning Powders to Crystal Structures by High-Resolution ^{1}H-^{1}H Double Quantum and ^{1}H-^{13}C J-INEPT Solid-State NMR Spectroscopy and First Principles Computation. A Case Study of Penicillin G," Phys. Chem. Chem. Phys. **8,** 3418–22 (2006).

[66] E. Salager, R. S. Stein, C. J. Pickard, B. Elena, and L. Emsley, "Powder NMR Crystallography of Thymol," Phys. Chem. Chem. Phys. **11,** 2610–21 (2009).

[67] J. M. Griffin, D. R. Martin, and S. P. Brown, "Distinguishing Anhydrous and Hydrous Forms of an Active Pharmaceutical Ingredient in a Tablet Formulation Using Solid-State NMR Spectroscopy," Angew. Chem., Int. Ed. Engl. **46,** 8036–38 (2007).

[68] P. Avenier, A. Lesage, M. Taoufik, A. Baudouin, A. De Mallmann, S. Fiddy, M. Vautier, L. Veyre, J. M. Basset, L. Emsley, and E. A. Quadrelli, "Well-Defined Surface Imido Amido Tantalum(V) Species from Ammonia and Silica-Supported Tantalum Hydrides," J. Am. Chem. Soc. **129,** 176–86 (2007).

[69] P. Avenier, M. Taoufik, A. Lesage, X. Solans-Monfort, A. Baudouin, A. de Mallmann, L. Veyre, J. M. Basset, O. Eisenstein, L. Emsley, and E. A. Quadrelli, "Dinitrogen Dissociation on an Isolated Surface Tantalum Atom," Science **317,** 1056–60 (2007).

[70] K. D. M. Harris, M. Tremayne, and B. M. Kariuki, "Contemporary Advances in the Use of Powder X-Ray Diffraction for Structure Determination," Angew. Chem., Int. Ed. Engl. **40,** 1626–51 (2001).

[71] K. D. M. Harris and E. Y. Cheung, "How to Determine Structures When Single Crystals Cannot Be Grown: Opportunities for Structure Determination of Molecular Materials Using Powder Diffraction Data," Chem. Soc. Rev. **33,** 526–38 (2004).

[72] G. M. Day *et al.*, "A Third Blind Test of Crystal Structure Prediction," Acta Crystallogr. Sect. B-Struct. Commun. **61,** 511–27 (2005).

[73] A. J. C. Cabeza, E. Pidcock, G. M. Day, W. D. S. Motherwell, and W. Jones, "Space Group Selection for Crystal Structure Prediction of Solvates (Vol 9, 2007)," Cryst. Eng. Comm. **9,** 611–11 (2007).

[74] G. M. Day, W. D. S. Motherwell, and W. Jones, "A Strategy for Predicting the Crystal Structures of Flexible Molecules: The Polymorphism of Phenobarbital," Phys. Chem. Chem. Phys. **9,** 1693–704 (2007).

[75] S. L. Price, "Computed Crystal Energy Landscapes for Understanding and Predicting Organic Crystal Structures and Polymorphism," Acc. Chem. Res. **42,** 117–26 (2009).

[76] H. Eckert, "Structural Characterization of Noncrystalline Solids and Glasses Using Solid-State NMR," Prog. Nucl. Magn. Reson. Spectrosc. **24,** 159–293 (1992).

[77] C. J. Pickard and F. Mauri, "All-Electron Magnetic Response with Pseudopotentials: NMR Chemical Shifts," Phys. Rev. B 63 (2001).

[78] J. R. Yates, C. J. Pickard, and F. Mauri, "Calculation of NMR Chemical Shifts for Extended Systems Using Ultrasoft Pseudopotentials," Phys. Rev. B 76 (2007).

[79] C. J. Pickard, E. Salager, G. Pintacuda, B. Elena, and L. Emsley, "Resolving Structures from Powders by NMR Crystallography Using Combined Proton Spin Diffusion and Plane Wave DFT Calculations," J. Am. Chem. Soc. **129,** 8932–33 (2007).

[80] J. R. Yates, T. N. Pham, C. J. Pickard, F. Mauri, A. M. Amado, A. M. Gil, and S. P. Brown, "An Investigation of Weak CH$\cdots$ O Hydrogen Bonds in Maltose Anomers by a Combination of Calculation and Experimental Solid-State NMR Spectroscopy," J. Am. Chem. Soc. **127,** 10216–20 (2005).

[81] S. A. Joyce, J. R. Yates, C. J. Pickard, and S. P. Brown, "Density Functional Theory Calculations of Hydrogen-Bond-Mediated NMR J Coupling in the Solid State," J. Am. Chem. Soc. **130,** 12663–70 (2008).

[82] M. Profeta, F. Mauri, and C. J. Pickard, "Accurate First Principles Prediction of ^{17}O NMR Parameters in SiO2: Assignment of the Zeolite Ferrierite Spectrum," J. Am. Chem. Soc. **125,** 541–48 (2003).

[83] M. Profeta, M. Benoit, F. Mauri, and C. J. Pickard, "First-Principles Calculation of the ^{17}O NMR Parameters in Ca Oxide and Ca Aluminosilicates: The Partially Covalent Nature of the Ca-O Bond, a Challenge for Density Functional Theory," J. Am. Chem. Soc. **126,** 12628–35 (2004).

[84] R. K. Harris, S. Cadars, L. Emsley, J. R. Yates, C. J. Pickard, R. K. R. Jetti, and U. J. Griesser, "NMR Crystallography of Oxybuprocaine Hydrochloride, Modification II Degrees," Phys. Chem. Chem. Phys. **9,** 360–68 (2007).

[85] R. K. Harris, S. A. Joyce, C. J. Pickard, S. Cadars, and L. Emsley, "Assigning ^{13}C

NMR Spectra to Crystal Structures by the INADEQUATE Pulse Sequence and First Principles Computation: A Case Study of Two Forms of Testosterone," Phys. Chem. Chem. Phys. **8,** 137–43 (2006).

[86] E. Zurek, C. J. Pickard, and J. Autschbach, "A Density Functional Study of the ^{13}C NMR Chemical Shifts in Functionalized Single-Walled Carbon Nanotubes," J. Am. Chem. Soc. **129,** 4430–39 (2007).

[87] M. A. L. Marques, M. d'Avezac, and F. Mauri, "Magnetic Response and NMR Spectra of Carbon Nanotubes from Ab Initio Calculations," Phys. Rev. B 73 (2006).

[88] E. D. L. Smith, R. B. Hammond, M. J. Jones, K. J. Roberts, J. B. O. Mitchell, S. L. Price, R. K. Harris, D. C. Apperley, J. C. Cherryman, and R. Docherty, "The Determination of the Crystal Structure of Anhydrous Theophylline by X-Ray Powder Diffraction with a Systematic Search Algorithm, Lattice Energy Calculations, and ^{13}C and ^{15}N Solid-State NMR: A Question of Polymorphism in a Given Unit Cell," J. Phys. Chem. B **105,** 5818–26 (2001).

[89] D. A. Middleton, X. Peng, D. Saunders, K. Shankland, W. I. F. David, and A. J. Markvardsen, "Conformational Analysis by Solid-State NMR and Its Application to Restrained Structure Determination from Powder Diffraction Data," Chem. Commun. pp. 1976–77 (2002).

[90] M. Rajeswaran, T. N. Blanton, N. Zumbulyadis, D. J. Giesen, C. Conesa-Moratilla, S. T. Misture, P. W. Stephens, and A. Huq, "Three-Dimensional Structure Determination of N-(P-Tolyl)-Dodecylsulfonamide from Powder Diffraction Data and Validation of Structure Using Solid-State NMR Spectroscopy," J. Am. Chem. Soc. **124,** 14450–59 (2002).

[91] R. K. Harris, P. Y. Ghi, R. B. Hammond, C. Y. Ma, K. J. Roberts, J. R. Yates, and C. J. Pickard, "Solid-State NMR and Computational Studies of 4-Methyl-2-Nitroacetanilide," Magn. Reson. Chem. **44,** 325–33 (2006).

[92] J. K. Harper, D. M. Grant, Y. G. Zhang, P. L. Lee, and R. Von Dreele, "Characterizing Challenging Microcrystalline Solids with Solid-State NMR Shift Tensor and Synchrotron X-Ray Powder Diffraction Data: Structural Analysis of Ambuic Acid," J. Am. Chem. Soc. **128,** 1547–52 (2006).

[93] E. M. Heider, J. K. Harper, and D. M. Grant, "Structural Characterization of an Anhydrous Polymorph of Paclitaxel by Solid-State NMR," Phys. Chem. Chem. Phys. **9,** 6083–97 (2007).

[94] L. Shao, J. R. Yates, and J. Titman, "^{13}C Chemical Shift Tensors of Disaccharides: Measurement, Computation and Assignment," J. Phys. Chem. A **111,** 13126 (2007).

[95] T. L. Threlfall, "Analysis of Organic Polymorphs - a Review (Vol 120, Pg 2435, 1995)," Analyst **121,** 269–69 (1996).

[96] D. C. Apperley, R. A. Fletton, R. K. Harris, R. W. Lancaster, S. Tavener, and T. L. Threlfall, "Sulfathiazole Polymorphism Studied by Magic-Angle Spinning NMR," J. Pharm. Sci. **88,** 1275–80 (1999).

[97] R. K. Harris, "NMR Studies of Organic Polymorphs and Solvates," Analyst **131,** 351–73 (2006).

[98] R. K. Harris, "Applications of Solid-State NMR to Pharmaceutical Polymorphism and Related Matters," J. Pharm. Pharmacol. **59,** 225–39 (2007).

[99] M. Geppi, G. Mollica, S. Borsacchi, and C. A. Veracini, "Solid-State NMR Studies of Pharmaceutical Systems," Appl. Spectros. Rev. **43,** 202–302 (2008).

[100] J. Schmidt, A. Hoffmann, H. W. Spiess, and D. Sebastiani, "Bulk Chemical Shifts in Hydrogen-Bonded Systems from First-Principles Calculations and Solid-State-NMR," J. Phys. Chem. B **110,** 23204–10 (2006).

[101] S. P. Brown, M. Pérez-Torralba, D. Sanz, R. M. Claramunt, and L. Emsley, "Determining Hydrogen-Bond Strengths in the Solid State by NMR: The Quantitative

Measurement of Homonuclear *J* Couplings," Chem. Commun. pp. 1852–53 (2002).

[102] T. N. Pham, J. M. Griffin, S. Masiero, S. Lena, G. Gottarelli, P. Hodgkinson, C. Fillip, and S. P. Brown, "Quantifying Hydrogen-Bonding Strength: The Measurement of $^{2h}J_{\mathrm{NN}}$ Couplings in Self-Assembled Guanosines by Solid-State ^{15}N Spin-Echo MAS NMR," Phys. Chem. Chem. Phys. **9,** 3416–23 (2007).

[103] B. Elena and L. Emsley, "Powder Crystallography by Proton Solid-State NMR Spectroscopy," J. Am. Chem. Soc. **127,** 9140–46 (2005).

[104] M. Mehring, *Principles of High Resolution NMR in Solids* (Springer-Verlag, 1983).

[105] M. H. Levitt, *Spin Dynamics* (Wiley, 2001).

[106] M. J. Duer, *Introduction to Solid-State NMR Spectroscopy* (Blackwell, 2004).

[107] P. J. Hore, J. A. Jones, and S. Wimperis, *NMR: The Toolkit* (Oxford University Press, 2000).

[108] O. W. Sørensen, G. W. Eich, M. H. Levitt, G. Bodenhausen, and R. R. Ernst, "Product Operator-Formalism for the Description of NMR Pulse Experiments," Prog. Nucl. Magn. Reson. Spectrosc. **16,** 163–92 (1983).

[109] U. Haeberlen and J. S. Waugh, "Coherent Averaging Effects in Magnetic Resonance," Phys. Rev. **175,** 453–67 (1968).

[110] W. Magnus, "On the Exponential Solution of Differential Equations for a Linear Operators," Commun. Pure and Appl. Math. **7,** 649–73 (1954).

[111] U. Haeberlen, *Advances in Magnetic Resonance* (Academic Press, 1976).

[112] M. Bak, J. T. Rasmussen, and N. C. Nielsen, "SIMPSON: A General Simulation Program for Solid-State NMR Spectroscopy," J. Magn. Reson. **147,** 296–330 (2000).

[113] D. J. States, R. A. Haberkorn, and D. J. Ruben, "A Two-Dimensional Nuclear Overhauser Experiment with Pure Absorption Phase in 4 Quadrants," J. Magn. Reson. **48,** 286–92 (1982).

[114] D. Marion and K. Wüthrich, "Application of Phase Sensitive Two-Dimensional Correlated Spectroscopy (COSY) for Measurements of ^{1}H ^{1}H Spin-Spin Coupling Constants in Proteins," Biochem. Biophys. Res. Commun. **113,** 967–74 (1983).

[115] D. Marion, M. Ikura, R. Tschudin, and A. Bax, "Rapid Recording of 2D NMR-Spectra without Phase Cycling - Application to the Study of Hydrogen-Exchange in Proteins," J. Magn. Reson. **85,** 393–99 (1989).

[116] G. Bodenhausen, H. Kogler, and R. R. Ernst, "Selection of Coherence-Transfer Pathways in NMR Pulse Experiments," J. Magn. Reson. **58,** 370–88 (1984).

[117] W. Sommer, J. Gottwald, D. E. Demco, and H. W. Spiess, "Dipolar Heteronuclear Multiple-Quantum NMR-Spectroscopy in Rotating Solids," J. Magn. Reson. Ser. A **113,** 131–34 (1995).

[118] G. Metz, X. L. Wu, and S. O. Smith, "Ramped-Amplitude Cross-Polarization in Magic-Angle-Spinning NMR," J. Magn. Reson. Ser. A **110,** 219–27 (1994).

[119] S. Hediger, B. H. Meier, N. D. Kurur, G. Bodenhausen, and R. R. Ernst, "NMR Cross-Polarization by Adiabatic Passage through the Hartmann-Hahn Condition (APHH)," Chem. Phys. Lett. **223,** 283–88 (1994).

[120] A. Pines, M. G. Gibby, and J. S. Waugh, "Proton-Enhanced NMR of Dilute Spins in Solids," J. Chem. Phys. **59,** 569–90 (1973).

[121] K. Schmidt-Rohr and H. W. Spiess, *Multidimensional Solid-State NMR and Polymers* (Academic, 1994).

[122] F. Bloch, "Theory of Line Narrowing by Double-Frequency Irradiation," Phys. Rev. **111,** 841–53 (1958).

[123] P. Hodgkinson, "Heteronuclear Decoupling in the NMR of Solids," Prog. Nucl. Magn.

Reson. Spectrosc. **46,** 197–222 (2005).

[124] E. Vinogradov, P. K. Madhu, and S. Vega, "Proton Spectroscopy in Solid State Nuclear Magnetic Resonance with Windowed Phase Modulated Lee-Goldburg Decoupling Sequences," Chem. Phys. Lett. **354,** 193–202 (2002).

[125] D. P. Burum, M. Linder, and R. R. Ernst, "Low-Power Multipulse Line Narrowing in Solid-State NMR," J. Magn. Reson. **44,** 173–88 (1981).

[126] G. Scheler, U. Haubenreisser, and H. Rosenberger, "High-Resolution ^{1}H-NMR in Solids with Multiple-Pulse Sequences and Magic-Angle Sample Spinning at 270-MHz," J. Magn. Reson. **44,** 134–44 (1981).

[127] R. K. Harris, P. Jackson, L. H. Merwin, B. J. Say, and G. Hagele, "Perspectives in High-Resolution Solid-State Nuclear Magnetic- Resonance, with Emphasis on Combined Rotation and Multiple- Pulse Spectroscopy," J. Chem. Soc.-Faraday Trans. **84,** 3649–72 (1988).

[128] A. Kubo and C. A. McDowell, "One-Dimensional and 2-Dimensional ^{31}P Cross-Polarization Magic-Angle-Spinning Nuclear-Magnetic-Resonance Studies on 2-Spin Systems with Homonuclear Dipolar Coupling and J Coupling," J. Chem. Phys. **92,** 7156–70 (1990).

[129] R. Challoner, T. Nakai, and C. A. McDowell, "J-Coupling in Chemically Equivalent Spin Pairs as Studied by Solid-State Nuclear-Magnetic-Resonance," J. Chem. Phys. **94,** 7038–45 (1991).

[130] L. Duma, W. C. Lai, M. Carravetta, L. Emsley, S. P. Brown, and M. H. Levitt, "Principles of Spin-Echo Modulation by J-Couplings in Magic-Angle-Spinning Solid-State NMR," Chem. Phys. Chem. **5,** 815–33 (2004).

[131] S. Dusold and A. Sebald, "Dipolar Recoupling under Magic-Angle Spinning Conditions," Annual Reports on NMR Spectroscopy, Vol 41 **41,** 185–264 (2000).

[132] D. K. Sodickson, M. H. Levitt, S. Vega, and R. G. Griffin, "Broad-Band Dipolar Recoupling in the Nuclear-Magnetic-Resonance of Rotating Solids," J. Chem. Phys. **98,** 6742–48 (1993).

[133] R. Tycko and G. Dabbagh, "Measurement of Nuclear Magnetic Dipole-Dipole Couplings in Magic Angle Spinning NMR," Chem. Phys. Lett. **173,** 461–65 (1990).

[134] R. Tycko and G. Dabbagh, "Double-Quantum Filtering in Magic-Angle-Spinning NMR-Spectroscopy - an Approach to Spectral Simplification and Molecular-Structure Determination," J. Am. Chem. Soc. **113,** 9444–48 (1991).

[135] N. C. Nielsen, H. Bildsøe, H. J. Jakobsen, and M. H. Levitt, "Double-Quantum Homonuclear Rotary Resonance - Efficient Dipolar Recovery in Magic-Angle-Spinning Nuclear-Magnetic-Resonance," J. Chem. Phys. **101,** 1805–12 (1994).

[136] Y. K. Lee, N. D. Kurur, M. Helmle, O. G. Johannessen, N. C. Nielsen, and M. H. Levitt, "Efficient Dipolar Recoupling in the NMR of Rotating Solids - a Sevenfold Symmetrical Radiofrequency Pulse Sequence," Chem. Phys. Lett. **242,** 304–09 (1995).

[137] D. A. Fletcher, R. F. McMeeking, and D. Parkin, "The United Kingdom Chemical Database Service," J. Chem. Inform. Comput. Sci. **36,** 746–49 (1996).

[138] J. P. Perdew, K. Burke, and M. Ernzerhof, "Generalized Gradient Approximation Made Simple," Phys. Rev. Lett. **77,** 3865–68 (1996).

[139] M. C. Payne, M. P. Teter, D. C. Allan, T. A. Arias, and J. D. Joannopoulos, "Iterative Minimization Techniques for Abinitio Total-Energy Calculations - Molecular-Dynamics and Conjugate Gradients," Rev. Mod. Phys. **64,** 1045–97 (1992).

[140] M. D. Segall, P. J. D. Lindan, M. J. Probert, C. J. Pickard, P. J. Hasnip, S. J. Clark, and M. C. Payne, "First-Principles Simulation: Ideas, Illustrations and the CASTEP Code," J. Phys.-Condes. Matter **14,** 2717–44 (2002).

[141] S. J. Clark, M. D. Segall, C. J. Pickard, P. J. Hasnip, M. J. Probert, K. Refson, and

M. C. Payne, “First Principles Methods Using CASTEP,” Z. Kristall. **220,** 567–70 (2005).

[142] K. Brandenburg and H. Putz, “Diamond Version 3,”, 2004.

[143] PARATEC, “(Parallel Total Energy Code) by B. Pfrommer and D. Raczkowski and A. Canning and S.G. Louie, Lawrence Berkeley National Laboratory (with contributions from F. Mauri and M. Cote and Y. Yoon and C. Pickard and P. Haynes) for more information see www.nersc.gov/projects/paratec,”.

[144] H. J. Monkhorst and J. D. Pack, “Special Points for Brillouin-Zone Integrations,” Phys. Rev. B **13,** 5188–92 (1976).

[145] C. Gervais, R. Dupree, K. J. Pike, C. Bonhomme, M. Profeta, C. J. Pickard, and F. Mauri, “Combined First-Principles Computational and Experimental Multinuclear Solid-State NMR Investigation of Amino Acids,” J. Phys. Chem. A **109,** 6960–69 (2005).

[146] J. R. Yates, S. E. Dobbins, C. J. Pickard, F. Mauri, P. Y. Ghi, and R. K. Harris, “A Combined First Principles Computational and Solid-State NMR Study of a Molecular Crystal: Flurbiprofen,” Phys. Chem. Chem. Phys. **7,** 1402–07 (2005).

[147] S. A. Joyce, J. R. Yates, C. J. Pickard, and F. Mauri, “A First Principles Theory of Nuclear Magnetic Resonance J-Coupling in Solid-State Systems,” J. Chem. Phys. 127 (2007).

[148] N. Troullier and J. L. Martins, “Efficient Pseudopotentials for Plane-Wave Calculations,” Phys. Rev. B **43,** 1993–2006 (1991).

[149] P. E. Blochl, “Projector Augmented-Wave Method,” Phys. Rev. B **50,** 17953–79 (1994).

[150] J. S. Frye and G. E. Maciel, “Setting the Magic Angle Using a Quadrupolar Nuclide,” J. Magn. Reson. **48,** 125–31 (1982).

[151] J. Baum, M. Munowitz, A. N. Garroway, and A. Pines, “Multiple-Quantum Dynamics in Solid-State NMR,” J. Chem. Phys. **83,** 2015–25 (1985).

[152] J. Baum and A. Pines, “NMR-Studies of Clustering in Solids,” J. Am. Chem. Soc. **108,** 7447–54 (1986).

[153] D. M. Gregory, G. M. Wolfe, T. P. Jarvie, J. C. Sheils, and G. P. Drobny, “Double-Quantum Filtering in Magic-Angle-Spinning NMR Spectroscopy Applied to DNA Oligomers,” Mol. Phys. **89,** 1835–49 (1996).

[154] B. Reif, C. P. Jaroniec, C. M. Rienstra, M. Hohwy, and R. G. Griffin, “^{1}H-^{1}H MAS Correlation Spectroscopy and Distance Measurements in a Deuterated Peptide,” J. Magn. Reson. **151,** 320–27 (2001).

[155] A. Lesage, L. Emsley, F. Penin, and A. Bockmann, “Investigation of Dipolar-Mediated Water-Protein Interactions in Microcrystalline Crh by Solid-State NMR Spectroscopy,” J. Am. Chem. Soc. **128,** 8246–55 (2006).

[156] J. P. Bradley, C. Tripon, C. Filip, and S. P. Brown, “Determining Relative Proton-Proton Proximities from the Build-up of Two-Dimensional Correlation Peaks in ^{1}H Double-Quantum MAS NMR: Insight from Multi-Spin Density-Matrix Simulations,” Phys. Chem. Chem. Phys. **11,** 6941–52 (2009).

[157] A. Lesage, M. Bardet, and L. Emsley, “Through-Bond Carbon-Carbon Connectivities in Disordered Solids by NMR,” J. Am. Chem. Soc. **121,** 10987–93 (1999).

[158] R. A. Olsen, J. Struppe, D. W. Elliott, R. J. Thomas, and L. J. Mueller, “Through-Bond ^{13}C-^{13}C Correlation at the Natural Abundance Level: Refining Dynamic Regions in the Crystal Structure of Vitamin-D-3 with Solid-State NMR,” J. Am. Chem. Soc. **125,** 11784–85 (2003).

[159] L. L. Chen, R. A. Olsen, D. W. Elliott, J. M. Boettcher, D. H. H. Zhou, C. M. Rienstra, and L. J. Mueller, “Constant-Time through-Bond ^{13}C Correlation Spectroscopy for

Assigning Protein Resonances with Solid-State NMR Spectroscopy," J. Am. Chem. Soc. **128,** 9992–93 (2006).

[160] D. Lee, J. Struppe, D. W. Elliott, L. J. Mueller, and J. J. Titman, "Sensitive Absorptive Refocused Scalar Correlation NMR Spectroscopy in Solids," Phys Chem Chem Phys **11,** 3547–53 (2009).

[161] A. Bockmann, "Structural and Dynamic Studies of Proteins by High-Resolution Solid-State NMR," C. R. Chim. **9,** 381–92 (2006).

[162] R. Tycko, "Molecular Structure of Amyloid Fibrils: Insights from Solid-State NMR," Q. Rev. Biophys. **39,** 1–55 (2006).

[163] P. Zhang, A. Klymachyov, S. Brown, J. G. Ellington, and P. J. Grandinetti, "Solid-State ^{13}C NMR Investigations of the Glycosidic Linkage in α-α' Trehalose," Solid State Nucl. Magn. Reson. **12,** 221–25 (1998).

[164] T. H. Sefzik, J. B. Houseknecht, T. M. Clark, S. Prasad, T. L. Lowary, Z. Gan, and P. J. Grandinetti, "Solid-State ^{17}O NMR in Carbohydrates," Chem. Phys. Lett. **434,** 312–15 (2007).

[165] D. K. Hincha, E. Zuther, and A. G. Heyer, "The Preservation of Liposomes by Raffinose Family Oligosaccharides During Drying Is Mediated by Effects on Fusion and Lipid Phase Transitions," Biochim. Biophys. Acta-Biomembr. **1612,** 172–77 (2003).

[166] P. Breeuwer, A. Lardeau, M. Peterz, and H. M. Joosten, "Desiccation and Heat Tolerance of Enterobacter Sakazakii," J. Appl. Microbiol. **95,** 967–73 (2003).

[167] A. Patist and H. Zoerb, "Preservation Mechanisms of Trehalose in Food and Biosystems," Colloid Surf. B-Biointerfaces **40,** 107–13 (2005).

[168] J. Ubbink and J. Kruger, "Physical Approaches for the Delivery of Active Ingredients in Foods," Trends Food Sci. Technol. **17,** 244–54 (2006).

[169] H. Feinberg, D. A. Mitchell, K. Drickamer, and W. I. Weis, "Structural Basis for Selective Recognition of Oligosaccharides by DC-SIGN and DC-SIGNR," Science **294,** 2163–66 (2001).

[170] F. Van Bambeke, "Glycopeptides in Clinical Development: Pharmacological Profile and Clinical Perspectives," Curr. Opin. Pharmacol. **4,** 471–78 (2004).

[171] A. Vyas and S. Saraf, "Cyclodextrin Based Novel Drug Delivery Systems," J. Incl. Phenom. Macrocycl. Chem. **62,** 23–42 (2008).

[172] M. E. Gress and G. A. Jeffrey, "Neutron-Diffraction Refinement of Crystal-Structure of β-Maltose Monohydrate," Acta Cryst. **B33,** 2490–95 (1977).

[173] R. Graf, D. E. Demco, J. Gottwald, S. Hafner, and H. W. Spiess, "Dipolar Couplings and Internuclear Distances by Double-Quantum Nuclear Magnetic Resonance Spectroscopy of Solids," J. Chem. Phys. **106,** 885–95 (1997).

[174] S. P. Brown, I. Schnell, J. D. Brand, K. Mullen, and H. W. Spiess, "The Competing Effects of $\pi - \pi$ Packing and Hydrogen Bonding in a Hexabenzocoronene Carboxylic Acid Derivative: A ^{1}H Solid-State MAS NMR Investigation," Phys. Chem. Chem. Phys. **2,** 1735–45 (2000).

[175] J. N. Dumez and C. J. Pickard, "Calculation of NMR Chemical Shifts in Organic Solids: Accounting for Motional Effects," J. Chem. Phys. **130,** 104701–08 (2009).

[176] S. Rossano, F. Mauri, C. J. Pickard, and I. Farnan, "First-Principles Calculation of ^{17}O and ^{25}Mg NMR Shieldings in Mgo at Finite Temperature: Rovibrational Effect in Solids," J. Phys. Chem. B **109,** 7245–50 (2005).

[177] K. Ruud, P. O. Astrand, and P. R. Taylor, "Zero-Point Vibrational Effects on Proton Shieldings: Functional-Group Contributions from Ab Initio Calculations," J. Am. Chem. Soc. **123,** 4826–33 (2001).

[178] S. Lena, S. Masiero, S. Pieraccini, and G. P. Spada, "Guanosine Hydrogen-Bonded

Scaffolds: A New Way to Control the Bottom-up Realisation of Well-Defined Nanoarchitectures," Chem.-Eur. J. **15,** 7792–806 (2009).

[179] J. L. Sessler and R. Z. Wang, "A New Base-Pairing Motif Based on Modified Guanosines," Angew. Chem., Int. Ed. Engl. **37,** 1726–29 (1998).

[180] G. Gottarelli, S. Masiero, E. Mezzina, G. P. Spada, P. Mariani, and M. Recanatini, "The Self-Assembly of a Lipophilic Deoxyguanosine Derivative and the Formation of a Liquid-Crystalline Phase in Hydrocarbon Solvents," Helv. Chim. Acta **81,** 2078–92 (1998).

[181] V. Andrisano, G. Gottarelli, S. Masiero, E. H. Heijne, S. Pieraccini, and G. P. Spada, "Enantioselective Extraction of Dinitrophenyl Amino Acids Mediated by Lipophilic Deoxyguanosine Derivatives: Chiral Discrimination by Self-Assembly," Angew. Chem., Int. Ed. Engl. **38,** 2386–88 (1999).

[182] S. B. Zimmerman, G. H. Cohen, and D. R. Davies, "X-Ray Fiber Diffraction and Model-Building Study of Polyguanylic Acid and Polyinosinic Acid," J. Mol. Biol. **92,** 181–84 (1975).

[183] J. A. Walmsley and J. F. Burnett, "A New Model for the K+-Induced Macromolecular Structure of Guanosine 5'-Monophosphate in Solution," Biochemistry **38,** 14063–68 (1999).

[184] D. Sen and W. Gilbert, "Formation of Parallel 4-Stranded Complexes by Guanine-Rich Motifs in DNA and Its Implications for Meiosis," Nature **334,** 364–66 (1988).

[185] W. I. Sundquist and A. Klug, "Telomeric DNA Dimerizes by Formation of Guanine Tetrads between Hairpin Loops," Nature **342,** 825–29 (1989).

[186] A. L. Marlow, E. Mezzina, G. P. Spada, S. Masiero, J. T. Davis, and G. Gottarelli, "Cation-Templated Self-Assembly of a Lipophilic Deoxyguanosine: Solution Structure of a K+-dG$_8$ Octamer," J. Org. Chem. **64,** 5116–23 (1999).

[187] T. C. Marsh and E. Henderson, "G-Wires - Self-Assembly of a Telomeric Oligonucleotide, D(GGGGTTGGGG), into Large Superstructures," Biochemistry **33,** 10718–24 (1994).

[188] J. T. Davis, "G-Quartets 40 Years Later: From 5'-GMP to Molecular Biology and Supramolecular Chemistry," Angew. Chem., Int. Ed. Engl. **43,** 668–98 (2004).

[189] J. T. Davis and G. P. Spada, "Supramolecular Architectures Generated by Self-Assembly of Guanosine Derivatives," Chem. Soc. Rev. **36,** 296–313 (2007).

[190] T. Giorgi, F. Grepioni, I. Manet, P. Mariani, S. Masiero, E. Mezzina, S. Pieraccini, L. Saturni, G. P. Spada, and G. Gottarelli, "Gel-Like Lyomesophases Formed in Organic Solvents by Self-Assembled Guanine Ribbons," Chem.-Eur. J. **8,** 2143–52 (2002).

[191] R. Rinaldi, E. Branca, R. Cingolani, S. Masiero, G. P. Spada, and G. Gottarelli, "Photodetectors Fabricated from a Self-Assembly of a Deoxyguanosine Derivative," Appl. Phys. Lett. **78,** 3541–43 (2001).

[192] A. Neogi, J. Li, P. B. Neogi, A. Sarkar, and H. Morkoc, "Self-Assembled Modified Deoxyguanosines Conjugated to GaN Quantum Dots for Biophotonic Applications," Electron. Lett. **40,** 1605–06 (2004).

[193] R. Rinaldi, G. Maruccio, A. Biasco, V. Arima, R. Cingolani, T. Giorgi, S. Masiero, G. P. Spada, and G. Gottarelli, "Hybrid Molecular Electronic Devices Based on Modified Deoxyguanosines," Nanotechnology **13,** 398–403 (2002).

[194] G. Maruccio, P. Visconti, V. Arima, S. D'Amico, A. Blasco, E. D'Amone, R. Cingolani, R. Rinaldi, S. Masiero, T. Giorgi, and G. Gottarelli, "Field Effect Transistor Based on a Modified DNA Base," Nano. Lett. **3,** 479–83 (2003).

[195] M. Gellert, M. N. Lipsett, and D. R. Davies, "Helix Formation by Guanylic Acid," Proc. Natl. Acad. Sci. U. S. A. **48,** 2013–18 (1962).

[196] P. Tougard, J. F. Chantot, and Guschlba.W, "Nucleoside Conformations. 10. X-Ray

Fiber Diffraction Study of Gels of Guanine Nucleosides," Biochimica Et Biophysica Acta **308,** 9–16 (1973).

[197] T. J. Pinnavaia, C. L. Marshall, C. M. Mettler, C. I. Fisk, H. T. Miles, and E. D. Becker, "Alkali-Metal Ion Specificity in Solution Ordering of a Nucleotide, 5'-Guanosine Monophosphate," J. Am. Chem. Soc. **100,** 3625–27 (1978).

[198] S. L. Forman, J. C. Fettinger, S. Pieraccini, G. Gottareli, and J. T. Davis, "Toward Artificial Ion Channels: A Lipophilic G-Quadruplex," J. Am. Chem. Soc. **122,** 4060–67 (2000).

[199] G. Gottarelli, S. Masiero, and G. P. Spada, "Self-Assembly in Organic Solvents of a Deoxyguanosine Derivative Induced by Alkali Metal Picrates," J. Chem. Soc.-Chem. Commun. pp. 2555–57 (1995).

[200] E. Mezzina, P. Mariani, R. Itri, S. Masiero, S. Pieraccini, G. P. Spada, F. Spinozzi, J. T. Davis, and G. Gottarelli, "The Self-Assembly of a Lipophilic Guanosine Nucleoside into Polymeric Columnar Aggregates: The Nucleoside Structure Contains Sufficient Information to Drive the Process Towards a Strikingly Regular Polymer," Chem.-Eur. J. **7,** 388–95 (2001).

[201] G. Gottarelli, S. Masiero, E. Mezzina, S. Pieraccini, J. P. Rabe, P. Samori, and G. P. Spada, "The Self-Assembly of Lipophilic Guanosine Derivatives in Solution and on Solid Surfaces," Chem.-Eur. J. **6,** 3242–48 (2000).

[202] J. L. Sessler, M. Sathiosatham, K. Doerr, V. Lynch, and K. A. Abboud, "A G-Quartet Formed in the Absence of a Templating Metal Cation: A New 8-(N,N-Dimethylaniline) Guanosine Derivative," Angew. Chem., Int. Ed. Engl. **39,** 1300–03 (2000).

[203] S. Lena, M. A. Cremonini, F. Federiconi, G. Gottarelli, C. Graziano, L. Laghi, P. Mariani, S. Masiero, S. Pieraccini, and G. P. Spada, "The Supramolecular Helical Architecture of 8-Oxoinosine and 8-Oxoguanosine Derivatives," Chem.-Eur. J. **13,** 3441–49 (2007).

[204] T. Giorgi, S. Lena, P. Mariani, M. A. Cremonini, S. Masiero, S. Pieraccini, J. P. Rabe, P. Samori, G. P. Spada, and G. Gottarelli, "Supramolecular Helices Via Self-Assembly of 8-Oxoguanosines," J. Am. Chem. Soc. **125,** 14741–49 (2003).

[205] T. N. Pham, S. Masiero, G. Gottarello, and S. P. Brown, "Identification by ^{15}N Refocused Inadequate MAS NMR of Intermolecular Hydrogen Bonding That Directs the Self-Assembly of Modified DNA Bases," J. Am. Chem. Soc. **127,** 16018–19 (2005).

[206] A. Wong, J. C. Fettinger, S. L. Forman, J. T. Davis, and G. Wu, "The Sodium Ions inside a Lipophilic G-Quadruplex Channel as Probed by Solid-State ^{23}Na NMR," J. Am. Chem. Soc. **124,** 742–43 (2002).

[207] W. Saenger, *Principles of Nucleic Acid Structure* (Springer-Verlag, 1984).

[208] E. Dias, J. L. Battiste, and J. R. Williamson, "Chemical Probe for Glycosidic Conformation in Telomeric DNAS," J. Am. Chem. Soc. **116,** 4479–80 (1994).

[209] J. W. Steed, "Should Solid-State Molecular Packing Have to Obey the Rules of Crystallographic Symmetry?," Cryst. Eng. Comm. pp. 169–79 (2003).

[210] G. R. Desiraju, "On the Presence of Multiple Molecules in the Crystal Asymmetric Unit (Z ' > 1)," Cryst. Eng. Comm. **9,** 91–92 (2007).

[211] G. R. Desiraju, *Crystal Engineering* (Elsevier Science, 1989).

[212] C. P. Brock and L. L. Duncan, "Anomalous Space-Group Frequencies for Monoalcohols C_nH_mOH," Chem. Mat. **6,** 1307–12 (1994).

[213] G. P. A. Yap, R. M. Claramunt, C. López, M. A. García, C. Pérez-Medina, I. Alkorta, and J. Elguero, "The Structures of Chiral and Racemic Campho[2,3-c]Pyrazole: A Combined Crystallographic, Solid-State NMR and Computational Study," J. Mol. Struct. **965,** 74–81 (2010).

[214] A. L. Llamas-Saiz, C. Foces-Foces, I. Sobrados, J. Elguero, and W. Meutermans,

“(4S,7R)-7,8,8-Trimethyl-4,5,6,7-Tetrahydro-4,7-Methano-^{1}H(2H)-Indazole (Campho 2,3-C Pyrazole) - Comparison between the X-Ray Structure and ^{13}C NMR Data in the Solid-State,” Acta Crystallogr. Sect. C-Cryst. Struct. Commun. **49,** 724–29 (1993).

[215] I. Alkorta and J. Elguero, “GIAO Calculations of Chemical Shifts in Heterocyclic Compounds,” Struct. Chem. **14,** 377–89 (2003).

[216] R. Ditchfield, “Self-Consistent Perturbation-Theory of Diamagnetism. 1. Gauge-Invariant LCAO Method for NMR Chemical-Shifts,” Mol. Phys. **27,** 789–807 (1974).

[217] K. M. Anderson, K. Afarinkia, H. W. Yu, A. E. Goeta, and J. W. Steed, “When Z ’=2 Is Better Than Z ’=1-Supramolecular Centrosymmetric Hydrogen-Bonded Dimers in Chiral Systems,” Cryst. Growth Des. **6,** 2109–13 (2006).

[218] G. R. Desiraju and T. Steiner, *The Weak Hydrogen Bond in Structural Chemistry and Biology* (Oxford University Press, 1999).

[219] G. R. Desiraju, “C-H $\cdots$ O and Other Weak Hydrogen Bonds. From Crystal Engineering to Virtual Screening,” Chem. Commun. pp. 2995–3001 (2005).

[220] G. R. Desiraju, “Hydrogen Bridges in Crystal Engineering: Interactions without Borders,” Acc. Chem. Res. **35,** 565–73 (2002).

[221] C. Ochsenfeld, S. P. Brown, I. Schnell, J. Gauss, and H. W. Spiess, “Structure Assignment in the Solid State by the Coupling of Quantum Chemical-Calculations with NMR Experiments: A Columnar Hexabenzocoronene Derivative,” J. Am. Chem. Soc. **123,** 2597–606 (2001).

[222] C. Ochsenfeld, F. Koziol, S. P. Brown, T. Schaller, U. P. Seelbach, and F. G. Klrner, “A Study of a Molecular Tweezer Host-Guest System by a Combination of Quantum-Chemical Calculations and Solid-State NMR Experiments,” Solid State NMR **22,** 128–53 (2002).

[223] M. Potrzebowski, X. Assfeld, K. Ganicz, S. Olejniczak, A. Cartier, C. Gardiennet, and P. Tekely, “An Experimental and Theoretical Study of the ^{13}C and ^{31}P Chemical Shielding Tensors in Solid O-Phosphorylated Amino Acids ,” J. Am. Chem. Soc. **125,** 4223 (2003).

[224] A. J. Dingley and S. Grzesiek, “Direct Observation of Hydrogen Bonds in Nucleic Acid Base Pairs by Internucleotide $^2J_{\mathrm{NN}}$ Couplings,” J. Am. Chem. Soc. **120,** 8293–97 (1998).

[225] S. Grzesiek, F. Cordier, V. Jaravine, and M. Barfield, “Insights into Biomolecular Hydrogen Bonds from Hydrogen Bond Scalar Couplings,” Prog. Nucl. Magn. Reson. Spectrosc. **45,** 275–300 (2004).

[226] A. Lesage, C. Auger, S. Caldarelli, and L. Emsley, “Determination of through-Bond Carbon-Carbon Connectivities in Solid-State NMR Using the INADEQUATE Experiment,” J. Am. Chem. Soc. **119,** 7867–68 (1997).

[227] S. P. Brown, M. Pérez-Torralba, D. Sanz, R. M. Claramunt, and L. Emsley, “The Direct Detection of a Hydrogen Bond in the Solid State by NMR through the Observation of a Hydrogen-Bond Mediated ^{15}N-^{15}N J Coupling,” J. Am. Chem. Soc. **124,** 1152–53 (2002).

[228] S. E. Ashbrook and M. E. Smith, “Solid State ^{17}O NMR - an Introduction to the Background Principles and Applications to Inorganic Materials,” Chem. Soc. Rev. **35,** 718–35 (2006).

[229] G. Wu, “Solid-State ^{17}O NMR Studies of Organic and Biological Molecules,” Prog. Nucl. Magn. Reson. Spectrosc. **52,** 118–69 (2008).

[230] G. Wu and S. Dong, “Two-Dimensional ^{17}O Multiple Quantum Magic-Angle Spinning NMR of Organic Solids,” J. Am. Chem. Soc. **123,** 9119–25 (2001).

[231] G. Wu, S. Dong, R. Ida, and N. Reen, “A Solid-State ^{17}O Nuclear Magnetic Resonance Study of Nucleic Acid Bases,” J. Am. Chem. Soc. **124,** 1768–77 (2002).

[232] R. F. Stewart and L. H. Jensen, "Redetermination of the Crystal Structure of Uracil," Acta Cryst. **23,** 1102–05 (1967).

[233] P. J. Langley, J. Hulliger, R. Thaimattam, and G. R. Desiraju, "Supramolecular Synthons Mediated by Weak Hydrogen Bonding: Forming Linear Molecular Arrays Via C C-H $\cdots$ N C and C C-H $\cdots$ O_2N Recognition," New J. Chem. **22,** 1307–09 (1998).

[234] J. P. Amoureux, J. Trébosc, J. W. Wiench, D. Massiot, and M. Pruski, "Measurement of J-Couplings between Spin-1/2 and Quadrupolar Nuclei by Frequency Selective Solid-State NMR," Solid State Nucl. Magn. Reson. **27,** 228–32 (2005).

[235] D. Massiot, F. Fayon, B. Alonso, J. Trébosc, and J. P. Amoureux, "Chemical Bonding Differences Evidenced from J-Coupling in Solid State NMR Experiments Involving Quadrupolar Nuclei," J. Magn. Reson. **164,** 160–64 (2003).

[236] V. Montouillout, C. M. Morais, A. Douy, F. Fayon, and D. Massiot, "Toward a Better Description of Gallo-Phosphate Materials in Solid-State NMR: 1D and 2D Correlation Studies," Magn. Reson. Chem. **44,** 770–75 (2006).

[237] J. E. Del Bene and J. Elguero, "Predicted Signs of Reduced Two-Bond Spin-Spin Coupling Constants (${}^{2h}K_{\text{X-Y}}$) across X-H-Y Hydrogen Bonds," Magn. Reson. Chem. **42,** 421–23 (2004).

[238] J. E. Del Bene and J. Elguero, "Predicted Signs of One-Bond Spin-Spin Coupling Constants (${}^{1h}J_{\text{H-Y}}$) across X-H-Y Hydrogen Bonds for Complexes with Y=^{15}N, ^{17}O, and ^{19}F," J. Phys. Chem. A **108,** 11762–67 (2004).

[239] K. J. Pike, V. Lemaitre, A. Kukol, T. Anupõld, A. Samoson, A. P. Howes, A. Watts, M. E. Smith, and R. Dupree, "Solid-State ^{17}O NMR of Amino Acids," J. Phys. Chem. B **108,** 9256–63 (2004).

[240] A. Wong, A. P. Howes, K. J. Pike, V. Lemaitre, A. Watts, T. Anupõld, J. Past, A. Samoson, R. Dupree, and M. E. Smith, "New Limits for Solid-State ^{17}O NMR Spectroscopy: Complete Resolution of Multiple Oxygen Sites in a Simple Biomolecule," J. Am. Chem. Soc. **128,** 7744–45 (2006).

[241] V. Lemaitre, M. R. R. de Planque, A. P. Howes, M. E. Smith, R. Dupree, and A. Watts, "Solid-State ^{17}O NMR as a Probe for Structural Studies of Proteins in Biomembranes," J. Am. Chem. Soc. **126,** 15320–21 (2004).

[242] I. C. M. Kwan, X. Mo, and G. Wu, "Probing Hydrogen Bonding and Ion-Carbonyl Interactions by Solid-State ^{17}O NMR Spectroscopy: G-Ribbon and G-Quartet," J. Am. Chem. Soc. **129,** 2398–407 (2007).